# Technical Annals

Vol 1, No 6 (2024)

Technical Annals

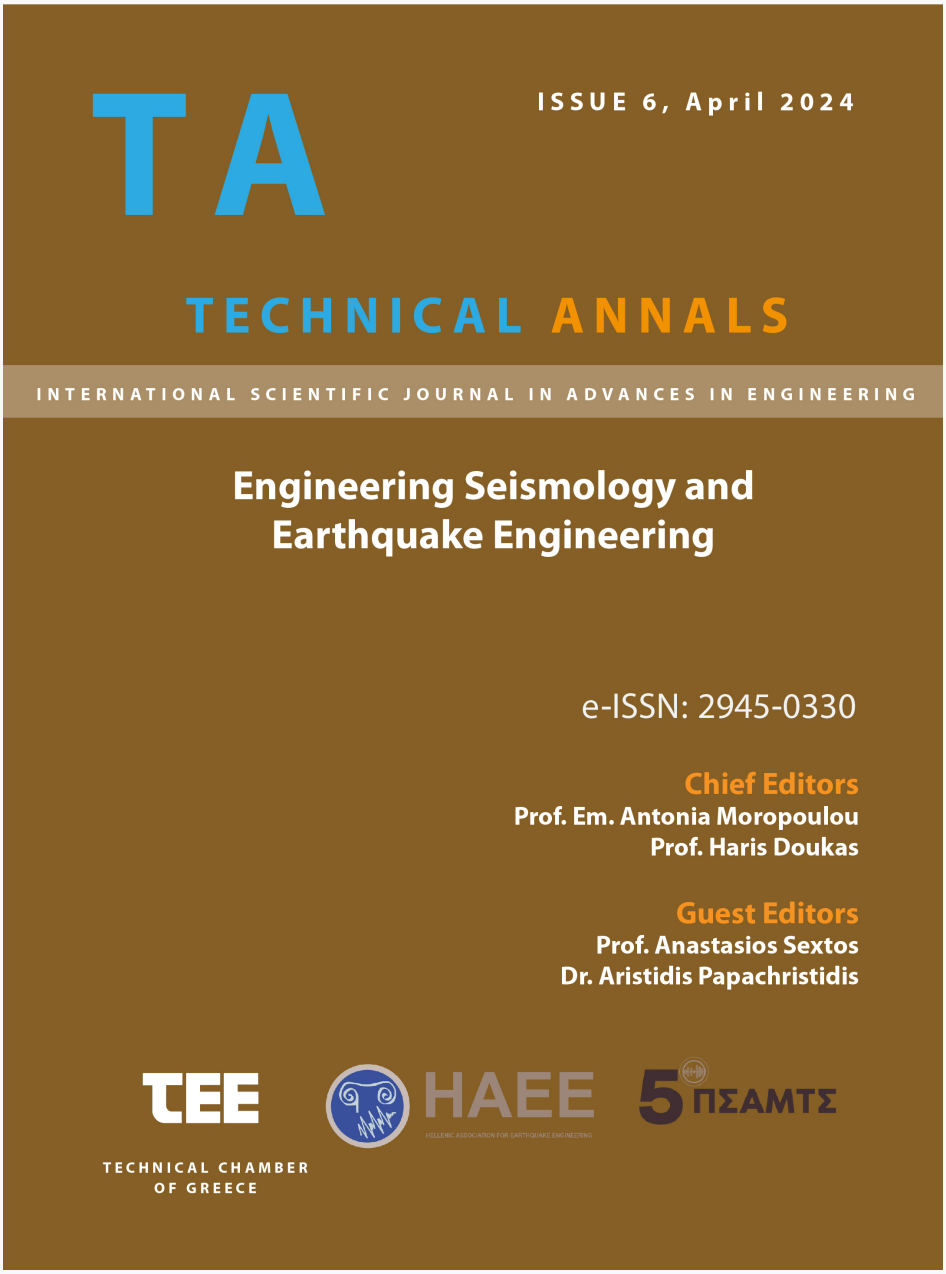

ISSUE 6, April 2024

# TA

# TECHNICAL ANNALS

INTERNATIONAL SCIENTIFIC JOURNAL IN ADVANCES IN ENGINEERING

## Engineering Seismology and Earthquake Engineering

e-ISSN: 2945-0330

**Chief Editors**
Prof. Em. Antonia Moropoulou
Prof. Haris Doukas

**Guest Editors**
Prof. Anastasios Sextos
Dr. Aristidis Papachristidis

TEE
TECHNICAL CHAMBER OF GREECE

HAEE
HELLENIC ASSOCIATION FOR EARTHQUAKE ENGINEERING

5 ΠΣΑΜΤΣ

# Technical Annals
Journal of the Technical Chamber of Greece

# Contents

# Technical Annals

## Editorial Board Members

Panas Antonios

Dr. Civil Engineer

Pla-Karidi Danae

Dr. Electrical and Computer Engineer, Post Doctoral Researcher

*Athina Research Center*

## Scientific Council Members

Triantafyllou Savvas

Dr. Civil Engineer, Assistant Professor

*National Technical University of Athens - School of Civil Engineering*

Klabatsea Irene

Dr. Architect Engineer, Assistant Professor

*National Technical University of Athens - School of Architecture*

Ioannidis Charalambos

Dr. Rural and Surveying Engineer, Professor

*National Technical University of Athens - School of Rural, Surveying and Geoinformatics Engineering*

Manolakos Dimitrios

Dr. Mechanical Engineer, Professor

*National Technical University of Athens - School of Mechanical Engineering*

Mansour Gabriel

Dr. Mechanical Engineer, Professor

*Aristotle University of Thessaloniki - Department of Mechanical Engineering*

Christodoulou Christos

Dr. Electrical and Computer Engineer, Adjunct Professor

*University of Thessaly - Department of Electrical and Computer Engineering*

Xenidis Anthimos

Dr. Mining and Metallurgical Engineer, Professor

*National Technical University of Athens - School of Mining and Metallurgical Engineering*

Loizidou Maria

Dr. Chemical Engineer, Emeritus Professor

*National Technical University of Athens - School of Chemical Engineering*

Ventikos Nikolaos

Dr. Naval Engineer, Assistant Professor

*National Technical University of Athens - School of Naval Architecture and Marine Engineering*

Gerogiannis Vasileios

Dr. Computer Engineer and Informatics, Professor

*University of Thessaly - Department of Digital Systems*

Tselios Vassilis

Dr. Regional Planning and Development Engineer, Associate Professor

*Panteion University of Social and Political Sciences - Department of Economic and Regional Development*

Saratsis Georgios

Dr. Mineral Resources Engineer, Laboratory Teaching Staff

*Technical University of Crete - School of Mineral Resources Engineering*

Akratos Christos

Dr. Envirovmental Engineer, Assistant Professor

*Democritus University of Thrace - Department of Civil Engineering*

## About

With particular joy, respect and commitment to the history of TEE (TCG), to the future of the scientific role of the Chamber and to the work of Greek Engineers as a whole, the Technical Chamber of Greece is proceeding with the publication of an international scientific journal. After several years without regular scientific publications, due to the special economic situation of the country, but having as a source of our history the TECHNICAL ANNALS, published by the TCG for decades, we undertake this role again to give another scientific podium to the Engineering community.

More specific, the Governing Committee of TCG, in accordance to Decisions No A14/Σ39/2021, A16/Σ7/2022 and A41/Σ16/2022, proceeded to publish of the Scientific Journal entitled «Technical Annals» by the Technical Chamber of Greece (TCG) concerned with Advances in Engineering, in English language. The content of the journal will be available electronically and via Open Access, through the e-Publishing service of the National Documentation Centre (EKT).

The Governing Committee of the TCG assigned the responsibility of the publication to the Editorial Board and the Scientific Board of the Journal.

We inform all Engineers IN Greece and in the World, the Academic and Research Community that we are proceeding with this publication in order to give the floor for communication, publicity and recognition, by the International Community, of the Research and Innovation that Engineers produce in practice, on construction sites,in urban space, in regional areas, in industry, in development, in environment, in energy, in the digital world, in universities, in research centers, in startups, in businesses, etc.

We aspire to attract your interest, find in you critical readers, feed your scientific work and publish the results of your research through the International Scientific Journal of TCG.

Looking forward to an important publication that we'd like to become everyone's business.

## Topics

The scope of the journal will include all Fields of Engineering:

1. Civil Engineering
2. Architectural Engineering
3. Mechanical Engineering
4. Electrical & Computer Engineering
5. Rural & Surveying Engineering
6. Chemical Engineering
7. Mining & Metallurgical Engineering
8. Naval Architecture & Marine Engineering
9. Electronic Engineering
10. Engineering of Urban Planning & Regional Development
11. Environmental Engineering
12. Mineral Resources Engineering
13. Production & Management Engineering

Furthermore, it will be concerned with Interdisciplinary Thematic Areas, which are at the cutting edge of Research and Innovation, such as:

Agricultural Engineering and Food Processing, Artificial Intelligence, Aerodynamics, Bioengineering, Circular Economy, Climate Change, Cultural Heritage, Education and Learning Processes, Energy, Environment, Economy, Geoinformatics, Human Modelling, Industrial Symbiosis, Management and Quality Control, Material Science and Engineering, Naval Coastal and Maritime Design Engineering and

Planning, Spatial Planning, Sustainable Development, Systems' and Processes Engineering, Technology, Transportation, Processes, among others, and the thematic areas will be dynamically adjusted and determined taking into account both the progress of Science and Engineering, as well as future trends and the trending concerns and needs of Society.

## Information for Volume Editors and Authors

Moreover, conferences, in which TCG is either co-organizing or participating in their Organizing and Scientific Committee, will be able to submit a request to publish their Proceedings (in either Greek or English language) always through the "e-Publishing" mechanism, as long as the request has been submitted to TCG and has the approval of TCG's Governing Bodies, either six months before the conference date *(in cases where the proceedings are to be published prior to the conference initiation)*, or three months before the conference date *(in cases where the proceedings are to be issued after the Conference)*.

The Governing Committee of the TCG assigned the responsibility of the publication to the Editorial Board and the Scientific Board of the Journal; the list of members of each board is herein attached.

Antonia Moropoulou · Haris Doukas · Anastatios Sextos · Aristidis Papachristidis

# ISSUE

# Engineering Seismology and Earthquake Engineering

Fifth National (Hellenic) Congress on Earthquake Engineering and Engineering Seismology
Athens, Greece, October 20–22, 2022
Revised Selected Papers

# Editors


## Antonia Moropoulou

Dr. Chemical Engineer, Emeritus Professor,

*National Technical University of Athens - School of Chemical Engineering*

## Haris Doukas

Dr. Mechanical Engineer, Professor

*National Technical University of Athens- School of Electrical and Computer Engineering*

## Anastasios Sextos

Dr., Civil Engineer, Professor

*National Technical University of Athens & University of Bristol*

## Aristidis Papachristidis

Dr. Civil Engineer, Managing Director,

*3DR Engineering Software LTD & President of HAEE*


The Technical Chamber of Greece (TCG) decided to republish in English a Scientific International Open Access e-Journal. The "Technical Annals" - a journal which was counting decades of life following T.C.G. activities – will be edited by the T.C.G. through e-Publishing Platform at the EKT (National Documentation Centre) and will concern all the advancements in Engineering, referring to the disciplines:

- Civil Engineering
- Architect Engineering
- Mechanical Engineering
- Electrical & Computer Engineering
- Rural & Surveying Engineering
- Chemical Engineering
- Mining & Metallurgical Engineering
- Naval Architecture & Marine Engineering
- Electronic Engineering
- Engineering of Urban Planning & Regional Development
- Environmental Engineering
- Mineral Resources Engineering
- Production & Management Engineering

Referring also to interdisciplinary Thematic Areas at the forefront of Research and Innovation such as: Agricultural Engineering and Food Processing, Artificial Intelligence, Aerodynamics, Bioengineering, Circular Economy, Climate Change, Cultural Heritage, Education and Learning Processes, Energy, Environment, Economy, Geoinformatics, Human Modelling, Industrial Symbiosis, Management and Quality Control, Material Science and Engineering, Naval Coastal and Maritime Design Engineering and Planning, Spatial Planning, Sustainable Development, Systems' and Processes Engineering, Technology, Transportation, Processes, et al as dynamically will be defined by the progress of science and engineering, the future trends and the social needs.

Through the e-journal, TCG is aiming to publish at least three volumes per year, to connect Greek Engineers with the International Community of Engineering Science and Innovation, for the benefit of the public interest and the promotion of science through research, innovation, and development, in compliance with its constitutional targets.

Technical Annals is a peer-reviewed journal.

# Preface

The 5th National Congress on "Earthquake Engineering and Engineering Seismology", organized by Hellenic Association for Earthquake Engineering (HAEE), and Technical Chamber of Greece (TCG), was held during October 20-22, 2022, in Athens, Greece.

The conference covered offered the opportunity to discuss, primarily at a national level, novel methods for assessing seismic hazard and vulnerability of structures, new methods for seismic design and strengthening as well as recent advancements on new materials and construction processes. The lessons learned from major earthquakes in Greece and worldwide, and the rapid increase in computational efficiency combined with the developments in the field of information and communication technologies were also discussed towards safer structures and infrastructure that operate increasingly in a coupled manner.

With the publication of the new generation of Eurocodes expected in 2027, and in the wake of the new reality shaped by the challenges of the pandemic, the 5th National Congress on 'Earthquake Engineering and Engineering Seismology' aimed to rekindle dialogue within the Greek scientific and professional communities of engineers and seismologists.

A summary of the Conference topics is outlined below:

- Seismic Analysis and Design of Buildings (R/C, Steel, Masonry)
- Seismic Analysis and Design of Bridges
- Seismic Performance of Monuments and Historical Structures
- Eurocode 8 & Modern Codes for Design, Assessment and Retrofit of Structures
- Pre-earthquake Assessment of Public Buildings and Critical Structures
- Resilience of Public Networks and Infrastructures
- Seismic Design Based on Performance
- Earthquake Damage Repair and Strengthening Interventions
- Seismic Insulation of Structures – Innovative Methods for Upgrading Seismic Performance Level
- Instrumentation and Strong Seismic Motion Recording Networks
- Modern Numerical Methods for the Analysis of Seismic Behavior of Structure
- High Performance Computational Methods
- Experimental Methods
- Mechanical / Recycling Behavior of Building Materials – New Materials
- Geotechnical Earthquake Engineering
- Soil-Structure Interaction. Soil Response.
- Technical Seismology
- Seismic Hazard Assessment
- Seismic Risk Assessment Methods and Management Strategy
- State Pre-earthquake Planning and Post-earthquake Crisis Management
- Energy Efficiency and Earthquake Protection
- Lessons Learned from recent Earthquakes in Samos (2020), Thessaly (2021) and Arkalochori (2021)

In total, 173 papers were accepted for oral presentation and publication, representing the work of 349 authors, after peer review and consequent revision. Despite the recent – at the time - COVID-19 pandemic, the Congress was attended by more than 600 delegates, researchers and practicing engineers, in physical presence.

In close collaboration with the Technical Chamber of Greece (TEE), and following the conclusion of the conference, HAEE issued an open call for the resubmission of selected papers in English, intended for publication in this special issue. A single-round, blind peer review process was conducted, with each paper receiving an average of three reviews. Accepted papers were subsequently published in this volume of *Technical Annals* following final peer review. Accordingly, 15 papers presented at the 5th National Congress on 'Earthquake Engineering and Engineering Seismology', encompassing all the above aspects, are featured in this special issue of *Technical Annals – International Scientific Journal in Advances in Engineering*.

The Conference highlighted the pressing need for continued research to enhance the seismic resilience of structures in Greece and other earthquake-prone regions. As new challenges emerge—ranging from aging infrastructure to evolving design standards and cascading/compounding multi-hazard related risks, ongoing innovation and collaboration are essential. This volume is a small contribution towards capitalizing on the knowledge shared, fostering future research and promoting integrated, forward-looking solutions for a safer, equitable and resilient build environment.

Prof. Anastasios Sextos, Conference Chair & Dr. Aristidis Papachristidis President of HAEE

# Special Issue Contents

## Artificial Intelligence



## Cultural Heritage



## Material Science and Engineering

## Earthquake Engineering

# Technical Annals
# Issue 6
# April 2024

# Artificial Intelligence

# Seismic risk assessment of buildings and infrastructures using Artificial Neural Networks: Empirical prediction equations

Morfidis Konstantinos[1], Sotiriadis Dimitrios[2], Stefanidou Sotiria[3], Markogiannaki Olga[3], Karatzetzou Anna[4], Margaris Basil[1]

[1]ITSAK,[2]Democritus University of Thrace,[3]REDI Engineering Solutions PC,
[4]Aristotle University of Thessaloniki
konmorf@gmail.com, dsotiria@civil.duth.gr,
sotiria.stefanidou@gmail.com, markogiannaki.olga@gmail.com,
akaratze@civil.auth.gr, margaris@itsak.gr

**Abstract.** The reliable assessment of the seismic risk, at urban, regional and national level, is extremely important for the government and society and contributes to the proper management of the pre-seismic crisis (interventions, strengthening of buildings and infrastructures), during the earthquake and post-earthquake. The seismic risk assessment involves many difficulties and uncertainties, as it depends on the successful implementation of several individual steps, starting with the identification of the elements at risk, continuing with the assessment of seismic risk and vulnerability and finishing with the estimation of the risk and losses of all types. In all the above methodological frameworks, the use of Artificial Neural Networks (ANNs) is proposed in the literature. Artificial Intelligence (AI)-based methodologies aim to improve the computational efficiency of simulations, by increasing the accuracy and reducing the computational cost. In this paper, a methodology using ANNs at the seismic hazard level is suggested to propose strong motion prediction equations (GMPE) derived from ANN training, by developing a methodological framework and a computational tool that enables continuous training and learning depending on the strong motion data that are fed to it. The proposed equations are compared with models in the literature to verify the reliability of their applicability.

**Keywords**: Seismic risk assessment, seismic hazard, artificial neural networks, ground motion prediction equations, seismic strong motion

## 1 Introduction

The methodologies for the assessment of seismic risk of buildings and infrastructures are a significant tool for the evaluation of the exposure, the prioritization of interventions and the development of a comprehensive upgrade plan. In this context, various methodologies have been developed over the last decades for the determination of the assessed exposure, seismic hazard and seismic fragility, which are the individual steps

for the assessment of seismic risk. At the same time, in several cases, computational tools have been developed which integrate the individual methodologies, but the computational cost and time required for the analysis and calculation of risk remain significant. For this purpose, methodologies have been developed, and utilized in the individual steps of seismic risk determination, that utilize ANNs for their direct and reliable determination. In particular, ANNs have been used to determine seismic vulnerability (Xie et al., 2020, Stefanidou et al., 2021), and very recently they have been proposed for seismic risk assessment (Ji et al., 2021). Additionally, the use of ANNs for seismic risk assessment can be applied to the prediction of seismic losses in areas with high seismicity (e.g. Leousis and Pnevmatikos, 2018, Pnevmatikos et al., 2020).

This paper presents a first step of a holistic seismic risk assessment methodology to be developed. The proposed methodology will be an integrated, versatile and easy-to-use methodology for assessing the vulnerability and seismic risk of buildings and infrastructures, fully adapted to the Greek data. It will be an important tool in the hands of the relevant authorities, contributing to the identification and recommendation of cost-effective lines of intervention and guidelines for addressing the problem pre-seismically and leading to the development of a common strategic plan to improve the resilience of buildings and infrastructures. More specifically, one of the most important steps of any seismic risk assessment methodology will be presented here, which is the assessment of the seismic hazard model. Ground motion predictive equations (GMPEs) derived from ANN training will be proposed, developing a methodological framework and a computational tool that enables continuous training and learning according to the strong motion (SM) data it is supplied with, and a comparison with models proposed in the literature will be presented to verify its applicability.

## 2 The method

The proposed methodology, part of which will be presented in the present paper, is illustrated in the form of a flowchart in Fig. 1.

The first step is the selection of the building stock and infrastructure to be studied and their visualization in a GIS application. The second step is the assessment of the seismic risk, which is the subject of the present study. The seismic hazard assessment of the study area is a necessary component in the seismic risk assessment. For this reason, a seismic hazard analysis is required. Rather than using a deterministic model for the worst earthquake that may affect the region of interest, probabilistic hazard analysis (PSHA) adopts a probability-based framework that considers all earthquake events that may occur in that region (Baker, 2008). PSHA begins by identifying potential earthquake sources and characterizing the distribution of earthquake magnitudes and distance from the source. Then the GMPEs are derived which give the earthquake intensity measure (IM) as a function of the earthquake source, path and local site conditions. One of the key steps of PSHA is therefore the calculation of appropriate GMPEs. There are several methodologies to derive these relationships and in some of them, the use of ANN is suggested (Ji et al., 2021).

The next step is the assessment of the seismic vulnerability through the vulnerability curves and the visualization of the vulnerability in a GIS platform. Numerical simulations based on the finite element method (FEM) are widely used to derive appropriate vulnerability curves. For reliable vulnerability assessment, a large number of numerical analyses are required, thus increasing the computational cost. One way to reduce this computational cost is the construction of meta-models, which can replace time-consuming FEM models. Meta-models, such as artificial neural networks (ANNs), represent a set of sophisticated statistical algorithms that capture input-output relations of physical models and make predictions according to these relations.

Finally, with the synthesis of all the above steps, the seismic risk for the study area and the exposed elements under study can be derived.

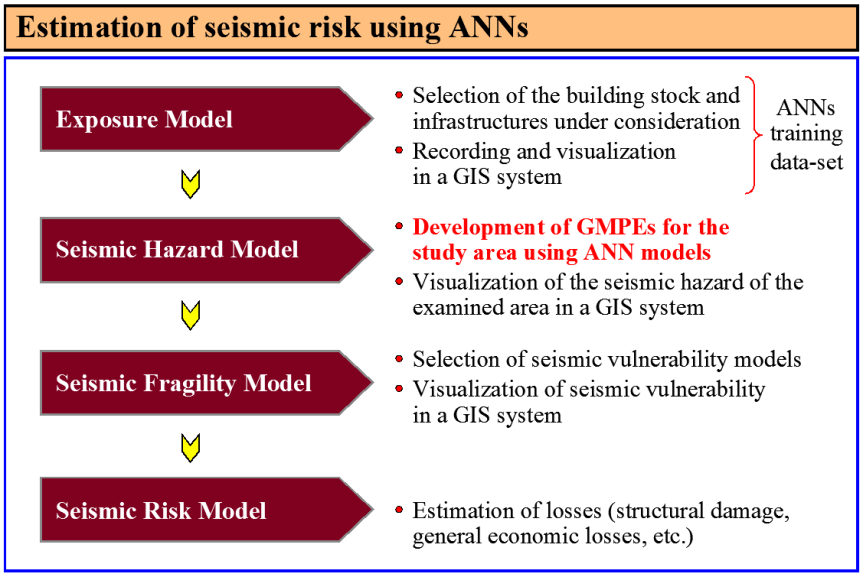


**Fig. 1.** Methodological framework for seismic risk assessment using ANNs

## 3 Development of equations by means of ANNs

In this section, the process of formulating the equations developed by applying ANNs will be briefly presented. These equations concern the correlation of PGA and PGV with the parameters of earthquake magnitude ($M_w$), its Focal Mechanism (FM), the shear wave velocity $V_{s30}$ at the site of recording, and the distance of the recording site from the projection of the rupture point on the surface ($R_{JB}$). The general form of the equations to be developed is:

$$\ln(\mathrm{PGA})=f_{\mathrm{PGA}}\left[M_w,\mathrm{FM},\ln(V_{s30}),\ln(R_{JB})\right] \text{ and } \ln(\mathrm{PGV})=f_{\mathrm{PGV}}\left[M_w,\mathrm{FM},\ln(V_{s30}),\ln(R_{JB})\right] \quad (1)$$

The equations were developed by applying Multilayered Feedforward Perceptron Neural Networks (MFPNN) (Haykin, 2009) which have the general form of Fig. 2. The application of MFPNNs and in particular those with a hidden layer has been proven to lead to the approximation of unknown functions (Hornik et al., 1989) by training them with appropriate training sample sets (training datasets). The procedure for deriving equations approximating unknown functions via MFPNN is described in detail in the paper of Morfidis and Kostinakis (2019).

As regards the training of the networks, it should be noted that a database consisting of 2492 samples was used. This database has been presented by Margaris et al. (2021) and is the most up-to-date in terms of SM data for the Greek region. An extensive parametric investigation was performed in order to identify the network configuration that leads to the optimal results. In the first stage, the criteria for the evaluation of the results extracted from the examined networks concerned the correlation factor R (R-factor) and the Mean Square Error (MSE). The parameters investigated are presented in Fig. 2.

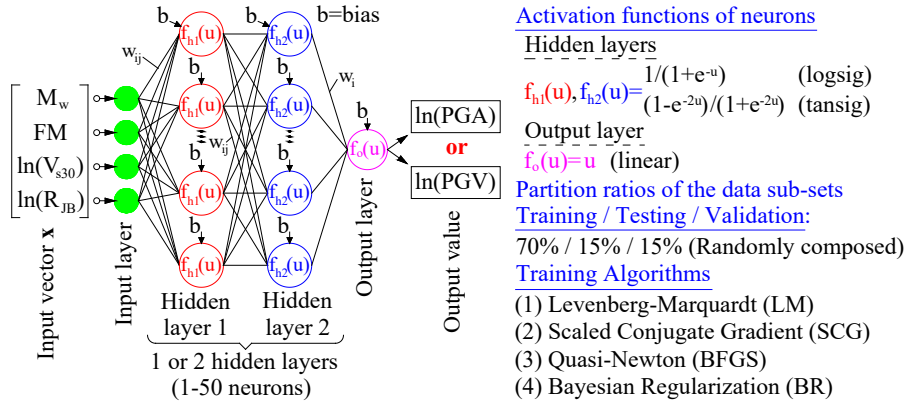


**Fig. 2.** Configuration and investigated parameters of the networks used

The training procedure applied is the cross-validation method for selecting the optimal model (Diamantaras and Botsis, 2019) which consists of the following 2 stages:

- Randomly dividing the set of training samples N times into three subsets and training the ANN with the training sub-set (training data sub-set, Fig. 2). In this process, all the ANN configuration parameters, as well as, the training algorithm are examined and finally the parameters that lead to the optimal performance (here based on the selected evaluation parameters R-factor and MSE) for the test sample portion (testing data sub-set, Fig. 2) are selected.
- After determining the parameters that compose the ANNs with optimal performance according to the criteria of the previous step, these networks are re-trained with the whole training dataset without splitting it into sub-sets.

In the context of the present study, the MFPNNs examined were initially classified into three general categories:

(a) Networks with one hidden layer and with a number of neurons ranging from 1 to 5. These networks were investigated to determine whether they can extract

reliable correlation equations of the examined parameters since the small number of neurons leads to the extraction of closed elegant relations.

(b) In networks with a hidden layer and with a number of neurons ranging from 6 to 30. These networks were investigated to examine how much a larger number of neurons can improve the correlation level.

(c) In networks with two hidden layers. Although networks with one hidden layer are capable of approximating unknown functions, the performance of networks with two hidden layers was also investigated. The addition of the second hidden layer significantly increases both the complexity and the training time especially when a large number of networks with different configurations are investigated as in the present case. Thus, the aim was to investigate whether this large increase in complexity is also reflected in the increase in performance of the corresponding networks.

The module of machine and deep learning of MATLAB R2022a was used for the development of ANNs and their training process. Table 1 summarizes the results for the optimal configurations of the networks of the three general categories.

**Table 1.** Comparative evaluation of the performance of the examined MFPNNs

| | | 1 Hidden layer | | | | 2 Hidden layers | |
|---|---|---|---|---|---|---|---|
| | | Number of neurons<=5 | | Number of neurons >5 | | Number of neurons 1-50 / layer | |
| SM Parameter / Evaluation Parameter | | Training Algorithm / Configuration | | Training Algorithm / Configuration | | Training Algorithm / Configuration | |
| PGA (cm/sec$^2$) | maxR | BR/log-5 | *0.934* | BR/tan-13 | 0.935 | BR/tan-log/36-24 | 0.936 |
| | minMSE | | *0.524* | BR/log-18 | 0.518 | BR/tan-tan/20-8 | 0.510 |
| PGV (cm/sec) | maxR | BR/log-5 | *0.921* | BR/log-23 | 0.922 | BR/log-log/14-38 | 0.924 |
| | minMSE | BR/tan-4 | *0.471* | | 0.467 | BR/tan-log/36-14 | 0.453 |

The most important conclusion drawn from the study in Table 1 is that adding a large number of neurons and/or a second hidden layer does not substantially improve the values of the R and MSE evaluation parameters. This means that it is possible to select MFPNN models with one hidden layer and number of neurons less than or equal to five. An additional important conclusion is that in all studied cases the BR algorithm led to the most reliable results however with very small differences from the other algorithms considered. Based on the above conclusions it was considered sufficient to focus on network models with a hidden layer. For these models it can be shown (see e.g. Morfidis and Kostinakis, 2019) that the correlation relationship they extract has the form of Eq. 2 and Eq. 3. More specifically:

(a) In the case where the activation function of the hidden layer neurons is the logsig function (Fig. 2):

$$\ln(\mathrm{PGA})=\frac{1}{2}\cdot\left\{\max\left[\ln(\mathrm{PGA})\right]_{ds}-\min\left[\ln(\mathrm{PGA})\right]_{ds}\right\}\cdot\left\{\left[\ln(\mathrm{PGA})\right]^{(norm)}+1\right\}+\min\left[\ln(\mathrm{PGA})\right]_{ds}$$

$$\left[\ln(\mathrm{PGA})\right]^{(norm)}=\sum_{i=1}^{nn}\left[\frac{w_i^{(o)}}{1+e^{-g_i}}\right]+b^{(o)} \qquad (2)$$

$$g_i=b_i^{(int)}+w_{i1}^{(int)}\cdot M_w^{(norm)}+w_{i2}^{(int)}\cdot FM^{(norm)}+w_{i3}^{(int)}\cdot\left[\ln(V_{S30})\right]^{(norm)}+w_{i4}^{(int)}\cdot\left[\ln(R_{JB})\right]^{(norm)}$$

(b) In the case where the activation function of the hidden layer neurons is the tansig function (Fig. 2) then the only difference with respect to Eq. 2 is the following:

Where in Eqs. 2 and 3:
nn is the number of neurons in the hidden layer,
$w_{ij}$ is the value of the synaptic weight of the synapse connecting neuron i of the hidden layer to neuron j of the input layer (the values of $w_{ij}$ comprise a dimensional matrix nxm where n=nn and m=4=number of input parameters as given in Fig. 2),
$w_i$ is the value of the synaptic weight of the synapse connecting the hidden layer neuron i to the output neuron (the values of $w_i$ comprise a vector nx1)
$b_i$ is the value of the bias of neuron i (for the neurons in the hidden layer, $b_i$ comprise a vector nx1, and since the output layer neuron is one, $b_i$ in this case is a scalar parameter),
the exponent (o) denotes the output level,
the exponent (int) denotes the hidden level,
the exponent (norm) denotes a normalized value, i.e. the value of the input or output parameter after transforming it through the following normalization function:

$$X^{(norm)}=2\cdot\left[\frac{X^{(input)}-\min(X)_{ds}}{\max(X)_{ds}-\min(X)_{ds}}\right]-1 \qquad X=M_w, FM, \ln(V_{S30}), \ln(R_{JB}) \qquad (3)$$

Where in the above function:
the subscript ds denotes the training sample (data set),
the exponent (input) indicates that the value X is the value of the parameter to be given as input to the trained network in order for it to extract the prediction for the PGA or PGV,
the value max refers to the max value of the parameter X in the training sample ds,
the value min refers to the min value of parameter X in the training sample ds.

Obviously, completely analogous equations to the above apply to the PGV parameter but with different values of the synaptic weights w and biases b as obtained after the training procedures of the respective MFPNNs.

Finally, it should be noted that values of synaptic weights and biases of all optimal trained networks in Table 1 with one hidden layer are available at the following hyper-link (link).

## 4 Comparison of ANN relations with SM data and other relations

Figs. 3a - 3d show comparisons of PGA estimates from the new ANN based equations, existing GMPEs and strong motion (SM) data for two ranges of seismic magnitudes. Of the existing equations presented, the Boore et al. (2021) equation is the most recent GMPE for the Greece, while the Kotha et al. (2020) and Chiou and Youngs (2014) equations have been shown to be accurate for ground motion estimation in Greece. Regarding PGA, it is observed that the ANN based equations show similar trends with both SM data and existing GMPEs. For earthquakes with magnitudes less than M6.0 and close distances, the BR_LOG_5F1 equation gives quite similar values to the equation of Boore et al. (2021), while for distances greater than 30 km the estimates of the former are lower than the latter. The pattern is similar for BR_TAN_13F1 equation, while BR_LOG_18F1 equation estimates higher values than Boore et al. (2021) in the near field. At long distances, where more data are available, the ANN based equations give similar estimates. The pattern is similar for earthquakes larger than M6.0, with the differences in the near-field between ANN equations and Boore et al. (2021) becoming sharper. In fact, the estimates of BR_LOG_18F1 and BR_TAN_13F1 equations yield higher estimates than all other equations presented. Regarding PGV, the proposed ANN equations give similar estimates to each other, except for the near-field (<10 km) and earthquakes larger than M6.0. For the same magnitude range, the estimates of the ANN equations are higher than those of Boore et al. (2021) and are close to the estimates of the Chiou and Youngs (2014) model. For smaller magnitude earthquakes, the estimates of the proposed relations are similar to those of Boore et al. (2021). It is notable that the differences between the displayed equations (new and existing) become sharper in regions where there is a lack of data.

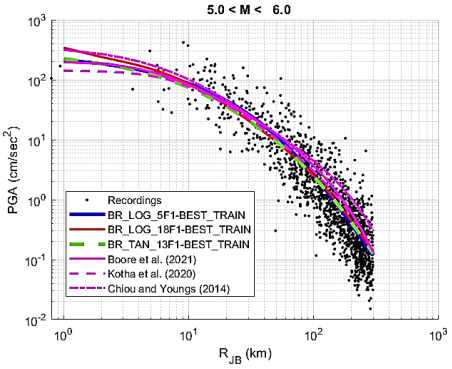


**Fig. 3a**. Comparison between PGA estimation from ANN equations, existing GMPEs and SM data for 5.0<M<6.0 earthquakes

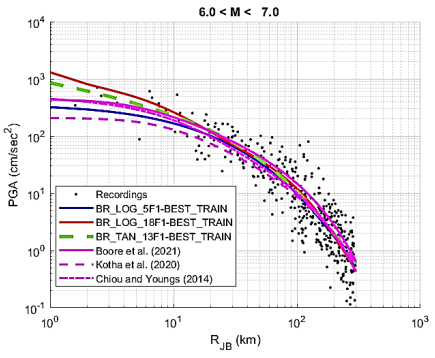


**Fig. 3b**. Comparison between PGA estimation from ANN equations, existing GMPEs and SM data for 6.0<M<7.0 earthquakes

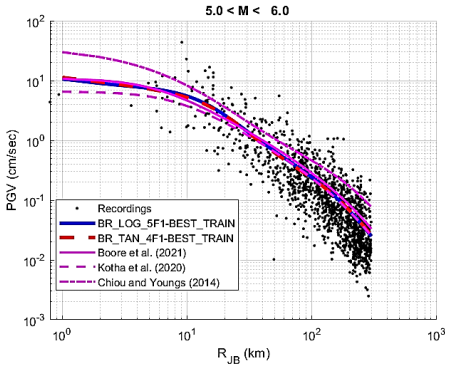


**Fig. 3c**. Comparison between PGV estimation from ANN equations, existing GMPEs and SM data for 5.0<M<6.0 earthquakes

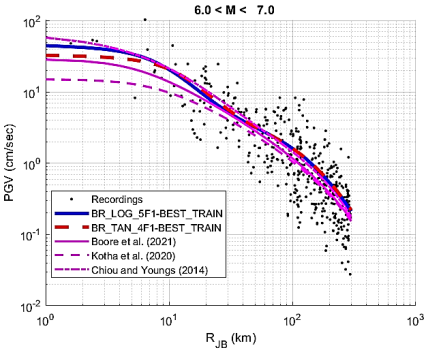


**Fig. 3d**. Comparison between PGV estimation from ANN equations, existing GMPEs and SM data for 6.0<M<7.0 earthquakes

## 5 Residual analysis

In the context of GMPE development, residuals are defined according to Eq. 4, where R is the residual, indices i and j indicate a seismic event and a location, respectively, $\ln(Y_{ij})$ is the observed value of the SM, and $\mu_{\ln Y}$ is the log mean estimate of the SM from a model.

$$R_{ij} = \ln\left(Y_{ij}\right) - \mu_{\ln Y}\left(M^{i}, R_{JB}^{ij}, V_{S30}^{j}, \text{mech}^{i}\right) \tag{4}$$

The mixed-effects analysis (Abrahamson and Youngs, 1992) is applied to the residuals in order to separate them into between-event residuals and within-event residuals, according to Eq. 5. In Eq. 5, B is the total bias, $\eta_i$ and $\varepsilon_{ij}$ are the between- and within-event residuals, respectively. These errors are assumed to be normally distributed with zero mean and standard deviation $\tau$ and $\varphi$, respectively. The overall standard deviation, $\sigma$, is given by Eq. 6.

$$R_{ij} = B + \eta_i + \varepsilon_{ij} \tag{5}$$

$$\sigma = \sqrt{\tau^2 + \varphi^2} \tag{6}$$

Residual analysis, between mean estimates and SM data, was conducted for the proposed ANN equations and the equation of Boore et al. (2021). The results are presented in Figs. 4 and 5 for the PGA and PGV parameters, respectively. It is observed that the use of ANNs smooths out the small deviation and trend observed in the error $\eta_i$ with respect to the earthquake magnitude for the Boore et al. (2021) model for both PGA and PGV. Regarding the error $\varepsilon_{ij}$ with respect to the $R_{JB}$ distance, the pattern is similar between ANN and Boore et al. (2021) models, while, a slight improvement in the error $\varepsilon$ with respect to the $V_{S30}$ velocity is observed from the ANN equations.

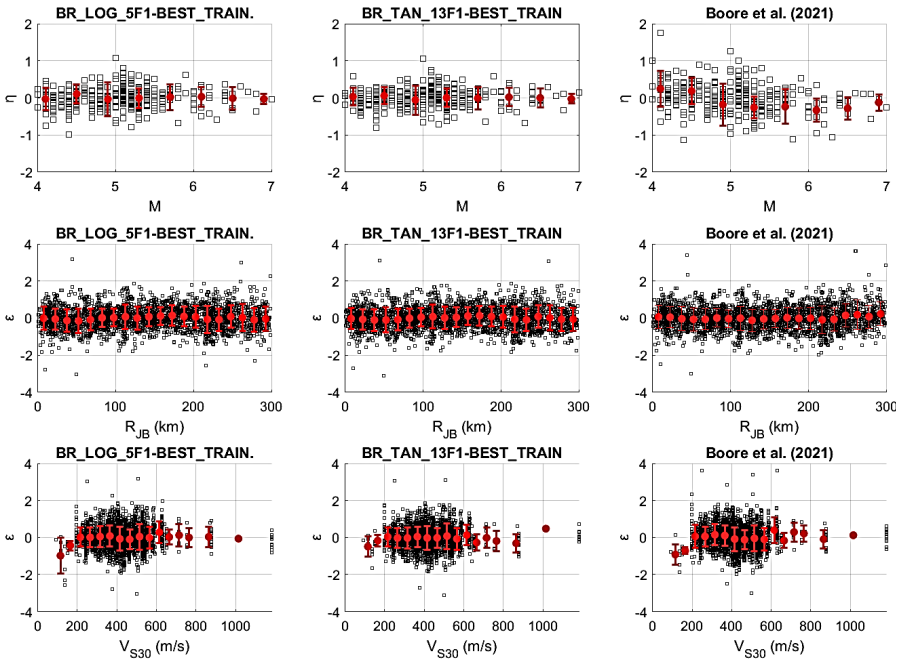


**Fig. 4.** Residual analysis between (η) and within (ε) seismic event for the proposed ANN and GMPE equations of Boore et al. (2021) for PGA

In Fig. 6, the values of the standard deviation of the between-event (τ) and within-event (ε) residuals, as well as, the total standard deviation (σ), for the ANN models, are presented with respect to the earthquake magnitude. These values are compared with the uncertainty model proposed by Boore et al. (2021). For the PGA (Fig. 6a), it is observed that the BR_TAN13F1 model has smaller standard deviations than the BR_LOG5F1 model. Also, the standard deviations of the two models are comparable to the values of Boore et al. (2021), however they seem relatively stable for all earthquake magnitudes, except for large magnitudes where there are not enough data. The pattern is similar for PGV (Fig. 6b), except that the ANN models show similar values of standard deviations. Table 2 shows the selected fixed standard deviation values for the ANN models, as selected based on Fig. 6, compared to the standard deviations of Boore et al. (2021). In general, similar standard deviations are observed between ANN and Boore et al. (2021), with ANN giving slightly smaller overall standard deviation values.

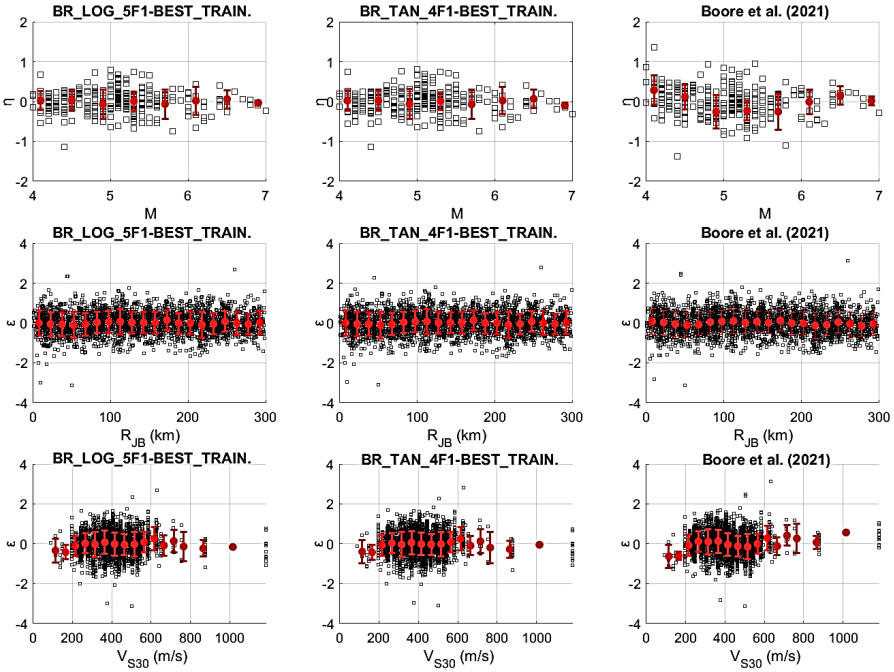


**Fig. 5.** Residual analysis between (η) and within (ε) seismic event for the proposed ANN and GMPE equations of Boore et al. (2021) for PGV

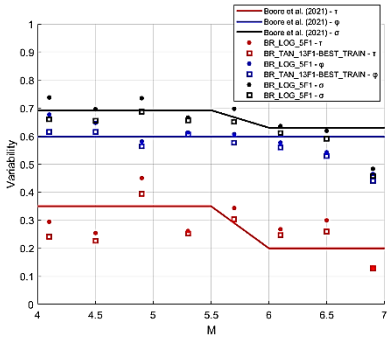


**Fig. 6a**. Uncertainty models of ANN equations compared to the GMPE of Boore et al. (2021), for PGA

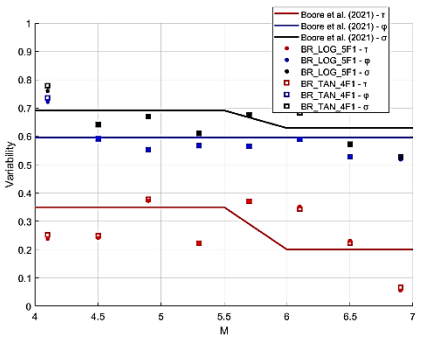


**Fig. 6b**. Uncertainty models of ANN equations compared to the GMPE of Boore et al. (2021), for PGV

**Table 2.** Selected standard deviation values for the ANN models

| GMPE | PGA | | | PGV | | |
|---|---|---|---|---|---|---|
| | **τ** | **φ** | **σ** | **τ** | **φ** | **σ** |
| **BR_LOG5F1** | 0.305 | 0.601 | 0.674 | 0.278 | 0.569 | 0.633 |
| **BR_LOG13F1** | 0.279 | 0.586 | 0.649 | - | - | - |
| **BR_TAN4F1** | - | - | - | 0.279 | 0.568 | 0.633 |
| **Boore et al. (2021)** | M≤5.5: 0.35<br>M≥6.0: 0.20 | 0.597 | 0.692<br>0.630 | M≤5.5: 0.35<br>M≥6.0: 0.20 | 0.596 | 0.691<br>0.629 |

## 6 Conclusions

In the present paper, a GMPE for Greece for seismic risk assessment, which has been derived from ANN training, is proposed and compared with models proposed in the literature to verify the reliability of its applicability. Based on the results presented in the previous sections, it is evident that the proposed relation can be used to estimate both PGA and PGV accurately, as the observed error is within reasonable limits. Also, similar standard deviations are observed between ANN and the equations in the literature with ANN giving slightly smaller overall standard deviation values.

## References

1. Xie, Y, Ebad Sichani, M., Padgett, J. E. & DesRoches, R. (2020) The promise of implementing machine learning in earthquake engineering: A state-of-the-art review. Earthquake Spectra, 36(4), 1769–180
2. Stefanidou S.P., Papanikolaou V.K., Paraskevopoulos E.A., Kappos, A.J., (2021) Machine learning techniques for the estimation of limit state thresholds and bridge-specific fragility analysis of RC bridges. 8th ECCOMAS Thematic Conference on Computational Methods in Structural Dynamics and Earthquake Engineering, COMPDYN 2021, Athens, 27-30 June
3. Ji, D., C. Li, C. Zhai, Y. Dong, E. I. Katsanos, and W. Wang (2021). Prediction of Ground-Motion Parameters for the NGA-West2 Database Using Refined Second-Order Deep Neural Networks, Bull. Seismol. Soc. Am. 111, 3278–3296, doi: 10.1785/0120200388
4. Leousis D., Pnevmatikos N., (2018) Earthquake losses assessment in the municipality of Kifissia (Athens – Greece) using the Earthquake Loss Estimation Routine (ELER). International Journal of Earthquake Engineering and Hazard Mitigation (IREHM), 6(1), 11-20
5. Pnevmatikos N, Konstandakopoulou F, Koumoutsos N (2020) Seismic vulnerability assessment and loss estimation in Cephalonia and Ithaca islands, Greece, due to earthquake events: a case study. Soil Dyn Earthq Eng 136:106252. https:// doi. org/ 10. 1016/j. soild yn. 2020. 106252
6. Baker, J. W. & Jayaram, N. (2008). Correlation of spectral acceleration values from NGA ground motion models. Earthquake Spectra, 24(1), 299–317

7. Haykin S. Neural networks and learning machines. 3rd ed. Prentice Hall; 2009
8. Hornik K, Stinchcombe M, White H. Multilayer Feedforward Networks are Universal Approximators. Neural Networks 1989;2(5):359-366
9. Konstantinos E. Morfidis and Konstantinos G. Kostinakis. Use of artificial neural networks in the R/C buildings' seismic vulnerability assessment: the practical point of view. In: Proceedings of 7th Conference in Computational Methods in Structural Dynamics and Earthquake Engineering (COMPDYN2019), Crete island, Greece, 24-26 June 2019 (Paper Number: C19299)
10. Margaris, B., E. Scordilis, J.P. Stewart, D.M. Boore, N. Theodoulidis, I. Kalogeras, N. Melis, A. Skarlatoudis, N. Klimis, and E.Seyhan (2021). Hellenic Strong-Motion Database with Uniformly Assigned Source and Site Metadata for period of 1972-2015, Seismological Research Letters, Vol. 92, No. 3, pp 2065– 2080
11. K. Diamantaras and D. Botsis, Machine Learning, "Klidarithmos" Publications, Athens 2019 (In Greek)
12. Boore, D. M., J. P. Stewart, A. A. Skarlatoudis, E. Seyhan, B. Margaris, N. Theodoulidis, E. Scordilis, I. Kalogeras, N. Klimis, and N. S. Melis. A Ground-Motion Prediction Model for Shallow Crustal Earthquakes in Greece, Bulletin of the Seismological Society of America 2021; 111(2): 857–874
13. Kotha S. R., Weatherhil G., Bindi D., Cotton F. A regionally-adaptable ground motion model for shallow crustal earthquakes in Europe, Bulletin of Earthquake Engineering 2020; 18: 4091 – 4125
14. Chiou B. S.-J., Youngs R. R. Update of the Chiou and Youngs NGA model for the average horizontal component of peak ground motion and response spectra, Earthquake Spectra 2014; 30: 1117 – 1153
15. Abrahamson N., Youngs R. A stable algorithm for regression analyses using the random effects model, Bulletin of the Seismological Society of America 1992; 82: 505 – 510

# Cultural Heritage

# Risk Assessment of Ancient Colonnades

Spyridon Diamantopoulos[0000-0002-5104-4850] and Michalis Fragiadakis[0000-0002-0698-822X]

National Technical University of Athens 9, Iroon Polytechniou st., 15780 Athens, Greece
sdiamadop@central.ntua.gr

**Abstract.** The paper introduces an innovative method to evaluate the fragility of ancient freestanding colonnades. It compares the seismic response and stability of colonnades with freestanding columns using a simplified modeling approach suitable for seismic design software. The methodology bypasses the need for time-consuming or complex simulations. Detailed discussion is provided on the performance criteria and the methodology for the fragility estimations. The case studies aim to address the proposed modeling and its effectiveness in simulating ancient structures and promptly generating accurate fragility curves. The Engineering Demand Parameter consistently focuses on column rotation over the slenderness angle, while various Intensity Measures are explored.

**Keywords:** ancient monuments, rocking structures, fragility, colonnades

## 1. Introduction

In many cases, ancient structures consist of freestanding columns that are either monolithic or multi-drum. If the structure consists of more than one column that are capped by an architrave, then they form a colonnade. Such structures have survived powerful earthquakes over their lifetime and are of main interest for civil engineers. They can be found in archaeological sites and are commonly made of marble. This study primarily focuses on monolithic column configuration with emphasis on column arrays.

Ancient freestanding colonnades exhibit rocking behavior, and their behavior has similarities with the behavior of a monolithic rocking column, as discussed by Diamantopoulos and Fragiadakis [1]. The rocking column stands as a fundamental problem in earthquake engineering, initially addressed by Housner [2] who proposed its equation of motion. Many researchers, e.g. DeJong and Dimitrakopoulos [3] and Dimitrakopoulos and Giouvanidis [4], among others, have worked on this topic while Cheng [5], Palermo et al. [6] and Priestley and Tao [7] demonstrated the impressive lateral load stability of these structures. Moreover, Psycharis et al. [8] proposed a seismic fragility framework for ancient columns, introducing a fully Performance-Based Earthquake Engineering (PBEE) approach. This work highlights the characteristics of ancient multi-drum columns stacked rigidly atop one another using the Discrete Element Modeling (DEM).

The current study proposes robust modeling techniques for assessing the seismic response of monolithic rocking structures, e.g. rocking frames (Fig. 1). Moreover, it presents a performance-based and rapid risk assessment framework for investigating their seismic response. The paper is built on previous research works of Diamantopoulos and Fragiadakis [1, 9], where it was demonstrated the Finite Element Modeling with simple beam elements and rotational springs with negative stiffness. This approach is easily extended to monuments yielding accurate solutions for a broad array of structures with members that can rock.

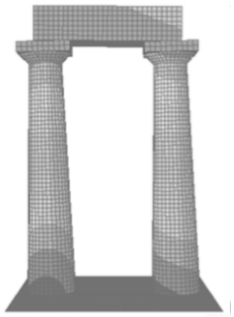

(a)

(b)

**Fig. 1.** Modeling of: (a) a rocking frame and (b) an array of freestanding columns using the Finite Element Method

## 2. Simplified models for rocking colonnades

Colonnades that exhibit uplift and rocking behavior can generally be represented using the model of Figure 2. This model builds upon the single-column framework addressed in Diamantopoulos and Fragiadakis [9]. It involves nonlinear rotational springs located at the rocking interfaces, namely between the ground and the columns, as well as between the epistyle and the top of the columns. Parameters to be defined include the mass matrix and the restoring moment, $M_{res}$, of the system through the $M - \theta$ relationship of the rotational springs. Essentially, the proposed model addresses the

generalized equation of motion governing a planar rocking structure, as initially studied in Diamantopoulos and Fragiadakis [1].

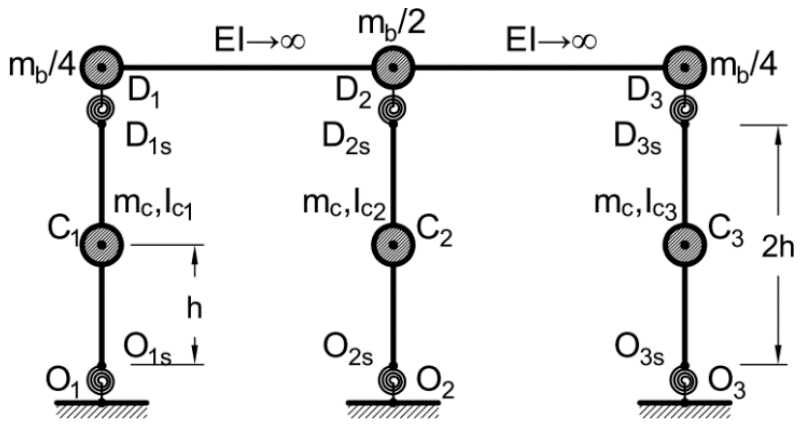


**Fig. 2.** A two-bay planar rocking structure using the proposed simplified modelling approach.

Based on Fig. 2, the mass of the piers is $m_c$, concentrated at their center of gravity and the mass of the deck/architrave is $m_b$, lumped at the nodes $D_1$, $D_2$ and $D_3$. Nonlinear springs are placed at the top and the bottom of the columns defining the total restoring moment. It is pointed out that sliding between the columns and the base or between the columns and the deck is always neglected. Furthermore, considering that the deck's mass is lumped at the top pivot point and its distance from the pivot point of the base is $2R$, it is assumed that the rotational moment of inertia at the center of gravity of each column is $I_{C1} = I_{C2} = I_{C3} = 1/3m_cR^2 + m_cb^2$. In the case of N columns, the epistyle mass is $m_b/(N-1)$ and $0.5m_b/(N-1)$ at the internal and the end nodes, respectively. The rotational moment of inertia at nodes $D_{1s}$ and $D_{Ns}$ will be equal to $I_{D1s} = \ldots = I_{DNs} = [0.5m_b/(N-1)](2b)^2$ and at nodes $D_{2s}, \ldots, D_{(N-1)s}$ it will be $I_{D2s} = \ldots = I_{D(N-1)s} = 2I_{D1s}$. The M-θ relationship of each spring is obtained from the restoring moment and is different at the bottom and the top spring due to the different axial load:

$$M^{btm}(\theta) = m_c gR\sin\left(\alpha\,\mathrm{sgn}\,\theta - \theta\right) + \frac{m_b}{k(N-1)}gR\sin\left(\alpha\,\mathrm{sgn}\,\theta - \theta\right)$$
$$M^{top}(\theta) = \frac{m_b}{k(N-1)}gR\sin\left(\alpha\,\mathrm{sgn}\,\theta - \theta\right) \quad (1)$$

where $k = 1, 2$ for the internal and the two external columns, respectively. It is mentioned that $\gamma = m_b/(Nm_c)$ while the maximum restoring moment is obtained for $\theta = 0$. The proposed model is adopted for the fragility and risk estimations described in the next sections.

## 3. Fragility assessment framework

Fragility curves serve as an essential tool for assessing the seismic risk of a system. They were initially developed to separate structural analyses from the hazard analyses that are referred to by engineering seismologists. Fragility curves refer to the probabilities of exceeding a damage state and thus these probabilities should be calculated. This probability is calculated conditioned on the seismic intensity and is referred to an Engineering Demand Parameter (*EDP*) that exceed a specified threshold *edp*:

$$F_R\left(IM\right) = P\left(EDP > edp \mid IM\right) \tag{2}$$

To calculate Eq. 2 three possible response cases are considered: (i) system at rest, (ii) system uplifted and (iii) system overturned. With the aid of the total probability theorem, the fragility can be calculated following the equation:

$$F_R = P\left(EDP \mid NoUplift\right) P_{NoUplift} + P\left(EDP \mid Uplift\right) P_{Uplift} + P\left(EDP \mid Ovtn\right) P_{Ovtn} \tag{3}$$

where *P(EDP | NoUplift)*, *P(EDP | Uplift)* and *P(EDP | Ovtn)* are the damage-state exceedance probabilities for *no-uplift*, *uplift* and *overturning*, respectively. For columns that will not uplift or overturn, *P(EDP | NoUplift)* = 0 and *P(EDP | Ovtn)* = 1, respectively. Thus, the fragility curve calculation is simplified to:

$$F_R = P(EDP \geq edp \mid Uplift)(1 - P_{Ovtn} - P_{NoUplift}) + P_{Ovtn} \tag{4}$$

It should be mentioned that rocking data are assumed as lognormally distributed. Hence, *P(EDP ≥ edp | Uplift)* is calculated once the mean and the standard deviation of the logs of the *EDP*, denoted as $\mu_{logEDP}$ and $\sigma_{logEDP}$ [11], respectively, are known. Once they are known they can be used to calculate the probability that the *EDP* exceeds a threshold *edp*:

$$P(EDP \geq edp \mid Uplft) = 1 - \Phi\left(\frac{log(EDP) - \mu_{logEDP}}{\sigma_{lnEDP}}\right) \tag{5}$$

where Φ is the standard normal distribution. The risk can be expressed as the mean annual frequency (MAF) of exceeding a damage-state. Adopting the PEER's formula, the damage-state MAF is:

$$\lambda_{EDP} = \int_{IM} P(EDP \mid IM) \left|\frac{d\lambda_{IM}}{dIM}\right| dIM \tag{6}$$

where $d\lambda_{IM}$ is the slope of the hazard curve. The MAF is obtained convolving the slope of the site hazard curve $\lambda_{IM}$ with the fragility curve P(EDP|IM) that is defined with respect to the EDP and the IM considered. The hazard curve is assumed known from site hazard analysis studies, as discussed in reference [13].

# 4. Fragility analysis methods

## 4.1 Multiple stripe analysis

Multiple stripe analysis provides a nuanced understanding of how the system's vulnerability changes as seismic intensity increases, allowing for more targeted risk assessment strategies. In the case of rocking structures, the damage-state fragility curves can be calculated using severe approaches or methods. The Incremental Dynamic Analysis (IDA) proposed in Ref. [10] is a valuable tool for such problems. In the IDA method, the system examined is subjected to ground motion records scaled to multiple intensity levels. Single record capacity curves are then produced as has been discussed in Diamantopoulos and Fragiadakis [12] and Fragiadakis and Diamantopoulos [13].

Multiple Stripe Analysis (MSA) method is another approach that has similarities to the IDA. In this case, the records are scaled to the same IM and thus the EDP values form a stripe. Stripes allow the direct calculation of the 50%, the 16% and 84% percentile capacity curves conditional on the IM. It should be mentioned here that in IDA the scaling factors are different, but the data can be converted to a stripe form using the interpolation method. In this work only MSA was performed.

If the *EDP* values form stripes conditional on the *IM* value, Eq. 4 is solved using an approach based on multiple stripe analysis. For every stripe, the mean and standard deviation conditional on the *IM*, are easily calculated. Considering the assumption that the data follow the lognormal distribution, the fragility is obtained as:

$$F_R = \Phi\left(\frac{\mu_{logEDP} - log(edp)}{\sigma_{logEDP}}\right)\left(1 - P_{Ovtn} - P_{NoUplift}\right) + P_{Ovtn} \tag{7}$$

$P_{NoUplift}$ and $P_{Ovtn}$ are determined as the proportion of simulations where there was no uplift and overturning, respectively. This is obtained for every stripe, i.e. $P_{NoUplift}$ and $P_{Ovtn}$ are calculated as the number of simulations of *NoUplift* or *Ovtn* over the total number of simulations, respectively.

## 4.2 Cloud analysis method

In case of unscaled, or scaled with the same factor, ground motions, they are not stripped and thus the data form a cloud. Thus, cloud analysis should be adopted to calculate the fragility curves. The mean value of the logarithms ($\mu_{logEDP}$) and a single constant value for the dispersion $\sigma_{logEDP}$ are provided through a linear fit. Knowing $\mu_{logEDP}$ and $\sigma_{logEDP}$ and using Eq. 7 it is possible to calculate the fragility of the rocking simulations. The latter requires knowledge of $P_{NoRock}$ and $P_{Ovtn}$. These probabilities can be obtained with a logistic regression model which yields a probability estimation as a function of the *IM*. Therefore, for the *NoUplift* and *Ovtn* cases the probabilities are:

$$P_{NoUplift} = \frac{1}{1+e^{-(b_1+b_2 log(IM))}}$$
$$P_{Ovtn} = \frac{1}{1+e^{-(b_3+b_4 log(IM))}} \quad (8)$$

where the constants $b_1$, $b_2$, $b_3$, $b_4$ are the parameters of the logistic regression model, obtained with binomial-based, generalized linear model (GLM) regression.

### 4.3 Maximum-Likelihood (MLE) fitting

The maximum-likelihood (MLE) fitting [14] is adopted in both striped and cloud data. The MLE fitting approach fits the Cumulative Distribution Function (CDF) of a lognormal distribution on the EDP-IM plane. The fragility function is simply a lognormal CDF of the form:

$$F_R = P(EDP \geq edp) = \Phi\left(\frac{log(EDP/\theta_a)}{\beta_a}\right) \quad (9)$$

where $\theta_a$ and $\beta_a$ are determined by maximizing the likelihood function and are the median and the dispersion.

In fact, Multiple-stripe analysis provides the number of successes $n_{suc}$, i.e. the number of simulations that the damage-state has been exceeded after $n_{tot}$ total simulations. Using the binomial distribution on the data of a single stripe, the probability of $n_{suc}$ successes after $n_{tot}$ simulations, is defined as:

$$P(Success = n_{suc}) = \binom{n_{tot}}{n_{suc}} P(EDP^{(s)})^{n_{suc}} (1 - P(EDP^{(s)}))^{n_{tot}-n_{suc}} \quad (10)$$

If there are k stripes, the MLE function is obtained substituting Eq. 9 to Eq. 10 as follows:

$$L = \prod_{i=1}^{k} \binom{n_{tot,i}}{n_{suc,i}} \Phi\left(\frac{log(EDP/\theta_a)}{\beta_a}\right)^{n_{suc,i}} \left(1 - \Phi\frac{log(EDP/\theta_a)}{\beta_a}\right)^{n_{tot,i}-n_{suc,i}} \quad (11)$$

The only variables to be determined are $\theta_a$ and $\beta_a$, which are identified as the values that optimize the likelihood function of Eq. 11. It's important to highlight that the fitting process encompasses the entire dataset, a task readily accomplished with a basic computer script. In cases where the EDP-IM pairs form a cloud, each simulation is considered a distinct stripe. Consequently, $k$ represents the number of simulations, while $n_{tot}$ is set to one ($n_{tot} = 1$), and $n_{suc}$ equals one or zero, depending on whether the simulation surpasses the damage-state threshold or not, respectively.

## 5. Numerical results and discussion

The structure under examination is a colonnade consisting of N = 3 columns of equal height. The colonnade possesses the following properties: 2h = 5m, 2b = 0.75m, and $\gamma = m_b/(3m_c) = 1$, where $m_b$ represents the mass of the epistyle, and $m_c$ signifies the mass of each column. Moreover, the colonnade is topped with a rigid beam weighing the sum of the weights of the columns. To validate the proposed modeling approach, the structure is subjected to both near-field and far-field ground motions. As illustrated in Fig. 3, the results obtained using the proposed model depicted in Fig. 2 are compared against the equation of motion governing the problem. Remarkably, for both seismic records, a high degree of agreement is observed, confirming the precision of the proposed model.

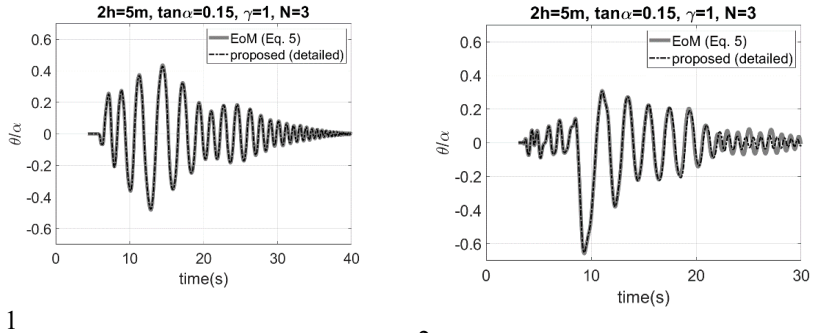


1 2

(a) (b)

**Fig. 3.** Evaluation of the colonnade's response using the suggested model under: (a) a Loma Prietta 1989, Saratoga - Aloha Ave, PGA=0.36g (near-field), (b) Northridge 1994, MUL279 component, PGA=0.52g (far-field).

Fragility analysis was conducted using a set of thirty ground motions representing a scenario earthquake. Three damage-states corresponding to θ/α= 0.15, 0.35, and 1.00 were considered, with the chosen intensity measure (IM) being the normalized peak ground acceleration, *PGA/gtanα.* In Fig. 4a fragility curves derived with different approaches are compared. Smooth curves represent Maximum Likelihood Estimation (MLE) fitting, while non-smooth curves were generated using Eq. 9. Notably, the two approaches exhibit close results.

Fig. 4b compares fragility curves derived from cloud analysis with those from multiple stripe analysis. While the fragility curves coincide for the two damage-states, differences are observed for the overturning damage-state. Insufficient records at high IM values bias fragility curves in cloud analysis. Furthermore, Fig. 5 compares the response of the colonnade with a single column using PGA/gtanα and PGV as IMs. All fragilities were determined using the MLE approach on stripped data. Overall, it is mentioned that colonnades demonstrate greater stability compared to single columns

irrespective of the IM. However, IM selection does not impact the fragilities of the two lower damage states, but it does for the near-collapse damage-state.

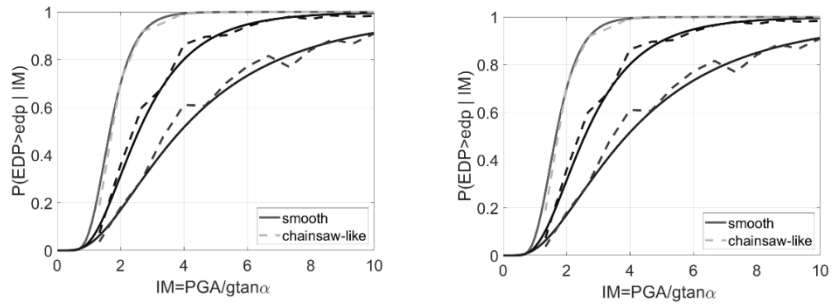


**Fig. 4.** (a) Definition of smooth fragility curves, (b) comparison of multiple stripe and cloud analysis. The damage-states considered are θ/α = 0.15, 0.35 and 1.00.

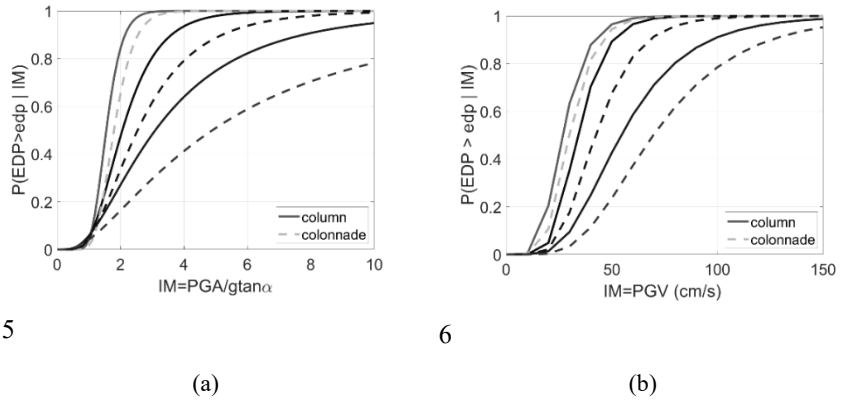


**Fig. 5.** Comparison of a column with a colonnade in case of N=3 (γ=1, 2h=5.0m, 2b=0.75m) using the fragility functions: (a) IM=PGA/gtanα, (b) IM=PGV. The damage-states considered are θ/α = 0.15, 0.35 and 1.00.

## 6. Conclusions

The paper presents a Performance-Based Earthquake Engineering (PBEE) framework for the fragility assessment of ancient structures mainly suitable for monolithic freestanding columns or colonnades. The numerical investigation validates the effectiveness of the modeling approach in addressing various scenarios and providing precise estimations. Initially, the simple models, relying on the direct stiffness method, offer a robust way to analyze different colonnade configurations that use basic structural assessment tools. Their advantage lies in reducing the computational cost by

avoiding complex relationships for the body interactions and the energy loss assessment. The latter are often required in commercial Finite Element Method (FEM) or Discrete Element Method (DEM) models. Furthermore, it is mentioned that the Engineering Demand Parameter (EDP) is consistently the normalized rotation $\theta/\alpha$, while different options for the Intensity Measure (IM) are considered. The fragility assessment is performed using either a cloud or multiple stripe analysis approach. Special attention is warranted for simulations that overturn or do not uplift the structure.

## References


1. Diamantopoulos S, Fragiadakis M. Modeling of rocking frames under seismic loading. Earthquake Engineering & Structural Dynamics 2022; 51 (1): 108–128
2. Housner G. The behavior of inverted pendulum structures during earthquakes. Bulletin of the Seismological Society of America 1963; 53(2): 404–417
3. DeJong M, Dimitrakopoulos E. Dynamically equivalent rocking structures. Earthquake Engineering and Structural Dynamics 2014; 43(10): 1543–1563
4. Dimitrakopoulos E, Giouvanidis A. Seismic response analysis of the planar rocking frame. Journal of Engineering Mechanics 2015, 141(7):04015003
5. Cheng C. Shaking table tests of a self-centering designed bridge substructure. Eng Struct 2008; 30(12): 3426–3433
6. Palermo A, Pampanin S, Marriott D, Design, modeling, and experimental response of seismic resistant bridge piers with posttensioned dissipating connections. J Struct Eng 2007; 133(11): 1648–1661
7. Priestley M, Tao J. Seismic response of precast prestressed concrete frames with partially debonded tendons. PCI J 1993; 38(1):58–69
8. Psycharis IN, Fragiadakis M, Stefanou I (2013). Seismic reliability assessment of classical columns subjected to near-fault ground motions. Earthquake Engineering & Structural Dynamics 2013; 42:2061-2079
9. Diamantopoulos S, Fragiadakis M. Seismic response assessment of rocking systems using single degree of freedom oscillators. Earthquake Engineering & Structural Dynamics 2019; 48(7), 689–708
10. Vamvatsikos D, Cornell CA. Incremental dynamic analysis. Earthq Eng Struct Dyn. 2002; 31(3):491–514
11. Vamvatsikos D, Fragiadakis M. Incremental Dynamic Analysis for seismic performance uncertainty estimation. Earthq Eng Struct Dyn. 2009; 39(2): 119-235
12. Diamantopoulos S, Fragiadakis M, Modeling, fragility and risk assessment of ancient freestanding columns and colonnades, Engineering Structures 2023, Volume 275, Part B, 115273
13. Fragiadakis M, Diamantopoulos S. Fragility and risk assessment of freestanding building contents. Earthquake Engineering & Structural Dynamics 2020; 49 (10): 1028- 1048
14. Baker JW. Efficient analytical fragility function fitting using dynamic structural analysis. Earthquake Spectra 2015; 31(1):579–599

# Material Science and Engineering

# Behavior of steel building structures subjected to strong and benchmark seismic actions: An overview of damage from the observations of the last 40 years

Anthimos Anastasiadis[1]

[1]ASAnastasiadis and Associates, Taskou Papageorgiou 10, 54631, Thessaloniki, Greece
anastasiadis@asacon.eu

**Abstract.** It is well known that steel structures have a high ductility capacity and a high strength-to-weight ratio, which theoretically, by nature, makes them one of the most efficient seismic structural systems against strong earthquakes. However, the recorded experience of failures that have befallen over the last 40 years as a result of strong seismic actions suggests that this by itself isn't always sufficient. Generally, it is essential that an appropriate and preferred conformation and configuration of the structural system, and in particular of its joints, be adopted. In any case, the steel building structures showed local failures without general or complete collapses. The work in this paper presents the seismic performance focused on steel building structures, as revealed by strong earthquakes such as those of Mexico (1985), Northridge (1994), USA, Kobe (1995), Japan, Christchurch (2010–2011), and New Zealand, which affected and changed the design of metal structures, as well as other earthquakes like Maule (2010), Chile, Emilia (2012), Amatrice (2016), and Italy, which completed the picture in the better understanding of failures and their reasons. On the basis of the lessons learned, a discussion on avoiding such situations is commented on and provided in this work.

**Keywords:** Steel Buildings, Seismic Performance, Benchmark Earthquakes

## 1. Introduction

Traditionally, steel structures are considered one of the most efficient earthquake-resistant systems due to their enhanced ductile capacity and high strength-to-weight ratio. However, as revealed by past earthquakes, these two very important mechanical parameters are not sufficient to avoid failures. Although it has been observed that no global collapses have occurred so far, except in a few special cases, only certain local failures are registered at joints and connections. This real fact was recognized by the engineering community through the reconstruction of Christchurch in New Zealand [1].

In fact, the way to learn and improve our design, detailing, and construction practices comes from two aspects: the first is to learn from failures, and the second is from successes. The first one reveals the level of vulnerability, while the second one reveals the level of capacity of any type of structural system. Both are very educational and form the dipole of engineering knowledge and judgment. In this direction, the seismic

performance is also defined by the aforementioned. The engineering community is mainly focused on failure, with success being self-evidenced. Associated with steel building structures, the avoidance of global collapse is considered a success of steel structures. Thus, it is of paramount importance to look at and provide a concise presentation of failures from past earthquakes that influenced the design and construction, and at the same time, a scope of discussion as well. Literally speaking, "*the light failing through the crack...*" as wrote Leo Tolstoy, 1869, in the book War and Peace (as in our cases is Failure and Success). The Northridge (1994), USA, Kobe (1995), Japan, and Christchurch (2010–2011), New Zealand, could be considered seminal earthquakes for steel building design practice, while other important earthquake events, such as Mexico (1985), Maule (2010), Chile, Emilia (2012), Amatrice (2016), and Italy, also contributed to providing information on the seismic performance of steel building structures.

Typically, the main structural systems used for steel buildings are the following: (i) moment-resisting frames, MRF, where the seismic resistance is provided mainly by the cyclic bending action of beams and columns, targeting through the capacity design to concentrate the inelastic action only in the beams; (ii) concentrically braced frames, CBF, where the seismic resistance is provided by the cyclic axial action of the braces; (iii) eccentrically braced frames, EBF, where the seismic resistance is provided by the axial, shear, and bending cyclic action of the eccentric region between the braces; and finally (iv) frames with buckling restrained braces, shear wall, and rocking systems [2]. From the above-mentioned structural systems, only (i), (ii), and (iii) are subjected to strong earthquakes, while the systems of (iv) have mainly progressed after the Northridge and Kobe earthquakes, and we have no signs of their behavior under real strong cyclic actions. Therefore, in the following discussion, only (i), (ii), and (iii) will be commented on. Moreover, in the steel building sector, due to its different structural requirements, we can distinguish between one-story buildings primarily for industrial applications and multi-story buildings for residential, office, retail, and hotel uses.

This paper provides an overview of the failure observed from the occurrence of strong earthquakes over the past 40 years that influenced the steel building industry, followed by a brief discussion related to the avoidance of such situations in European engineering design practice.

## 2. Seismic performance of steel building structures

### 2.1 Mexico City, Mexico, 1985

On September 19, 1985, a strong earthquake of Ms = 8.1 magnitude, with its epicenter 400 km from Mexico City, affected Mexico City, which is situated in a highly compressible clay of an old lake bed [3]. High amplitude, along with a large number of strong cycles and a long duration of about 30 seconds, led to the collapse of many high-rise resilient buildings. The specific characteristic of this earthquake was that the epicenter, localized in Michoacán State, was about 400 km away from Mexico City, where the severe damage occurred; the soft clay geotechnical conditions led to the amplification of the period at around 2.0 seconds, which coincided with the period of the collapsed buildings [4,5]. The Michoacán earthquake, due to the unique soil conditions of

the Mexico City basin, mainly unveiled the site effects and their influence on period amplification, long duration, large amplitude of ground motion, and high accelerations as well. Generally, structures of six to twenty stories, interestingly built between 1956 and 1976 and made of reinforced concrete, were severely damaged, while buildings with less than six and more than twenty stories also sustained significant damage [3,6,7].

Steel buildings in Mexico date from the '20s, they are generally considered more expensive than reinforced concrete structures. Mainly starting in the '40s, many tall buildings, ranging from 25 stories to 43 stories, were constructed [7]. In any case, steel buildings behaved very well, except the Pino Suarez building complex, and especially those with a natural period of 2.0 seconds, which was critical for resonance [7,8].

The Pino Suarez complex was constructed in early 1970 and consisted of five steel moment resisting frames, (three central buildings of 21-stories and two of 14-stories). The structural system of the 21-story collapsed building, which failed onto the 14-story building, was a moment-resisting frame consisting of welded plates forming box columns with truss beams and moment-resisting connections. The collapse was attributed to the buckling of the exterior box columns, in the fourth storey [8,9], Fig. 1.

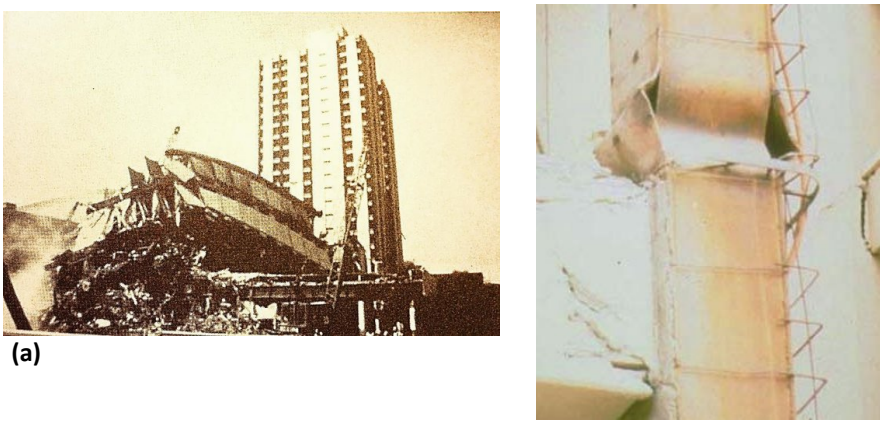


**Fig. 1.** (a) Collapsed building and (b) buckled column of the Pino Suarez building [3]

The lessons learned from the 1985 Mexico earthquake were not focused on steel structures that behaved well. The geological setting, the effect of local geotechnical site conditions, and the soil-structure interaction that strongly alters the strong ground motion, affecting the inelastic behavior of structures, were the main aftermaths. Nevertheless, this earthquake marked the first notable collapse of a steel structure and, moreover, begged questions about steel conformation practices and redundancy, the level of available ductility to withstand severe earthquakes, and the slenderness of box sections as well.

### 2.2 Northridge earthquake, USA, 1994

On January 17, 1994, a strong earthquake of Mw = 6.7 magnitude, with the epicenter near Northridge, about 30 km northwest of downtown Los Angeles, California, damaged more than 40.000 buildings of all structural systems. More than 150 tall and short (from one to 26-stories), new and old, steel moment-resisting frames suffered widespread brittle damage. It should be underlined that no steel building collapsed and no loss of life was registered. The typical US pre-Northridge flange welded-web bolted with shear tab connection is presented in Fig 2. The failure is concentrated at the joint region, especially at the beam-column connection and mainly at the bottom flanges [10,11], Fig. 3. The damage was observed in the welded connections, with complete penetration welds between the beam and column flanges. In some cases, cracks were propagated into the column's web and, as such, developed a column fracture or cracks into the beam's flanges. Prior to the Northridge earthquake, this connection type was believed to have adequate ductility capacity to withstand high seismic forces. Despite this, experimental testing of a large scale of such connections between 1970 and 1992 revealed relatively low beam plastic rotations between 0.010 and 0.030 rad [12,13,14]. Moreover, for economic reasons, a lot of buildings were constructed only with perimeter moment-resisting connections, while the rest were bolted with simple supported connections, and in many cases, the moment-resisting connections had no continuity and/or doubler plates or lapped plating. The brittle failure was attributed to the mechanical properties of materials, insufficient practices of constructional conformation, detailing, welding, and design, and poor workmanship [15,16], although an additional important contributing parameter was the near-field ground motion, which introduced a high strain rate leading to brittle mode failures [17,18,19].

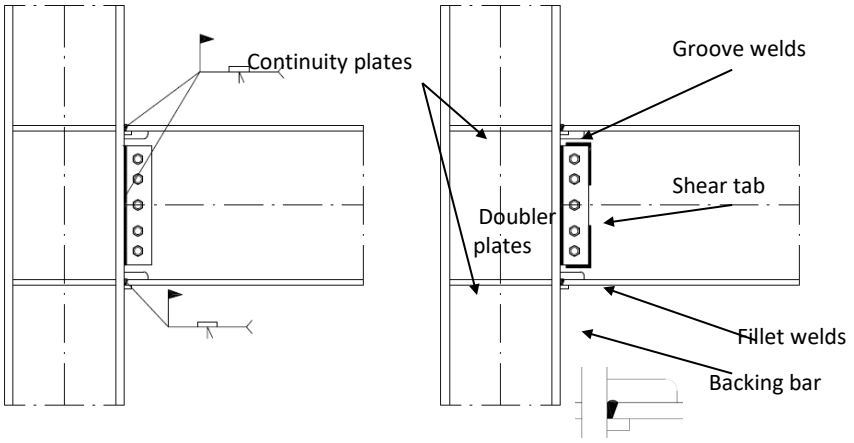


**Fig. 2.** Typical US pre-Northridge flange welded-web bolted beam-column connection, with and without weld at shear plate, for welded steel moment frames

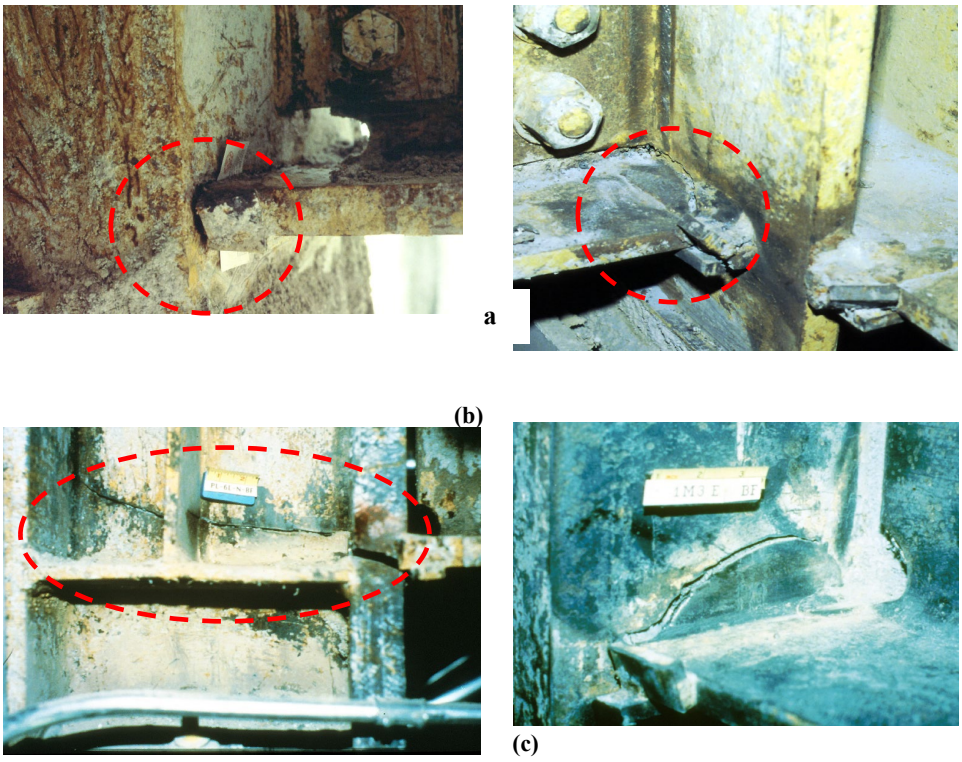


**Fig. 3.** Typical damage observed after the Northridge earthquake, (a) Fracture at fuse zone, (b) column fracture, and (c) column flange "divot" fracture [10]

The Northridge earthquake, 1994, USA, is a benchmark point in the history of seismic design of steel structures, especially steel welded moment-resisting frames. The unexpected damage greatly surprised the US structural engineering community [20]. The response was immediate and radical; a great research program was initiated, starting in 1994 and ending in 2000, through the cooperation of The Structural Engineers Association of California (SEAOC), Applied Technology Council (ATC), and California Universities for Earthquake Engineering (CUREE) in cooperation with the Federal Emergency Management Agency (FEMA), forming the SAC Joint Venture with the main goal of "developing reliable, practical, and cost-effective guidelines and standards of practice for the repair or upgrading of damaged steel moment frame buildings, the design of new steel buildings, and the identification and rehabilitation of at-risk steel buildings" [21, 22]. It was an exemplary program; the result was design-oriented, namely, the development of guidelines, which were the basis for the further processing of new standards and codes not only for new structures and for the rehabilitation of existing ones [23, 24,25], but also sound information related to the metallurgy of structural steel, welding, inspection, and quality control [26,27,28].

It was realized that the column face, at the connection, is a highly stressed zone; therefore, constructional detailing using the concept of weakening (reducing the upper and lower flanges at a selected distance from the column face) [29,30] or strengthening (adding ribs, cover plates, and haunches) could be applied [31]; the plastic hinge must be removed from the column face to a zone of lesser stress. In addition, the detrimental effect of the slab, when it is coupled compositely with the beam, which converts the strong column-weak beam concept into a weak column-strong beam mechanism, was also evaluated [32,33].

Related to moment-resisting frames, among the "constructional novelties," the reduced beam section was introduced in the current practice of designing welded moment connections. Further on, the welding details of the flange-welded-web bolted connections are strongly improved. Additionally, new lateral load-resisting systems were introduced in practice, such as the buckling restrained braces [34] and steel plate shear walls systems [35].

Associated with the improvement of the seismic design, all the traditional steel structural systems (moment-resisting frames, concentrically and eccentrically braced frames) were scrutinized, and improvements related to ductility and capacity design were provided [36]. Another important step was the development of loading protocols for the assessment of the inelastic behavior of the steel subassemblies and components [37,38]; moreover, understanding the differences in near-field ground motion-related protocols was also developed and used [39]. Nevertheless, the most important issue was the implementation of performance-based design, where a qualitative concept was transformed into a quantitative methodology based on reliability engineering [22,40,41].

In the USA, the codification is rather complex and is not harmonized as in Europe or other countries; the seismic design of steel structures was fragmented between different codes according to region and jurisdiction [42]. However, the impact of the Northridge earthquake was crucial. The American Institute of Steel Constructions (AISC), representing the US steel industry, took initiatives and, exploiting the results of the SAC Joint Venture research program, starting in 1997 and continually revising the standards every five to six years, developed a complete design framework. Nowadays, there exist three major standards related to (i) Seismic Provisions for Structural Steel Buildings (ANSI/AISC 341/22), (ii) Prequalified Connections for Special and Intermediate Steel Moment Frames for Seismic Applications (ANSI/AISC 358/22), (iii) Seismic Provisions for Evaluation and Retrofit of Existing Structural Steel Buildings (ANSI/AISC 342/22) [43]. Three issues are of particular consideration. The first is connected to prequalified connections, where the prescribed eleven types of moment connections, in ANSI/AISC 358/22, are prequalified and no testing is required; this means that the corresponding moment connection is sufficiently examined (testing, analysis, evaluation, review), providing a sufficient level of confidence. The second issue is that among the prequalified connections, there are seven that are non-proprietary (reduced beam section (RBS), bolted unstiffened and stiffened extended end-plates, bolted flange plate (BFP), welded unreinforced flange-welded web (WUF-W), cast bolted bracket (CBB), double-tee moment connection, slotted web (SW) moment connection) and four that are proprietary connections (ConXtech CONXL connection, SidePlate connection,

Simpson strong-tie strong frame, DuraFuse Frames moment connection). The third issue prescribed in ANSI/AISC 341/22 is the protected zone; this means that in locations where large strains are expected (i.e., plastic hinges in beams), there are no attachments, discontinuities, or welded shear studs. Finally, the ANS/AISC 341 cancels the prequalification in the case of composite slabs that are present. All the aforementioned provisions follow the concept to ensure a reliable capacity design (i.e., the formation of plastic hinges in beams and not in columns, as well as to not cancel the predetermined designed plastic mechanism).

### 2.3 Kobe earthquake, Japan, 1995

On January 17, 1995, a powerful earthquake of Mw = 6.9 magnitude hit Kobe city. The severely damaged area was a narrow, concentrated band of approximately one kilometer in width and extending, in length, for about 25 km. The epicenter region was located on Awaji Island, 20 km from the city of Kobe. It was a near-field ground motion with impulsive characteristics and a short duration of about 10–15 seconds. Furthermore, close to the epicenter area, large vertical accelerations were also recorded, with a vertical to horizontal peak ground acceleration ratio (V/H of more than 1.5 and a mean value close to 0.90 [44]. For instance, in the case of the Northridge earthquake, a V/H ratio of 1.79 was recorded [45]. Ground motions varied significantly at the different sites due to local soil and geological conditions (i.e., infill-reclaimed land, alluvium, soft rock, and variations in the thickness of the soil at different sites).

Steel is the second most popular structural material after wood in Japan [46]. The typical beam-column connection for moment resting frames used in Japan is depicted in Fig. 4. Generally, a box column (cold-formed or built-up) is connected with the use of groove welds, by the aide of the steel diaphragms, with the beam; the column is divided in three parts, one for the lower storey, one for the upper storey, and the middle segment to form the rigid node of the beam-column connection. A shear plate welded at the shop is used to facilitate the easy on-site welding of the beam to the column. This is the through-diaphragm connection, which was the most popular before the Kobe earthquake. There was also a solution with interior and exterior diaphragms, which are the most costly.

It was surprising that the same brittle damage at the beam-column connection, as it was in the case of the Northridge earthquake exactly a year ago, was observed. The same failure at the welds, heat-affected zone, and base material fracture is recorded, although the general conformation of a typical joint between US and Japanese practice is different, Fig. 4. Moreover, brittle failure also occurred at: (i) columns (of square hollow section mainly cold formed), with fracture at the base material of approximately 50–55 mm thickness, at welded column splices, and beam to brace connections; (ii) column bases at anchor bolts; and (iii) braces of small cross section and large slenderness like rods, angles, and flat plates for older buildings, while for modern buildings with larger cross sections, the damage was concentrated at the connection zone [46,47,48,49], Fig. 5,6.

The causes of damage attributed to the fracture toughness of steel material, general configuration and detailing of the beam to column connection, low toughness of weld metal and the severity of the strong ground motion having strong pulses and high V/H

PGA ratio as well. The repeatability of the damage observed for both Northridge, 1994, USA, and Kobe 1995, Japan, unveiled the enhanced vulnerability of the welded beam-to column connection of the steel moment resisting frames. Moreover, the practice was to execute the welding on site. Hence, considering that joints are severely stressed, then the weldments that characterized by a potential brittleness, must be very well executed, inspected and assured the quality control; this was not the case. It was a failure of the seismic design and construction practice for both countries.

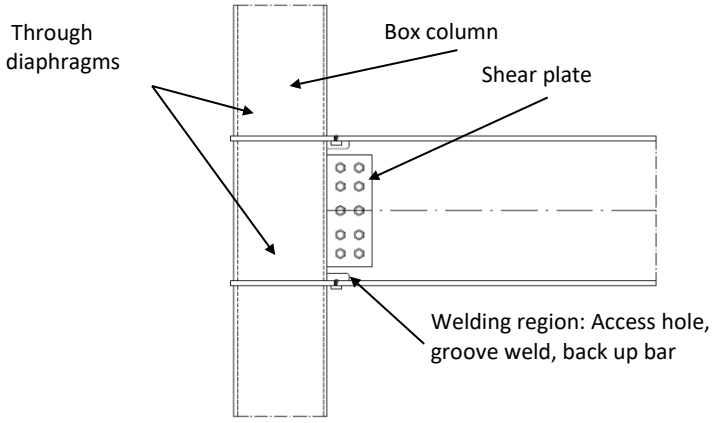


**Fig. 4.** Typical beam-column through diaphragm connection before Kobe earthquake

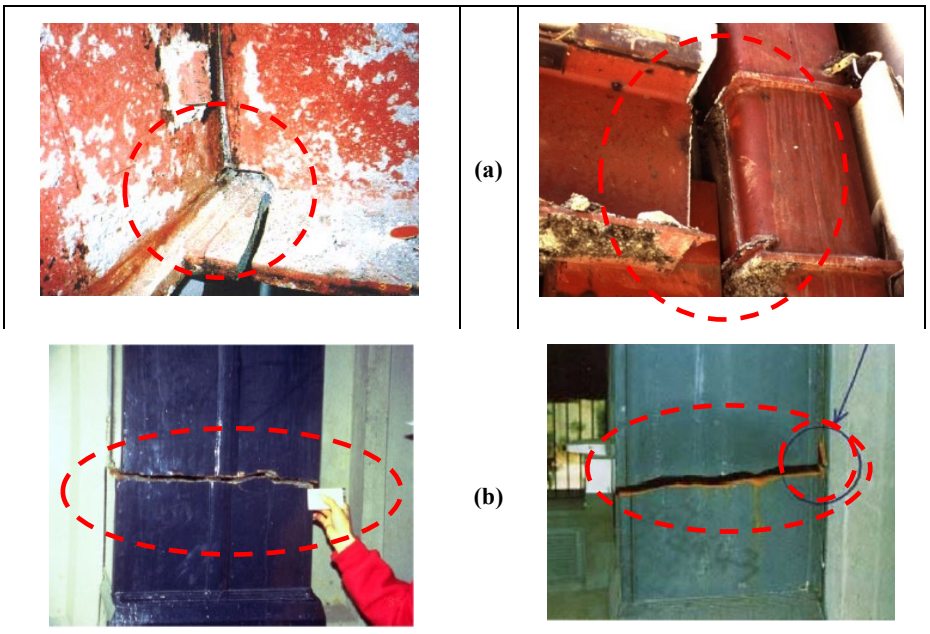

**Fig. 5.** Brittle damage from Kobe earthquake, (a) beam to column fracture, (b) column fractures [48,49]

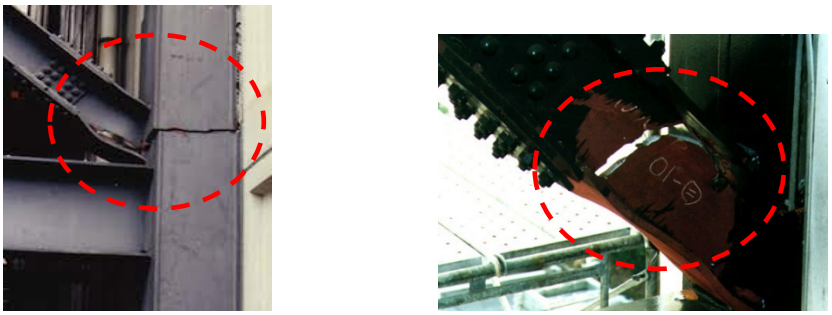

**Fig. 6.** Brittle damage from Kobe earthquake, brace fracture [48,49]

As was the case for the USA after the Northridge, Japan also funded many research programs targeting to investigate the material and welding practices, evaluate the inelastic behavior and the ductility capacity of moment-resisting connections, and improve the welded connections [50]. Certainly, the design code was revised towards performance-based design [51]; however, the main progress was the development of high-strength steels, fire-resistant steels, low-yield steels (with yield limits between 100 and 200 MPa for use in steel hysteretic dampers), the introduction of buckling restrained braces, as well as the use of shear panel dampers [50]. The Kobe earthquake triggered the construction of the world's largest shaking table 3-D Full-Scale Earthquake Testing Facility, nicknamed "E-Defense" [52].

### 2.4 Maule earthquake, Chile, 2010

On February 27, 2010, a strong earthquake of magnitude Mw=8.8 struck Chile. The epicenter was located 8 km from the town of Curanipe and 115 km from the second-largest Chilean city of Conception, with peak ground acceleration in that city of the order of 0.65g. This ground motion was the second largest in Chilean earthquake history, after the Valdivia earthquake (1960). The most popular structural material in Chile is reinforced concrete; however, steel is used for the construction of industrial facilities, and therefore damage was observed in such structures [53, 54]. Generally, the steel structures performed well in that severe ground motion. Brace buckling, anchorage failure, roof truss failure, and buckling of the leg and wall tank are observed in Fig. 7 [53]. In addition, extended damage was observed to non-structural elements, such as the unreinforced masonry used as a façade, infill and interior partition masonry (mainly due to out-of-plane action), ceilings, and other architectural elements.

This positive performance of steel structures was correlated to the overstrength provided by the seismic design code (which is based on US codes) rather than the ductility capacity [53]. It is important to mention that for many industrial facilities, the snow or wind load is the predominant one, providing the design of the building and not the seismic actions. One can observe that this powerful ground motion unveiled the following: (i) the resilience of steel structures used in the industrial sector; (ii) the importance

of anchorage and bracing the equipment in order to avoid production and business interruption.

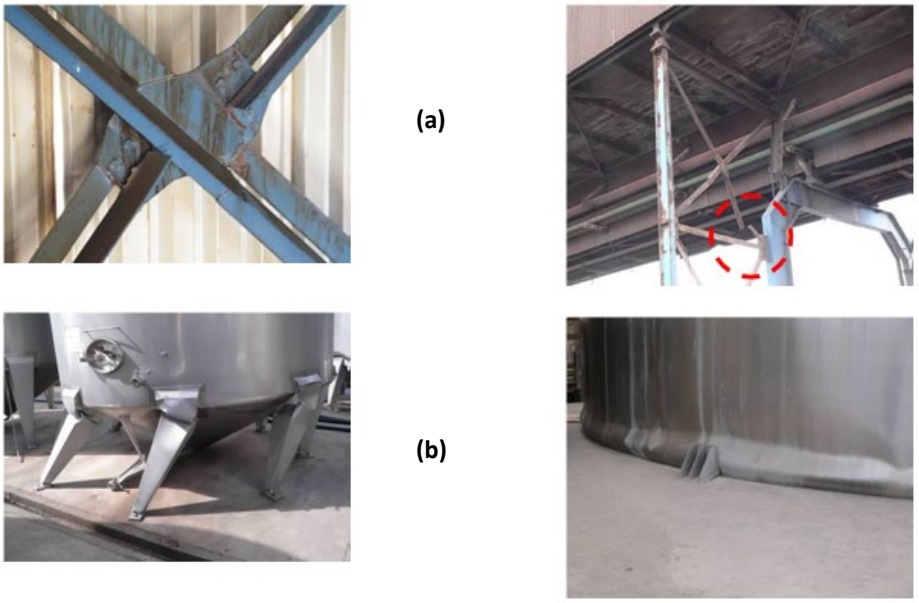


**Fig. 7.** Maule earthquake failure, (a) brace buckling and fracture, (b) buckling at the base of tanks [53]

The Maule earthquake has not had the same global impact as the Northridge, 1994, USA, and Kobe, 1995, Japan earthquakes; it was a strong earthquake that subjected steel structures beyond their limits in one of the highest seismicity countries in the world. In fact, it was a test of industrial facilities built with structural steel, largely used all over the world. Chile has a special design code for the seismic design of industrial facilities, Ch2369.Of2003 [55], which also includes provisions coming from the US seismic design codes (AISC) [56, 57]. It is important to notice that, concerning industrial facilities, except for life safety, it is of paramount importance to be functional after severe earthquakes; thus, they are designed to remain in the elastic field of behavior. Concentrically braced frames respect such conditions. Studies revealed the effectiveness of the existing code; however, in order to satisfy continuity and operational functionality after a strong earthquake, the drift is the controlling parameter [58]. Moreover, there are many situations where sensitive industrial equipment is also controlled by floor accelerations [59].

### 2.5 Christchurch earthquake, New Zealand, 2010-2011

On September 3, 2010, and on February 22, 2011, strong earthquakes struck the city of Christchurch; the second one was more catastrophic for the built environment. The focal depth was 5 km, and the epicenter was 10 km from Christchurch's Central

Business District, causing collapses and widespread damage to reinforced concrete and unreinforced masonry buildings.

With regard to steel structures, they generally performed well [60]. A specific fracture was observed in the active links of the eccentrically braced frames at Pacific Residential Tower, completed in 2010, with a perimeter EBF as part of a lateral load resisting system, and at a hospital parking garage designed to accommodate two additional floors [60], the first known recording of such failure worldwide, Fig. 8. Related to the EBF links, many studies were performed in order to explain this unexpected fracture, supporting the lack of redundancy, constructional inefficiency, and material inefficiency. However, this type of failure was concentrated on the aforementioned cases and was not a systematic observed fracture. The other types of failure are the classical ones related to steel structures when subjected to severe shaking [46].

Of paramount importance to be underlined is that the steel structures were the preferred material for the reconstruction of Christchurch [1, 60], due to their repairability as compared to the reinforced concrete structures. New types of steel frames were proposed and constructed, namely low-damage systems, shifting the current seismic design philosophy from ductility to repairability and performance [62].

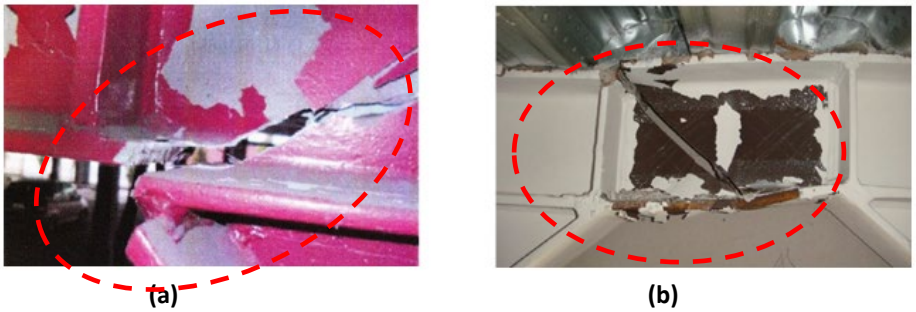


**Fig. 8.** Fracture of EBF's links, a) at hospital parking garage, b) at Pacific Residential Tower, [60]

Moreover, typical fractures in braces and local buckling in braces and columns of storage rack pallets were also observed [60], Fig. 9. However, the same damage was also reported in the USA in a series of medium and strong ground motions, such as the Whittier earthquake in 1987, the Loma Prieta earthquake in 1989, the Landers earthquake in 1992, the Northridge earthquake in 1994, the Nisqually earthquake in 2001, and San Simenone in 2003. Storage rack pallets are light, although they carry heavier live loads than dead loads. These structures have complex inelastic behavior due to thin-walled and unsymmetrical cross sections and asymmetry of connections as well, making them prone to buckling. For instance, in the USA, after the repeated and extended damage to the steel storage rack pallets, the FEMA 460 document was published [64] in order to guide the industry.

**Fig. 9.** Failures of steel rack pallets in Christchurch earthquake, 2011 [60]

This New Zealand earthquake of 2010–2011 was once again an alarming sign that not only the life safety but also the functionality of buildings (and also the infrastructure) must be ensured after a strong earthquake. The structural engineering community realized that ductility is a property that saves lives; however, this one should be balanced with sufficient stiffness in order to avoid extended non-structural damage that interrupts the operation of a building facility. New types of structural systems are proposed (such as self centering steel systems, eccentrically braced frames with replaceable links, braced frames with controlled rocking [65,66], dissipative fuses for steel moment and braced frames [67,68,69] in order to ensure a controlled inelastic behavior, with predetermined collapsed mechanisms, however, easily repairable after a strong earthquake.

### 2.6 Emiglia Romagna earthquake, Italy, 2012

On May 20 and 29, 2012, two strong ground motions of magnitudes of Mw = 6.1 and 5.8 hit the Emilia Romagna region in the northern part of Italy. A special characteristic of this earthquake was the high peak vertical acceleration of the order of 1.0g [63,70].

This earthquake affected the urban and industrial areas, where, for the second one, many reinforced concrete one-story precast buildings were severely damaged or collapsed. With regard to steel structures, this quake could be associated with the damage to cold-formed steel racks that are or are not part of the lateral load-resisting system of the building (Fig. 10). Column local buckling, plastification of connections, anchor failure, and buckling of braces are the main types of damage [63,70]. This earthquake unveiled, once again, the lack of seismic design for such structures.

In response to the aforementioned failures, in Europe, after intensive research, [71,72], the EN 16681 design code for “Steel static storage systems. Adjustable pallet racking systems. Principles for seismic design” was developed and implemented as a European regulation, [73].

**Fig. 10.** Failure of steel racks making part, or not of the lateral load resisting system, Emilia earthquake, 2012 [70]

## 2.7 Amatrice earthquake, Italy, 2012

A sequence of earthquakes on August 24, October 26, and 30 hit the region of Central Italy, causing severe damage mainly to buildings and the architectural heritage. Related to the steel buildings, a characteristic failure was pointed out in the case of an moment resisting frame interacting with masonry infill, Fig. 11, [74]. There are many situations where infill masonry is used instead of braces to limit lateral deformation. However, for such cases, special detailing should be used; for instance, we can distinguish between two main ways: (i) detaching the infill masonry from the main frame and filling the gap with a compressible material, or (ii) connecting it with steel angles or other steel elements anchored to the main frame. In both cases, out-of-plan bending of the infill masonry must be ensured.

**Fig. 11.** Steel frame with infill masonry interaction, Amatrice earthquake, 2016, [74]

## 3. Discussion and aftermaths

A brief overview of the seismic performance of steel building structures reveals the vulnerable points and defines the limits of capacity. Principally, the accumulated experience from past earthquakes revealed that a steel structure must be detailed ensuring: (i) a continue flow of forces, without concentrations, (for instance using continuity plates, diaphragms), (ii) a compatibility of connecting systems, (i.e. in case of a combination of bolts and welds employed in a connection), (iii) alternative load paths when a structural component buckles, through the use of high redundant systems, (iv) proper bracing in all directions of action and (v) suitable anchoring not permitting undesirable sliding or movements, (vi) the differences between near field, (predominant strain rate effect and vertical acceleration component), vs. far field, (predominant cyclic effect and influence of geotechnical conditions), earthquake actions [2,75,76,77].

It is well known that old structures designed without using the capacity design philosophy are more prone to damage and have a higher probability of collapse. Even the newer structures dimensioned according to capacity design must be detailed in such a way to move the plastic hinge away from the column face; this is done because, by definition, in moment-resisting frames, the beam-column connection is the most stressed region. Therefore, over-stress mitigation techniques (by strengthening, adding cover plates and haunches to the beam's flanges, or by weakening and reducing the beam's flanges, namely the reduced beam section concept) should be applied [75]. In the case of MRFs governed by drift design, it is proper to use the strengthening solution to improve the rigidity of the joints, while in the case of prevalent seismic design, the weakening solution is preferred to relocate the plastic hinge in the lower stressed zone [31,33,78]. Furthermore, the application of the "column tree concept" is also a suitable solution, where shop welded and field bolted connections are employed (beam-column shop welded connection and a field bolted splice of beams, applied at a point of low bending moment, within the beam span). Finally, a simple conforming rule is to use higher steel quality for columns than the beams, forcing the formation of the plastic hinge in a region of lower strength (i.e., columns made from steel quality S355 or S460 and beams from steel quality S235 or S275, or even S355 when the steel quality of the column is S460) [79,80,81]. Generalizing this rule, for elements that by definition are preferred to remain in the elastic region, a higher steel quality should be employed. For steel moment-resisting frames subjected to near-field actions, some measures would be to use thinner plates, high steel ultimate to yield stress ratio, sections with wider flanges, forcing longer flange buckling lengths [82].

The aforementioned discussion is associated with the ductility concept, which accepts a high level of inelastic deformation, namely a high level of damage. Nowadays, we can distinguish two new design trends: (i) a new concept of low-damage beam-to-column connections, as accepted and widely used in the Christchurch reconstruction [1, 62], and (ii) a design philosophy of connections free of damage [83] and prequalification of connections (applicable to Europe [84,85]). In practice, the seismic design should balance stiffness, strength, ductility, and repairability according to seismicity, geotechnical conditions, building importance, cost of business interruption, and construction budget.

Globally, both in academia and industry, a shift from the traditional forced base design, considering ductility as the only vital mechanical property, to a resilient base seismic design is under debate and investigation. In fact, ductility is connected with life safety and collapse prevention. Currently, the structural engineering community is striving with issues of sustainability (to reduce material consumption, to reuse the structural elements and structures, and to recycle the steel material) and structural resiliency (predictable and timely functional recovery after a strong earthquake [86]). Such examples are presented in [87, 88]. Nevertheless, any type of action requires collaboration, combination, and the development of strong relationships between research, construction practices, and policies.

## 4. Conclusions

The present work, through a qualitative analysis, records the failures in steel building structures observed in the last 40 years after strong earthquakes. Such review studies are very useful; in the evolution of time and in a centralized way, one can monitor the seismic performance of steel building structures, unveiling the vulnerabilities and capacities. Learning from failures is part of education and development. From failures, we mainly understand the system vulnerabilities. Nevertheless, we also learn from success; this reveals the system's capacities. To this end, we must remark that unfortunately, in academic studies and also in university curricula, there are not such lectures to educate young students or professionals about the successes and failures of the different structural systems.

Focused on the current analysis, the following conclusions could be drawn:

- Usually steel building structures, except in the case of the Pino Suarez building in Mexico City, present only local failures that are repairable and not global failures or collapses. They ensure the criteria of life safety.
- In the case of multistory buildings, care should be given, after strong earthquakes, to the inspection of the welded or bolted connections, which are covered in fireproof protective intumescent coating, gypsum boards, or ceilings. In these cases, the architectural and fire-protective elements should be removed in order to make the connections visible. This was the aftermath, especially from the Northridge earthquake in 1994, where damage was found in welds probable from previous earthquakes (e.g., Loma Prieta, 1989).
- The repeated damage observed from Northridge, 1995, USA, and Kobe, 1995, Japan, unveiled the vulnerability of the improperly detailed welded connections. If this zone, especially at the column face, is highly stressed, then special care should be given to the onsite executed welds, and a thorough inspection must be performed as well.
- Under certain circumstances, steel buildings provide a viable solution for rapid and safe mass construction after a devastating earthquake. This was the case with the Christchurch reconstruction in New Zealand after the strong earthquakes of 2010–2011.

- Steel structures are the leading material and structural bearing systems for one- or two-story industrial building facilities and platforms. Mainly, this is due to the reduced dead load influencing, positively, not only the seismic action but also the foundation system. However, for low-rise, medium-rise, and tall buildings, there is a choice mainly in the USA and Japan, and at a lower level in Europe and other countries. In any case, this is a viable solution respecting the sustainability and resilient mode of constructing buildings.
- The long list of vulnerabilities of steel storage pallet racking systems is unveiled, and currently, in both the USA and Europe, there is a framework to design such structures subjected to earthquakes. The research projects SEISRACKS1 and SEISRACKS2 provided proposals for the revision of the existing code; however, they are still not implemented. Open issues remain: loading protocols, experimental tests to simulate seismic actions, and more tests with regard to full racks, base connections, and beam-to-inside connections.
- Certainly, from the accumulated experience of the past 40 years, it has been demonstrated that steel structures, when properly designed and constructed, respect the performance levels of life safety and collapse prevention. However, the next challenge is to ensure the performance of the operation and immediate occupancy. Due to their inherent flexibility, this task would be addressed in the near future in order to conform resilient steel buildings to a capacity for easy repair not only of the bearing structure (this is done) but also of the non-structural components, through design, and proper constructional detailing.

## References

1. Bruneau, M., MacRae, G.: Reconstructing Christchurch: A seismic shift in building structural systems. The Quake Center. University of Canterbury. Report, (2017)
2. Gioncu V, Mazzolani FM.: Seismic design of steel structures. 1st edn. CRC Press, London (2014)
3. Stone W., Yokel F., Celebi M., Hanks T. and Leyendecker E.: Engineering Aspects of the September 19, 1985 Mexico Earthquake (NBS BSS 165), Building Science Series, National Institute of Standards and Technology, (1987)
4. Seed H.B., Romo M.P., Sun J., Jaime A., Lysmer J.: Mexico Earthquake of 1985 - Relationships between Soil Conditions & Earthquake Ground Motions, Earthquake Spectra, 4(4), 687-729, (1988)
5. Beck J.L., Hall J.F.: Factors Contributing to the Catastrophe in Mexico City during the Earthquake of September 19, 1985, Geophysical Research Letters, 13(6), 593-596 (1986)
6. Aguilar J., Juarez H., Ortega R., Iglesias J.: The Mexico earthquake of September 19, 1985-Statistics of damage and retrofitting techniques in reinforced concrete buildings affected by the 1985 earthquake. Earthquake Spectra, 5(1), 145-151 (1989)
7. Martinez-Romero, E.: The behaviour, overview of damage and retrofit of steel buildings after the earthquakes of September 1985. Bulletin of the New Zealand Society for Earthquake Engineering, 20(1), 30–41 (1987)
8. Osteeras J, Krawinkler H.: The Mexico Earthquake of September 19, 1985-Behavior of steel structures. Earthquake Spectra, 5(1), 51-88 (1989)

9. Scholl, R.: Observations of the performance of buildings during the 1985 Mexico earthquake, and structural design implications. International Journal of Mining and Geological Engineering, 7, 69-99 (1989)
10. SAC Joint Venture: State of Art Report on Connection Performance, Report FEMA 355D, September 2000, Federal Emergency Management Agency, Washington D.C
11. SAC Joint Venture: State of Art Report on Past Performance of Steel Moment-Frame Buildings in Earthquakes, Report FEMA 355E, September 2000, Federal Emergency Management Agency, Washington D.C
12. Popov E., Pinkey B.: Cyclic yield reversal in steel building connections. Journal of the Structural Division, ASCE, 95(ST3),66-79 (1971)
13. Popov E.: Seismic moment connections for MRFs. Journal of Constructional Steel Research, 10, 163-198, (1988)
14. Engelhardt M.D., Husain A.A.: Cyclic loading performance of welded flange-bolted web connections. Journal of Structural Engineering, 119(12), 3537-3550, 1993
15. Popov, E.P., Yang, T-S., Chang, S-P.: Design of steel MRF connections before and after 1994 Northridge earthquake. Engineering Structures, 12(20), 1030-1038 (1998)
16. Sabol, T.: An assessment of seismic design practice of steel structures in the United States since the Northridge earthquake. The Structural Design of Tall and Special Buildings, 13, 409-423 (2004)
17. Uang C.M., Bondad D.M. Dynamic testing of full-scale steel moment connections. In: 11th World Conference of Earthquake Engineering, paper no. 407, Elsevier, (1996)
18. Toyoda, M.: Failure experience in Hansin Great Earthquake. Materials Science Research International, 1(3), 198-199 (1995)
19. Hassouni A.E., Plumier A., Cherrabi A.: Experimental and numerical analysis of the strain-rate on fully welded connections. Journal of Constructional Steel Research, 67, 533-546 (2011)
20. Hamburger R.O.: Welded steel moment resisting frames. Strucuter Magazine, February (2019)
21. SAC Steel Project. https://www.sacsteel.org/project/index.html, last accessed in 2024/3/2024)
22. Mahin S., Malley J., Hamburger R.: Overview of the FEMA/SAC program for reduction of earthquake hazards in steel moment resisting frames. Journal of Constructional Steel Research, 58, 511-528 (2002)
23. SAC Joint Venture: Recommended Seismic Design Criteria for New Steel Moment-Frame Buildings, Report FEMA 350, June 2000, Federal Emergency Management Agency, Washington D.C.
24. SAC Joint Venture: Recommended Seismic Evaluation and Upgrade Criteria for Existing Welded Steel Moment-Frame Buildings, Report FEMA 351, June 2000, Federal Emergency Management Agency, Washington D.C.
25. SAC Joint Venture: Recommended Postearthquake Evaluation and Repair Criteria for Welded Steel Moment-Frame Buildings, Report FEMA 352, June 2000, Federal Emergency Management Agency, Washington D.C.
26. SAC Joint Venture: State of Art Report on Base Metals and Fracture, Report FEMA 355A, September 2000, Federal Emergency Management Agency, Washington D.C.
27. SAC Joint Venture: State of Art Report on Welding and Inspection, Report FEMA 355B, September 2000, Federal Emergency Management Agency, Washington D.C.
28. SAC Joint Venture: Recommended Specifications and Quality Assurance Guidelines for Steel Moment-Frame Construction for Seismic Applications, Report FEMA 353, June 2000, Federal Emergency Management Agency, Washington D.C.

29. Plumier A: The Dogbone: Back to the future. Engineering Journal, AISC, Second Quarter, 1997
30. Engelhardt M. D., T. Winneberger, A. J. Zekany, T. Potyraj: The dogbone connection: Part II, Modern Steel Construction, AISC,August, (1996)
31. Engelhardt M. D., T. A. Sabol: Reinforcing of steel moment connections with cover pates: benefits and limitations, Engineering Structures, 20(4-6), 510-520 (2002)
32. Civjan S., Engelhardt M., Gross J.: Retrofit of pre-Northridge moment-resisting connections. J. Struct. Eng., ASCE 126, 445–452 (2000)
33. Uang C.M., Yu Q., Noel S., Gross J., Cyclic testing of steel moment connections rehabilitated with RBS or welded haunch, J. Struct. Eng. ASCE 126, 57–68 (2000)
34. Sabeli R., Mahin S., Chang C.: Seismic demands on steel braced frame buildings with buckling restrained braces. Engineering Structures, 25, 655-666 (2003)
35. Astaneh A., Zhao Q.: "Cyclic Test of Steel Shear Walls –Final Report." Department of Civil and Environmental Engineering, College of Engineering, University of California at Berkeley. August, (2002)
36. Uang C.M., Bruneau M.: State-of-the-Art review on seismic design of steel structures. J. Struct. Eng., 144(4), 03118002 (2018)
37. Krawinkler H., Gupta A., Medina R., Luco N.: Loading histories for seismc performance testing of SMRF components ans assemblies, SAC Joint Venture. Report No. SAC/BD-00/10. SAC Joint Venture, Sacramento, CA, (2000)
38. Clark P., Frank K., Krawinkler H., Shaw, R.: Protocol for Fabrication, Inspection, Testing, and Documentation of Beam-Column Connection Tests and Other Experimental Specimens. Report No. SAC/BD-97/02, SAC Joint Venture, Sacramento, CA, (1997)
39. Uang C.M., Yu Q.S., Gilton C.S.: Effects of loading history on cyclic performance of steel RBS moment connections. In: 12th World Conference of Earthquake Engineering, New Zealand, paper 1294, (2000)
40. Hamburger R., Fouthch D.A., Cornell C.A.: Performance basis of guidelines for evaluation, upgrade and design of moment-resisting steel frames. In: 12th World Conference of Earthquake Engineering, New Zealand, paper 2543, (2000)
41. FEMA P-58-6: Guidelines for Performance-Based Seismic Design of Buildings, prepared by the Applied Technology Council for the Federal Emergency Management Agency, Washington, D.C., December, (2018)
42. Leon R., Rossberg J.: Evolution and future building codes in the USA. Structural Engineering International 22(2), 265-269 (2012)
43. American Institute of Steel Construction: https://www.aisc.org/publications/steel-standards/, last accessed 2024/3/17
44. Silva, W., Iwasaki, Y.: Assessment of liquefaction potential for the 1995 Kobe, Japan earthquake including finite source effects. U.S Army Engineer Waterways Experiment Station, Corps of Engineers. Final Report, (1999)
45. Norton, J., King, A.B., Bull, D.K., Champan, E.H., MacVerry, G.H., Larkin, T.J., Spring. K.C.: The Northridge earthquake report reconnaissance. Bulletin of Earthquake Engineering, 27(4), 235-344 (1994)
46. Nakashima, M., Inoue, K., Tada, M.: Classification of damage to steel buildings observed in the 1995 Hyogoken-Nanbu earthquake. Engineering Structures, 20 (4-6), 271-281 (1998)
47. Tremblay, R., Bruneau, M., Nakashim,a M., Prion, H., Filiatrault, A., DeVall, R.: Seismic design of steel buildings: lessons from the 1995 Hyogoken-Nambu earthquake. Canadian Journal of Civil Engineering, 23, 727-756 (1998)
48. Architectural Institute of Japan: Report on 1995 Great Hanshin-Awaji Earthquake by

Building Earthquake Investigation Committee, (1996)
49. Editorial Committee for the Report on the Hanshin-Awaji Earthquake Disaster: Report on the Hanshin-Awaji Earthquake disaster, General Issues, Vol. 1. Architectural Institute of Japan, 2000
50. Nakashima M., Kato M., Okazaki T.: Collaboration between practice and research for development of steel construction in Japan. Steel Structures, 4, 249-262 (2004)
51. Midorikawa M., Okawa I., Iiba M., Teshigaware M.: Performance-based seismic design provisions newly introduced to building standard law of Japan. Journal of Japan Association for Earthquake Engineering, 4(3), 162-173 (2004)
52. National Research Institute for Earth Science and Disaster Resilience (NIED): https://www.bosai.go.jp/hyogo/ehyogo/profile/profile.html, last accessed 2024/3/17
53. Herrera, R., Beltran, J.F.: Performance of steel structures during the February 27, 2010, Chile earthquake. In: 15th World Conference on Earthquake Engineering, Lisbon, Portugal, paper 4249, (2015)
54. Saatcioglu, M.,Tremblay, R.,Mitchell, D.,Ghobarah, A.,Palermo, D.,Simpson, R., Adebar, P., Ventura, C., Hong, H.: Performance of steel buildings and nonstructural elements during the 27 February 2010 Maule (Chile) Earthquake. Canadian Journal of Civil Engineering. 40, 722–734 (2013)
55. INN (2003). Diseño Sísmico de Estructuras e Instalaciones Industriales, NCh2369.Of2003. Santiago, Chile: Instituto Nacional de Normalización.
56. AISC. LRFD Specification for Structural Steel Buildings, 1999, American Institute of Steel Construction, Chicago, IL
57. AISC. ANSI/AISC 341-02. Seismic Provisions for Structural Steel Buildings, American Institute of Steel Construction, Chicago, IL
58. Riquelme R., Herrera R.: Seismic performance of Chilean concentrically braced frame industrial structures: effects of recent code modifications. Front. Built Environ., 9,1155915 (2023)
59. Medalla M., Pena C., Lopez-Garcia D., Illanes R.: NCh2396 vs ASCE7-Strength vs Ductility ?. In. 16th World Conference on Erthqauke Engineering, Chile, paper no. 4629, (2017)
60. Clifton, C., Bruneau, M., MacRae, G., Leon, R., Fussell, A.: Steel structures damage from the Christchurch earthquake series of 2010 and 2011. Bulletin of the New Zealand Society for Earthquake Engineering, 44 (4), 297-318 (2011)
61. Bruneau, N., MacRae, G.: Building Structural Systems in Christchurch's Post-Earthquake Reconstruction. Earthquake Spectra, 35(4), 1953-1978 (2019)
62. MacRae, G.A., Clifton, G.C.: New Zealand research applications of and developments in low damage technology for steel structures. In Proceedings of New Zealand Society of Earthquake Engineering, 1-14, (2017)
63. Castiglioni, C.A.: Seismic behavior of steel storage pallet racking systems.1st edn. Springer, Switzerland (2016)
64. FEMA 460.: Seismic Considerations for Steel Storage Racks Located in Areas Accessible to the Public. September (2015)
65. Fang C., Wang W., Qiu C., Shuling H., MacRae A., Eartherton M.: Seismic resilient steel structures: A review of research, practice, challenges and opportunities. Journal of Constructional Steel Research, 191, 107172 (2022)
66. Zhong C., Christopoulos C.: Self-centering seismic-resistant structures: Historical overview and stat-of-the art. Earthquake Spectra. 38(2), 1321-1356 (2022)
67. Vayas I., Thanopoulos P.: Innovative Dissipative (INERD) Pin Connections for Seismic Resistant Braced Frames, International Journal of Steel Structures, 5(5), 453-464 (2005)

68. Vayas I., Karydakis Ph., Dimakogianni D., Dougka G., Castiglioni C. A., Kanyilmaz A. et al.: Dissipative devices for seismic-resistant steel frames (FUSEIS), Research Fund for Coal and Steel, European Commission EU 25901 EN 2013. DOI: 10.2777/88177
69. Castiglioni C.A., Calado L., Kanyilmaz A.: Experimental analysis of seismic resistant composite steel frames with dissipative devices, Journal of Constructional Steel Research, 76,1-12 (2012)
70. Liberatore, L., Sorrentino, L., Liberatore, D., Decanini, L.: Failure of industrial structures induced by the Emilia (Italy) 2012 earthquakes. Engineering Failure Analysis, 34, 629-647 (2013)
71. EU-RFCS Steel RTD Programme RFSR-CT-2004-00045 SEISRACKS1: Storage Racks in Seismic Areas, 2004.12.01 - 2007.05.31
72. EU-RFCS Steel RTD Programme RFSR-CT-2011-00031 SEISRACKS2: Seismic Behavior of Steel Storage Pallet Racking Systems 2011.07.01 - 2014.06.30
73. EN 16681:2016. Steel static storage systems - Adjustable pallet racking-Principles for seismic design. European Committee for Standardization, CEN-CENELEC, (2016)
74. DiSarno, L., Paolacci, F., Sextos, A.G.: Seismic performance assessment of existing steel buildings: A case study. Key Engineering Materials, 763, 1067-1076 (2018)
75. Bruneau M., Uang C.M., Sabelli R.: Ductile design of steel structures. 2nd edn. McGraw Hill, New York (2011)
76. Papageorgiou T., Gantes C.J.: Mixed In-Height Concrete-Steel Buildings Under Seismic Actions: Modeling and Analysis. In: Beer, M., Kougioumtzoglou, I.A., Patelli, E., Au, SK. (eds) Encyclopedia of Earthquake Engineering. Springer, Berlin, Heidelberg, (2015)
77. Alavi B., Krawinkler H.: Behavior of moment-resisting frame structures subjected to near-fault ground motion. Earthquake engineering and Structural Dynamics, 33, 687-706 (2004)
78. Chambers J., Almudhafar S., Stenger F.: Effect of reduced beam section frmae elements on stiffness of moment frames. Journal of Structural Engineering, 129(3), 383-393 (2003)
79. Anastasiadis, A., Mateescu, G., Gioncu, V.: Improved ductile design of steel MR-frames based on constructional details. In Proceedings: 9th International Conference of Metal Structures, Timisoara, Romania, 2000
80. Dubina D., Stratan A., Dinu F.: Dual high-strength steel eccentrically braced frames with removable links. Earthquake Engineering and Structural Dynamics 37(15),1703–1720 (2008)
81. Dubina D.: High strength steel and fuse dissipative solutions for seismic resistant building structures. In. EuroSteel 2021, Sheffield, 4(2-4), 25-33, Ernst & Sohn Verlag, Berlin
82. Gioncu, V., Mosoarca, M., Anastasiadis, A.: Local ductility of steel elements under near field earthquake loading. Journal of Constructional Steel Research, 101, 33-52 (2014)
83. Piluso, V., Rizzano, G., Latour, M., Montuori, R., Nastri, E., Francavilla, A., Di Benedetto, S., Landolfo, R., D' Aniello, M., Da Silva, L.S., Santiago, A., Santos, A.F., Jaspart, J.P., Demonceau, J.F.: Seismic design of steel structures with free from damage steel connections. European Convention for Constructional Steelwork, 2022
84. Landolfo R., D'Aniello M., Costanzo S., Tartaglia R., Stratan A., Dubina D., Vulcu C., Maris C., Zub C., Da Silva L., Rebelo C., Augusto H., Shahbazian A., Gentili F., Jaspart J.P., Demonceau J.F., Hoang L.L., Elghazouli A., Tsitos A., Vassart O., Moreno E. Nunez, V. Dehan, C. Hamreza, European pre-QUALified steel JOINTS (EQUALJOINTS), Final Report, 2018-05-04, Directorate-General for Research and Innovation, European Commission, (2018)
85. Landolfo R., D'Aniello M., Vayas I.: Valorisation of knowledge for European

prequalified steel joints: The EqualJoints plus project. In: COMPDYN 2019, 7th ECCOMAS Thematic Conference on Computational Methods in Structural Dynamics and Earthquake Engineering, M. Papadrakakis, M. Fragiadakis (eds.), 64-72 (2019)
86. Earthquake Engineering Research Institute: Functional Recovery: A conceptual framwork with policy options. A white paper of the Earthquake Engineering Research Institute, December, (2019)
87. Skidmore J., Granello G., Palermo A.: Drivers and challenges in using low damage seismic designs in Christchurch buildings. Bulletin of the New Zealand Society for Earthquake Engineering, 55(4), 214-228 (2022)
88. Lignos D., Paronesso M: Low damage steel structures for enhanced life-cycle seismic performance. Stahlbau, 9(5), 315-325 (2022)

# Next Generation of Inorganic Composite Materials for Structural Strengthening: Development of Geopolymer Matrix

Ioanna Skyrianou[1[0000-0002-0231-9387]], Christos G. Papakonstantinou[1[0000-0001-9165-8307]] and Lampros N. Koutas[1[0000-0002-7259-6910]]

[1]Department of Civil Engineering, University of Thessaly, Pedion Areos, GR-38334, Volos, Greece
iskyrianou@uth.gr, cpapak@uth.gr, koutas@uth.gr

**Abstract.** With the increasing need to strengthen seismically vulnerable structures, the use of composite materials, particularly textile-reinforced mortars (TRMs), has gained significant attention. In efforts to improve the mechanical properties of these materials while reducing their environmental impact, new alternatives are being explored. Geopolymer mortars, used as a matrix in composite materials, present a sustainable alternative to traditional cement-based mortars. The current study experimentally investigates the compressive and flexural strength of metakaolin-based geopolymer mortars, aiming to optimize their mix design. The properties of these geopolymer mortars are compared with commercially available cement-based mortars suitable for use as a matrix in TRMs. The study focuses on two key mix design parameters: the activator-to-precursor ratio and the sand gradation. Results indicate that the activator-to-precursor ratio significantly influences the strength and workability of the mortars, while the sand gradation primarily affects workability rather than strength. In comparison to the cement-based mortars studied, the geopolymer mortars demonstrated comparable, and in some cases superior, compressive and flexural strength.

**Keywords:** Geopolymers, Metakaolin, Composite materials, Structural strengthening

## 1. Introduction

More than 88% of the Greek building stock was constructed before 2000, with nearly half of these buildings being constructed before 1970, according to the 2011 Building Census [1]. As a result, a significant portion of the existing buildings in Greece were designed and built using outdated construction methods, materials, and specifications, which do not meet modern standards for structural safety or environmental sustainability. This is particularly concerning given the high seismicity of Greece, where earthquakes pose a substantial threat to public safety. This combination of aging infrastructure and seismic risk underscores the urgent need for retrofitting and strengthening older buildings to ensure their safety and prolong their service life. As a result, the

demand for effective, sustainable strengthening methods has grown significantly, with the research community seeking to explore innovative materials and technologies that can provide enhanced performance while minimizing environmental impact.

Traditionally, one of the most widely used methods for strengthening existing buildings has been the application of externally bonded fibre-reinforced polymers (FRP). FRPs are known for their high strength-to-weight ratio and ability to enhance the structural integrity of buildings, particularly in seismic zones. However, while FRPs offer several advantages, their use is not without limitations, such as their vulnerability to environmental degradation over time, including UV radiation and moisture exposure. Recently, the use of textile-reinforced mortars (TRM) has been gaining popularity as an alternative or complement to FRPs in structural retrofitting. TRMs utilize an inorganic, usually cement-based, mortar matrix in combination with textile reinforcements, offering improved durability, fire resistance, and ease of application compared to traditional organic composites [2]. Despite the advantages of cement-based TRMs, the environmental impact of cement production—responsible for approximately 8% of global carbon dioxide emissions—has prompted a significant shift towards the search for more sustainable materials. In response to these environmental concerns, alkali-activated materials, also known as geopolymers, have emerged as a promising alternative to traditional cement-based binders [3]. Geopolymers are synthesized by activating aluminosilicate-rich materials, such as metakaolin, fly ash, and slags, with an alkaline solution, producing a highly durable and environmentally friendly binder. The use of geopolymer mortars has been expanding across various applications, including the repair and rehabilitation of structures, corrosion protection, and in environments subjected to high temperatures and aggressive chemical exposure [4-7].

The use of geopolymers in strengthening applications, such as reinforced concrete beams [8] and masonry [9-11], has shown promising results in comparison to conventional materials. The benefits of geopolymers include not only a reduced carbon footprint but also enhanced fire resistance, chemical durability, and mechanical properties such as high early strength. Despite these advantages, the widespread adoption of geopolymer mortars has been hindered by several challenges, primarily related to the lack of standardized mix design guidelines. The variability in the chemical composition of the precursor materials, such as metakaolin, fly ash, or slag, significantly influences the physical and mechanical properties of the geopolymer product, making it difficult to establish universal mix design standards [15].

Research into geopolymer mortars has intensified in recent years, driven by the need for sustainable construction materials and a growing understanding of their unique properties. One of the key factors influencing the properties of geopolymer mortars is the binder composition, particularly the activator-to-precursor ratio. Recent studies have demonstrated a clear correlation between activator content and the compressive and flexural strength of geopolymer mortars, with the optimal range of activator content leading to the highest mechanical performance [16-18]. The activator solution typically consists of alkali hydroxides or silicates, which are responsible for dissolving the aluminosilicate precursors and initiating the polymerization process. However, excessive activator content can lead to undesirable side effects, such as efflorescence, where salts

are deposited on the mortar's surface, which compromises both its aesthetic appearance and its mechanical properties [19].

Another important design consideration for geopolymer mortars is the type and gradation of sand used in the mixture. The gradation of the sand affects the mortar's consistency, packing density, and shrinkage behavior. Studies have shown that a well-graded sand mix, with a maximum nominal size of 1.18 mm, provides higher compressive and flexural strength compared to using either very fine or coarser sand fractions. The optimal sand gradation facilitates the formation of a dense, compact microstructure, contributing to enhanced strength and durability of the final mortar [20,21].

The aim of this study is to evaluate the mechanical properties of metakaolin-based geopolymer mortars and optimize the mix design for their use as a sustainable matrix in textile-reinforced mortars (TRM). The investigation focuses on optimizing key parameters, such as the activator-to-precursor ratio and sand gradation, and how these factors influence the strength, consistency, and workability of the geopolymer mortars. Additionally, the study benchmarks the performance of the optimized geopolymer mortars against commercial cement-based mortars commonly used in TRM applications. Through this study, the feasibility of geopolymer mortars as a sustainable and high-performance alternative to cement-based mortars for TRM applications will be assessed, with a focus on improving the longevity, safety, and environmental impact of retrofitted structures.

## 2. Experimental programme

In the current study, the mechanical properties of metakaolin-based geopolymer mortars were investigated to optimize the mix design for use as a matrix in textile-reinforced mortars. In the first phase of the investigation, the effect of the activator-to-precursor ratio was evaluated for five mortar mixtures (A1-A5). Based on the results from compressive and flexural strength tests, an optimal ratio was selected. In the second phase of the experimental program, the effect of limestone sand gradation on the strength and consistency of six geopolymer mortar mixtures (B1-B6) was examined. Finally, the geopolymer mortars were compared with various commercially available cement-based mortars used in strengthening applications (T1-T7).

### 2.1 Materials

For the preparation of the geopolymer mortars a metakaolin with a content of >92% in aluminium and silicon oxides and particle size distribution of $d_{10}$ = 2 μm, $d_{50}$ = 30 μm, $d_{90}$ = 100 μm was used. The activator comprised a potassium silicate solution with molar ratio between silicon and potassium oxide equal to 1.68 and total dry weight equal to 45%. Crushed limestone sand with maximum particle size 1 mm divided in 2 gradations, 0.5-1 mm and < 0.5 mm, was used as filler. 6 mm-long polypropylene fibres were also added at a volume fraction of 1% in each geopolymer mortar. A commercial cement-based mortar (T1) was experimentally investigated and consisted of a cement-based dry mix with fine sand of maximum particle size 1.3 mm and polypropylene fibres. The cement-based mortar was mixed with water according to the manufacture's

provisions. The examined geopolymer-based mortars are still under development; however, both metakaolin and the potassium silicate solution, the primary components, are commercially available.

## 2.2 Mix design optimisation

The mix design of the geopolymer mortars in the first optimisation phase is presented in Table 1. The activator to metakaolin (A:M) weight ratios chosen ranged between 1.2:1 and 2:1. Ratios below this range resulted in dense mixtures that were difficult to apply, while ratios exceeding this range led to highly fluid mixtures, which were deemed unsuitable for the current study. During this phase, the sand gradation ratio was kept constant. For the mixtures in the second phase, presented in Table 2, the gradation of the sand (F:P ratio) was investigated. The two sand gradations used were fine sand with particle sizes of 0.5-1 mm (F) and powdered sand with particle sizes of < 0.5 mm (P). In this phase, the A:M ratio was maintained at 1.2:1, as it was identified as optimal in the first optimization phase. To ensure adequate workability of the mortars, the total amount of sand was adjusted accordingly.

**Table 1.** Mix design of geopolymer mortars of the first optimisation phase

| Mortar ID | A:M ratio | Weight ratio | | | |
|---|---|---|---|---|---|
| | | Potassium silicate | Metakaolin | Sand 0.5-1 mm | Sand < 0.5 mm |
| A1 | 1.2:1 | 1.2 | 1 | 1 | 2 |
| A2 | 1.3:1 | 1.3 | 1 | 1 | 2 |
| A3 | 1.5:1 | 1.5 | 1 | 1 | 2 |
| A4 | 1.7:1 | 1.7 | 1 | 1 | 2 |
| A5 | 2:1 | 2 | 1 | 1 | 2 |

**Table 2**. Mix design of geopolymer mortars of the second optimisation phase

| Mortar ID | F:P ratio | Weight ratio | | | |
|---|---|---|---|---|---|
| | | Potassium silicate | Metakaolin | Sand 0.5-1 mm | Sand < 0.5 mm |
| B1 | 1:1 | 1.2 | 1 | 1.25 | 1.25 |
| B2 | 1:1.5 | 1.2 | 1 | 1 | 1.5 |
| B3 | 1:2 | 1.2 | 1 | 0.75 | 1.5 |
| B4 | 1:2.5 | 1.2 | 1 | 0.6 | 1.5 |
| B5 | 1.5:1 | 1.2 | 1 | 1.42 | 0.95 |
| B6 | 2:1 | 1.2 | 1 | 1.77 | 0.88 |

## 2.3 Mortar preparation

A mechanical mixer was employed for the preparation of all mortars. For the geopolymer mortars, metakaolin and sand were initially dry-mixed for 1 minute. Subsequently, the alkali solution, to which polypropylene fibers had been added, was gradually incorporated into the dry ingredients. The mixture was then blended at medium speed for 2–3 minutes until homogenized, followed by an additional 5 minutes of

mixing at high speed. The preparation of the cement-based mortar (T1) followed a similar procedure. The cement-based binder was combined with water, which was added gradually at medium speed for 5 minutes, followed by mixing at high speed for a further 5 minutes. After mixing, all mortars were poured into molds in two layers to form prisms with dimensions of 40×40×160 mm, and subsequently vibrated to ensure proper compaction. The prisms were removed from the molds after 2 days and cured under ambient room conditions for a total of 28 days prior to testing. Representative prisms of both the cement-based and geopolymer mortars are depicted in Fig 1. To evaluate the flexural strength, each prism was subjected to 3-point bending, after which each half was tested under monotonic compression using a 40 mm cube, in accordance with EN 1015-11 [22].

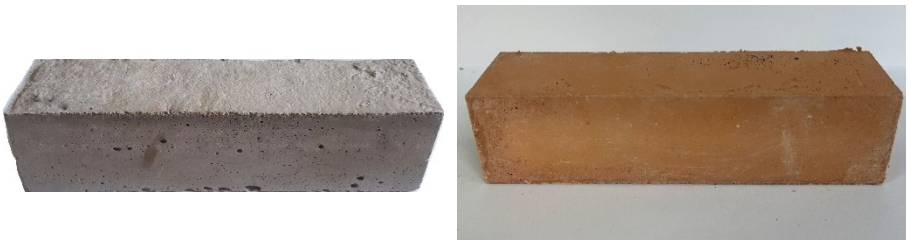

(a) (b)

**Fig. 1.** Typical prism of (a) cement-based and (b) geopolymer mortar

## 3. Results and discussion

### 3.1 Mix design optimisation

The results of the compressive and flexural strength of both optimisation phases are presented in Table 3. Based on the results of the first phase, mortar A1 exhibited the highest strength, with an A:M ratio of 1.2:1. Its flexural and compressive strengths were measured at 6.6 MPa and 38.3 MPa, respectively. Increasing the A:M ratio led to a progressive decrease in strength, with mortar A5 showing values of 3 MPa in flexure and 18.3 MPa in compression. The increase in activator content also improved workability, leading to a more fluid and less stable consistency in the mortars. However, excessive activator content caused efflorescence in mortars A3, A4, and A5 (as shown in Fig. 2) and led to a decrease in strength. The efflorescence was more pronounced with higher activator content and progressed over time. As a result, mortar A1 exhibited the best strength, and its A:M ratio of 1.2:1 was selected as the optimal mix.

**Table 3.** Strength results from the mix design optimisation

| Mortar ID | Flexural strength (MPa) | Compressive strength (MPa) |
|---|---|---|
| A1 | 6.61 | 38.27 |
| A2 | 6.00 | 34.38 |
| A3 | 4.93 | 26.14 |
| A4 | 3.81 | 22.05 |
| A5 | 3.04 | 18.32 |
| B1 | 6.08 | 35.55 |
| B2 | 5.30 | 35.00 |
| B3 | 6.09 | 31.18 |
| B4 | 5.17 | 29.35 |
| B5 | 5.16 | 33.52 |
| B6 | 5.02 | 33.47 |

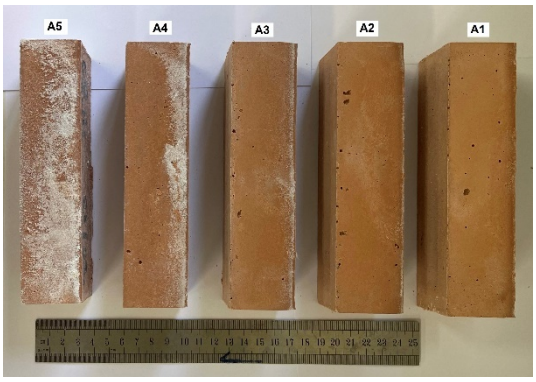


**Fig. 2.** Mortars of the first optimisation phase with efflorescence

As for the mortars in the second optimization phase, since the A:M ratio was already optimal, no signs of efflorescence were observed. The flexural and compressive strength ranged from 5 MPa to 6.1 MPa and from 29.3 MPa to 35.5 MPa, respectively. In this case, the effect of the sand gradation ratio (P:F) was not as significant as the A:M ratio. On the contrary, the total amount of sand, as well as its gradation, seemed to have a greater impact on the consistency of the geopolymer mortars. When more powdered sand (< 0.5 mm) was used, as in mortars B2, B3, and B4, the mortars were denser. In contrast, mortars B5 and B6, which contained more fine sand (0.5-1 mm), were more watery, granular, and had a tendency to segregate from the geopolymer paste. This is a deterrent for applications as a matrix in composite materials, as the mortar needs to adequately impregnate the fiber textile; thus, a well-graded mix is preferred. Based on both strength and consistency, mortar B3, with a F:P ratio of 1:2, was selected as the optimal mix. Mortar B1, which had similar flexural strength and slightly higher compressive strength compared to B3, contained more fine sand and could be considered a good alternative. However, B3 was chosen as the optimal due to its better consistency.

### 3.2 Comparison between cement-based and geopolymer mortars

**Table 4.** Strength results from cement-based mortars

| Mortar ID | Flexural strength (MPa) | Compressive strength (MPa) |
|---|---|---|
| T1 | 4.25 | 21.51 |
| T2 [23] | 9.80 | 39.20 |
| T3 [24] | 3.28 | 8.56 |
| T4 [24] | 4.24 | 30.61 |
| T5 [25] | 3.50 | 20.00 |
| T6 [25] | 8.30 | 40.00 |
| T7 [25] | 4.30 | 30.00 |

For comparison purposes, several commercial cement-based mortars used in strengthening applications were investigated and their strength is presented in Table 4. Mortar T1 is a common mortar used by the authors in strengthening applications, while mortars T2-T7 were used as a matrix in TRMs in other studies from literature [23-25]. It is evident that both optimised geopolymer mortars (A1 and B3) exhibited higher strength than mortar T1. Specifically, mortar A1 had higher flexural and compressive strength by 55.6% and 77.9%, respectively. Likewise, mortar B3 had 43.4% and 44%, higher flexural and compressive strength, respectively. Mortars T2-T7 had a flexural and compressive strength that ranged between 3.3-9.8 MPa and 8.5-40 MPa, respectively. It is noticeable that there is a significant variation in the results due to the different compositions of the cement-based mortars, with some also incorporating additive polymers to enhance strength (T2 and T4). When comparing the cement-based mortars with the geopolymer mortars A1 and B3, it is evident that the latter exhibited similar, and in some cases, higher strength. As shown in Fig 3, the optimal geopolymer mortars from both phases (A1 and B3) were able to achieve strengths comparable to the investigated cement-based mortars, surpassing their mean values for both flexural and compressive strength, which were 5.38 MPa and 27.1 MPa, respectively. Therefore, based on these preliminary results, geopolymer mortars could be a promising alternative to cement-based mortars in TRMs.

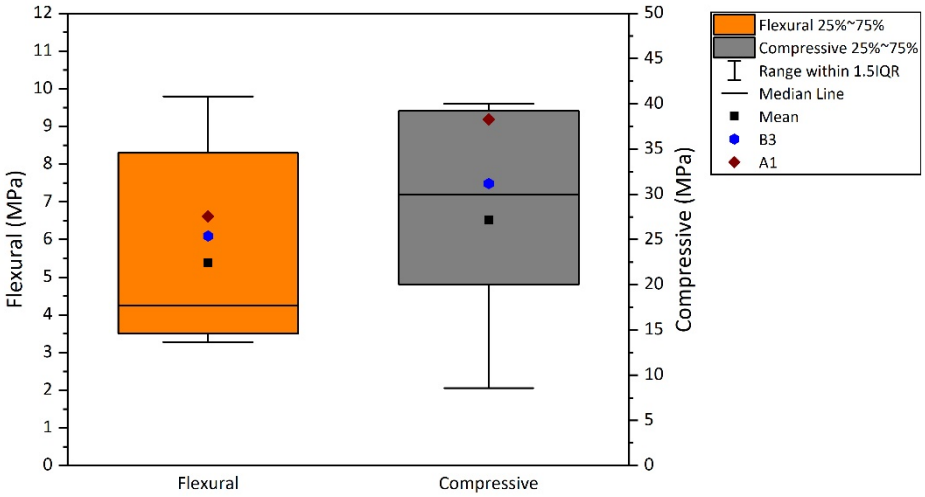


**Fig. 3.** Comparison between geopolymer and cement-based mortar strength

## 4. Conclusions

In the current study the mechanical properties of geopolymer mortars with the intend to be used as a matrix in composite materials as an alternative to cement-based mortars were investigated. Two optimisation phases were conducted investigating the effect of the activator to precursor ratio and the gradation of sand ratio on the strength and consistency of the mortars. In the end a comparison of the optimal geopolymer mortars with various cement-based ones was carried out. Based on the results the following conclusions were drawn:

- The activator to precursor ratio (A:M) played a significant role on the strength of the geopolymer mortars, while the sand gradation ratio (F:P) affected more their consistency and workability.
- The experimental programme resulted in the selection of the optimal A:M and F:P ratios equal to 1.2:1 and 1:2, respectively, based on the raw materials used.
- The flexural and compressive strength of the optimal geopolymer mortar, which was measured equal to 6.1 MPa and 31.2 MPa, respectively, had similar strength to cement-based mortars.

Based on the above conclusions, it is evident that geopolymer mortars could be a promising sustainable alternative to cement-based mortars in TRMs. However, further investigation on the mechanical properties of the optimal mortar as well as its compatibility with various textiles should be carried out to evaluate its performance and find an optimal solution for strengthening applications.

It is also important to consider the cost implications. Cement-based mortars are priced at approximately 1 euro per kilogram, whereas geopolymer mixtures are estimated to cost around 1.5 euros per kilogram. However, it should be noted that geopolymer pricing is based on small-scale production, and bulk costs could potentially be

significantly lower, which may make geopolymers more economically competitive in the future.

## Acknowledgements

The research was conducted in the operating framework of the Center of Research, Innovation and Excellence of University of Thessaly and was funded by the Special Account of Research Grants of University of Thessaly. The Department of Materials and Quality Control of Public Works of Thessaly of the Decentralized Administration of Thessaly - Central Greece is highly acknowledged for the utilisation of their facilities.

## References

1. Hellenic Statistical Authority, 2011 Building Census, Press Release, https://www.statistics.gr/census-buildings-2011, last accessed 2024/02/22
2. Koutas, L. N., Tetta, Z., Bournas, D. A., Triantafillou, T. C.: Strengthening of concrete structures with textile reinforced mortars: State-of-the-art review. Journal of Composites for Construction, 23(1), 03118001 (2019). https://doi.org/10.1061/(ASCE)CC.1943-5614.0000882
3. Provis, J. L., Van Deventer, J. S. J.: Alkali Activated Materials: State-of-the-Art Report, RILEM TC 224-AAM (Vol. 13). Springer Netherlands (2014). https://doi.org/10.1007/978-94-007-7672-2_1
4. Pacheco-Torgal, F., Abdollahnejad, Z., Miraldo, S., Baklouti, S., Ding, Y.: An overview on the potential of geopolymers for concrete infrastructure rehabilitation. Construction and Building Materials, 36, 1053-1058 (2012). https://doi.org/10.1016/j.conbuildmat.2012.07.003
5. Giancaspro, J. W., Papakonstantinou, C. G., Balaguru, P. N.: Flexural Response of Inorganic Hybrid Composites With E-Glass and Carbon Fibers. Journal of Engineering Materials and Technology, 132(2), 0210051-0210058 (2010). https://doi.org/10.1115/1.4000670
6. Al-Majidi, M. H., Lampropoulos, A. P., Cundy, A. B., Tsioulou, O. T., Al-Rekabi, S.: A novel corrosion resistant repair technique for existing reinforced concrete (RC) elements using polyvinyl alcohol fibre reinforced geopolymer concrete (PVAFRGC). Construction and Building Materials, 164, 603-619 (2018). https://doi.org/10.1016/j.conbuildmat.2017.12.213
7. Sakkas, K., Sofianos, A., Nomikos, P., Panias, D.: Behaviour of passive fire protection K-geopolymer under successive severe fire incidents. Materials, 8(9), 6096-6104 (2015). https://doi.org/10.3390/ma8095294
8. Skyrianou, I., Papakonstantinou, C. G., Koutas, L. N.: Advanced Composites with Alkali-Activated Matrices for Strengthening of Concrete Structures: Review Study. Key Engineering Materials, 919, 65-71 (2022). https://doi.org/10.4028/p-sm2iot
9. Gkournelos, P. D., Azdejković, L. D., Triantafillou, T. C.: Innovative and eco-friendly solutions for the seismic retrofitting of natural stone masonry walls with textile reinforced mortar: In-and out-of-plane behavior. Journal of Composites for Construction, 26(1), 04021061 (2022). https://doi.org/10.1061/(ASCE)CC.1943-5614.0001173
10. Cholostiakow, S., Koutas, L. N., Papakonstantinou, C. G.: Geopolymer versus cement-

based textile-reinforced mortar: Diagonal compression tests on masonry walls representative of infills in RC frames. Construction and Building Materials, 373, 130836 (2023). https://doi.org/10.1016/j.conbuildmat.2023.130836
11. Cholostiakow, S., Skyrianou, I., Koutas, L., Papakonstantinou, C.: Out-of-plane performance of structurally and energy retrofitted masonry walls: geopolymer versus cement-based textile-reinforced mortar combined with thermal insulation. Open Research Europe, 3, 186 (2023). https://doi.org/10.12688/openreseurope.16724.1
12. Purdon, A. O.: The action of alkalis on blast furnace slag. Journal of the Society of Chemical Industry, 59(9), 191-202 (1940)
13. Weil, M., Dombrowski, K., Buchwald, A.: Life-cycle analysis of geopolymers. In: Provis, J. L., van Deventer, J. S. J. (eds.) Geopolymers, pp. 194-210. Woodhead Publishing (2009). https://doi.org/10.1533/9781845696382.2.194
14. Zhang, P., Zheng, Y., Wang, K., Zhang, J.: A review on properties of fresh and hardened geopolymer mortar. Composites Part B: Engineering, 152, 79-95 (2018). https://doi.org/10.1016/j.compositesb.2018.06.031
15. Provis, J. L.: Alkali-activated materials. Cement and Concrete Research, 114, 40-48 (2018). https://doi.org/10.1016/j.cemconres.2017.02.009
16. Samantasinghar, S., Singh, S. P.: Effect of synthesis parameters on compressive strength of fly ash-slag blended geopolymer. Construction and Building Materials, 170, 225-234 (2018). https://doi.org/10.1016/j.conbuildmat.2018.03.026
17. Wang, H., Wu, H., Xing, Z., Wang, R., Dai, S.: The Effect of Various Si/Al, Na/Al Molar Ratios and Free Water on Micromorphology and Macro-Strength of Metakaolin-Based Geopolymer. Materials, 14(14), 3845 (2021). https://doi.org/10.3390/ma14143845
18. Haruna, S., Mohammed, B. S., Wahab, M. M. A., Kankia, M. U., Amran, M., Gora, A. U. M.: Long-term strength development of fly ash-based one-part alkali-activated binders. Materials, 14(15), 4160 (2021). https://doi.org/10.3390/ma14154160
19. Longhi, M. A. et al.: Metakaolin-based geopolymers: Efflorescence and its effect on microstructure and mechanical properties. Ceramics International, 48(2), 2212-2229 (2022). https://doi.org/10.1016/j.ceramint.2021.09.313
20. Gismera, S., Alonso, M. D. M., Palacios, M., Puertas, F.: Rheology of alkali-activated mortars: Influence of particle size and nature of aggregates. Minerals, 10(8), 726 (2020). https://doi.org/10.3390/min10080726
21. Chen, W., Xie, Y., Li, B., Li, B., Wang, J., Thom, N.: Role of aggregate and fibre in strength and drying shrinkage of alkali-activated slag mortar. Construction and Building Materials, 299, 124002 (2021). https://doi.org/10.1016/j.conbuildmat.2021.124002
22. CEN (European Committee for Standardization): EN 1015-11:2019 Methods of test for mortar for masonry - Part 11: Determination of flexural and compressive strength of hardened mortar. CEN, Brussels (2019).
23. Raoof, S. M., Koutas, L. N., Bournas, D. A.: Textile-reinforced mortar (TRM) versus fibre-reinforced polymers (FRP) in flexural strengthening of RC beams. Construction and Building Materials, 151, 279-291 (2017). https://doi.org/10.1016/j.conbuildmat.2017.05.023
24. Triantafillou, T. C., Papanicolaou, C. G., Zissimopoulos, P., Laourdekis, T.: Concrete confinement with textile-reinforced mortar jackets. ACI structural journal, 103(1), 28-37 (2006). https://doi.org/10.14359/15083
25. Wakjira, T.G., Ebead, U.: Hybrid NSE/EB technique for shear strengthening of reinforced concrete beams using FRCM: Experimental study. Construction and Building Materials 164, 164-177 (2018). https://doi.org/10.1016/j.conbuildmat.2017.12.224

# Retrofit Strategies for Seismic Protection of Multi-Story Structures with Extended KDamper Devices

K. Kapasakalis[1*] [0000-0002-6619-7374], A. Mantakas[1] [0000-0001-8136-5922], M. Kalderon[2] [0000-0002-1593-9892] and E.J. Sapountzakis[1]

[1]Institute of Structural Analysis and Antiseismic Research, School of Civil Engineering, National Technical University of Athens, Zografou Campus, GR-157 80 Athens, Greece
[2]Dynamics and Acoustics Laboratory, School of Mechanical Engineering, National Technical University of Athens, Zografou Campus, GR-157 80 Athens, Greece
kostiskapasakalis@hotmail.com*, mantakasantonis@gmail.com, cvsapoun@central.ntua.gr, moriska@mail.ntua.gr

**Abstract.** This paper evaluates the efficiency of the extended version of the KDamper (EKD) as a seismic retrofitting solution for existing multi-story building structures. Two distinct approaches are investigated. The first one considers the implementation of an EKD device at the structure's base level, a straightforward approach that simplifies the design process. The second one involves the dispersion of multiple EKDs throughout the height of the structure, a more computationally demanding approach, that aims to control higher modes, especially in high-rise structures. Three test cases are investigated, representing low, mid, and high-rise building structures. The primary objective is to provide insights into the effectiveness of each retrofitting strategy based on the structure's height and number of stories, presenting a comprehensive assessment of the advantages and disadvantages of each option. Overall, the results underscore the positive influence of the EKD system on the dynamic response of all examined multi-story structures, establishing it as a compelling technology for seismic retrofitting. Designers can compare different retrofitting strategies based on building height and number of stories to choose the most efficient option.

**Keywords:** Seismic Retrofitting, Damping, Negative Stiffness, KDamper

## 1. Introduction

In recent years, seismic events have caused significant devastation, particularly in densely populated areas. Consequently, seismic regulations for buildings, bridges, and infrastructure have undergone changes to enhance their seismic performance. When it comes to the horizontal component of seismic forces, seismic isolation has emerged as a highly effective alternative to conventional seismic techniques. Unlike traditional methods that focus on increasing the structural capacity of constructions, seismic isolation operates by reducing seismic loads [1].

However, the application of seismic isolation at the base of structures inevitably leads to substantial displacements during seismic activity [2]. This drawback is not universally acceptable due to various reasons. For instance, seismically isolated structures may be sensitive to wind loads, necessitate specific provisions for plumbing, heating, and drainage systems, and require substantial seismic joints to prevent collisions between neighboring buildings. These considerations render the seismic isolation approach unsuitable for existing structures.

The Tuned Mass Damper (TMD), a widely adopted method for passive vibration control, involves adding an oscillating mass, stiffness element, and damper to a structure. Introduced by Frahm [3] and optimized by Den Hartog [4], it was initially designed for undamped single-degree-of-freedom structures under harmonic excitations. While the TMD has shown improvements in dynamic behavior across various systems [5-16], it presents some drawbacks. Its efficiency depends on the optimum frequency and damping properties [17,18], and requires heavy masses, posing challenges in real applications. Moreover, seismic protection with a single TMD (STMD) may not be universally efficient due to the broad frequency spectrum of earthquakes [19,20].

To address the limitations of single TMD systems, researchers have proposed the use of multiple TMDs (MTMDs), either placed at the top floor or distributed across various levels (d-MTMDs). Initially introduced by Ayorinde and Warburton [21] for seismic control in civil engineering, MTMDs have been optimized by various researchers, showing increased efficiency compared to single TMDs, even when the total additional mass remains the same. The consensus is that optimizing the number of MTMDs expands the control frequency bandwidth. Recent research explores spatially distributed MTMDs to enhance the system's efficiency and to reduce the concentrated masses, as studied by Chen and Wu [22] on a six-story building structure.

A cutting-edge solution to these challenges comes in the form of the KDamper, developed in the National Technical University of Athens. This innovative approach relies on a meticulous combination of appropriate stiffness elements, including one with a negative stiffness constant [23,24]. The KDamper offers a unique advantage – the total stiffness of the superstructure can be maintained. This overcomes a key limitation of the "Quazi Zero Stiffness" (QZS) vibration isolation systems [25], which typically require a significant reduction in stiffness and, consequently, lead to decrease of the structure's load bearing capacity [26-29]. In comparison to traditional TMD, the KDamper achieves superior vibration absorption and damping characteristics without the need for additional heavy masses, a requirement that TMD has [30]. The KDamper stands out by replacing the high inertial forces of added masses with the force generated by the negative stiffness element [30-32]. Moreover, their isolation and damping properties primarily result from the stiffness elements of the system, making them less susceptible to issues like detuning, a challenge faced by conventional TMDs.

The effectiveness of the KDamper system has been explored for the protection of engineering structures against environmental loading, i.e bridges [33,34], wind turbines [35,36], and various other structural applications [24,37-40]. The mechanism has proven its ability to reduce displacement demands at the base level of seismically excited structures. In particular, Kapasakalis et al. [24] introduced the extended version of the KDamper concept (EKD) as a vibration absorber, while Mantakas et al. [38,41]

examined the system's efficiency as a seismic retrofitting measure for low-rise buildings. In 2023, Kapasakalis et al. [42] introduced a multiple Extended KDamper (d-EKD) approach to enhance the performance of retrofitting strategies. Similar to one of the d-Multiple Tuned Mass Dampers (d-MTMDs), this approach strategically places EKD devices between specified building floors. The study's findings indicated that the d-EKD devices outperformed d-MTMDs devices, achieving superior results with significantly less additional mass.

This study assesses the effectiveness of the EKD system as a seismic retrofitting measure for multi-storey structures. It explores two distinct approaches: the first involves employing an EKD as a seismic base absorber at the base level of the structure, while the second entails distributing multiple EKDs throughout the structure's height. Parametric analyses are carried out, considering factors such as the number of storeys and EKD devices. The overarching goal is to offer insights into the efficiency of each retrofitting strategy based on the structure's height and storeys, providing a comprehensive evaluation of the pros and cons of each option. In general, the findings highlight the positive impact of the EKD system on the dynamic response of all examined multi-storey structures, establishing it as a compelling seismic retrofitting technology. Designers can compare various retrofitting strategies based on building height and storeys to select the most efficient option.

## 2. Extended KDamper Concept

### 2.1 Overview of the EKD Absorber

The examined passive vibration absorption concept, illustrated in Fig. 1 and labeled as the EKD system [24], is an extension of the original KDamper concept.

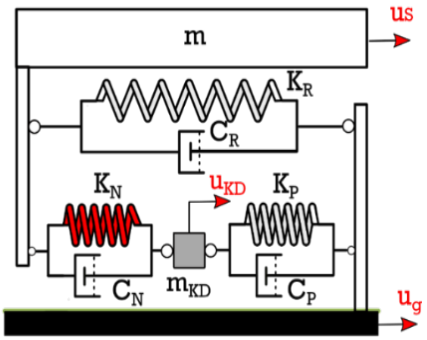


**Fig. 1.** Schematic presentation of the Extended KDamper (EKD) absorber excited at its base

Similar to the QZS oscillator, a negative stiffness (NS) element is introduced. The NS element is attached to the primary and additional masses, and an additional positive stiffness element connects the added mass to the base. In contrast to the QZS, the primary essential condition for the KDamper (and its variants) is to maintain overall static

and dynamic stability. The total equivalent stiffness of the system can be maintained at any desired level, as calculated in Eq. (1):

$$K_R + \frac{K_P K_N}{K_P + K_N} = K_0 = (2\pi f_0)^2 \left(m + m_{KD}\right) \tag{1}$$

The EKD system integrates an additional mass connected to a primary oscillator through a combination of negative stiffness (NS) and positive stiffness elements, while also incorporating artificial dampers. However, the primary distinction lies in the system configuration. In the EKD system, the damper added mass ($m_{KD}$) is linked to the base via a positive stiffness spring ($K_P$), while the negative stiffness element ($K_N$) is positioned between the damper's mass ($m_{KD}$) and the oscillating mass ($m$). Additionally, an extra artificial damper is introduced, positioned in parallel with the negative stiffness element. Consequently, the system includes two stiffness elements and dampers, identified as $K_P$ and $K_N$ and $C_P$ and $C_N$, respectively. Employing a simplifying approximation, the system can be treated as linear, suggesting that the negative stiffness (NS) element generates a force proportional to the relative displacement between its terminals. The governing equations of motion for the EKD system under base excitation is formulated as follows:

$$\begin{aligned} &m\ddot{u}_{S,rel} + C_R\dot{u}_{S,rel} + C_N(\dot{u}_{s,rel} - \dot{u}_{KD,rel}) + K_R u_{S,rel} + K_N(u_{s,rel} - u_{KD,rel}) = -m\ddot{u}_g \\ &m_{KD}\ddot{u}_{KD,rel} + C_N(\dot{u}_{KD,rel} - \dot{u}_{S,rel}) + C_P\dot{u}_{KD,rel} + K_N(u_{KD,rel} - u_{S,rel}) + K_P u_{KD,rel} = -m_{KD}\ddot{u}_g \end{aligned} \tag{2}$$

where $u_{s,rel}=u_s-u_g$ and $u_{KD,rel}=u_{KD}-u_g$.

## 2.2 Experimental prototype & proof of concept

Recently, an experimental prototype of the Extended version of the KDamper (EKD) was designed, constructed, and tested on the shaking table of the Soil Mechanics Laboratory of the National Technical University of Athens. The experiment functions as validation and proof of concept of the initial analytical and numerical frameworks [39]. The simplified experimental setup, depicted in Fig. 2, incorporates various components such as steel plates, aluminum parts, roller bearings, and a prismatic pre-stressed coil spring, employed for the realization of the NS element.

The design specifically aims for an oscillating mass ($m$) of approximately 16 kg (primary structure), with an internal added mass ($m_{KD}$) of around 0.82 kg, constituting 5% of the total mass ($m$). The prototype is constructed based on a constrained engineering-criteria based optimization methodology. Furthermore, additional calculations are performed to ensure structural members resist buckling, and relative displacements of device parts (e.g., maximum internal mass displacement, maximum negative stiffness relative displacement, maximum lever arm rotation, etc.) fall within predefined design limits. In the pursuit of exclusively assessing the efficiency of this negative stiffness (NS)-based mechanism, without considering the potential impact of additional damping, no artificial dampers were introduced to the device, further validating its vibration absorption capabilities.

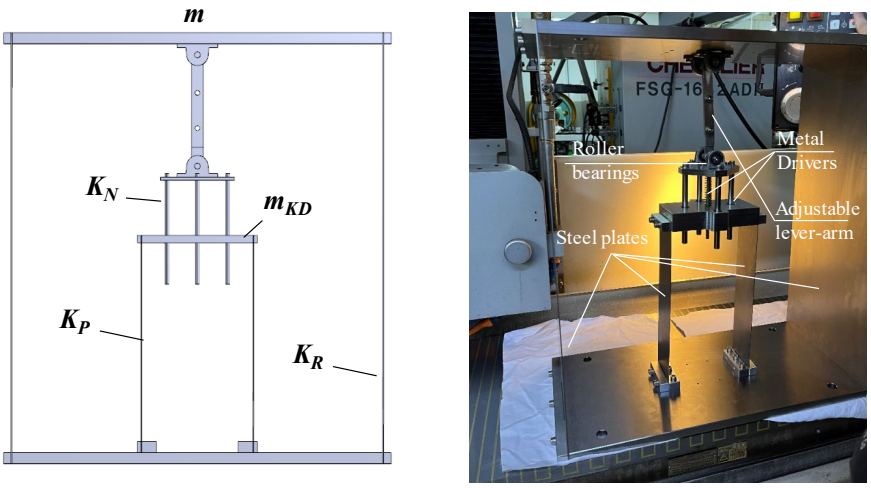


**Fig. 2.** Schematic presentation of the Extended KDamper (EKD) absorber excited at its base

In Fig. 3, the experimentally estimated frequency response of the EKD vibration absorber is juxtaposed to the response of an equivalent Single Degree of Freedom (SDoF) oscillator. The obtained results provide validation for the expected behavior of the KDamper, thereby confirming the accuracy of the analytically derived equations of motion and dynamic performance.

Notably, when examining the magnification factor of the system, particularly when the seismic mass ($m$) is exclusively mounted on the $K_R$ stiffness elements (indicated by the black dashed-line), the efficacy of the system is highlighted. More specifically, there is an approximate 60% reduction in the fundamental resonance peak, highlighting the significant increase of the controlled systems equivalent damping, leading to an isolation frequency of approximately 1.4 Hz, aligning seamlessly with the intended objective of the device.

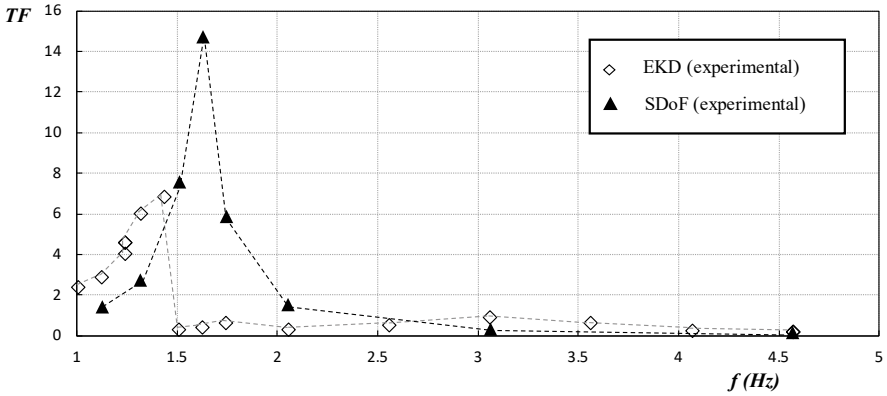


**Fig. 3.** Frequency response of the EKD device compared to the SDoF oscillator

## 3. Optimization approach and performance assessment

The primary emphasis in designing the EKD is on determining the dimensions of its stiffness elements. While theoretically these values can be computed based on the equivalent static stiffness of the EKD setup, Eq. (1), practical implementation necessitates considerations such as adherence to manufacturing tolerances and thorough attention to nonlinearity [43]. To ensure both static and dynamic stability of the EKD, the design treats $K_P$, $K_N$, and $K_R$ as design parameters with adjustable values. Introducing perturbations $\varepsilon_P$, $\varepsilon_N$, and $\varepsilon_R$ to the stiffness variables $K_P$, $K_N$, and $K_R$, respectively, allows for the computation of the configuration's sensitivity in terms of stiffness instabilities. Instability occurs when the determinant of the stiffness matrix is equal to zero:

$$\det\left([K]_{static}\right)=0 \Rightarrow \left(1-\varepsilon_R\right)K_R+\frac{\left(1-\varepsilon_P\right)K_P\left(1+\varepsilon_N\right)K_N\left(u_{NS}=0\right)}{\left(1-\varepsilon_P\right)K_P+\left(1+\varepsilon_N\right)K_N\left(u_{NS}=0\right)}=0 \tag{3}$$

It's important to note that by ensuring the stability of the EKD in static conditions ($u_{NS}$ = 0), dynamic stability is also guaranteed. This is attributed to the mechanics of the NS configuration employed, where the highest absolute value of the generated NS is observed at the equilibrium position. Consequently, the positive stiffness elements $K_P$ and $K_R$, are derived as functions of $f_0$, and $K_N$. Assuming that the mass $m_{KD}$, the mass matrix of the initial structure to be controlled, the horizontal stiffness of the flexural elements of the floors $K_1$, …, $K_N$ .and the stability factors $\varepsilon_P$, $\varepsilon_N$, and $\varepsilon_R$ are known, the (free) independent design variables sought in the optimization process are as follows: (i) nominal frequency $f_0$, (ii) NS element value $K_N$, and (iii) damping coefficients $C_N$ and $C_P$.

With the equations of motion Eq. (1) and the free design variables of the EKD established, the objective is to obtain an optimal set of EKD parameters aiming to reduce the dynamic responses of the superstructure. Simultaneously, it is crucial to ensure that the maximum accelerations remain below a predetermined percentage of the peak ground acceleration (filter). Hence, the mechanism serves a dual purpose by aiming to reduce both floor drifts and floor absolute accelerations. The EKD design follows a constrained engineering criterion-driven optimization approach [24]. This approach considers the geometrical and constructional limitations, such as the NS stroke, imposed by the respective structural system, and retains the values of its individual components within reasonable ranges. The Harmony Search (HS) algorithm, a novel metaheuristic algorithm, is utilized [44],to determine the optimum values of the design parameters $K_N$, $f_0$ and $C_N$ and $C_P$ , assuming that the additional mass $m_{KD}$ factors $\varepsilon_P$, $\varepsilon_N$, and $\varepsilon_R$ are known. It is important to note that the optimal EKD set of parameters obtained by the proposed optimization methodology corresponds to the specific initial structure, and thus no analytical formulations can be derived for the EKD design.

Regarding the incorporation of parameters into the HS algorithm, a common approach involves adopting values frequently encountered in relevant literature, such as HMS=75, HMCR=0.5, and PAR=0.1. The optimization procedure uses an excitation input selected from a database of artificial accelerograms [24] designed to be spectrum-

compatible with the EC8 (spectral acceleration 0.36 g, ground type C, spectrum type I, and importance class II). Fig. 4 illustrates a sample artificial accelerogram, and the generated spectrum, compared to the EC8. Based on the feasibility and technological constraints imposed in the analysis, appropriate ranges are attributed to both the design variables of the optimization problem, as well as to the yielded dynamic responses.

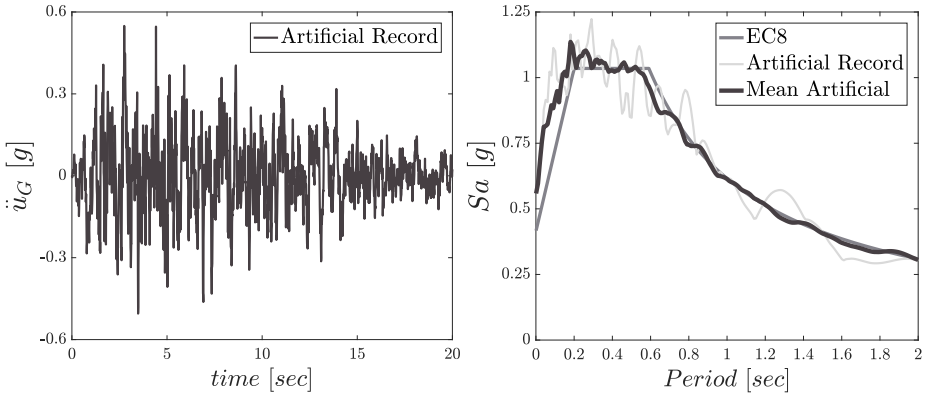


**Fig. 4.** (a) Artificial accelerogram, and (b) mean acceleration spectrum compared to the EC8

The EKD devices are optimized according to the optimization methodology presented previously with the artificial accelerograms in order incorporate the EC8 provisions in the design process. To confirm the effectiveness of the seismic retrofit strategies and assess the dynamic behavior of the structures, a set of eight (8) real earthquake motions is utilized as input seismic excitation. These chosen records, sourced from the US, European, and Asian regions, encompass a diverse array of crucial seismic features, including Peak Ground Acceleration (PGA), magnitude (Mw), wide frequency spectrum, duration, and the count of notable acceleration cycles. Detailed information about the seismic characteristics of the selected excitations can be found in Table 1.

**Table 1.** Seismic characteristics of the selected real earthquake records

| No | Earthquake | Year | Station | Ground Motion | Mw | PGA (g) | PGA/PGV (gsec/m) | $R_{JB}$ (km) | $Dur_{5\text{-}75\%}$ (sec) |
|---|---|---|---|---|---|---|---|---|---|
| 1 | Northridge | 1994 | N Hollywood | Near fault | 6.69 | 0.3087 | 1.4389 | 7.89 | 7.0 |
| 2 | L'Aquila | 2009 | V. Aterno | Near fault | 6.3 | 0.4018 | 1.2548 | 0.0 | 4.7 |
| 3 | Kocaeli | 1999 | Izmit | Near fault | 7.51 | 0.1651 | 0.7396 | 3.62 | 8.2 |
| 4 | Tabas | 1978 | Tabas | Near fault | 7.35 | 0.8540 | 0.8639 | 1.79 | 8.3 |
| 5 | Kobe | 1995 | Amagasaki | Near fault | 6.9 | 0.2758 | 0.8214 | 11.34 | 6.9 |
| 6 | Landers | 1992 | Joshua tree | Near fault | 7.28 | 0.2736 | 1.0125 | 11.03 | 21.7 |
| 7 | Duzce | 1999 | Lamont 1059 | Near fault | 7.14 | 0.1524 | 1.1844 | 4.17 | 10.4 |
| 8 | Friuli | 1976 | Tolmezzo | Near fault | 6.5 | 0.3571 | 1.5629 | 14.97 | 2.5 |

## 4. Implementation of the EKD at the base level of the structure

In this section, an EKD device is implemented at the base level of a multi-story building structure as a seismic protection/retrofitting measure, as illustrated in Fig. 5. This approach is straightforward, as the placement of the EKD is predetermined, and thus the optimization process is simplified. The EKD components are the stiffness elements and artificial dampers $K_N$-$C_N$ and $K_P$-$C_P$. It is noted that no stiffness element is placed in parallel to the original stiffness of the structure. The superstructure is modeled as a lumped mass system, with uniform masses and stiffnesses for all floors ($m_F$ = 360 *tn*, $k_F$ = 650 *MN/m*). The structure represents a typical medium-sized building whose floor weights correspond to about 400 $m^2$ of floor area, and the height of each story is assumed 3.2 *m*. Modal damping is considered, with a damping ratio of 2% for all modes.

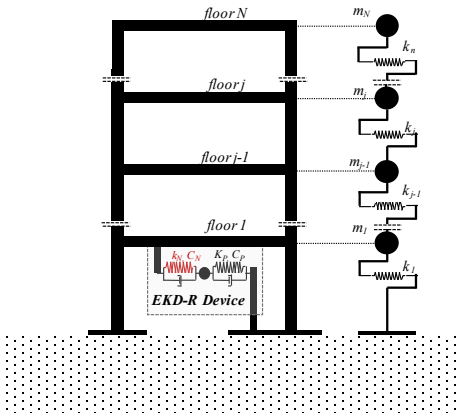


**Fig. 5.** Schematic representation of the EKD implemented at the base level of a multi-story structure, along with the lumped mass model of the superstructure

The structure nominal base frequency controlled with the EKD can be expressed as:

$$K_0 = K_F + \frac{K_P K_N}{K_P + K_N} = \left(2\pi f_0\right)^2 m_{tot}$$
$$m_{tot} = \sum_1^N \left(M_{F,i}\right) + m_{KD} \tag{4}$$

The EKD introduces a negative stiffness element to the base level of the structure. The stability of the structure is ensured by properly selecting the stiffness elements of the EKD according to Eq. (4). However, to avoid significant alterations in the structural properties of the initial uncontrolled building and thus further ensure its stability, the nominal EKD frequency $f_0$ is selected to vary in the range of:

$$\left(\frac{2}{3}\right)\sqrt{\frac{K_F}{m_F}} \le \omega_0 = 2\pi f_0 \le \left(\frac{4}{3}\right) \times \sqrt{\frac{K_F}{m_F}} \tag{5}$$

Thus, the number of design variables of this retrofit strategy are four and can be obtained following the optimization methodology presented previously. To better understand the EKD dynamic behavior, the damping ratios of the $C_N$ and $C_P$ are defined as:

$$\zeta_N = \frac{C_N}{2\sqrt{K_0\left(M_F + m_{KD}\right)}}$$
$$\zeta_P = \frac{C_P}{2\sqrt{K_0\left(M_F + m_{KD}\right)}} \tag{6}$$

Three test cases are considered to examine the efficiency of the proposed retrofit strategy with the EKD: a 5-story, a 10-story, and a 15-story structure, representing low-rise, mid-rise, and high-rise buildings, respectively. In Table 2, the optimized parameters and the damping ratios of the artificial dampers of the EKD device are provided for all the examined test cases. The EKD mass implemented at the base of the structure is assumed 0.1% of the total structure mass. Finally, the variation foreseen in the values of the stiffness elements $K_P$, $K_R$, and $K_N$ is assumed 2, 2, and 5%, respectively.

**Table 2.** Optimized parameters of EKD device implemented at the base level of the structure

| Test case | $f_0$ (*Hz*) | $K_N$ (*MN/m*) | $K_P$ (*MN/m*) | $C_N$ (*kNs/m*) | $\zeta_N$ (*%*) | $C_P$ (*kNs/m*) | $\zeta_P$ (*%*) |
|---|---|---|---|---|---|---|---|
| 5-story | 4.78 | -92.8 | 130.1 | 4989.1 | 0.229 | 412.3 | 0.021 |
| 10-story | 4.91 | -69.2 | 89.2 | 4994.6 | 0.2231 | 385.7 | 0.022 |
| 15-story | 5.11 | -55.2 | 65.84 | 4781.6 | 0.2038 | 487.3 | 0.0208 |

In Fig. 6, the dynamic responses of the controlled structures with the EKD at the base are presented for an EC8 spectrum-compatible artificial accelerogram, for all the examined test cases, and are compared to the uncontrolled structure (NC). The EKD

manages to significantly reduce the superstructure's dynamic response (drifts and absolute accelerations) for the low-rise structure, however, as the number of floor increases, its performance diminishes. To assess the performance of the proposed seismic upgrade methodology, the EKD system is also subjected to 8 real earthquake records, provided in Table 1. Fig. 7 presents the maximum values of the dynamic responses of the EKD structure, compared to the NC one, in the form of bar charts. The floor drifts and absolute accelerations are significantly reduced in the case of the 5-story structure, and again it is observed that the EKD is less effective for more flexible structures.

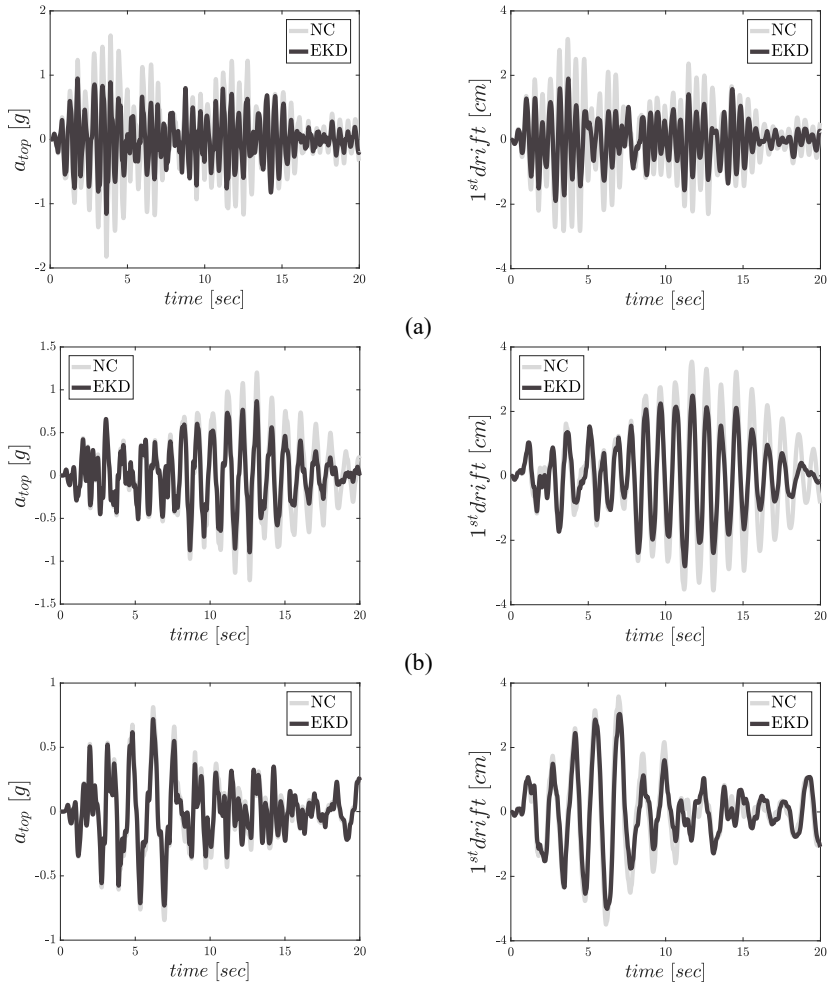


**Fig. 6.** Comparative dynamic response results (time histories) of the controlled multi-story structures with EKD device at its base (left: top floor absolute acceleration $a_{top}$, right: first floor drift *1st drift*), compared to the NC, for an EC8-compatible artificial accelerogram. (a) 5-story, (b) 10-story, and (c) 15-story buildings

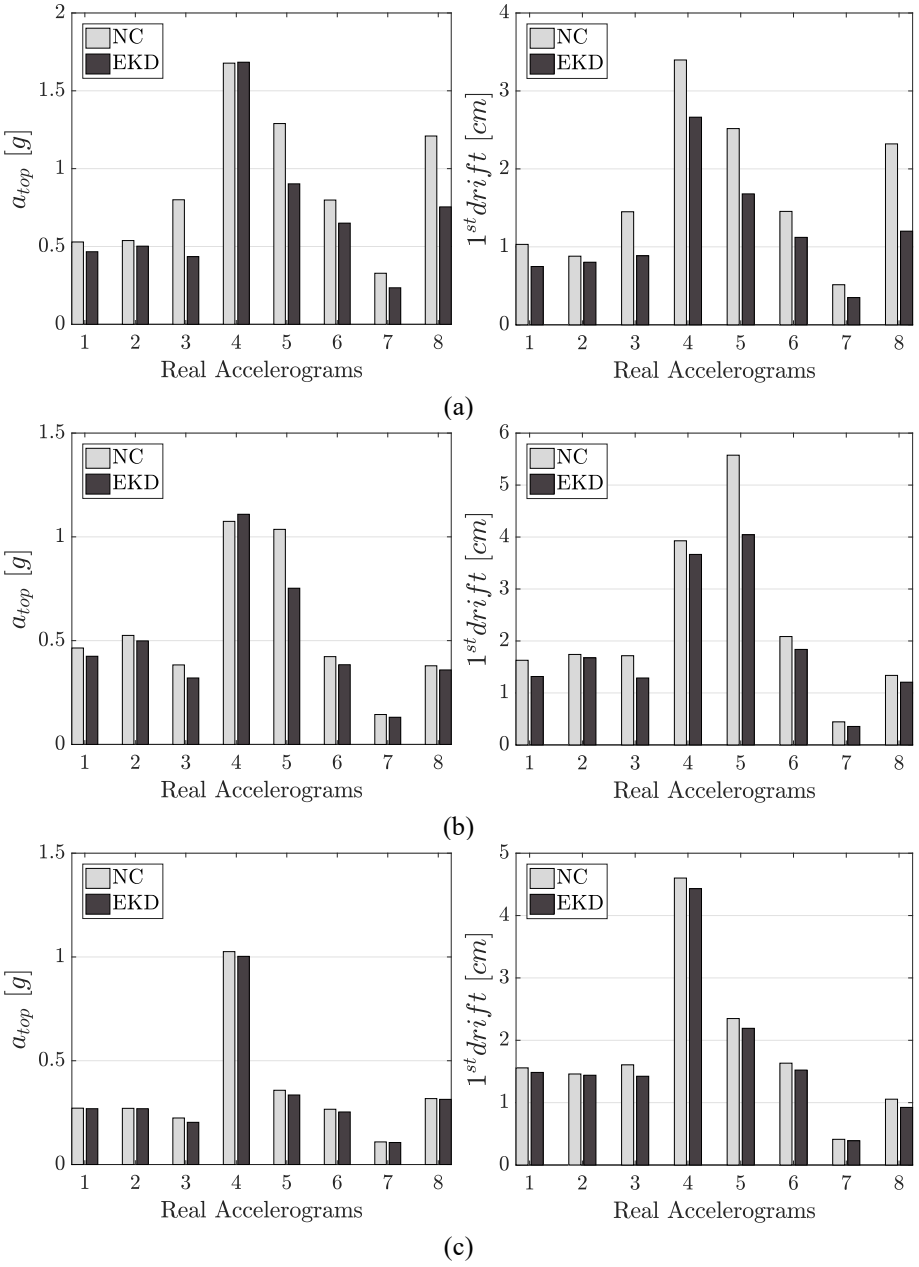


**Fig. 7.** Comparative dynamic response results (maximum values) of the controlled multi-story structures with EKD device at its base (left: top floor absolute acceleration $a_{top}$, right: first floor drift *1st drift*), compared to the NC, for all the selected real earthquake records. (a) 5-story, (b) 10-story, and (c) 15-story buildings

## 5. Distribution of EKD devices along the height of the structure

An alternative, and more computationally demanding seismic retrofit approach, is to distribute a number of EKD devices along the height of the multi-story building structure, enabling the control of higher modes. The retrofit elements of each EKD device are the stiffness and damping elements $K_N$-$C_N$ and $K_P$-$C_P$. The total added mass is the same with the previous seismic protection approach, in order to have an equal comparison basis for the numerical results. The multi-story structures to be controlled are modeled as lumped mass systems and have the same properties as the ones presented in the previous retrofit strategy (Section 4). A schematic representation of this seismic upgrade method is presented in Fig. 8, where an EKD device is implemented between two consecutive floors (j) and (j-1).

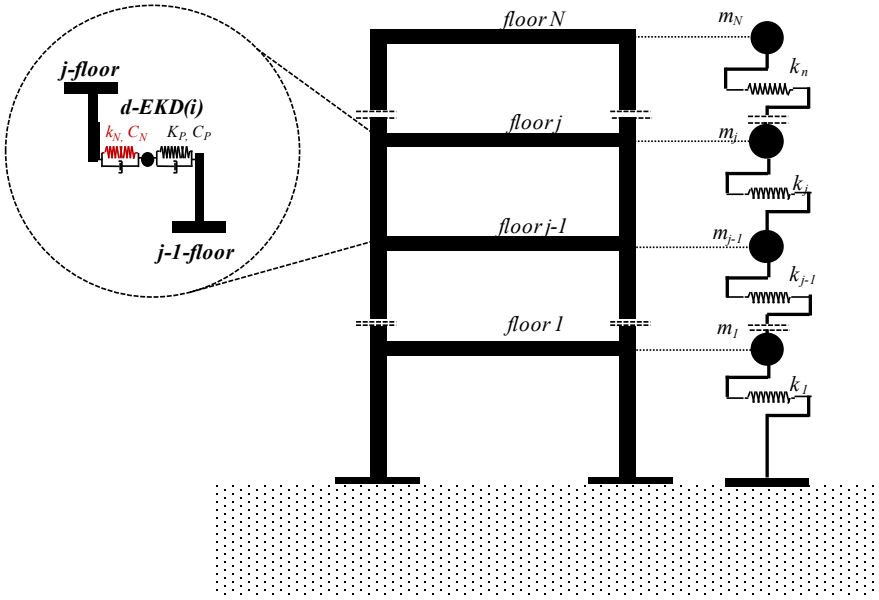


**Fig. 8.** Implementation of a EKD device (number *i*) between two consecutive floors (*j*) and (*j-1*) of the multi-story building structure

By introducing the EKD negative stiffness mechanism (device number i) between two consecutive floors (j) and (j-1), the equivalent stiffness of the (j) floor is modified, and can be expressed as follows:

$$K_{F,eq}^{j} = K_F^j + \frac{K_P^i K_N^i}{K_P^i + K_N^i} = \left(2\pi f_F^j\right)^2 \left(M_F + m_{KD}\right) \tag{7}$$

The proposed approach introduces negative stiffness elements distributed along the height of the structure, and thus, it is necessary to ensure the stability of each floor, and

as a result, the structures. For this reason, the equivalent nominal frequency of the (j) floor is selected to vary in the range:

$$\left(\frac{2}{3}\right)\sqrt{\frac{K_F}{m_F}} \le \omega_F^j = 2\pi f_F^j \le \left(\frac{4}{3}\right)\times\sqrt{\frac{K_F}{m_F}} \tag{8}$$

The number of free design variables per device is in this case also four (4), and the spatial allocation of the devices is set as a variable, ranging from the first up to the top floor of the building structure. As a result, each EKD device has five (5) design variables. The optimal design of the proposed retrofit strategy follows the optimization methodology presented in Section 3. The same three test cases are examined, in order to verify the effectiveness of this approach to low, mid, and high-rise buildings. In Table 3, the optimal values of all EKD components, along with the optimum placement of the devices, are presented. It is noted that since the EKD devices are distributed along the height of the structure, large additional masses are undesirable, and thus, the sum of the EKD additional masses is 0.1% of the total superstructure mass. Finally, the variation foreseen in the values of the negative stiffness elements ($\varepsilon_N$) is assumed 10%.

**Table 3.** Optimized parameters and spatial allocation of the implemented EKD devices along the height of the building structure

| Test case | #Device/ floor | $f_0$ (*Hz*) | $K_N$ (*kN/m*) | $K_P$ (*kN/m*) | $C_N$ (*kNs/m*) | $\zeta_N$ (*%*) | $C_P$ (*kNs/m*) | $\zeta_P$ (*%*) |
|---|---|---|---|---|---|---|---|---|
| 5-story | #1/floor 2 | 5.023 | -81.55 | 113.2 | 4625.5 | 13.14 | 114.2 | 1.3 |
| | #2/floor 1 | 5.435 | -47.99 | 60.63 | 4124.1 | 12.14 | 381.5 | 2.1 |
| | #3/floor 3 | 5.037 | -74.01 | 99.43 | 3824.3 | 13.10 | 563 | 2.8 |
| 10-story | #1/floor 4 | 5.067 | -62.71 | 80.39 | 4997.3 | 12.16 | 16.3 | 1.2 |
| | #2/floor 5 | 4.983 | -67.51 | 87.36 | 3824.5 | 10.3 | 427.1 | 2.8 |
| | #3/floor 6 | 5.116 | -79.74 | 111.82 | 4624.2 | 13.64 | 269.4 | 2.2 |
| 15-story | #1/floor 5 | 5.011 | -65.86 | 84.95 | 4673.4 | 13.68 | 463.2 | 2.8 |
| | #2/floor 6 | 4.97 | -66.88 | 86.17 | 4173.9 | 11.75 | 389.4 | 2.3 |
| | #3/floor 2 | 5.027 | -65.79 | 85.04 | 3994.7 | 10.34 | 210.8 | 1.9 |

Fig. 9 presents the time history responses of the controlled buildings with 3 EKD devices, distributed along the height of the building, for one artificial accelerogram, and are compared with the NC building. The proposed distributed approach effectively reduces the peak dynamic responses, in terms of drifts and absolute accelerations in all the examined test cases. The effectiveness of the distributed retrofit strategy is also verified with real earthquake records. In Fig. 10, the peak of the dynamic responses of the D-EKD and the NC structures are presented in the form of bar charts for all 8 ground motions presented in Table 1. The D-EKD manages to significantly reduce the seismic responses in the case of the low and mid-rise structures. It is worth noting that in the case of the high-rise structure, its dynamic behavior is also improved.

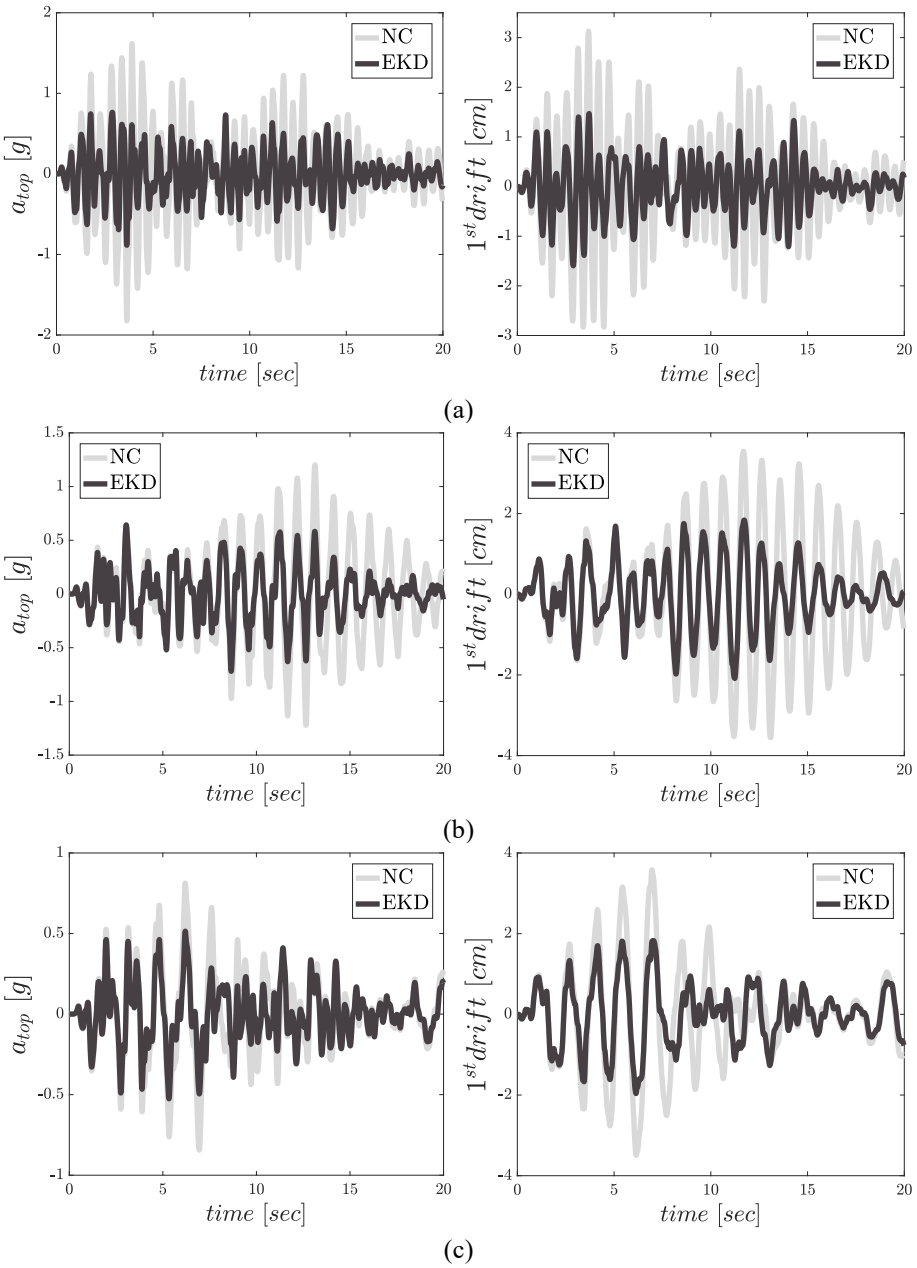


**Fig. 9.** Comparative dynamic response results (time histories) of the controlled multi-story structures with distributed EKD devices (left: top floor absolute acceleration $a_{top}$, right: first floor drift *1st drift*), compared to the IN, for an EC8-compatible artificial accelerogram. (a) 5-story, (b) 10-story, and (c) 15-story buildings

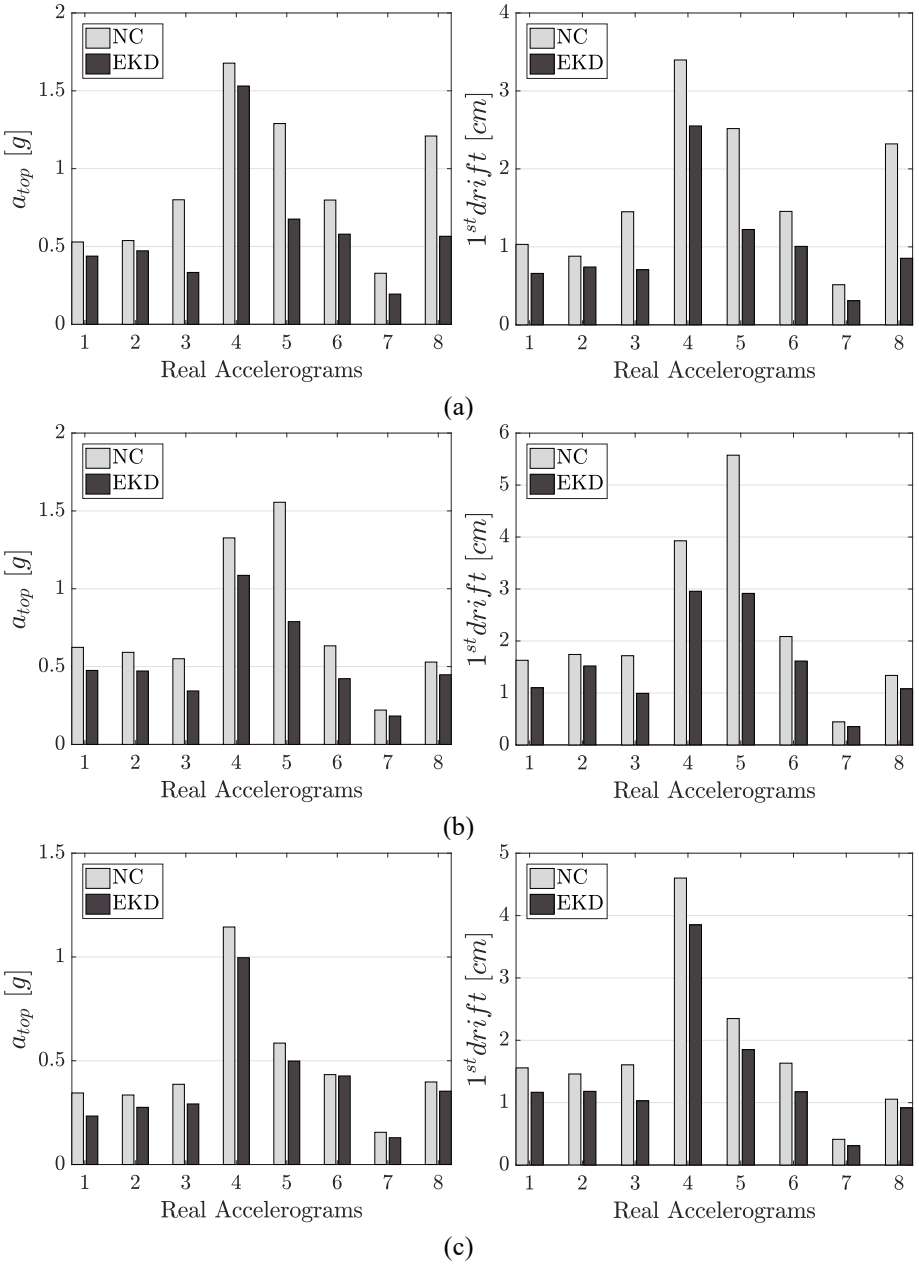


**Fig. 10.** Comparative dynamic response results (maximum values) of the controlled multi-story structures with distributed EKD devices (left: top floor absolute acceleration $a_{top}$, right: first floor drift *1st drift*), compared to the IN, for all the selected real earthquake records. (a) 5-story, (b) 10-story, and (c) 15-story buildings

## 6. Conclusions

This paper investigates the performance of multi-story building structures that incorporate novel negative stiffness-based vibration absorbers (EKD), as seismic retrofitting measures. Three test cases of multi-story buildings are thoroughly investigated, representing low, mid and high-rise structures. Two distinct retrofit approaches are investigated, with the primary objective to provide insights into the effectiveness of each strategy based on the structure's height and number of stories, providing a comprehensive evaluation of the pros and cons of each option.

More specifically, the first approach presents the implementation of the EKD mechanism at the base of the structures. The design of this configuration is straightforward, significantly simplifying the optimization process of the employed device. As an alternative, a more computationally demanding seismic retrofit approach, is to distribute a number of EKD devices along the height of the multi-story building structure, enabling the control of higher modes.

The optimal parameters of the retrofit strategies are obtained following a constrained engineering-criteria driven optimization approach. In addition, the design process follows the provisions of the EC8 by selecting the excitation input from a database of EC8 spectrum-compatible artificial accelerograms. The performance of the controlled structures is finally assessed with real strong ground motions. Based on the dynamic analysis and the numerical results obtained, the following key concluding remarks may be summarized as follows:

i. The design of the EKD devices in both approaches is realistic, as it is based on a constrained optimization approach with proper constraints and limitations in the structural dynamic responses and EKD components values
ii. The stability of the system is ensured, as the design foresees simultaneous variation in the values of all stiffness elements, including the one with negative constant, and avoids significant alterations in the structural properties
iii. The retrofit strategy with the EKD implemented at the base of the structure manages to significantly reduce the peak responses of the low-rise building. However, this approach has proven to be less effective for flexible structures
iv. The distribution of EKD devices along the height of the multi-story buildings significantly improves the seismic responses of the superstructure in the case of the low and mid-rise structures. It is also worth noting that in the case of the high-rise structure, the dynamic behavior is notably improved

## 7. Acknowledgments

Konstantinos Kapasakalis would like to acknowledge the support by the Bodossaki Foundation – Scholarship for Postdoctoral studies. Antonios Mantakas and Moris Kalderon would like to acknowledge the financial support provided by the EU's Horizon 2020 research and innovation program under the Marie Sklodowska-Curie grant (Grant Agreement No. INSPIRE-813424, 'INSPIRE, Innovative Ground Interface Concepts for Structure Protection').

## References


1. Naeim F, Kelly JM. Design of seismic isolated structures: from theory to practice. John Wiley & Sons; 1999
2. Symans MD, Charney FA, Whittaker AS, Constantinou MC, Kircher CA, Johnson MW, et al. Energy Dissipation Systems for Seismic Applications: Current Practice and Recent Developments. Journal of Structural Engineering 2007;134:3–21. https://doi.org/10.1061/(asce)0733-9445(2008)134:1(3)
3. Frahm H. Device for damping of bodies. US patent #989958, 1911
4. Den Hartog JP. Mechanical Vibrations. 4th ed. New York: 1956. https://doi.org/10.1038/161503c0
5. Kareem A. Mitigation of wind induced motion of tall buildings. Journal of Wind Engineering and Industrial Aerodynamics 1983;11:273–84. https://doi.org/10.1016/0167-6105(83)90106-X
6. Elias S, Matsagar V. Optimum Tuned Mass Damper for Wind and Earthquake Response Control of High-Rise Building. Advances in Structural Engineering: Dynamics, Volume Two 2015:751–1616. https://doi.org/10.1007/978-81-322-2193-7
7. Hoang N, Fujino Y, Warnitchai P. Optimal tuned mass damper for seismic applications and practical design formulas. Eng Struct 2008;30:707–15. https://doi.org/10.1016/J.ENGSTRUCT.2007.05.007
8. Kareem A, Kijewski T, Tamura Y. Mitigation of motions of tall buildings with specific examples of recent applications. Wind and Structures, An International Journal 1999;2:201–51. https://doi.org/10.12989/WAS.1999.2.3.201
9. Taniguchi T, Der Kiureghian A, Melkumyan M. Effect of tuned mass damper on displacement demand of base-isolated structures. Eng Struct 2008;30:3478–88. https://doi.org/10.1016/j.engstruct.2008.05.027
10. Xiang P, Nishitani A. Optimum design for more effective tuned mass damper system and its application to base-isolated buildings. Struct Control Health Monit 2014;21. https://doi.org/10.1002/stc.1556
11. De Domenico D, Ricciardi G. Earthquake-resilient design of base isolated buildings with TMD at basement: Application to a case study. Soil Dynamics and Earthquake Engineering 2018;113:503–21. https://doi.org/10.1016/j.soildyn.2018.06.022
12. Kamgar R, Samea P, Khatibinia M. Optimizing parameters of tuned mass damper subjected to critical earthquake. The Structural Design of Tall and Special Buildings 2018;27:e1460. https://doi.org/10.1002/TAL.1460
13. Khatibinia M, Gholami H, Kamgar R. Optimal design of tuned mass dampers subjected to continuous stationary critical excitation. Int J Dyn Control 2018;6:1094–104. https://doi.org/10.1007/S40435-017-0386-7/FIGURES/10
14. Kamgar R, Gholami F, Zarif Sanayei HR, Heidarzadeh H. Modified Tuned Liquid Dampers for Seismic Protection of Buildings Considering Soil–Structure Interaction Effects. Iranian Journal of Science and Technology - Transactions of Civil Engineering 2020;44:339–54. https://doi.org/10.1007/S40996-019-00302-X/TABLES/5
15. Dadkhah M, Kamgar R, Heidarzadeh H, Jakubczyk-Galczyńska A, Jankowski R. Improvement of Performance Level of Steel Moment-Resisting Frames Using Tuned Mass Damper System. Applied Sciences 2020, Vol 10, Page 3403 2020;10:3403. https://doi.org/10.3390/APP10103403
16. Salimi M, Kamgar R, Heidarzadeh H. An evaluation of the advantages of friction TMD over conventional TMD. Innovative Infrastructure Solutions 2021;6:1–12. https://doi.org/10.1007/S41062-021-00473-5/FIGURES/7

17. Nagarajaiah S, Sonmez E. Structures with Semiactive Variable Stiffness Single/Multiple Tuned Mass Dampers. Journal of Structural Engineering 2007;133:67–77. https://doi.org/10.1061/(asce)0733-9445(2007)133:1(67)
18. Weber B, Feltrin G. Assessment of long-term behavior of tuned mass dampers by system identification. Eng Struct 2010;32:3670–82. https://doi.org/10.1016/j.engstruct.2010.08.011
19. Sladek JR, Klingner RE. Effect of TunedMass Dampers on Seismic Response. Journal of Structural Engineering 1983;109:2004–9. https://doi.org/10.1061/(ASCE)0733-9445(1983)109:8(2004)
20. Clark a. J. Multiple passive tuned mass damper for reducing earthquake induced building motion. 9th World Conference in Earthquake Engineering 1988:779–784
21. Ayorinde EO, Warburton GB. Minimizing structural vibrations with absorbers. Earthq Eng Struct Dyn 1980;8:219–36. https://doi.org/10.1002/EQE.4290080303
22. Chen G, Wu J. Optimal Placement of Multiple Tune Mass Dampers for Seismic Structures. Journal of Structural Engineering 2001;127:1054–62. https://doi.org/10.1061/(ASCE)0733-9445(2001)127:9(1054)
23. Antoniadis IA, Kanarachos SA, Gryllias K, Sapountzakis IE. KDamping: A stiffness based vibration absorption concept. JVC/Journal of Vibration and Control 2018;24:588–606. https://doi.org/10.1177/1077546316646514
24. Kapasakalis KA, Antoniadis IA, Sapountzakis EJ. Constrained optimal design of seismic base absorbers based on an extended KDamper concept. Eng Struct 2021;226. https://doi.org/10.1016/j.engstruct.2020.111312
25. Molyneaux W. Supports for Vibration Isolation. G. Britain: ARC/CP-322, Aer Res Council; 1957
26. Carrella A, Brennan MJ, Waters TPÃ. ARTICLE IN PRESS Static analysis of a passive vibration isolator with quasi-zero-stiffness characteristic 2007;301:678–89. https://doi.org/10.1016/j.jsv.2006.10.011
27. Sun T, Lai Z, Nagarajaiah S, Li HN. Negative stiffness device for seismic protection of smart base isolated benchmark building. Struct Control Health Monit 2017. https://doi.org/10.1002/stc.1968
28. Sarlis AA, Pasala DTR, Constantinou MC, Reinhorn AM, Nagarajaiah S, Taylor DP. Negative Stiffness Device for Seismic Protection of Structures: Shake Table Testing of a Seismically Isolated Structure. Journal of Structural Engineering 2016. https://doi.org/10.1061/(asce)st.1943-541x.0001455
29. Pasala DT, Sarlis A, Nagarajaiah S, Reinhorn A, Constantinou M, Taylor D. Adaptive Negative Stiffness: New Structural Modification Approach for Seismic Protection. Adv Mat Res 2013;639–640. https://doi.org/10.4028/www.scientific.net/AMR.639-640.54
30. Kapasakalis KA, Antoniadis IA, Sapountzakis EJ. Performance assessment of the KDamper as a seismic Absorption Base. Struct Control Health Monit 2020;27. https://doi.org/10.1002/stc.2482
31. Paradeisiotis A, Kalderon M, Antoniadis I. Advanced negative stiffness absorber for low-frequency noise insulation of panels. AIP Adv 2021;11:65003. https://doi.org/10.1063/5.0045937
32. Kalderon M, Paradeisiotis A, Antoniadis I. A Meta-structure for Low-frequency Acoustic Treatment Based on a KDamper-Inertial Amplification Concept. Euronoise 2021, 2021, p. 1333–43
33. Sapountzakis EJ, Syrimi PG, Antoniadis IA. KDamper Concept in Seismic Isolation of Bridges. In: Proc of the 1st ICONHIC 2016, Chania, Crete, Greece: 2016, p. 28–30

34. Antoniou M, Alvertos A, Sapountzakis EJ, Anastasopoulos I. Application of the Extended KDamper to the Seismic Protection of Bridges: Design Optimization, Nonlinear Response, SSI and Pounding Effects. Journal of Earthquake Engineering n.d.:1–35. https://doi.org/10.1080/13632469.2023.2250463
35. Kapasakalis KA, Antoniadis IA, Sapountzakis EJ, Kampitsis AE. Vibration Mitigation of Wind Turbine Towers Using Negative Stiffness Absorbers. Journal of Civil Engineering and Construction 2021;10:123–39. https://doi.org/10.32732/JCEC.2021.10.3.123
36. Kampitsis A, Kapasakalis K, Via-Estrem L. An integrated FEA-CFD simulation of offshore wind turbines with vibration control systems. Eng Struct 2022;254:113859. https://doi.org/10.1016/J.ENGSTRUCT.2022.113859
37. Kapasakalis KA, Alvertos AE, Mantakas AG, Antoniadis IA, Sapountzakis EJ. Advanced negative stiffness vibration absorber coupled with soil-structure interaction for seismic protection of buildings. Proceedings of the International Conference on Structural Dynamic , EURODYN 2020;2:4160–76. https://doi.org/10.47964/1120.9340.19963
38. Mantakas AG, Kapasakalis KA, Alvertos AE, Antoniadis IA, Sapountzakis EJ. A negative stiffness dynamic base absorber for seismic retrofitting of residential buildings. Struct Control Health Monit 2022;29:e3127. https://doi.org/10.1002/STC.3127
39. Mantakas A, Chondrogiannis KA, Kalderon M, Kapasakalis K, Chatzi E, Sapountzakis E, et al. Design and Experimental Verification of an Extended KDamper - Based Vibration Absorber. Proceedings of EURODYN 2023, EASD Procedia; 2023
40. Kapasakalis K, Mantakas A, Kalderon M, Antoniou M, Sapountzakis EJ. Performance Evaluation of Distributed Extended KDamper Devices for Seismic Protection of Mid-Rise Building Structures. Journal of Earthquake Engineering 2023. https://doi.org/10.1080/13632469.2023.2226227
41. Mantakas A, Kapasakalis K, Kalderon M, Antoniou M, Antoniadis IA, Sapountzakis E. 3D Numerical Investigation of an Extended KDamper Absorber for Seismic Retrofitting of Low-Rise Buildings. COMPDYN Proceedings 2023. https://doi.org/10.7712/120123.10453.20434
42. Kapasakalis K, Mantakas A, Kalderon M, Antoniou M, Sapountzakis EJ. Performance Evaluation of Distributed Extended KDamper Devices for Seismic Protection of Mid-Rise Building Structures. Journal of Earthquake Engineering 2023. https://doi.org/10.1080/13632469.2023.2226227
43. Li H, Li Y, Li J. Negative stiffness devices for vibration isolation applications: A review. Advances in Structural Engineering 2020;23:1739–55. https://doi.org/10.1177/1369433219900311
44. Zong Woo Geem, Joong Hoon Kim, Loganathan GV. A New Heuristic Optimization Algorithm: Harmony Search. Simulation 2001;76:60–8. https://doi.org/10.1177/003754970107600201

# An approximate method to assess the seismic capacity of existing RC buildings

Lamprini D. Zochiou[1][0009-0006-7182-5837], Maria D. Panagopoulou[1][0009-0002-2522-6375] and Stefanos E. Dritsos[1]

[1]University of Patras, Department of Civil Engineering, Aristotelous 26500, Rion, Greece
lamprini.zochiou@gmail.com

**Abstract.** An approximate method to assess the seismic capacity of existing RC buildings is demonstrated, which is applied to the methodology of the Second-level pre-earthquake inspection according to its recent first revision (2022). This method is validated by comparing the obtained results with the ones of a non-linear static analysis. In particular, the following points are being examined: (a) the effect of masonry infill walls on the seismic resistance of the building and its failure index, taking into account their construction detailing, (b) the effect of unknown information regarding steel reinforcement amounts and (c) the difference in results when the prior to the revision methodology is applied (version of 2018). The results obtained from the examination, show that the values of the failure indices of a building, for the case of known amounts of reinforcement, provided by the Second-level pre-earthquake inspection, were in great convergence with the corresponding ones in terms of acceleration obtained by the non-linear static analysis, for reasonable geometry and location of openings on infill walls. When the maximum failure index of the column elements was considered as the main failure index for the non-linear static analysis, differences in results were observed in some cases.

**Keywords:** Second-level pre-earthquake inspection, Approximate method, Preliminary seismic analysis, Non-linear static analysis, Building assessment, Reinforced concrete

## 1. Introduction

For a country like Greece, which faces frequent and often intense earthquake events, it is of great importance for a comprehensive framework of regulations to apply when assessing the seismic capacity of existing buildings before or after a seismic event or other severe destructive causes [9]. This necessity becomes more obvious considering the fact that most of the existing buildings in Greece were constructed before 1984, when the National Earthquake Codes were updated. Therefore, not only are they designed based on older regulations or even with a very low level of seismic design, but in the majority of them, they have already exceeded the intended life span, equal to 50 years for ordinary structures [8].

The assessment of the seismic capacity of an existing structure is a complex and time-consuming process, especially when there are no reliable data on the design and reinforcement amounts and details of the RC structural members as well as the strength of the materials used [11]. Besides, it is important to have a way of prioritizing structures with an, even approximate, assessment of their seismic vulnerability [2].

There are several techniques developed for the damage detection and assessment of existing structures as well as for its structural control. Structural Health Monitoring (SHM) enables for the real-time and early detection, localization and evaluation of damage points or structural degradation, with its non-destructive character and proven accuracy, making it suitable for the assessment and control of various types of structures [1]. Active, passive or hybrid control techniques are designed to improve the performance and stability of structures subjected to earthquake excitation, altering their dynamic response by applying direct or indirect control forces [10]. When combined with advanced sensing and data acquisition systems they can be valuable for assessment purposes, giving real-time information. Destructive testing techniques are often necessary to gain insight on the structure's material properties and failure mechanisms, whereas, numerical modeling and simulations is the most common method to accurately predict damage patterns and progression under various load scenarios.

The seismic assessment is structured into several levels, to avoid time-consuming and often high-cost advanced analysis methods for all potentially vulnerable structures and to allow for a way to prioritize the structures, by classifying them according to their structural vulnerability. The first level refers to a preliminary evaluation of the seismic safety of a building and the determination of those who are in need of a more detailed examination [1]. The Rapid Visual Screening (RVS) procedure as defined in the FEMA P-154 Report, is such a first level methodology, developed to identify potential seismic hazard and to classify the structures into those with acceptable expected seismic performance and those that need to be further investigated [7].

Similarly, the second-level pre-earthquake inspection [5-6] that is applied in the current study, was created specifically for this reason. For existing RC structures, an approximate estimation of their failure index is used as the main criterion, based on the seismic demand, as defined in current assessment provisions. The proposed methodology includes a series of approximate calculations, that can provide the failure index of the structure, without the need to create a detailed numerical model or to use a specific analysis software. It is possible, in fact, for this methodology to be applied, but with less reliability, for the case where there are insufficient data on the structure's reinforcement amount and details as well as the material properties.

In order to validate the reliability of the proposed method of the Second-level pre-earthquake inspection, in this current work, a comparison is made between the results of this method and the corresponding results of a non-linear static analysis. The comparison is made using the revised version of the Second-level pre-earthquake inspection [5] and in particular for the following points:

- The effect of the masonry infill walls
- The lack of sufficient information on the reinforcement amounts and details of column elements

It is noted that in this aforementioned revision of the Second-level pre-earthquake inspection regulation (v.2022) [5], the main points that differentiate it from the pre-revised version (v.2018) are the following:

- The addition of the contribution of infill walls to the seismic resistance of the structure
- The use of higher values for the behavior factor q

## 2. Description of the case study RC buildings

Both of the structures that are being examilned consist of frame RC load-bearing structural system and were built before 1984. The first structure has a symmetrical rectangular floor-plan (building A) and the second one is non-symmetrical Γ-shaped (building Γ) with structural floor-plans as shown in Fig.1. Both buildings are three-storey with a floor height of 3.00m and accessible roof. In order to examine the effect of masonry infill walls, different conditions of their participation are considered. More specifically, they are being categorized according to the quality of their construction detailing and wedging and the existence or not of openings on them. The presence of openings is considered for the case that their size and location reduce the contribution of the infill walls in earthquake resistance to 50%. Table 1 and 2 briefly present the cases to be further examined.

**Table 1.** Different cases of structural systems and masonry infill walls contribution

| Building A | Building Γ | Description of case study RC buildings |
|---|---|---|
| $A_n$ | $\Gamma_n$ | Reference buildings without taking into account the contribution of masonry infill walls |
| $A_1$ | $\Gamma_1$ | Buildings considering presence and contribution of masonry infill walls in all levels without openings |
| $A_0$ | $\Gamma_0$ | Buildings considering presence and contribution of masonry infill walls in all levels with openings |

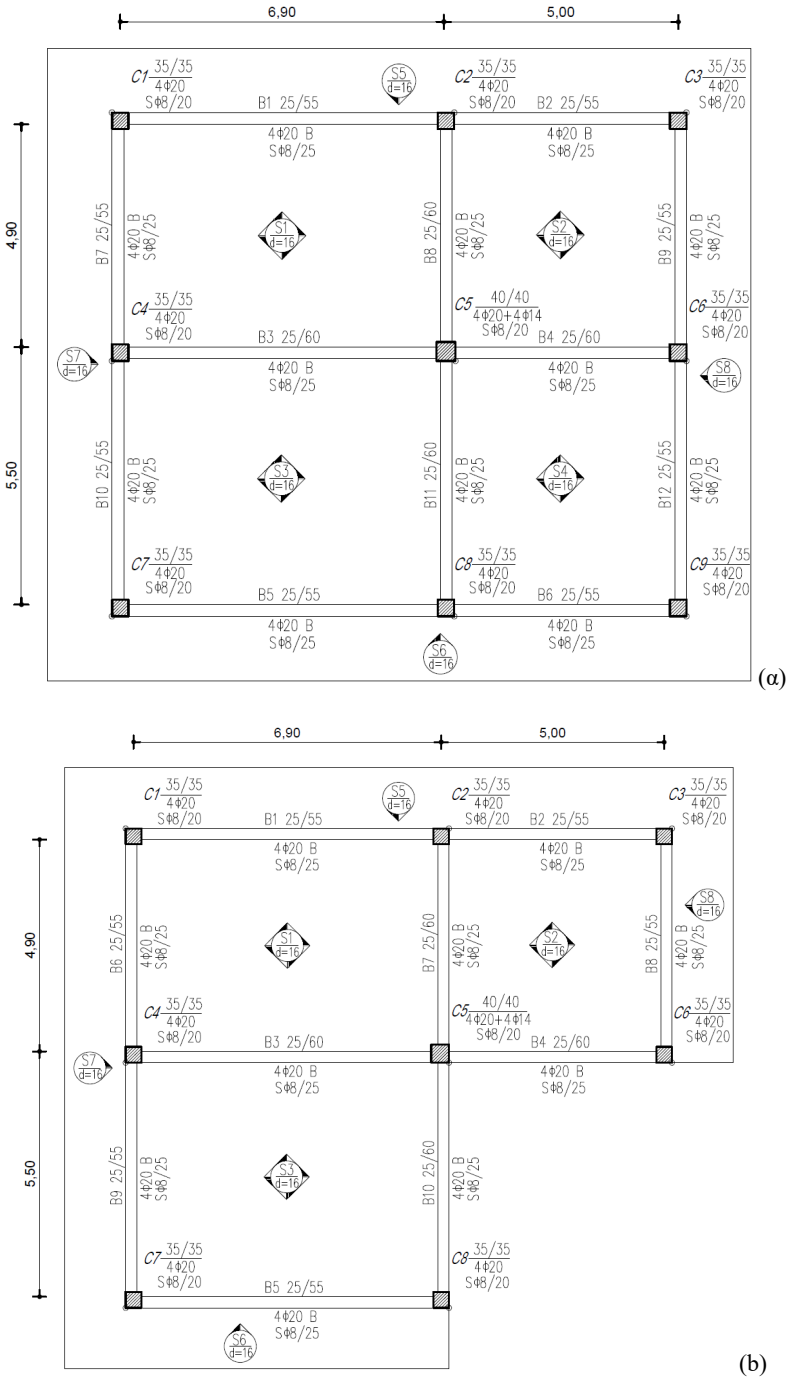


**Fig. 1.** Structural floor-plans of the two buildings A (a) and Γ (b)

**Table 2.** Different categories of masonry infill walls

| Building A | Description of case study RC buildings |
|---|---|
| Inf.Wall.1 | Good construction detailing and wedging of masonry infill walls without considering the presence of openings |
| Inf.Wall.2 | Good construction detailing and wedging of infill walls considering the presence of openings |
| Inf.Wall.3 | Poor construction detailing and wedging of masonry infill walls without considering the presence of openings |
| Inf.Wall.4 | Poor construction detailing and wedging of infill walls considering the presence of openings |

### 2.1 Reinforcement amount and details, Loads and Design Spectrum

The columns located on the perimeter of the building have a cross-section of 35x35cm and the one located at the center has a cross-section of 40x40cm. External beam elements have a cross-section of 25/55 and have 4Φ16 bottom reinforcement at mid-span from which 2Φ16 are bent at the supports. Internal beam elements have a cross-section of 25/60 and have 4Φ20 bottom reinforcement at mid-span from which 2Φ20 are bent at the supports. All beam elements have 2Φ8 top reinforcement which does not participate in moment resistance at the supports, due to insufficient anchorage length. Columns located on the perimeter are reinforced with 4Φ20 at the corners and the one located at the center of the building is reinforced with 4Φ20 at the corners and 4Φ14 (1Φ14 in the middle of each side). Ties are rectangular Φ8/20 in all column elements and Φ8/25 in all beam elements with adequate anchorage. The thickness of the slabs is taken equal to 16cm.

Material properties are considered as follows assuming Data Reliability Level (DRL) to be "Sufficient" [4]: the average value for the compressive strength of concrete is considered 18 MPa and characteristic value 14 MPa, whereas the corresponding values of the tensile strength of reinforcement bars and ties are 460 MPa and 400 MPa respectively. The dead loads (G) of the structure include the self-weight of the RC elements ($25\ \mathrm{kN/m^3}$), the floor toppings ($1.3\ \mathrm{kN/m^2}$) and the outer and inner masonry walls ($3.6\ \mathrm{kN/m^2}$ and $2.0\ \mathrm{kN/m^2}$ respectively). The live loads (Q) include the ones in the floors and roof ($2.0\ \mathrm{kN/m^2}$). Axial loads at the base of the ground floor columns were calculated by considering the effective slab areas for each column, dividing the slabs in triangular and trapezoidal subareas, for the $\mathrm{G} + 0.3\mathrm{Q}$ loading combination.

The seismic loads (E) were calculated in accordance with the EC8 design spectrum [3], with a ground acceleration equal to $\mathrm{a_g} = 0.24\mathrm{g}$, (where $g$ denotes the acceleration due to gravity, 9.81 m/sec2), soil type B (medium dense sand or stiff clay) and seismic

zone II. For the Second-level pre-earthquake inspection the soil index is taken equal to 1.00 and the design spectrum is used with behavior factor q equal to 2.00. For the non-linear static analysis the elastic spectrum is used and the soil index is considered equal to 1.20.

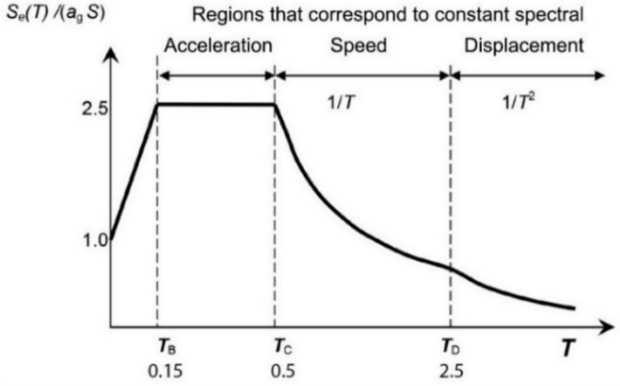


**Fig. 2.** Elastic spectrum

## 2.2 Dynamic characteristics

When applying the methodology of the Second-level pre-earthquake inspection, the period T of the building was determined according to the approximate equation from the Greek Code of Structural Interventions - *KANEPE* [4] as following:

$$T = C_t H^{0.9} \quad (1)$$

where $C_t$ is equal to 0,052 and H is the height of the building equal to 9.90 m.

When conducting the non-linear static analysis, the period T was determined based on the direction and distribution of the seismic loading and the structural properties of the structures. Table 3 presents the results that were obtained by the two methods.

**Table 3.** Empirical and analytical periods T

| | Second-level pre-earthquake inspection | Non-linear static analysis | |
|---|---|---|---|
| | | A | Γ |
| No infill walls | 0.41 | 1.36 | 1.32 |
| Inf.Wall.1 | 0.41 | 0.61 | 0.58 |
| **Inf.Wall.2** | **0.41** | **0.71** | **0.75** |
| Inf.Wall.3 | 0.41 | 0.72 | 0.68 |
| **Inf.Wall.4** | **0.41** | **1.06** | **0.78** |

It is worth mentioning that the period T obtained by the approximate equation from *KANEPE* [4], is equal for both structures with values much smaller than those resulting from the non-linear static analysis. In the analysis, periods in all cases correspond to values higher than $T_c = 0.50s$, i.e. they are in the descending branch of the spectrum. Consequently, a lower demand is expected compared to the one Second-level pre-earthquake inspection predicts, where period values correspond to the plateau of the spectrum ($T < T_c$) which means that the seismic demand will be higher.

## 3. Application of the approximate method

In the Second-level pre-earthquake inspection, the seismic demand, $V_{req}$, is determined for each direction of the earthquake according to the design spectrum as follows:

$$V_{req} = M\, S_d(T) \tag{2}$$

where, M is the total mass of the structure and is calculated by the sum of the axial loads at the base of each column:

$$M = N_{tot}/g \tag{3}$$

and $S_d(T)$ is the design spectrum acceleration at period T:

$$S_d(T) = a_g\, S \left(\frac{2.5}{q}\right) \tag{4}$$

Analysis is performed for the "Significant Damage Performance" level (Level B) [4] and the behavior factor q is taken equal to 2.00 according to Table 4 of the methodology of the Second-level pre-earthquake inspection [5]. As observed, proposed values for the factor q, for structures built before 1984, are slightly higher than the corresponding ones proposed by the methodology of *KANEPE* (Table S4.4 [4]).

**Table 4.** Proposed values of the behavior factor q for "performance level B – Severe damage" [5] according to the Second-level pre-earthquake inspection

| Standards applied for design (and construction) | Favourable presence or absence of infill walls (1) | | Generally unfavourable presence of infill walls (1) | |
|---|---|---|---|---|
| | Substantial damage in primary elements | | Substantial damage in primary elements | |
| | No | Yes | No | Yes |
| 1995<… | 3.0 | 2.3 | 2.3 | 1.7 |
| 1985<…<1995(2) | 2.3 | 1.7 | 1.7 | 1.3 |
| …<1985 | 1.7 | 1.3 | 1.3 | 1.1 |

For each earthquake direction, the value of the basic seismic resistance ($V_{R0}$) of the members of the critical floor (generally the ground floor) is determined using the following Eq.5:

$$V_{R0} = \alpha_1 \sum V_{Ri}^{\text{RC col.}} + \alpha_2 \sum V_{Ri}^{\text{RC walls}} + \alpha_3 \sum V_{Ri}^{\text{RC short.col.}} + \sum V_{Ri}^{\text{infill walls}} \quad (5)$$

where for this particular case (frame structural system without RC walls and without short columns) the values are considered according to the proposed method as $\alpha_1 = 0.85$ and $\alpha_2 = \alpha_3 = 0$.

According to the proposed methodology, the maximum shear force that elements can carry is determined by checking their failure mechanism (shear or flexural) as defined at Eq.6 in which $V_{Rd}$ is the shear strength and $V_M$ is the flexural strength of the element. When data for reinforcement amounts are not available, the method is applied by assuming that $V_{R,i} = V_{Rd}$. In this paper, results are given for both cases (Second-level pre-earthquake inspection with and without reinforcement information).

$$V_{R,i} = \min (V_{Rd}, V_M) \quad (6)$$

The value of the shear force $V_{Rd}$ is determined using the equations from Appendix 7C of *KANEPE* [4]. When no data for reinforcement amounts are available, values of $\mu_\theta^{pl}$ and x, are being calculated in an approximate way. In this paper, according to the data presented in §2.1 the value $\mu_\theta^{pl} = 2.5$ was considered (Second-level pre-earthquake inspection [5]). The height of the compressive zone was taken equal to $x = 0.35d$ which results from the approximate equation of the curvature adopted by *KANEPE* (Appendix 7A [4]) as follows:

$$\varphi_y = \frac{1.52\ f_y}{E_S\ d} \quad (7)$$

and the mechanics of materials equation:

$$\varphi_y = \frac{\varepsilon_S}{d - x} = \frac{f_y}{E_S\ (d - x)} \quad (8)$$

Resulting to:

$$x = d - \frac{d}{1.52} \cong 0.35\ d \quad (9)$$

In order to examine the effect of the aforementioned estimations regarding x and $\mu_\theta^{pl}$, a comparison was made between the shear resistance values of the column elements and the corresponding results of the non-linear static analysis (with known data about reinforcement amounts and details). The results are presented in Table 5 and it is worth mentioning that their convergence is great.

**Table 5.** Shear resistance of RC columns – Approximate method and analysis

| Second-level pre-earthquake inspection | | | | |
|---|---|---|---|---|
| COLUMNS | BUILDING A | | BUILDING Γ | |
| | Reinf. data | No reinf. data | Reinf. data | No reinf. data |
| | $V_R$ (KN) | $V_R$ (KN) x = 0.35d, $\mu_\theta^{pl} = 2.5$ | $V_R$ (KN) | $V_R$ (KN) x = 0.35d, $\mu_\theta^{pl} = 2.5$ |
| 1 | 107.31 | 108.35 | 107.31 | 108.35 |
| 2 | 126.11 | 133.52 | 126.50 | 134.32 |
| 3 | 100.40 | 101.94 | 104.75 | 105.94 |
| 4 | 126.22 | 133.76 | 126.70 | 134.73 |
| 5 | 185.46 | 173.30 | 177.57 | 181.45 |
| 6 | 122.10 | 126.27 | 98.06 | 99.84 |
| 7 | 109.16 | 110.12 | 115.09 | 115.93 |
| 8 | 127.11 | 135.58 | 108.05 | 109.06 |
| 9 | 102.13 | 103.52 | - | - |

The shear resistance of the masonry infill walls $V_{Ri}^{\text{infill walls}}$ is calculated by the following Eq.10:

$$V_{Ri}^{\text{infill walls}} = 0.3\, f_{wc,s}\; t_w\; b_w \left(\frac{l}{L}\right) \tag{10}$$

where $f_{wc,s}$ is the compressive strength of the infill walls in the diagonal direction and can be obtained from Table 3 of Appendix D [6], whereas $t_w$ $b_w$ stands for the thickness and the effective width of the infill wall respectively. §7.4.1. describes how to take into account the contribution of infill walls in the resistance of the structure. Approximately, $b_w$ can be considered as $b_w \approx L \cdot (f_{wv}/f_{wc,s})$, where $f_{wv}$ is the strength in diagonal cracking.

The final seismic resistance, $V_R$ , is defined for each main direction by the following Eq.11:

$$V_{R,x} = \beta_x \times V_{R0,x} \quad , \quad V_{R,y} = \beta_y \times V_{R0,y} \tag{11}$$

The reduction factor β is determined based on 13 criteria, each one of which participates with a weight corresponding to its influence on reducing the seismic capacity of the structure and is evaluated with a value of 1 to 5, where 1 corresponds to the highest reduction.

For the case of the two structures that are being examined on this paper, criterion 3 (normalized axial load) was graded equal to $\beta_3 = 3$ for both buildings A and Γ. These values were obtained because in building A, the maximum value of the axial load in a column element was $0.40 \le v_d^i = 0.402 < 0.50$, whereas in building Γ, the average value of the normalized axial load of column elements was $0.25 \le v_d = 0.275 < 0.35$. Criterion 5 (the stiffness distribution in plan-torsion), for building Γ only, was graded

with $\beta_5 = 4$, given the fact that the normalized eccentricity for x direction was $\varepsilon_x = 0.14 > 0.05$, which corresponds to grade 4 and for y direction was $\varepsilon_y = 0.03 < 0.05$, which corresponds to grade 5. In all other cases the criteria were graded with $\beta_i = 5$. As a result of the above, values of the reduction factor for buildings A and Γ were $\beta_x = \beta_y = 0.98$ and $\beta_x = 0.96$, $\beta_y = 0.98$ respectively.

The failure index λ of the structure for each main direction x and y is calculated by the available seismic resistance and the seismic demand according to Eq.12 as follows:

$$\lambda_x = \frac{V_{req,x} + 0.30V_{req,y}}{V_{R,x} + 0.30V_{R,y}} \ , \ \lambda_y = \frac{V_{req,y} + 0.30V_{req,x}}{V_{R,y} + 0.30V_{R,x}} \tag{12}$$

## 4. Application of the non-linear static analysis method

A non-linear static analysis is also employed, in accordance with the provisions of *KANEPE* [4] for a "performance level B".

In this paper, the failure indices of the buildings are being defined in two ways. In the first way, based on the minimum horizontal ground acceleration for which first failure occurs for an acceptable level performance B and for all possible loading combinations. The failure index is calculated by the following Eq.13 as:

$$\lambda_{ag} = \frac{a_{g,ref}}{\alpha_g} \tag{13}$$

where $a_{g,ref}$ is the reference horizontal ground acceleration, which in this case equals to 0.24g, with a probability of exceeding the seismic action of 10% in the structure's intended life span, which equals to 50 years for ordinary structures.

In the second way, through the maximum failure index of column elements for a "performance level B1" and for all possible loading combinations.

## 5. Results comparison

### 5.1 Seismic Resistance obtained by Second-level pre-earthquake inspection and Non-linear static analysis

Table 6 shows the results of the seismic resistance in terms of base shear force of the buildings examined in this paper. The results obtained by applying the methodology of Second-level pre-earthquake inspection are presented for both cases mentioned above, i.e. for the case that there are available data about reinforcement amounts of the column elements and for the case that they are not available. Regarding the non-linear static analysis, the value of the shear force presented on Table 6 is the maximum value obtained by the capacity curve of the structure, which appears before or during the point when the structure reaches "performance level B".

**Table 6.** Maximum Seismic Resistance.

| BUILDING A | | | |
|---|---|---|---|
| | Second-level pre-earthq. Insp.– Reinf. data | Second-level pre-earthq. Insp.– No reinf. data | Non-linear static analysis |
| No Infill Walls | 770.39 | 938.26 | 620.75 |
| Inf.Wall.1 | 1358.44 | 1523.31 | 930.22 |
| **Inf.Wall.2** | **1064.42** | **1232.29** | **660.62** |
| Inf.Wall.3 | 987.02 | 1154.89 | 746.85 |
| **Inf.Wall.4** | **878.70** | **1046.57** | **654.40** |
| BUILDING Γ | | | |
| | Second-level pre-earthq. Insp.– Reinf. data | Second-level pre-earthq. Insp.– No reinf. data | Non-linear static analysis |
| No Infill Walls | 697.44 | 807.53 | 499.91 |
| Inf.Wall.1 | 1296.75 | 1382.87 | 884.71 |
| **Inf.Wall.2** | **997.10** | **1095.20** | **614.47** |
| Inf.Wall.3 | 920.04 | 1021.23 | 697.11 |
| **Inf.Wall.4** | **808.74** | **914.38** | **528.94** |

In all cases examined, the failure mechanism determined by applying the Second-level pre-earthquake inspection with known reinforcement data, was found to be flexural, in full agreement with the analysis results for both buildings. Seismic resistance values obtained when the Second-level pre-earthquake inspection was applied without reinforcement data, were higher than those obtained when using reinforcement data. This is reasonable considering that, for this case, only the shear strength of the members is taken into account, as flexural failure, which was the critical one, is not being checked.

Fig.3 presents the results of the seismic resistance of the buildings for good and poor construction detailing and wedging. It is important mentioning that, according to the provisions of Second-level pre-earthquake inspection, the contribution of infill walls to the total seismic resistance must not exceed 40% of the seismic resistance provided by the vertical structural members (i.e. RC columns, RC walls). In Fig.3 this is demonstrated as “Limit 40%”.

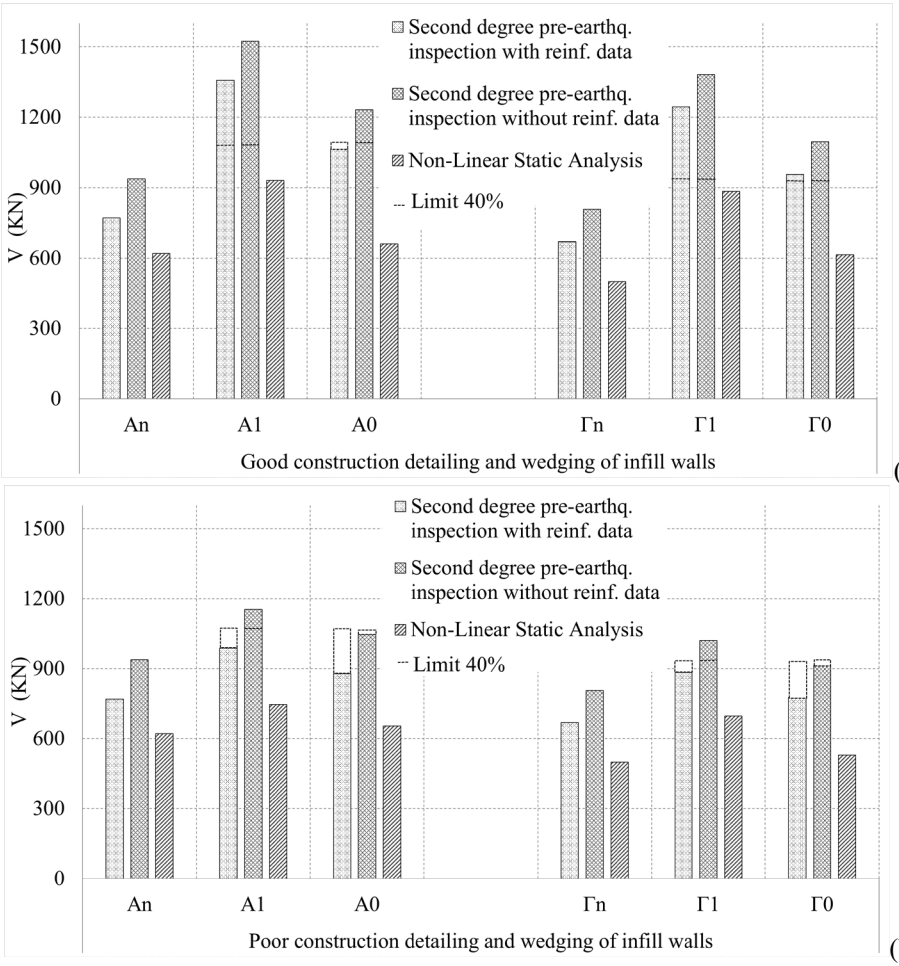


**Fig. 3.** Earthquake resistance obtained by Second-level pre-earthquake inspection (with and without considering reinforcement data) and Non-linear static analysis for good (a) and poor (b) construction detailing and weding of infill walls

It is observed that in all buildings, the maximum seismic resistance (V) provided by the vertical structural elements as well as the contribution of the infill walls, as determined by the Second-level pre-earthquake inspection, always result to slightly higher values than the corresponding ones of the non-linear static analysis. For the case of good construction detailing and wedging of infill walls without openings, the contribution of infill walls was high, to the extent that it exceeded the maximum contribution limit set by the Second-level pre-earthquake inspection (40% of vertical elements resistance). However, this case is not realistic and was considered only for the purpose of investigating the limits of the acceptable contribution of infill walls.

### 5.2 Failure indices obtained by Second-level pre-earthquake inspection and Non-linear static analysis

Fig.4 and Fig.5 demonstrate the values of the failure indices obtained by the Second-level pre-earthquake inspection [1] for both the cases that reinforcement data are available ($\boldsymbol{\lambda_{\Delta}}$) and not available ($\boldsymbol{\lambda_{\Delta,v}}$), together with the corresponding values obtained by the non-linear static analysis. For this case, indices are determined in terms of base acceleration ($\boldsymbol{\lambda_{ag}}$) and in terms of maximum failure index ($\boldsymbol{\lambda_{max}}$) for good and poor construction detailing and wedging of masonry infill walls.

As can be observed in Fig.4 and Fig.5, failure indices $\lambda_{\Delta}$ are in very good convergence with $\lambda_{ag}$ compared to the failure indices $\lambda_{max}$ of the columns. In fact, for the common cases of buildings with infill walls with openings, failure indices $\lambda_{\Delta}$were in great convergence with the corresponding results of the non-linear static analysis for both buildings and for all the cases that were examined in this study. However, for $\lambda_{\Delta,v}$ lower values were obtained as expected, due to the higher value of the seismic resistance that was calculated for this case (Table 6).

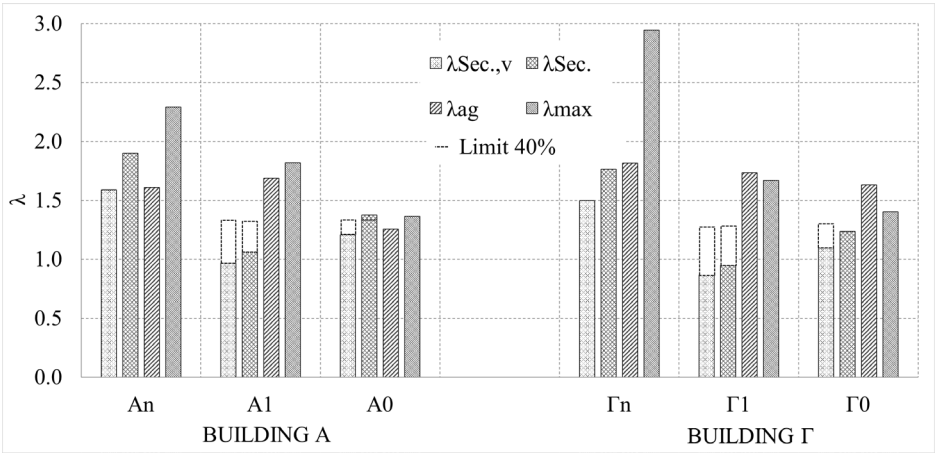


**Fig. 4.** Failure indices obtained by Second-level pre-earthquake inspection and Non-linear static analysis for good construction detailing and wedging of infill walls

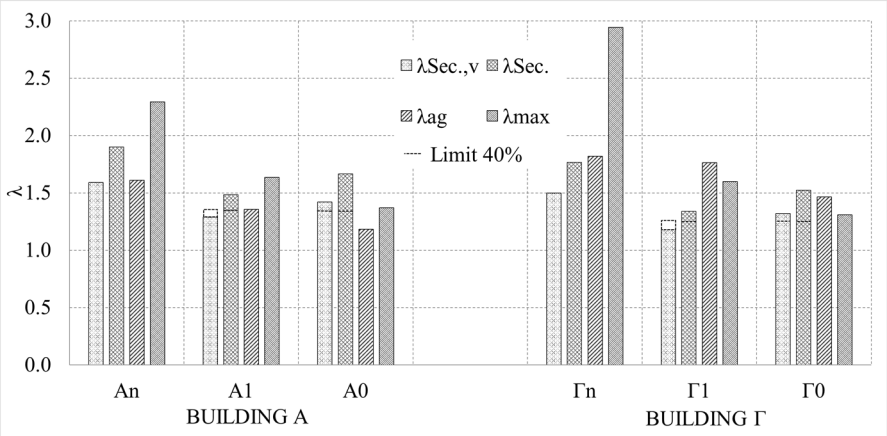


**Fig. 5.** Failure indices obtained by Second-level pre-earthquake inspection and Non-linear static analysis for poor construction detailing and wedging of infill walls

In order to evaluate the effect on the results, of the changes made in the recently revised version of the Second-level pre-earthquake inspection, the values of the failure indices obtained by applying both versions of the provisions [5-6] are presented in Table 7 together with the corresponding results from the non-linear static analysis.

As can be observed, the values of the failure indices obtained by the methodology of the pre-revised version [6] are always quite higher than the corresponding ones obtained by the methodology of the revised version [5], are independent of the presence of masonry infill walls and deviate more from the results of the non-linear static analysis. The main reason for these differences is that in the pre-revised version [6]: (a) lower values are used for the behavior factor q (which for the cases examined is considered equal to $\mathbf{q = 1.7}$ instead of $\mathbf{q = 2.0}$ that is dictated by the revised version) and (b) the contribution of masonry infill walls to the seismic resistance of the structure is ignored.

**Table 7.** Failure indices λ

| Second-level pre-earthquake inspection | | | | | |
|---|---|---|---|---|---|
| | | v.2022 - Reinf. data | v.2022 – No reinf. data | v.2018 – Reinf. data | v.2018 – No reinf. data |
| BUILDING A | No Infill Walls | 1.90 | 1.56 | 2.24 | 1.84 |
| | Inf.W.1 | 1.08 | 0.96 | 2.24 | 1.84 |
| | **Inf.W.2** | **1.38** | **1.19** | **2.24** | **1.84** |
| | Inf.W.3 | 1.48 | 1.27 | 2.24 | 1.84 |
| | **Inf.W.4** | **1.67** | **1.40** | **2.24** | **1.84** |
| BUILDING Γ | No Infill Walls | 1.76 | 1.46 | 2.07 | 1.72 |
| | Inf.W.1 | 0.95 | 0.85 | 2.07 | 1.72 |
| | **Inf.W.2** | **1.23** | **1.08** | **2.07** | **1.72** |
| | Inf.W.3 | 1.33 | 1.15 | 2.07 | 1.72 |
| | **Inf.W.4** | 1.52 | 1.29 | 2.07 | 1.72 |

| Non-linear Static Analysis | | | |
|---|---|---|---|
| | | $\lambda_{max}$ | $\lambda_{ag}$ |
| BUILDING A | No Infill Walls | 2.30 | 1.61 |
| | Inf.W.1 | 1.82 | 1.69 |
| | **Inf.W.2** | **1.37** | **1.26** |
| | Inf.W.3 | 1.64 | 1.36 |
| | **Inf.W.4** | **1.37** | **1.18** |
| BUILDING Γ | No Infill Walls | 2.95 | 1.82 |
| | Inf.W.1 | 1.67 | 1.73 |
| | **Inf.W.2** | **1.41** | **1.63** |
| | Inf.W.3 | 1.60 | 1.76 |
| | **Inf.W.4** | **1.31** | **1.47** |

## 6. Conclusions

In this present study, a comparison was made between the results of the approximate methodology described in the Second-level pre-earthquake inspection of RC buildings [5-6] and the corresponding ones obtained from a non-linear static analysis in order to validate the reliability of the approximate method. This method, because of its approximate nature, simplifies the procedure of estimating the seismic capacity of an existing RC structure. This methodology was applied for both the cases where reinforcement data for the vertical structural elements are and are not available. Based on the results obtained from this study for both buildings and for all different cases the following conclusions can be drawn. It is out of the question that further research is needed to be conducted by testing different types of buildings so that solid and safe conclusions can be drawn for a wider range of structures:

- The failure indices λ of the Second-level pre-earthquake inspection, when reinforcement data of columns are available, were in great convergence with the corresponding results in terms of base acceleration obtained by a non-linear static analysis for the cases where the infill walls had a reasonable size and location of openings. When the maximum column failure index was used as the main failure index of the non-linear analysis, case-by-case differences were observed.
- When applying the methodology of the Second-level pre-earthquake inspection, a greater seismic demand is estimated compared to the one resulting from the non-linear static analysis, due to the lower value of the period obtained by the empirical equation (Table 4), but also a relatively greater seismic resistance (Table 6). Thus, despite these discrepancies, the values of the failure indices λ obtained from both methods have eventually a good convergence.
- The contribution of masonry infill walls to the seismic resistance of the buildings was in all cases higher than the one that was determined by the non-linear static analysis. The deviation was significant when infill walls were of high resistance and without openings.
- In the buildings examined, the failure mechanism determined by the Second-level pre-earthquake inspection with available reinforcement data, was found to be flexural for all RC columns, in full agreement with the results of the non-linear static analysis. When the Second-level pre-earthquake inspection was applied for the case that no reinforcement data were available, the failure indices were found to have lower values, but even in this case analysis results were approximated quite satisfactorily.
- The results obtained by the Second-level pre-earthquake inspection according to its recent first revision (v.2022) [5] were in better convergence with the ones obtained by the non-linear static analysis, compared to the results obtained when the pre-revised version was applied (v.2018) [6].

## References


1. Damikoukas, S.; Chatzieleftheriou, S.; Lagaros, N.D. First Level Pre- and Post-Earthquake Building Seismic Assessment Protocol Based on Dynamic Characteristics Extracted In Situ. Infrastructures 2022, 7, 115. https:// doi.org/10.3390/ infrastructures7090115
2. Dritsos, S. E. (2005). Seismic retrofit of buildings: A Greek perspective. Bulletin of the New Zealand Society for Earthquake Engineering, 38(3), 165–181. https://doi.org/10.5459/bnzsee.38.3.165-181
3. EN 1998–1 (2004) Eurocode 8: Design of structures for earthquake resistance, Part 1: General rules, seismic actions and rules for buildings, European Standard, European Committee for Standardization, Brussels, Belgium
4. EPPO, Greek code for structural interventions (KAN.EPE.), Earthquake Planning and Protection Organization of Greece, Greek Ministry for Environmental Planning and Public Works, Athens, Greece (2017)
5. EPPO, Second level pre-earthquake assessment of RC buildings, Earthquake Planning and Protection Organization of Greece (EPPO), Greek Ministry for Environmental Planning and Public Works, Athens, Greece (1st Revision 2022)
6. EPPO, Second level pre-earthquake assessment of RC buildings, Earthquake Planning and Protection Organization of Greece (EPPO), Greek Ministry for Environmental Planning and Public Works, Athens, Greece (2018)
7. FEMA. P-154: Rapid Visual Screening of Buildings for Potential Seismic Hazards: A Handbook; Federal Emergency Management, Agency: Washington, DC, USA, 2015
8. Kappos, A.J. (2013). Seismic Vulnerability and Loss Assessment for Buildings in Greece. In Seismic Vulnerability of Structures, P. Gueguen. (Ed.). https://doi.org/10.1002/9781118603925.ch3
9. Pitilakis, K., Riga, E., Apostolaki, S. et al. Seismic hazard zonation map and definition of seismic actions for Greece in the context of the ongoing revision of EC8. Bull Earthquake Eng 22, 3753–3792 (2024). https://doi.org/10.1007/s10518-024-01919-8
10. Pnevmatikos, N., Gantes, C. (2014). Actively and Semi-actively Controlled Structures Under Seismic Actions: Modeling and Analysis. In: Beer, M., Kougioumtzoglou, I., Patelli, E., Au, IK. (eds) Encyclopedia of Earthquake Engineering. Springer, Berlin, Heidelberg. https://doi.org/10.1007/978-3-642-36197-5_146-1
11. Vasileiadi M., Dritsos S. An approximate method to assess the seismic capacity of existing RC buildings. 7th ECCOMAS Thematic Conference on Computational Methods in Structural Dynamics and Earthquake Engineering, Crete, Greece, 24–26 June (2019)

# Experimental of the Tsonos model for predicting joint behavior in reinforced concrete frames

Emmanouil A. Golias[1], Martha A. Karabini[1], Ioanna P. Vlasakidou[1], Filareti V. Papavasileiou[1], Emmanouil A. Vougioukas[2]

[1]Democritus University of Thrace, Kimmeria , Xanthi, Greece
[2]National Technical University of Athens 9, Iroon Polytechniou st., 15780 Athens, Greece
egkolias@civil.duth.gr

**Abstract.** Pushover analysis is widely regarded as the most accurate method for determining the bearing capacity of existing structures. To achieve a realistic assessment, it is essential to consider all possible failure modes. In many existing structures, joints are often designed with minimal or no transverse reinforcement, making joint failure more likely to occur before the failure of the connected members. This study employs a well-known joint behavior simulation to examine this scenario. The pushover analysis is terminated upon detecting joint failure, as it signifies a brittle failure. Analyses are performed on typical frames using both conventional criteria and the proposed joint failure criteria. The results are presented, ranked, and discussed.

**Keywords:** Beam-Column Joints, Design Criteria, Construction Joints

## 1 Object of the research

Experience from earthquakes in Greece and worldwide has demonstrated that one of the most critical safety issues for reinforced concrete structures under seismic stresses is the occurrence of failures in the joint areas of column beams. These joints experience the highest shear forces and moments transferred from the ends of beams and columns. The joints' response to these highly cyclic actions should ideally remain elastic, avoiding any damage. However, if plastic deformation occurs, the joints must maintain their maximum strength during inelastic deformation cycles and absorb significant hysteretic energy.

Non-linear static (pushover) analysis is used to estimate the magnitude of inelastic deformations that structural elements will undergo during seismic events. This paper presents an experimental investigation that includes cyclic loading results for two full-scale 1:1 beam-column external joint specimens of medium ductility class, not in accordance with Eurocodes 2 and 8. The analytical part of the study examines the overall behavior of these experimental samples. Specifically, it evaluates an internationally recognized model from the literature for predicting the shear strength and failure modes of external joints.

The specimens are assessed using this model, particularly focusing on the collapse prevention framework established by Professor A.D. Tsonos. The paper aims to draw conclusions about the adequacy of construction joints and to determine whether well-constructed older buildings, which show no visible damage, remain fit for their intended purpose.

The geometry and the cross-section dimensions were common for all specimens for obvious comparison reasons; the total length of the column was 3.0 m and its cross section dimensions 350/250 mm whereas the length of the beam was 1.875 m and its cross section dimensions 350/250 mm. The reinforcing arrangements of all specimens are presented in **Fig. 1**. The compressive strength of the concrete used for the specimens was measured by supplementary compression tests of six standard D×h = 150×300 mm cylinders. The mean value at the age of 28 days was fc = 35,5 MPa. The steel of the longitudinal bars and the stirrups was S500 with yield tensile strength fy = 500 MPa.

**Specimen 1**

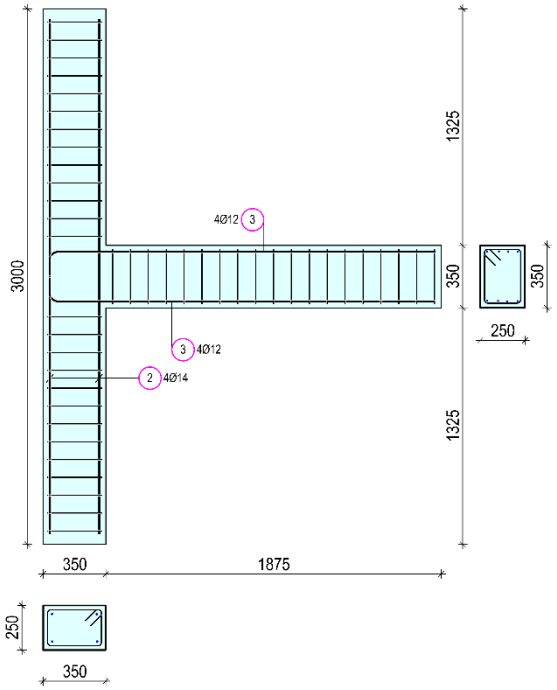

**Specimen 2**

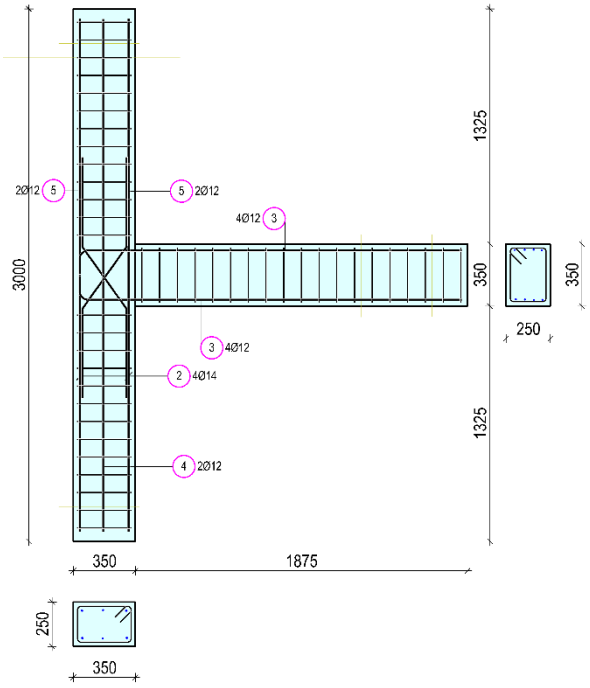


**Fig. 1.** Geometrical characteristics of the specimens 1 and Specimen 2

The beam in both Specimens 1 and 2 is reinforced with 4 bars of 12 mm diameter at the top and 4 bars of 12 mm diameter at the bottom (Fig. 1 and Table 1). The column reinforcement in Specimens 1 and 2 consists of 1Ø14 bars at the edges. In Specimen 2, there are also two pairs of X-type reinforcement bars 2Ø12 and two intermediate vertical bars Ø12. The stirrups in both the beam and column are the same in both specimens, Ø8/10. Detailed reinforcement is shown in Fig. 1.

The reinforcements of all specimens are presented in Fig. 1 and Table 1.

**Table 1.** Reinforcements in the joints of the specimens

| Reinforcements | Specimen 1 | Specimen 2 |
|---|---|---|
| ① | - | - |
| ② | 2Ø14 | 2Ø14 |
| ③ | 4Ø12 | 4Ø12 |
| ④ | - | 2Ø12 |
| ⑤ | - | 2Ø12 |

# 2 Analytical models for behaviour predicting and failure modes

## 2.1 Cross Section Analysis

Next, an analysis of the cross-section of both the beam and the column is conducted to determine the actual flexural strength at the yielding of the tensile reinforcement.

Here's the interpretation of each symbol:

d: Effective depth of the section

ξ: Neutral axis coefficient

$\varepsilon_c$: Compressive strain in the concrete

$f_y$: Yield stress of the steel

$f_{cm}$: Compressive strength of concrete

x: Distance from the extreme compression fiber to the neutral axis d: Effective depth of the section

$F_c$: Compressive force in the concrete

$\varepsilon_{s1}$: Strain in the first steel reinforcement

$\varepsilon_{sy}$: Yield strain of the steel

$\varepsilon_{s2}$: Strain in the second steel reinforcement

$E_s$: Modulus of elasticity of the steel

$\sigma_{s1}$: Stress in the first steel reinforcement

$\sigma_{s2}$: Stress in the second steel reinforcement

ΣF: Sum of forces in the section

**Specimen 1 and Specimen 2**

| BEAM<br>4Ø12 up[1]+down[2] | | | | | | | |
|---|---|---|---|---|---|---|---|
| $A_{s,prov} = 4.524$ cm$^2$<br>$d = 0.316$ m<br>$d_1 = 0.034$ m<br>$\varepsilon_c = -3.5$ ‰<br>$f_y = 500$ MPa<br>$f_{cm}$=35.5 MPa | $x_c$ (m) | $\lvert F_c \rvert$ (kN) | $\varepsilon_{si}$ (‰) | $\sigma_{si}$ (MPa) | $F_{si}$ (kN) | $\sum F$ | $M_{Rb}$ (kN*m) |
| | 0.033 | 236.54 | 1: 30.092 | 1: 500 | 1: 226.19 | 0 | 66.80 |
| | | | 2: 0.114 | 2: 22.88 | 2: 10.35 | | |

**Specimen 1**

| COLUMN<br>2Ø14 up[1]+down[2] | | | | | | | |
|---|---|---|---|---|---|---|---|
| $A_{s,prov} = 3.079$ cm$^2$<br>N=-122.5 kN<br>$d = 0.315$ m<br>$d_1 = 0.035$ m<br>$\varepsilon_c = -3.5$ ‰<br>$f_y = 500$ MPa<br>$f_{cm}$=35.5 MPa | $x_c$ (m) | $\lvert F_c \rvert$ (kN) | $\varepsilon_{si}$ (‰) | $\sigma_{si}$ (MPa) | $F_{si}$ (kN) | $\sum F - N$ | $M_{Rc}$ (kN*m) |
| | 0.037 | 265.24 | 1: 26.363 | 1: 500 | 1: 153.94 | 0 | 61.00 |
| | | | 2: -0.182 | 2:-36.37 | 2:-11.20 | | |

**Specimen 2**

| COLUMN<br>2Ø14 left[1]+right[2] 2Ø12 in the middle[3] | | | | | | | |
|---|---|---|---|---|---|---|---|
| $A_{s,prov}$ =3.079 cm²<br>$A_{s,prov}$ =2.262 cm²<br>N=-122.5 kN<br>$d = 0.315$ m<br>$d_1 = 0.035$ m<br>$\varepsilon_c = -3.5$ ‰<br>$f_y = 500$ MPa<br>$f_{cm}$=35.5 MPa | $x_c$ (m) | $\lvert F_c \rvert$ (kN) | $\varepsilon_{si}$ (‰) | $\sigma_{si}$ (MPa) | $F_{si}$ (kN) | $\sum F - N$ | $M_{RC}$ (kN*m) |
| | 0.048 | 335.53 | 1: 20.107 | 1: 500 | 1: 153.94 | 0 | 81.31 |
| | | | 2: 9.615 | 2: 500 | 2: 113.10 | | |
| | | | 3: -0.877 | 3: -175.40 | 3: -54 | | |

## 2.2 Theoretical Model

The model of the Professor of Antiseismic Structures of the Aristotle University of Thessaloniki, Alexandros Dimitrios Tsonos, focuses on the control and design of reinforced concrete beam-column joints. Using the model, the failure stress of the joint $t_{ult}$ is calculated with great accuracy. When the applied shear stress in the joint is less than or equal to half the failure stress of the joint, $\tau_{cal} \leq 0.5\tau_{ult}$, then the joint in a strong earthquake will work in the elastic region safely driving the failure to the beam, where all the damage will concentrate leaving columns intact. In old buildings, the value of the proposed model is highlighted even more since it safely indicates which structural element (beam, column, joint) will cause failure initiation, and in general, it shows us the safe hierarchy of failures between these structural elements.

## 2.3 Capacity Check

Specimen 1

$\sum M_{RC} \geq 1.3 * \sum M_{Rb} \rightarrow 2 * M_{Rc} \geq 1.3 * M_{Rb} \rightarrow 2 * 61 \geq 1.3 * 66.80 \rightarrow 122 \geq 86.84$, which is satisfied

according to EN1998-1-§4.4.2.3.

Since, $\sum M_{RC} \geq \sum M_{Rb} \rightarrow 122\ \text{kN} * \text{m} > 66.80\ \text{kN} * \text{m}$, it will be valid for DCM:

- Finding Competent Design Shear Force of Beam

$$M_{1d} = \gamma_{Rd} * M_{Rb} = 1 * 66.80 = 66.80\ \text{kN} * \text{m},$$
$$V_{capacity} = \frac{M_{1d}}{l_{cl}} = \frac{66.80}{1.475} = 45.29\ \text{kN}$$

- Finding Competent Design Shear Force of Column

$$M_{1d} = M_{2d} = \gamma_{Rd} * M_{Rc} = 1.1 * 2 * 61 = 134.20\ \text{kN} * \text{m}$$
$$V_{capacity} = \frac{M_{1d}}{l_{cl}} = \frac{134.20}{2.50} = 53.68\ \text{kN}$$

Specimen 2

$\sum M_{RC} \geq 1.3 * \sum M_{Rb} \rightarrow 2 * M_{Rc} \geq 1.3 * M_{Rb} \rightarrow 2 * 81.31 \geq 1.3 * 66.80 \rightarrow 162.62 \geq 86.84$, which is satisfied according to EN1998-1-§4.4.2.3.

Since, $\sum M_{RC} \geq \sum M_{Rb} \rightarrow 162.62\ \text{kN} * \text{m} > 66.80\ \text{kN} * \text{m}$, it will be valid for DCM:

- Finding Competent Design Shear Force of Beam

$$M_{1d} = \gamma_{Rd} * M_{Rb} = 1 * 66.80 = 66.80\ \text{kN} * \text{m},$$

$$V_{capacity} = \frac{M_{1d}}{l_{cl}} = \frac{66.80}{1.475} = 45.29\ \text{kN}$$

- Finding Competent Design Shear Force of Column

$$M_{1d} = M_{2d} = \gamma_{Rd} * M_{Rc} = 1.1 * 2 * 81.31 = 178.882\ \text{kN} * \text{m}$$

$$V_{capacity} = \frac{M_{1d}}{l_{cl}} = \frac{178.882}{2.50} = 71.56\ \text{kN}$$

## 2.4 Application of Tsonos Model (2007-2019)

Specimen 1

Initially, the increased compressive strength of the concrete due to overtightening is calculated, using the model of Scott at al. (1982)

$$h_o = h_c - 2 * c_{nom} - 2 * \emptyset_w/2 = 350 - 2 * 20 - 2 * 4 = 302\ \text{mm}$$

$$b_o = b_c - 2 * c_{nom} - 2 * \emptyset_w/2 = 250 - 2 * 20 - 2 * 4 = 202\ \text{mm}$$

$$\rho_s = 0, \qquad k = 1 + \frac{\rho_s * f_{yw}}{f_c'} = 1, \qquad f_c = k * f_c' = 1 * 35.5 = 35.5\ \text{MPa}$$

$$\alpha = \frac{h_b}{h_c} = \frac{350}{350} = 1.0$$

The system of equations (1), (2) and (3) is solved:

$$x = \frac{\alpha \cdot \gamma_{ult}}{2\sqrt{f_c}} \quad (1), \quad \psi = \frac{\alpha \cdot \gamma_{ult}}{2\sqrt{f_c}} \cdot \sqrt{1 + \frac{4}{a^2}} \quad (2), \quad x - \psi = -0.1 \quad (3)$$

resulting in:

The failure deformation of the joint: $\gamma_{ult} = 0.96$

- The failure stress of the joint:

$$\tau_{ult} = \gamma_{ult} * \sqrt{f_c} = 0.96 * \sqrt{35.5} = 5.72\ \text{MPa}$$

Horizontal shear force at the external joint, when a flexural crack forms in the beam:

$$V_{cal} = 1.25 * A_{s1} * f_y - V_{col} = 1.25 * 4.52 * 500 * 10^{-1} - 29.89 = \ 252.61 \text{ kN}$$

Based on the geometry of the specimen, it follows that, when the maximum shear force develops in the beam, then a shear force develops in the column is equal to:

$$V_{col} = V_{Ed,max} * \frac{l}{h} = 45.29 * \frac{1.475 + \left(\frac{0.35}{2}\right)}{2.5} = 29.89 \text{ kN}$$

- The deformation in the joint, when the beam fails:

$$\gamma_{cal} = \frac{V_{cal}}{h_c * b_c * \sqrt{f_c}} = \frac{252.61 * 10^3}{0.35 * 0.25 * \sqrt{35.5} * 10^6} = \ 0.485$$

- The shear stress exerted on the joint, when the beam fails:

$$\tau_{cal} = \gamma_{cal} * \sqrt{f_c} = 0.485 * \sqrt{35.5} = 2.89 \text{ MPa}$$

Since, $\tau_{cal} < \tau_{ult}$ , the yielding of the beam will be preceded.

SPECIMEN 2

$$\rho_s = A_{sw} * \frac{2b_o \ + \ 2h_o}{b_o * \ h_o \ * \ s} = 4.524 * \frac{2 * 20.2 \ + \ 2 * 30.2}{20.2 * \ 30.2 \ * \ 35} = 0.0214$$

$$k = 1 + \frac{\rho_s * f_{yw}}{f_c{}'} = 1 + \frac{0.0214 * 500}{35.5} = 1.3 \, , \qquad f_c = k * f_c' = 46.2 \text{ MPa},$$

$$\alpha = \frac{h_b}{h_c} = 1.0$$

The system of equations (1), (2) and (3) is solved. Resulting in:

- The failure deformation of the joint: $\gamma_{ult} = 1.1$
- The failure stress of the joint:

$$\tau_{ult} = \gamma_{ult} * \sqrt{f_c} = 1.1 * \sqrt{46.2} = 7.48 \text{ MPa}$$

- Horizontal shear force at the external joint, when a flexural crack forms in the beam:

$$V_{cal} = 1.25 * A_{s1} * f_y - V_{col} = 1.25 * 4.52 * 500 * 10^{-1} - 47.23 = \ 235.27 \text{ kN}$$

Where,

$$V_{col} = V_{capacity} * \frac{l}{h} = 71.56 * \frac{1.475 + \left(\frac{0.35}{2}\right)}{2.5} = 47.23 \text{ kN}$$

The deformation in the joint, where the beam fails:

$$\gamma_{cal} = \frac{V_{cal}}{h_c * b_c * \sqrt{f_c}} = \frac{235.27 * 10^3}{0.35 * 0.25 * \sqrt{46.2} * 10^6} = \ 0.4$$

The shear stress exerted on the joint, when the beam fails:

$$\tau_{cal} = \gamma_{cal} * \sqrt{f_c} = 0.4 * \sqrt{46.2} = 2.7 \text{ MPa}$$

Since $\tau_{cal} < \tau_{ult}$ , the yielding of the beam will be preceded.

# 3 Experimental program

## 3.1 Experimental Layout

Test rig and setup along with the instrumentation details are shown in Fig. 2. Each beam-column specimen is rotated 90°, so that the beam is in the vertical direction and the column in the horizontal direction. Supporting devices that allow rotation are used to simulate the inflection points in the middle of the column height in a real laterally loaded frame.

Column compressive axial load $N_c$ equal to $N_c=0.05A_cf_c$ was constantly applied during the experimental procedure in all specimens. The value of the column axial load was controlled to remain constant during the loading procedure at the level of $N_c$=150 kN for all specimens. Although the influence of a variation of axial load values is not examined in this study, the effect of high axial load on the shear capacity of beam–column joints can be considered as favourable. On the other hand, varying the axial load during the test can lead to low level of axial load in some steps of the test, which would tend to emphasize a weak column–strong beam hierarchy. This could lead to a possibility of a predominant flexural behaviour due to column hinging.

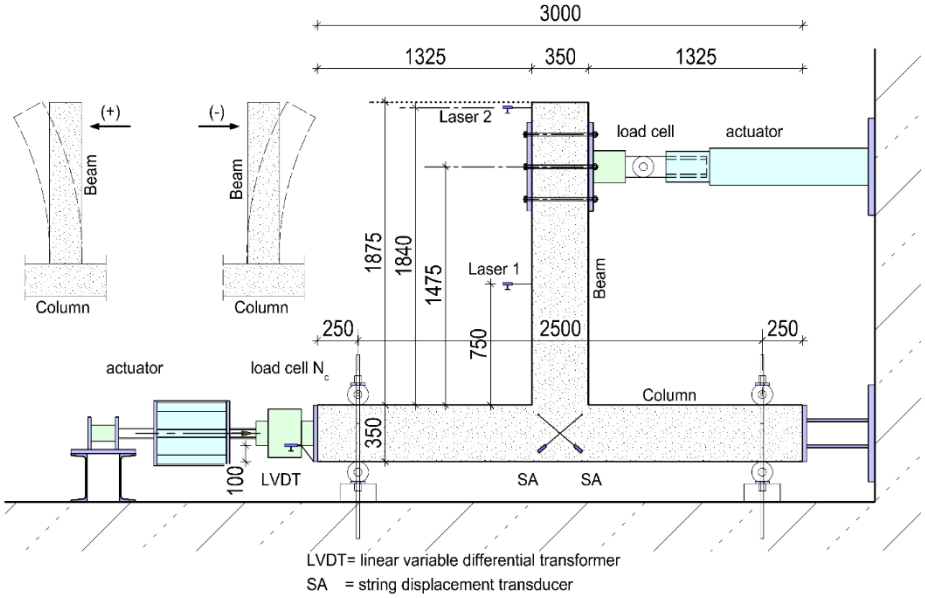


**Fig. 2.** Experimental layout

### 3.2 Load History

All specimens were subjected to the same loading sequence. They were subjected to full cyclic deformation imposed near the free and of the beam which as it can be observed in the test setup is in the vertical direction (Fig. 2). The moment arm for the applied load is equal to 1.475m.

Tested specimens suffered seven loading steps with maximum displacements equal to ±8.5mm, ±12.75mm, ±17.0mm, ±25.5mm, ±34.0mm, ±51.0mm and ±68.0mm at each step, respectively. Each of the seven loading steps included three full loading cycles; thus the loading sequence was performed the way it is shown in Fig. 3. All beam-column joints were subjected to full-cycle deformations. The specimens were subjected to an eight-step loading history. Each loading step consists of three full loading cycles.

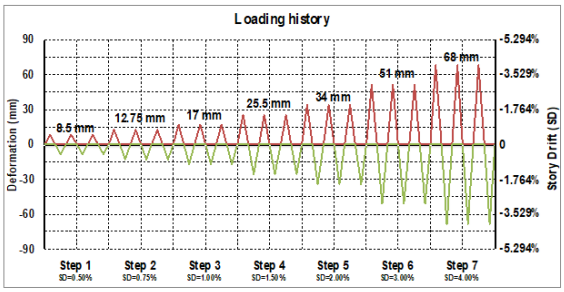


| STEP | SD | δ |
|---|---|---|
| | (%) | (mm) |
| 1 | 0.50 | 8.50 |
| 2 | 0.75 | 12.75 |
| 3 | 1.00 | 17.00 |
| 4 | 1.50 | 25.50 |
| 5 | 2.00 | 34.00 |
| 6 | 3.00 | 51.00 |
| 7 | 4.00 | 68.00 |
| 8 | 5.00 | 85.00 |

**Fig. 3.** Loading sequence. Eight loading steps and each step includes three full loading cycles

To effectively use results from quasi-static cyclic loading tests on reinforced concrete structural elements for overall performance evaluation, it is crucial to establish a loading history that encompasses both the critical capacity issues of the element and the seismic demands. In inelastic seismic scenarios, capacity and demands are interdependent, with each potentially influencing the other. Key seismic capacity parameters for a structural element include strength, stiffness, inelastic deformation capacity (ductility), and cumulative damage capacity, such as energy dissipation. These parameters are expected to deteriorate with an increase in the number of damaging cycles and the amplitude of the cycles.

Every inelastic excursion results in cumulative damage to a structural element. The adopted loading program emphasizes a multi-cycle loading sequence, as repeated loading cycles can cause damage similar to that seen after moderate seismic events, which is a focus of this investigation. Therefore, each loading step in the program includes three full loading cycles, and the entire program consists of steps with progressively increasing displacements (Fig. 3). The effects of loading sequence have not been thoroughly researched, and the sequence of large versus small excursions in a structural element during a severe earthquake does not follow a consistent pattern. The number of inelastic excursions increases as the period of the structural system decreases, with a particularly high rate of increase for short-period systems.

It is important to recognize that seismic demands on structures depend on numerous variables, and a single loading history will always involve some compromise. However, a conservative loading program for most practical cases must be applied. Thus, the chosen loading program is a comprehensive cumulative damage testing approach that allows the determination of structural

performance parameters. These parameters, combined with a cumulative damage model, can be used to evaluate performance under various seismic excitations.

### 3.3 Hysteretic Response Diagrams

To understand some important details regarding the acquired experimental hysteretic response of the tested samples, Fig. 4a and 5a present the load versus slip curves for each loading step. Each step includes three loading cycles. The points where cracking initiated are marked on the diagrams for the first cycles of step 1 for both loading directions (positive and negative).

Furthermore, steel yielding due to the propagation of damage caused by the increased applied load may also lead to more extensive damage during the initial cycles of steps 5, 6, and 7.

As the imposed displacement on Specimens 1 and 2 increased (steps 5 and 6), it led to an increase in the crack width at the beam's initial section (damage concentration), while at step 7, cracks were also observed at the joint area. Although damage was concentrated in the beam area, cracks also appeared in the joint body.

In Specimen 2, a better performance is observed in the joint area due to the contribution of the X-type reinforcements. The plastic hinge is formed clearly in the beam, which is the desired outcome. Minimal cracking is observed in the joint area.

The load-bearing capacity for both specimens remains approximately at the same level. Fig. 4b and 5b.

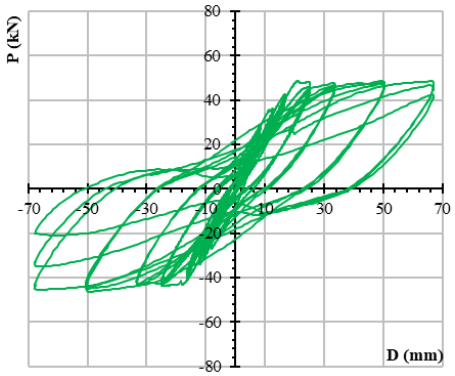


(a) Hysteretic Response

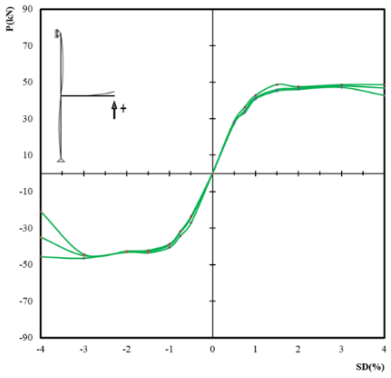


(b) Envelope curves of maximum loads at all cycles

**Fig. 4.** Hysteretic response and load envelope of all cycles of Specimen 1

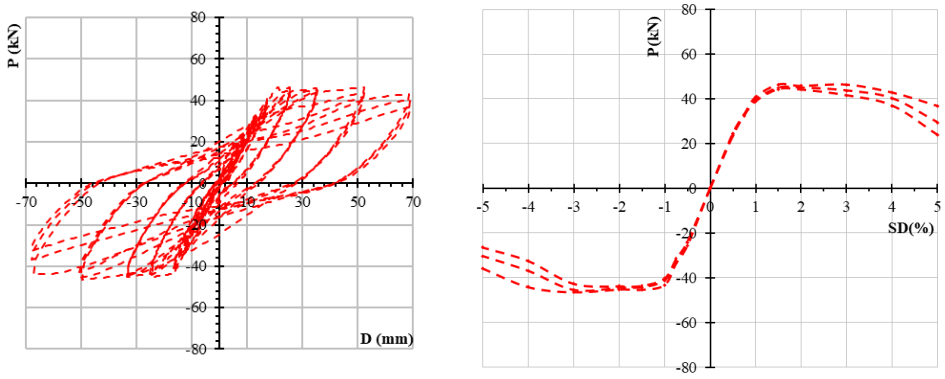


(a) Hysteretic Response (b) Envelope curves of maximum loads at all cycles

**Fig. 5.** Hysteretic response and load envelope of all cycles of Specimen 2

## 4 Conclusions

In this work, the application of the Tsonos model to two specimens was rigorously analyzed and compared with the corresponding experimental results. The study aimed to evaluate the model's effectiveness in predicting the behavior of reinforced concrete beam-column joints, particularly under seismic loading conditions. The Tsonos model focuses on calculating key parameters such as joint failure stress and the stress at beam failure, which are critical for assessing the structural integrity and safety of such joints.

The results of the analysis demonstrated that the Tsonos model could accurately predict the joint failure stress and the stress at beam failure. The model's predictions closely matched the observed experimental data, with only minor deviations. This high level of accuracy indicates that the model can effectively capture the complex interactions and stress distributions that occur within the joint during loading.

A key finding from the study was that the yielding of the beam occurred prior to any significant failure at the joint. This observation is crucial because it suggests that the Tsonos model accurately predicts the sequence of failure events, which is essential for designing safe and reliable structures. Ensuring that beams yield before joints fail is a fundamental principle in structural design, as it allows for energy dissipation and prevents catastrophic collapse.

The study concluded that both the analytical calculations based on the Tsonos model and the experimental results were in excellent agreement. This alignment validates the Tsonos model as a reliable tool for predicting the performance of beam-column joints in reinforced concrete structures. The model's accuracy and reliability make it a valuable asset for engineers seeking to design buildings that can withstand seismic forces without experiencing critical structural failures.

However, it is important to note that the conclusions drawn from this study are primarily qualitative. While the qualitative observations support the model's reliability, future work should focus on providing quantitative comparisons. This involves detailed explanations and discussions that relate the experimental results to the assumptions and

conditions of the analytical model, such as the specifics of the experimental setup and loading conditions. Providing such detailed quantitative analysis would further solidify the confidence in the Tsonos model and clarify its limitations and applicability in various structural scenarios.n this work, the application of the Tsonos model to the two samples was examined and a comparison was made with the experimental results. In particular, applying Tsonos' theoretical model, the joint failure stress and the joint stress at beam failure are calculated with excellent accuracy. Based on these, it follows that the yielding of the beam will precede the joint. It is concluded that both calculations and experimental tests are in complete agreement. It thus proves that the "Tsonos model" is a reliable model for designing joints and preventing the collapse of reinforced concrete buildings.

Specimen 1

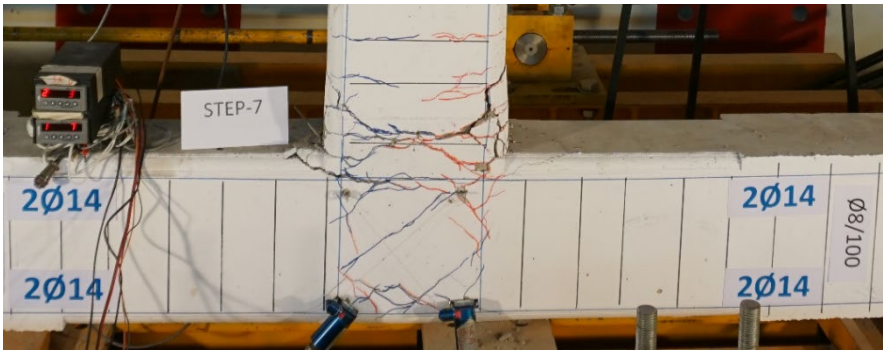


Specimen 2

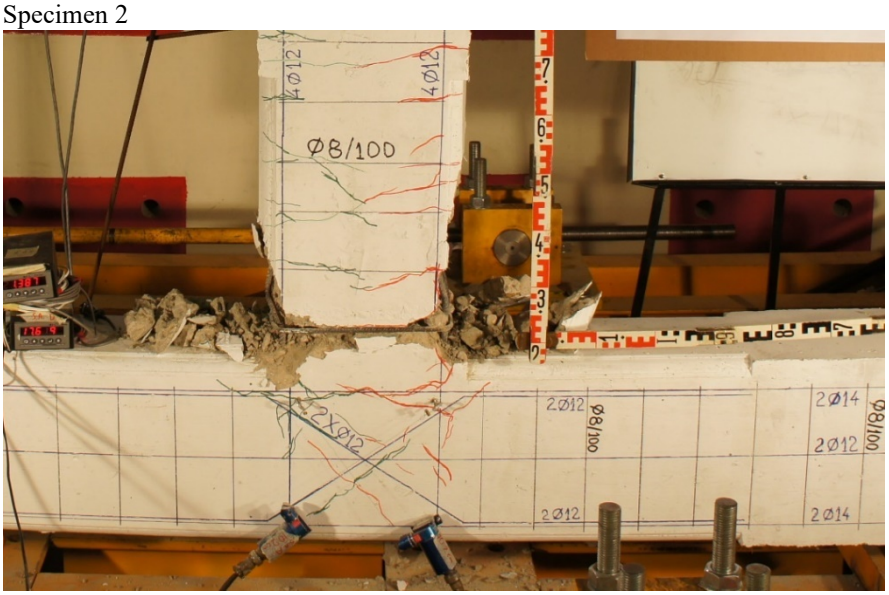


**Fig. 6.** Final state of damage to the beams of specimens

## References


1. Karagiannis, C.G. "Design of Reinforced Concrete Structures' Behavior Against Earthquakes." Sofia A.E. Publishing, Thessaloniki, 2013, pp. 320, 463, 475
2. Scott, A., Park, R., & Priestley, M. J. N. (1982). "Seismic resistance of reinforced concrete beam-column joints." *Journal of Structural Engineering*, 108(4), 891-912
3. Tsonos A.G. (2010), "Performance enhancement of R/C building columns and beam-column joints through shotcrete jacketing", Engineering Structures, 32, 726-740
4. Tsonos, A.D. "Towards a New Approach in the Design of Beam-Column Joints in Reinforced Concrete." *Technical Chronicles, Scientific Edition of TEE, Scientific Section A,* Jan.–Aug. 1996, Vol. 16, No. 1-2, pp. 69-82
5. Tsonos A.G. (2007), "Cyclic load behavior of reinforced concrete beam-column subassemblages of modern structures", ACI Structural Journal, 194(4), 468-478
6. Tsonos, A.D. "Design of Reinforced Concrete Structures According to Eurocodes." Sofia A.E. Publishing, Thessaloniki, 2017, pp. 231, 232, 240-242
7. Karayannis C.G. & Golias E. "Strengthening of deficient RC joints with diagonally placed external C-FRP ropes" Journal Earthquakes and Structures, Vol. 20 No. 1 (2021), 123-132
8. DOI: https://doi.org/10.12989/eas.2021.20.1.123
9. Karayannis, C.G., Golias, E. "Full-scale Experimental Testing of RC Beam-column Joints Strengthened using CFRP Ropes as External Reinforcement."
10. Engineering Structures 2022, 250,113305
11. https://doi.org/10.1016/j.engstruct.2021.113305
12. Pohoryles, D.A., J. Melo, T. Rossetto, H. Varum. 2019. "Seismic Retrofit Schemes with FRP for Deficient RC Beam-Column Joints: State-of-the-Art Review." J. Compos. Constr., 23(4): 03119001
13. https://doi.org/10.1061/(ASCE)CC.1943-5614.0000950.
14. Al-Mahmoud F., Castel, A., François, R., C. Tourneur. 2009. "Strengthening of RC members with near-surface mounted CFRP rods", Composite Structures, 91(2), pp. 138-147
15. Yurdakul Ö, Ö. Avşar. 2016. "Strengthening of substandard reinforced concrete beam-column joints by external post-tension rods." Engineering Structures, 107, 9-22

# Novel Method for the Stochastic Generation of Hazard-Consistent Artificial Accelerograms: A practical application

Hera Yanni[1[0009-0003-0314-0519]], Michalis Fragiadakis[1[0000-0002-0698-822X]] and Ioannis P. Mitseas[1,2[0000-0001-5219-1804]]

[1]National Technical University of Athens, 9 Iroon Polytechniou St., 15780 Athens, Greece
[2]School of Civil Engineering, University of Leeds, Leeds, UK
heragian@mail.ntua.gr, mfrag@mail.ntua.gr,
Imitseas@mail.ntua.gr, I.Mitseas@leeds.ac.uk

**Abstract.** In contemporary engineering practice, the investigation of the dynamic response of structures through time-history analysis requires the use of suites of acceleration ground motions. The paper studies the response of structures subjected to a novel methodology for the generation of target spectrum compatible artificial accelerograms. Existing spectrum-based models are used for the ground motion generation, whereas hazard consistency is achieved by matching these records either to a design spectrum or to a ground motion model. The obtained suites are used for the non-linear response history analysis (NRHA) of a benchmark multi-degree-of-freedom structure. Two study examples are presented. In the first example the generated suite matches only a spectral mean and in the second example the suite matches both the target spectral mean and variability. The results indicate that using the generated ground motion suites for the target NRHAs produces results that are consistent with record selection algorithms, thus confirming the efficiency of the proposed methodology.

**Keywords:** artificial accelerogram, non-linear dynamic analysis, non-stationary, spectrum-compatible, variability, ground motion model

## 1 Introduction

The increasing availability of powerful personal computers and advanced engineering software has facilitated the use of dynamic time-history analysis in everyday engineering practice. This type of analysis is deemed the most realistic for assessing the seismic behavior of structures, especially when non-linear response is expected. Non-linear response history analysis (NRHA) is influenced by multiple sources of uncertainties stemming from the calibration of the non-linear structural model (e.g. material properties, design assumptions), as well as the modeling of the seismic excitation. The latter is recognized to have a significant effect on the seismic response of structures.

Accelerograms that model the input seismic motion for the NRHAs can be either previously recorded, synthetic or artificially generated. The most common practice followed is the careful selection and scaling of recorded ground motion records from online databases; however, this approach still has limitations. Selected accelerograms are often recorded in other locations than the site of interest and correspond to different magnitude-distance scenarios and soil characteristics. Moreover, the scarcity of recorded ground motions of earthquakes with large magnitudes at small epicentral distances can often confine the analysis, especially for high-limit states like collapse. As a result, the task of selecting and scaling earthquake records remains a highly controversial issue in the literature [1], and various algorithms have been proposed [2–3] for addressing these challenges.

The use of artificially generated acceleration time-histories provides a valid alternative to circumvent the issues linked with the selection of recorded ground motions and is also recommended by seismic codes [4]. Their main advantage is that they can be modeled to have the desired target features that are required within the framework of dynamic analysis. The use of artificial accelerograms in seismic simulations has found widespread applications in the field of structural engineering, ranging from Monte Carlo Simulation techniques [5], to stochastic dynamics simulations [6–7] for structural reliability assessment. Furthermore, practice-oriented probabilistic models that model the seismic demand based on specific values assumed by an intensity measure can also use artificial ground motions [8].

Seismic codes do not propose specific methods for the generation of artificial accelerograms; they only define some basic requirements related to their matching to the design code spectrum. For example, Eurocode 8 [4] mainly requires that the mean response spectrum of the generated accelerograms should match the code's elastic response spectrum for 5% viscous damping. Therefore, engineers are focused on the target spectrum matching requirement and thus can choose from a wide range of proposed methods in the literature.

Given the inherently stochastic nature of earthquakes, artificial ground motion time-histories are typically generated as stochastic processes. The spectral representation method proposed by Shinozuka and Deodatis [9], is the most widespread method in the literature. The method simulates ground motion time-histories as a superposition of harmonic components with random phase angles. In this approach, the power spectral density (PSD) function is directly related to the amplitude of each harmonic, thus providing the basis for generating target spectrum-compatible accelerograms. As highlighted by Vanmarcke and Gasparini [10], spectrum compatibility can be achieved by matching the values of the PSD function of the ground motion to the response spectral values for a given damping ratio.

The desired ground motion time-histories for NRHAs that are simulated using the PSD function are typically non-stationary both in amplitude and frequency. Several methods have been proposed in order to generate fully non-stationary accelerograms. One approach is the use of an evolutionary power spectral density (EPSD) function, i.e. a PSD function that varies in time [11]. This is typically achieved by introducing an envelope function that modifies a stationary accelerogram both in time and in frequency in order to simulate the characteristic behavior of natural accelerograms [12,13]. Other

approaches include using a real record as a seed [14,15]. For example, the method proposed by Cacciola [15] produces fully non-stationary accelerograms as the superposition of two waveforms: a fully non-stationary counterpart modeled by a real accelerogram and a stationary process that is used to achieve spectrum compatibility.

Seismic response assessment through the NRHA requires the use of suites of hazard-consistent acceleration time-histories. Depending on the performance assessment type, hazard consistency may be achieved by matching the records either to a uniform hazard spectrum (UHS) which is typically a code spectrum [4], to a conditional mean spectrum (CMS) [16], or to a spectrum obtained from a ground motion model (GMM) ]. NIST [18] mentions three types of performance assessment: intensity-based, scenario-based, and risk-based. More specifically, intensity-based assessment focuses on the seismic response of a structure for a specified ground motion intensity, which is typically defined as a 5% damped elastic spectral acceleration spectrum (e.g. a code spectrum). Scenario-based assessments compute the structural responses to user-specified seismic events that are defined by the earthquake magnitude and the distance of the source from the site of interest. The typical products of a scenario-based assessment are the average response of a structural parameter and the corresponding variability. Finally, risk-based assessments provide information on the response of a structure over a user-specified time period, involving multiple intensity-based assessments for the ground motion levels of interest.

Based on the objectives of the seismic performance assessment, there are cases where the input ground motions may match only a target mean response spectrum, while in other cases the variability of the response spectra should also be incorporated [18]. For example, in order to predict stable mean responses of structural parameters for a given intensity of shaking, matching ground motions to a target spectrum may be a suitable approach that enhances the confidence in the predictions of the mean structural responses for a given number of input ground motions. However, in applications where the prediction of both the mean value and variability of a structural parameter is required (e.g. estimation of collapse probabilities), the ground motions should be matched to a target spectral mean and the respective spectral variability.

Jayaram et al. [2] in their paper proposed a new algorithm for selecting ground motions that match a target response spectrum mean and variance. Moreover, they applied their proposed methodology to conduct NRHAs on single-degree-of-freedom (SDOF) and multi-degree-of-freedom (MDOF) systems in order to assess the influence of the consideration of the response spectrum variance on the structural response. They concluded that using ground motion suites that also match the target response spectrum variance increases the dispersion of the obtained structural responses. This dispersion, as observed in their analyses, impacts the distribution of structural responses, damage states, loss estimations, and the probability of structural collapse.

The paper studies the application of suites of fully non-stationary artificial accelerograms that have a target spectral mean and variability in order to achieve hazard consistency [12,19–21] on structural performance assessment. The model that is used first produces an ensemble of target spectra with a given mean and variability and then a methodology based on spectral representation method is used to generate the corresponding fully non-stationary ground motions. The stochastic methodology is briefly

presented first, and it is followed by a numerical application where the NRHA of a benchmark multi-degree-of-freedom (MDOF) structure is carried out. The seismic hazard is quantified with a GMM, and the impact of the spectrum variability matching on the structural response is assessed.

## 2 Generation of Artificial Accelerograms

A practical and computationally efficient methodology for the stochastic generation of suites of fully non-stationary artificial accelerograms that are compatible with a target spectral mean and a target variability [12,19–21] is employed. The artificial ground motion time histories are simulated as stochastic processes using existing spectrum-based models [15]. The seismic hazard is defined by a target spectrum or a GMM. Therefore, given the seismic scenario ($M$, $R$) and the soil conditions, the target spectral mean and variability for each period are obtained. Based on those data, multiple target response spectra are generated as a random vector that follows the normal distribution. Artificial accelerograms whose response spectra individually match the produced spectra are subsequently generated. The basis for generating spectrum-compatible accelerograms relies on the relationship between the values of the power spectral density (PSD) function of the ground motion and the response spectral values for a given damping ratio [10,21]. Corrective iterations in the frequency domain are performed in order to achieve enhanced matching for controlling the variability. The methodology provides with suites of fully nonstationary artificial ground motion time histories that are compatible with a target spectral mean and a target variability, which then can be used to conduct NRHAs in structures.

### 2.1 Target spectra generation

The proposed methodology first produces a suite of target spectra $S_a^{*,j}(T_i,\zeta)$ that have a target spectral mean $S_a^*(T_i,\zeta)$ and variability $\beta^*(T_i,\zeta)$, where $\zeta$ is the target spectrum's damping ratio. In the case where a GMM is used for the analysis, the method relies on the empirically verified observation that the logarithmic spectral accelerations follow the normal distribution, characterized by a mean value and standard deviation [12,20]. Therefore, the target logarithmic spectral accelerations $\ln[S_a^{*,j}(T_i,\zeta)]$ at each period $T_i$ can be modeled as a normally distributed (Gaussian) random variable with mean $\ln[S_a^*(T_i,\zeta)]$ and standard deviation $\sigma^*_{\ln(S_a)}(T_i,\zeta)$:

$$\ln[S_a^{*,j}(T_i,\zeta)] = \ln[S_a^*(T_i,\zeta)] + a_j\sigma^*_{\ln(S_a)}(T_i,\zeta) \quad (1)$$

where $1 \le j \le n$, $n$ is the total number of the generated accelerograms in a suite, $a_j$ is a standard Gaussian random variable with mean value $\mu_\alpha = 0$ and standard deviation $\sigma_\alpha = 1$, and $T_i$ are period values of the response spectrum. The target mean in Eq. 1 is obtained from the GMM at the desired period range. The variability around the target spectrum is defined as the standard deviation of the natural logarithms of the spectral values given from the GMM, thus $\beta^*(T_i,\zeta) = \sigma^*_{\ln(S_a)}(T_i,\zeta)$. It is noted that Eq. 1 considers that the correlation $\rho(T_i,T_j)$ between the spectral accelerations at different

periods is equal to 1, thus assuming a perfect direct correlation. Based on Eq. 1, for a suite containing $n$ accelerograms, each individual target response spectrum $S_a^{*,j}(T_i,\zeta)$, can be produced as:

$$S_a^{*,j}(T_i,\zeta) = S_a^*(T_i,\zeta)\exp\left[a_j\beta^*(T_i,\zeta)\right] \tag{2}$$

In the case of a smooth code spectrum [26], each of the suite's accelerograms is generated compatible with a specific target response spectrum $S_a^{*,j}(T_i,\zeta)$ that is defined as:

$$S_a^{*,j}(T_i,\zeta) = S_a^*(T_i,\zeta) + a_j\,\sigma_{S_a}^*(T_i,\zeta) \tag{3}$$

In this case, the variability around the target spectrum is defined as the coefficient of variation (CoV) for each period:

$$\beta^*(T_i,\zeta) = CoV = \frac{\sigma_{S_a}^*(T_i,\zeta)}{S_a^*(T_i,\zeta)} \tag{4}$$

Next, $\sigma_{S_a}^*(T_i,\zeta)$ is calculated as $\sigma_{S_a}^*(T_i,\zeta) = \beta^*(T_i,\zeta)S_a^*(T_i,\zeta)$, and Eq. (3) becomes:

$$S_a^{*,j}(T_i,\zeta) = S_a^*(T_i,\zeta)\left[1 + a_j\beta^*(T_i,\zeta)\right] > 0 \tag{5}$$

In order to ensure that the target spectrum $S_a^{*,j}(T_i,\zeta)$ will take no negative values, the value of $\left[1 + a_j\beta^*(T_i,\zeta)\right]$ must be greater than zero. This results in the following limit for the values of $a_j$:

$$a_j > -\frac{1}{\beta^*(T_i,\zeta)} \tag{6}$$

### 2.2 Generation of the Artificial Accelerograms

The target spectrum compatible artificial accelerograms can be modeled using existing real earthquake ground motions as seed records. In this study, the Cacciola 2010 [15] method was employed, which generates fully non-stationary, spectrum compatible accelerograms by superimposing a seed record $a_R(t)$ and a corrective term which is a quasi-stationary zero-mean Gaussian stochastic process, defined with the spectral representation method [16]:

$$a_g(t) \;=\; a_{sc}a_R(t) + \varphi(t)\sum_{i=1}^{N} A_i(\omega)\cos(\omega_i t + \theta_i) \tag{7}$$

In the first part of Eq. 7 $a_R(t)$ is a recorded accelerogram used as a seed and $a_{sc}$ is a scaling coefficient associating the target spectral acceleration $S_a^*(\omega_i,\zeta)$ with the recorded accelerogram's spectral acceleration $S_a^R(\omega_i,\zeta)$:

$$a_{sc} = min\left[\frac{S_a^*(\omega_i,\zeta)}{S_a^R(\omega_i,\zeta)}\right] \tag{8}$$

Moreover, if $a_{sc} > 1$, then $a_{sc}$ =1 is assumed instead [15]. In the second part of Eq. 7, $\varphi(t)$ is the time-modulating function, $N$ is the number of harmonics to be superimposed, $\omega_i$ is the angular frequency of the i[th] harmonic, $\theta_i$ are random phase angles uniformly distributed over the interval [0, 2π], and $A_i(\omega)$ are the amplitudes, related to the one-sided PSD function of the stochastic process $G(\omega_i)$ at each frequency $\omega_i$ as:

$$A_i(\omega) = \sqrt{2G(\omega_i)\Delta\omega} \tag{9}$$

where $\Delta\omega$ is the constant integration step. Spectrum compatibility is achieved by the computation of the one-sided PSD function $G(\omega_i)$ [15]:

$$G(\omega_i) = \begin{cases} \dfrac{4\zeta}{\omega_i\pi - 4\zeta\omega_{i-1}} U\left[\dfrac{S_a^{*2}(\omega_i,\zeta) - \left(a_{sc}S_a^R(\omega_i,\zeta)\right)^2)}{\eta_{X_i}^2(\omega_i,\zeta)} - \Delta\omega\sum_{k=1}^{i-1} G(\omega_k)\right] \times \\ \quad \times\left[\dfrac{S_a^2(\omega_i,\zeta) - \left(a_{sc}S_a^R(\omega_i,\zeta)\right)^2)}{\eta_{X_i}^2(\omega_i,\zeta)} - \Delta\omega\sum_{k=1}^{i-1} G(\omega_k)\right], & \omega_o \le \omega_i \le \omega_u \\ 0, & 0 \le \omega_i < \omega_o \end{cases}$$

where $U(\cdot)$ is the unit step function that is used to avoid negative solutions, $\omega_u$ is an upper cut-off frequency, $\omega_o$ = 0.36 rad/s is the lowest frequency bound for $\eta_{X_i}$ to exist [21], and $\eta_{X_i}$ is the peak factor, which can be approximated with reference to a white noise input [21] as:

$$\eta_{X_i}(\omega_i,\zeta) = \sqrt{2\ln\left\{\frac{T_s}{\pi}\omega_i\left(-\ln\frac{1}{2}\right)^{-1}\left[1 - \exp\left(-\delta_{X_i}^{1.2}\sqrt{\pi\ln\left(\frac{T_s}{\pi}\omega_i\left(-ln\frac{1}{2}\right)^{-1}\right)}\right)\right]\right\}} \tag{11}$$

where $T_s$ is the duration of the stationary accelerogram, the mean zero crossing rate $N_{X_i}$ is included in the equation, and the spread factor $\delta_{X_i}$ is approximated as:

$$\delta_{X_i} = \sqrt{1 - \frac{1}{1-\zeta^2}\left[1 - \frac{2}{\pi}\arctan\left(\frac{\zeta}{\sqrt{1-\zeta^2}}\right)\right]^2} \tag{12}$$

Finally, regarding $\varphi(t)$, the time modulating function proposed by Jennings *et al.* [22] has been adopted:

$$\varphi(t) = \begin{cases} \left(\dfrac{t}{t_1}\right)^2, & t < t_1 \\ 1, & t_1 \le t \le t_2 \\ \exp\left[-\dfrac{3}{t_f - t_2}(t - t_2)\right], & t > t_2 \end{cases} \tag{13}$$

where $t_f$ is the total duration of the accelerogram. The time points $t_1$ and $t_2$ define the strong motion duration of the generated record and they can be obtained from the

Husid function ($H(t)$) of a real recorded accelerogram (Fig. 1) as $H(t_1)$ = 5% and $H(t_2)$ = 95% respectively (Fig. 2(a)). Alternatively, default values can be used instead [27]. In this frame, $T_s$ is the duration of the strong motion, calculated as $T_s = t_2 - t_1$. Note that $T_s$ signifies the constant amplitude region on the envelope function $\varphi(t)$ (Fig. 2(b)).

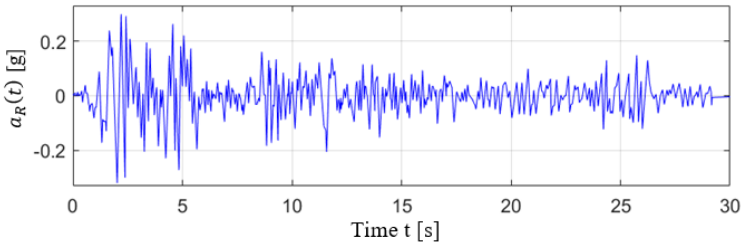


**Fig. 1.** A seed record accelerogram: El Centro earthquake (Imperial Valley, 1940, N-S component). The total duration of the accelerogram is $t_f = 30\ s$ and the strong motion duration is $T_s = t_2 - t_1$= 25.48s – 1.64 s = 23.84 s

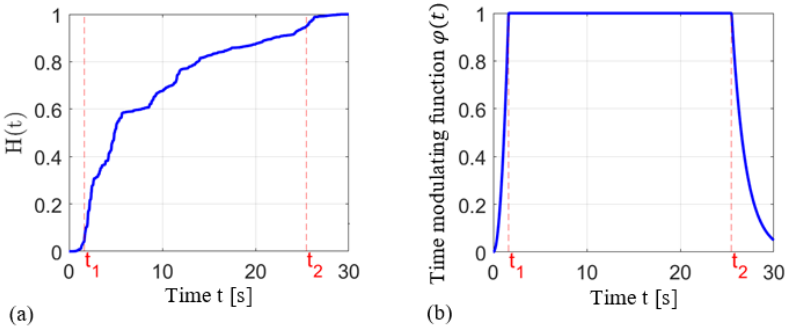


**Fig. 2.** (a) Husid plot of the El Centro recorded accelerogram of Fig.1, (b) the time modulating function of Eq. 13 obtained from the Husid plot of Fig. 2(a).

## 2.3 Record Correction

Artificial accelerogram generation methods usually require corrective iterations in the frequency domain in order to achieve good matching between the generated accelerogram's spectrum and the target spectrum. The most common corrective iteration method applied in the literature [e.g. in 15] utilizes the PSD function:

$$G(\omega_i)^{(k+1)} = G(\omega_i)^{(k)} \left[ \frac{S_a^*(\omega_i, \zeta)}{S_a^{(k)}(\omega_i, \zeta)} \right]^2 \tag{14}$$

where $S_a^{(k)}(\omega_i, \zeta)$ is the generated accelerograms' mean response spectrum determined at the k$^{th}$ iteration. In the proposed model, however, in order to control the variability of the analysis, the corrective iterations are applied in each of the generated

accelerograms spectrum $S_a^j(\omega_i, \zeta)$ individually, with their respective target spectrum $S_a^{*,j}(\omega_i, \zeta)$. Moreover, it is essential that the spectrum matching should be perfect, as it was observed that insufficient matching would result in significant differences between the target and the analysis variability. Corrective iterations with the aforementioned requirements and the use of the PSD function were proved to not be sufficient enough to control the variability of the analysis. Therefore, as corrective iterations are conducted in the frequency domain, the Fourier Transform (FT) was employed. For each frequency, the accelerogram's Fourier Transform (FT) is modified by the quotient of $S_a^{*,j}(\omega_i, \zeta)$ and $S_a^j(\omega_i, \zeta)$, as follows [23]:

$$FT_{a_g(t)}^{(k+1)}(\omega_i) = FT_{a_g(t)}^{(k)}(\omega_i)\left[\frac{S_a^{*,j}(\omega_i, \zeta)}{S_a^j(\omega_i, \zeta)}\right] \tag{15}$$

where $FT_{a_g(t)}^{(k)}(\omega_i)$ is the Fourier Transform of the generated accelerogram at the k[th] iteration. Then, by applying the inverse Fourier Transform, a new time-history $a_g^{(k+1)}(t)$ is determined, along with its response spectrum $S_a^{j,(k+1)}(\omega_i, \zeta)$. The iteration scheme provided by Eq. 15 modifies the spectral amplitude characteristics of the generated accelerogram. Fig. 3 shows an example of the difference in the Fourier amplitude of an accelerogram simulated with the seed record approach before the corrective iterations (i.e. as generated) and after.

Finally, each of the generated accelerograms requires baseline correction in order to yield realistic velocity and displacement time-histories. In this study, a simple cubic polynomial curve is used for baseline correcting the generated ground motions.

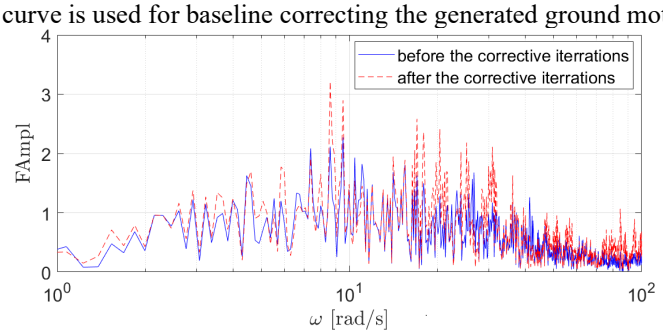


**Fig. 3.** Comparison of the Fourier amplitude of a simulated accelerogram before and after the corrective iterations for spectrum compatibility

# 3 Seismic Performance Assessment to Artificial Ground Motions Records

## 3.1 Case Study Considered

The aim of this paper is to present a practical application of the methodology proposed in [12,19–21], through the NRHA of a benchmark multi-degree-of-freedom

(MDOF) structure. Two cases are considered where: i) the generated suite of ground motions matches only a mean target spectrum, and ii) the generated suite of ground motions matches both a mean target spectrum and target variability. The seismic hazard is quantified with a GMM which provides the median target spectrum and the logarithmic standard deviations. The GMM employed in this study is the BSSA 14 [17]. The seismic scenario considered is of moment magnitude $M_w$ = 6.5, Joyner-Boore distance $R_{JB}$ = 10 km, and ε = 1. The shear wave velocity averaged over the top 30 m $V_{S30}$ is set equal to 360 m/s, the damping ratio is ζ = 5%, the fault type is normal, and the basin depth is set unknown. The case study frame is an eight-storey steel moment-resisting frame with the properties shown in Fig. 4(a).

The frame and the analysis are implemented with OpenSees v3.5.0. The gravity loads (q=40 kN/m) and the respective masses are concentrated at the nodes. The members are modeled as force-based, beam-column fiber elements with four integration sections for the NRHA and the material is a uniaxial bilinear steel material object with kinematic hardening. No geometric non-linearities are incorporated. After performing modal analysis with elastic beam-column elements, the fundamental period was found equal to $T_1$ = 3.59 s with mass modal participation of the first mode equal to 82% of the total mass. Thus, the frame is dominated by the first mode (Fig. 4(b)), however the second mode also contributes to the response with $T_2$ = 1.17 s and mass modal participation equal to 10% (82% + 10% = 92% > 90% as defined by the Eurocode 8 [4]). Rayleigh damping is used with Rayleigh damping coefficients $\alpha_0$ = 0.13 and $\alpha_1$ = 0.014.

For each case, seven accelerograms are generated in order to conduct NRHAs on the eight-storey steel moment-resisting frame. The investigated response parameters are the maximum interstorey drift ratios (MIDR) in terms of median and dispersion ($16^{th}$ and $85^{th}$ percentile values). The chosen number of generated accelerograms is consistent with seismic code provisions, which require at least seven NRHAs in order to characterize statistically the seismic input and structural seismic response.

The seed record method [15] is applied to generate the artificial non-stationary accelerograms, following Eqs. 7–13. The frequency range is $\omega_0$=1 rad/s, $\omega_u$=100 rad/s, $N$ = 1000, and $\Delta\omega$ = 0.10 rad/s. In this example, the seed record selected is the 24/2/1981 Gulf of Corinth earthquake (Corinth Greece, 24/2/1981, Corinth, T component, Fig. 5) from the Pacific Earthquake Engineering Centre (PEER) [24], as it belongs to a compatible scenario of $M_w$ = 6.6, $R_{JB}$ = 10.27 km, $V_{S30}$ = 361.40 m/s, and normal oblique fault type. The total duration of the accelerogram is $t_f$ = 40.93 s and the strong motion duration is $T_s = t_2 - t_1$ = 17.72 s – 3.78 s = 13.94 s. Finally, corrective iterations are performed following Eq. 15 and baseline correction is applied.

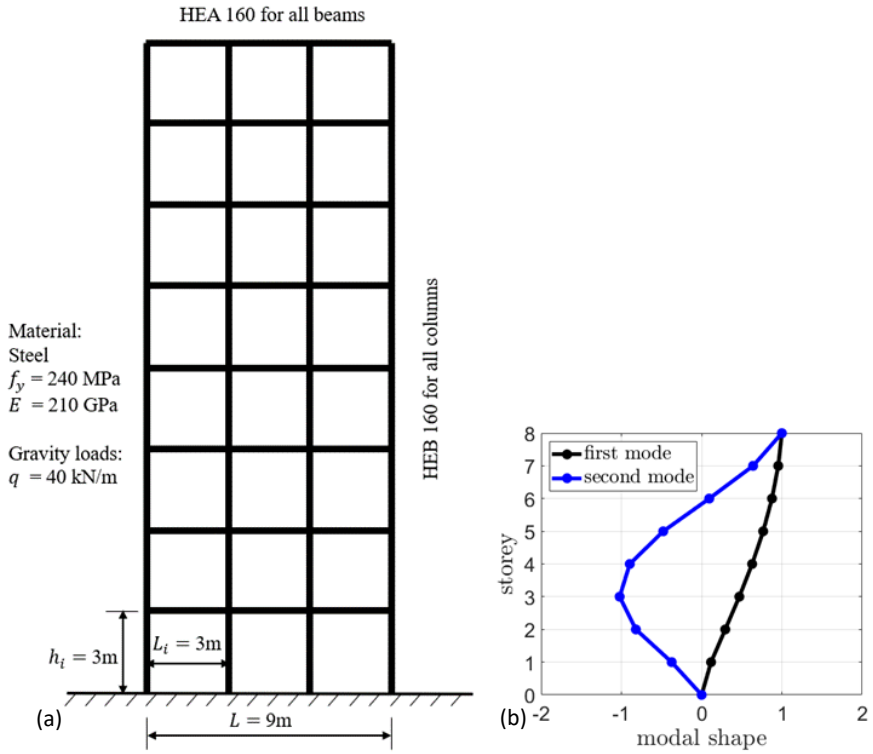


**Fig. 4.** (a) The benchmark structure: the eight-story steel frame of the second numerical application, used for the NRHAs, (b) The first and second mode of the benchmark eight-storey steel moment-resisting frame

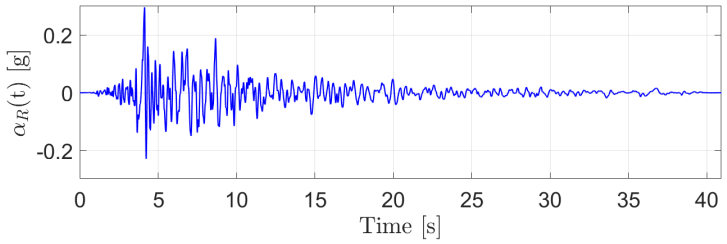


**Fig. 5**. The seed record accelerogram of the second numerical application: Corinth Greece, 24/2/1981, Corinth, T component

### 3.2 Case 1: NRHAs using a generated suite of ground motions that matches only a mean target spectrum

A suite of seven fully non-stationary accelerograms is generated using Eqs. 1–2 for the target median spectrum $S_a^*(T_i, \zeta)$ obtained from the GMM and the variability is set equal to $\beta^*(T_i, \zeta) = 0$. The median response spectrum of the produced accelerograms

is shown in Fig. 6 along with the target $S_a^*(T_i, \zeta)$. The comparisons are made in median values, considering the mathematical property that the median of data that follow a lognormal distribution is approximately equal to the mean of the logarithms.

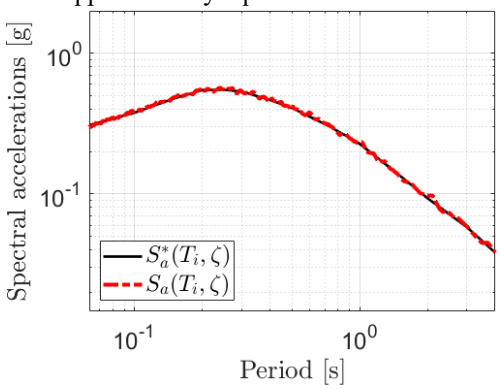


**Fig. 6.** The produced target response spectra $S_a^{*,j}(T_i, \zeta)$ of the second numerical application following Eqs. 1–2, for the generation of 7 accelerograms

The produced accelerograms are used for the NRHAs of the benchmark eight-storey steel moment-resisting frame and the median and dispersion values of the MIDRs are obtained and plotted in Fig. 7.

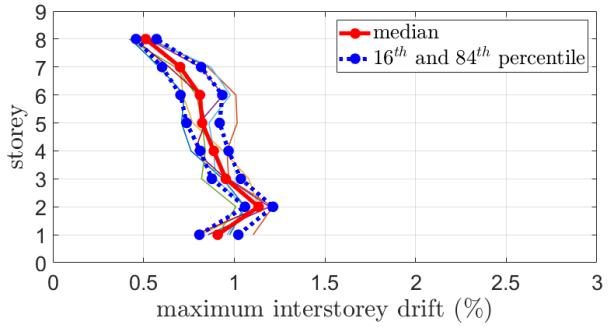


**Fig. 7.** The MIDRs of the eight-storey steel moment-resisting frame using a generated suite of ground motions that matches only the mean target spectrum

### 3.3 Case 2: NRHAs using a generated suite of ground motions that matches both a target mean spectrum and variability

A suite of seven fully non-stationary accelerograms is generated, and the target mean $S_a^*(T_i, \zeta)$ and variability $\beta^*(T_i, \zeta) = \sigma^*_{\ln(S_a)}(T_i, \zeta)$ of the suite are obtained from the GMM. The produced spectra $S_a^{*,j}(T_i, \zeta)$ are obtained following Eqs. 1–2 and they are shown in Fig. 8 along with the target $S_a^*(T_i, \zeta)$ that is obtained from the aforementioned GMM. Note that the assumed perfect direct correlation results in equally distanced values of a produced spectrum $S_a^{*,j}(T_i, \zeta)$ from the target $S_a^*(T_i, \zeta)$.

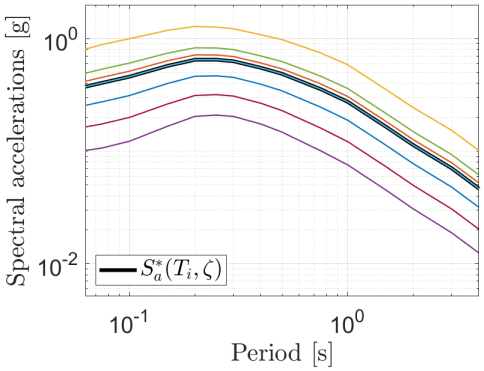


**Fig. 8.** The produced target response spectra $S_a^{*,j}(T_i,\zeta)$ of the second numerical application following Eqs. 1–2, for the generation of seven accelerograms

The comparison between the target spectrum $S_a^*(T_i,\zeta)$ and the median response spectrum $S_a(T_i,\zeta)$ of the generated accelerograms is shown in Fig. 9(a). Furthermore, Fig. 9(b) shows the matching of the analysis variability $\beta(T_i,\zeta) = \sigma_{\ln(S_a)}(T_i,\zeta)$ achieved with the proposed model (standard deviation of the natural logarithms) to the target $\beta^*(T_i,\zeta) = \sigma^*_{\ln(S_a)}(T_i,\zeta)$. As it can be observed, for both the spectral mean and variance, the simulated values are remarkably close to the set targets, thus proving the efficiency of the proposed algorithm.

The produced accelerograms are then used for the NRHAs of the case study frame and the median and 16$^{th}$ and 85$^{th}$ percentile values of the MIDRs are obtained and plotted in Fig. 11.

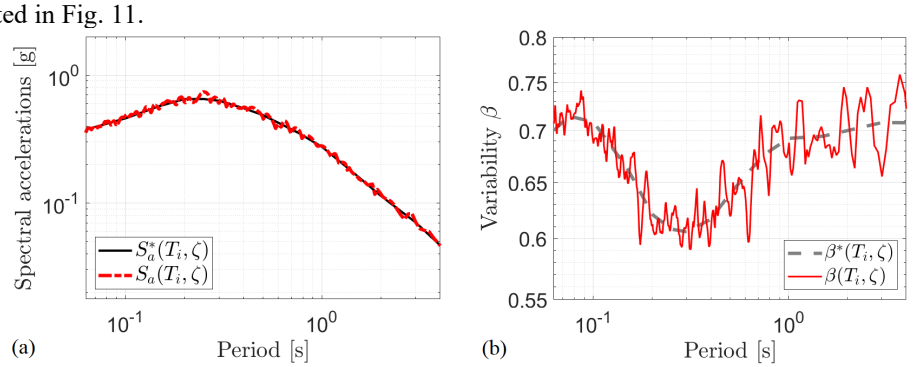


**Fig. 9.** (a) Comparison of the generated accelerograms' median response spectrum $S_a(T_i,\zeta)$ matching to the target median spectrum $S_a^*(T_i,\zeta)$ of the second numerical application, (b) comparison of the analysis variability $\beta(T_i,\zeta) = \sigma_{\ln(S_a)}(T_i,\zeta)$ with the target $\beta^*(T_i,\zeta) = \sigma^*_{\ln(S_a)}(T_i,\zeta)$

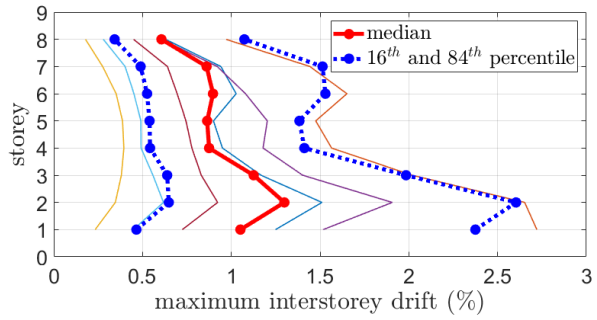


**Fig. 11.** The MIDRs of the eight-storey steel moment-resisting frame estimated through NRHAs using a generated suite of ground motions that matches both a target mean spectrum and variability

### 3.4 Result Comparison

Table 1 summarizes the MIDR estimates of the two cases in terms of median and 16$^{th}$ and 85$^{th}$ percentile values. It is observed that the median values are close for both cases, whereas the dispersion values differ significantly. Specifically, in the case where the variability of the target spectrum is incorporated in the generation of the ground motion suite, the dispersion of the MIDRs is larger, as expected. These results are compatible with the similar observations of Jayaram et al. [2] for their record selection algorithm, which state that when the response spectrum variability is considered in the ground motion selection procedure, the median structural response is not significantly affected, whereas the dispersion in the response tends to increase. These results prove that the proposed methodology produces realistic results for NRHAs and complete the testing of the efficiency of the proposed methodology for practical applications.

**Table 1.** MIDR estimates of the case study frame. The Case 1 results correspond to the suite of ground motions who match only the target spectral mean, whereas the Case 2 results correspond to the suite of ground motions who match both the target spectral mean and variability

| Storey | Median MIDR % | | | Dispersion of MIDR % | | |
|---|---|---|---|---|---|---|
| | Case 1 | Case 2 | error % | Case 1 | Case 2 | error % |
| 1 | 0.91 | 1.05 | 15.7 | 11.79 | 81.49 | 590.95 |
| 2 | 1.13 | 1.30 | 14.5 | 6.82 | 69.54 | 919.09 |
| 3 | 0.95 | 1.13 | 18.0 | 8.36 | 56.68 | 577.70 |
| 4 | 0.89 | 0.87 | -1.4 | 8.79 | 47.83 | 444.28 |
| 5 | 0.82 | 0.86 | 4.9 | 11.04 | 47.10 | 326.41 |
| 6 | 0.81 | 0.90 | 10.6 | 14.18 | 53.42 | 276.74 |
| 7 | 0.70 | 0.86 | 22.6 | 15.26 | 56.48 | 270.06 |
| 8 | 0.51 | 0.61 | 18.5 | 10.99 | 57.10 | 419.79 |

## 4 Conclusions and Discussion

The efficiency of a novel stochastic methodology for the generation of suites of fully non-stationary artificial accelerograms that are compatible both with a target mean spectrum and a target variability has been tested through the NRHAs of a benchmark frame. Hazard consistency has been defined by obtaining the target spectral mean and variability from a GMM and the ground motions have been generated using widely known spectral representation techniques. This paper assumes that the correlations between spectral acceleration values at multiple periods are equal to 1. It should be noted that Eq. 1 in [12] is extended to a more general case, where the CMS can also be employed in the analyses and the correlations will also be possible to be included in the spectra simulation process.

The methodology has been tested in order to ensure that the produced suites of ground motions provide realistic NRHA estimates. The results of the NRHAs of an eight-storey steel moment-resisting frame which was subjected to two cases of ground motion suites were compared. One suite of ground motions matched only a mean target spectrum, whereas the other suite of ground motions matched both a mean target spectrum and target variability. The results showed that in the latter case, the median structural response is not significantly affected, whereas the dispersion in the response tends to increase.

A point worth noting is that the present work simplifies the methodology proposed in [12] and uses accelerograms with a fixed power spectrum and modulating function values. This results in suites of artificial accelerograms that have very similar time-frequency features, however, this simplification has been adopted in order to focus on the influence of the target spectrum variability on the structural estimates without having additional uncertainties added.

In conclusion, the obtained results of this study were compatible with similar observations from relative ground motion selection algorithms in the literature. Thus, the proposed methodology produces realistic results for NRHAs and is efficient for practical applications.

## 5 Acknowledgements

The authors gratefully acknowledge the support by the Hellenic Foundation for Research and Innovation (Grant No. 1261).

## References

1. Dávalos, H., Miranda, E.: Evaluation of bias on the probability of collapse from amplitude scaling using spectral-shape-matched records. Earthquake Engineering & Structural Dynamics 48(8), 970–986 (2019). https://doi.org/10.1002/eqe.3172
2. Jayaram, N., Lin, T., Baker, J.: A Computationally efficient ground-motion selection algorithm for matching a target response spectrum mean and variance. Earthquake Spectra 27(3), 797–815 (2011). https://doi.org/10.1193/1.3608002

3. Georgioudakis, M., Fragiadakis, M.: Selection and Scaling of Ground Motions Using Multicriteria Optimization. American Society of Civil Engineers (ASCE) 146(11), 04020241 (2020). https://doi.org/10.1061/(ASCE)ST.1943-541X.0002811
4. Comité Européen de Normalisation (CEN): EN 1998-1-1 (Eurocode 8): Design of structures for earthquake resistance, part 1: general rules, seismic actions and rules for buildings, Brussel, (2004)
5. Song, C., Kawai, R.: Monte Carlo and variance reduction methods for structural reliability analysis: A comprehensive review. Probabilistic Engineering Mechanics 73, 103479 (2023). https://doi.org/10.1016/j.probengmech.2023.103479
6. Mitseas, I.P., Beer. M.: Fragility analysis of nonproportionally damped inelastic MDOF structural systems exposed to stochastic seismic excitation. Computers and Structures 226, 106129 (2020). https://doi.org/10.1016/j.compstruc.2019.106129
7. Mitseas, I.P., Beer, M.: First-excursion stochastic incremental dynamics methodology for hysteretic structural systems subject to seismic excitation. Computers and Structures 242 (2021). https://doi.org/10.1016/j.compstruc.2020.106359
8. Psycharis, I.N., Fragiadakis, M., Stefanou, I.: Seismic reliability assessment of classical columns subjected to near-fault ground motions. Earthquake Engineering & Structural Dynamics 42(14), 2061–2079 (2013)
9. Shinozuka, M., Deodatis, G.: Simulation of Stochastic Processes by Spectral Representation. Applied Mechanics Reviews 44(4), 191–204, (1991). https://doi.org/10.1115/1.3119501
10. Vanmarcke, E.H., Gasparini, D.A.: Simulated earthquake ground motions. In: Proceedings of the 4th international conference on structural mechanics in reactor technology, K1/9, San Francisco, CA, USA, (1977)
11. Spanos, P., Vargas Loli L.M.: A statistical approach to generation of design spectrum compatible earthquake time histories. International Journal of Soil Dynamics and Earthquake Engineering 4(1), 2–8 (1985). https://doi.org/10.1016/0261-7277(85)90029-4
12. Yanni, H., Fragiadakis, M., Mitseas, I.P.: Probabilistic method for the generation of hazard-consistent suites of fully non-stationary seismic records. Earthquake Engineering & Structural Dynamics 53(10), 3140–3164 (2024). https://doi.org/10.1002/eqe.4153
13. Preumont A.: The generation of non-separable artificial earthquake accelerograms for the design of nuclear power plants. Nuclear Engineering and Design 88(1), 59–67 (1985). https://doi.org/10.1016/0029-5493(85)90045-7
14. Yanni, H., Fragiadakis, M., Mitseas, I.P.: Stochastic generation of artificial accelerograms using the continuous wavelet transform method. In: Proceedings of the 9th International Conference on Computational Methods in Structural Dynamics and Earthquake Engineering (COMPDYN 2023), June 12-14, Athens, Greece (2023)
15. Cacciola, P.: A stochastic approach for generating spectrum compatible fully nonstationary earthquakes. Computers & Structures 88(15–16), 889–901 (2010)
16. Baker, J.: Conditional Mean Spectrum: Tool for Ground-Motion Selection. Journal of Structural Engineering 137(3), 322–331 (2011). https://doi.org/10.1061/(ASCE)ST.1943-541X.0000215
17. Boore, D.M., Stewart, J.P., Seyhan, E., Atkinson, G.M.: NGA-West2 Equations for Predicting PGA, PGV, and 5% Damped PSA for Shallow Crustal Earthquakes. Earthquake Spectra 30(3), 1057–1085 (2014). https://doi.org/10.1193/070113EQS184M
18. National Institute of Standards and Technology (NIST): Selecting and scaling earthquake ground motions for performing response history analyses. Rep. No. NIST GCR 11-917-15. East Lansing, MI: NEHRP Consultants Joint Venture, (2011)

19. Yanni, H., Fragiadakis, M., Mitseas, I.P.: A novel method for the stochastic generation of artificial accelerograms. In: Proceedings of the 5th Panhellenic Conference on Earthquake Engineering and Engineering Seismology. Hellenic Association for Earthquake Engineering. October 20-22, Athens, Greece (2022)
20. Yanni, H., Fragiadakis, M., Mitseas, I.P.: A novel stochastic methodology for the generation of artificial seismic accelerograms. In: Proceedings of the XII International Conference on Structural Dynamics (EURODYN 2023), European Association for Structural Dynamics. June 02-05, Delft, The Netherlands (2023)
21. Cacciola, P., Colajanni, P., Muscolino, G.: Combination of Modal Responses Consistent with Seismic Input Representation. Journal of Structural Engineering 130(1), 47–55 (2004). https://doi.org/10.1061/(ASCE)0733-9445(2004)130:1(47)
22. Jennings, P.C., Housner, G.W., Tsai, C.: Simulated earthquake motions for design purpose In: Proceedings of the 4th World Conference Earth. Eng., Santiago, Vol. A-1, pp. 145–60; (1969)
23. Ferreira, F., Moutinho, C., Cunha, Á., Caetano, E.: An artificial accelerogram generator code written in Matlab. Engineering Reports 2(3), 92020). https://doi.org/10.1002/eng2.12129
24. PEER (Pacific Earthquake Engineering Research Center). Shallow crustal earthquakes in active tectonic regimes. https://ngawest2.berkeley.edu/site
25. MathWorks. MATLAB version 2021a [Computer Program]. https://www.mathworks.com/products/matlab.html

# Assessment of the seismic capacity of existing RC buildings short columns or soft storey, in accordance with the Second-Degree Pre-earthquake Inspection

Maria D. Panagopoulou[0009-0002-2522-6375], Lamprini D. Zochiou[0009-0006-7182-5837] and Stephanos E. Dritsos

[1]University of Patras, Department of Civil Engineering, Aristotelous 26500, Rio, Greece
mariapanag.1859@gmail.com

**Abstract.** The seismic capacity assessment of two three-storey reinforced concrete buildings constructed prior to 1984 is being conducted in this paper. Specifically, the case of short columns or soft storey on the ground floor is investigated and a comparison is made regarding the seismic response obtained for each case. The approximate method of the Second-degree pre-earthquake inspection is applied for the case of known and unknown reinforcement amounts. The obtained results are then compared to results obtained from non-linear static analysis. The primary criterion for the comparison is the failure index of the buildings, as derived from each method. The buildings are categorized into seismic categories according to the Second-degree pre-earthquake inspection. These are compared with the seismic classifications determined by *KANEPE*. The results of the failure indices and seismic categories according to the Second-degree pre-earthquake inspection were in good agreement with the corresponding results of failure indices in terms of acceleration and the seismic classifications according to *KANEPE* obtained when the non-linear static analysis is applied. This agreement is particularly pronounced when known amounts of reinforcement are considered for the vertical elements. Furthermore, the seismic vulnerability of buildings with soft storey or short columns was confirmed in both methods in a similar manner.

**Keywords:** Reinforced concrete, Non-linear static analysis, Pushover analysis, Second-degree pre-earthquake inspection, Building assessment, soft storey, short columns, failure index

## 1 Introduction

The Second-degree pre-earthquake inspection [1-2] for reinforced concrete buildings (RC) employs a failure index $\lambda$ as the main criterion for building classification. This failure index is derived from an approximate method based on seismic demand, as defined in current assessment provisions. The methodology involves several approximate estimates without the need of using a detailed analysis model. The method focuses on the strength of the vertical elements of the structure and can be applied, albeit with reduced reliability, even when there is insufficient information about the amount of

reinforcement and detailing. In this paper the revised version (2022) of the methodology is applied, whereas results from the application of the method based on the pre-existing version (2018) of [2] are presented in [6].

The capability of rapidly estimating the structural capacity of a building under seismic loads using approximate assessment methods, according to the current design and assessment provisions (Eurocodes, *KANEPE* [3], *KADET* [4]), poses a challenge. Therefore, the critical question, concerns the reliability level of the results obtained from this method. In the study of Zochiou et al. [5], a preliminary answer is attempted within the framework of investigating a group of RC buildings. In [5] the main objective of the study was to assess the influence of masonry infill walls and the absence of data regarding the reinforcement of the columns.

In this study, the investigation focuses on the influence of the presence of short columns or a soft storey (pilotis), and for comparison purposes, the building types remain the same as in the first study [5]. In both studies, the reliability check of the results of the approximate Second-degree pre-earthquake inspection method is conducted based on comparison with the results of a non-linear static analysis (pushover analysis). The comparison is made according to the recent revision of the Second-degree pre-earthquake inspection (2022) [1]. Specifically, in this study, the following aspects are investigated:

- The effect of the presence of short columns in the structure.
- The impact of the presence of a soft story (pilotis) on the ground floor of the building.
- The effect of applying the methodology without sufficient information on the reinforcement amounts and details of vertical elements.

It should be noted that in the aforementioned revision of the Second-degree pre-earthquake inspection [1], there were fundamental changes in the way the failure index $\lambda$ is determined compared to the original text [2]. The original text did not consider the contribution of masonry infill walls to the seismic resistance of the building, and the adopted values for the behavior factor $q$ were lower. Thus, in order to assess the impact of the aforementioned changes, the failure indices $\lambda$ are determined based on the original text [2], and the respective results are compared. Similar to [5], two typical RC buildings with different plan view layout are assessed. The assessment is conducted for the "performance level B".

## 2 Description of the case study RC building

Two RC frame buildings have been examined which have been constructed prior to 1984. The first structure (building A) has a rectangular floor-plan. The second structure (building B) has an L-shape floor plan. The corresponding structural drawings are provided in Fig. 1. Both buildings have three storeys, with a floor height of 3.00m and accessible roof. Each building is examined under conditions of short columns or a soft storey on the ground floor, assuming the presence of infill walls. To examine the effect of masonry infill walls on both buildings, different conditions of their participation are considered. More specifically, they are being categorized according to the quality of

their construction detailing and wedging and the existence or not of openings. The cases to be investigated are presented in Tables 1 and 2.

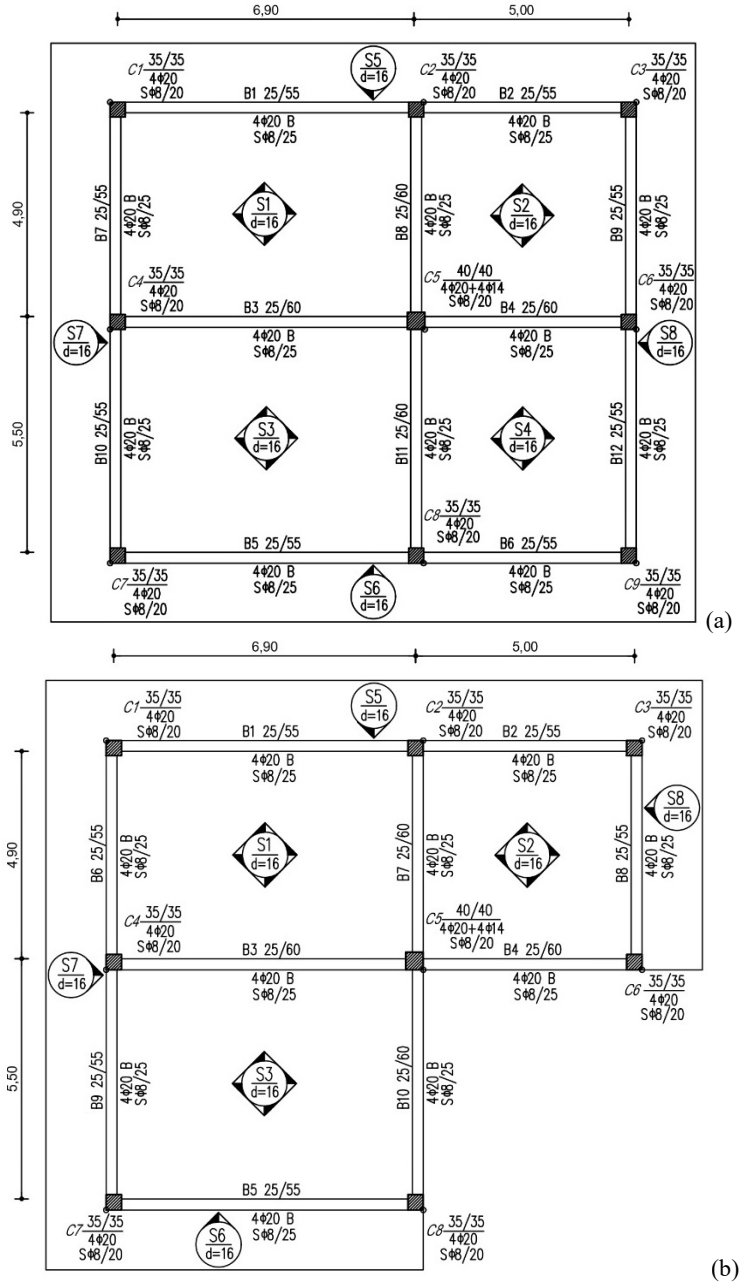


**Fig. 1.** Structural floor-plans of the two buildings: (a) Building A and (b) Building B

**Table 1.** Different cases of structural systems and masonry infill walls contribution

| Building A | Building B | Description of the case study RC Buildings |
|---|---|---|
| $A_n$ | $B_n$ | Reference buildings without considering the contribution of masonry infill walls |
| A | B | Reference buildings considering presence and contribution of masonry infill walls with openings in all levels |
| $A_s$ | $B_s$ | Buildings with short columns at the perimeter of the ground floor at a height of 1.10m considering the contribution of masonry infill walls with openings in the two upper floors |
| $A_p$ | $B_p$ | Buildings with soft storey (pilotis) on the ground floor considering the contribution of masonry infill walls with openings in the two upper floors |

**Table 2.** Different categories of masonry infill walls

| | |
|---|---|
| Inf. Wall.g | Good construction detailing and wedging of masonry infill walls considering the presence of openings |
| Inf. Wall.p | Poor construction detailing and wedging of masonry infill walls considering the presence of openings |

## 2.1 Reinforcement amount and details, Loads and Design Spectrum

The perimeter columns have a cross-section of 35x35cm. The central one has a cross-section of 40x40cm. The perimeter beams have a cross-section of 25/55 with 4Φ16 bottom reinforcement at mid-span, from which 2Φ16 are bent at the supports. The internal beams have a cross-section of 25/60 with 4Φ20 bottom reinforcement at mid-span, from which 2Φ20 are bent at the supports. All beams have 2Φ8 top reinforcement which do not participate in shear resistance at the supports due to their insufficient anchorage length. The perimeter columns are reinforced with 4Φ20 bars at the corners, and the central one with 4Φ20 and 4Φ14 bars (1Φ14 in the middle of each side). The transverse reinforcement is rectangular Φ8/20 for all columns and Φ8/25 for the beams with poor anchorage. The thickness of the slabs is assumed to be 16cm.

The concrete compressive strength was considered with an average value of 18 MPa, and a "quasi" characteristic value was 14 MPa, assuming a "Sufficient" Data Reliability Level (DRL) [3]. The corresponding values for the tensile strength of longitudinal steel reinforcement and ties were considered 460 MPa and 400 MPa respectively.

The dead loads (G) of the structure include the self-weight of the RC elements ($25\ \mathrm{kN/m^3}$), the non-structural screed ($1.3\ \mathrm{kN/m^2}$) and the outer and inner masonry walls ($3.6\ \mathrm{kN/m^2}$ and $2.0\ \mathrm{kN/m^2}$ respectively). The live loads (Q) include the surface loads of all floors and the roof ($2.0\ \mathrm{kN/m^2}$). Axial loads at the base of the ground floor columns were calculated by considering the effective slab areas for each column, dividing the slabs in triangular and trapezoidal subareas, for the $G + 0.3Q$ loading combination.

The seismic loads (E) were calculated in accordance with the EC8 [7] design spectrum, with a ground acceleration equal to $a_g = 0.24g$, (where $g$ denotes the acceleration due to gravity, 9.81 $\mathrm{m/sec^2}$), soil type B (medium dense sand or stiff clay) and seismic zone II. For the Second-degree pre-earthquake inspection, the soil index is taken equal to $S = 1.00$ and the design spectrum is used with behavior factor equal to $q = 2.00$. For the non-linear static analysis (pushover analysis), the elastic spectrum is used and the soil index is considered equal to $S = 1.20$.

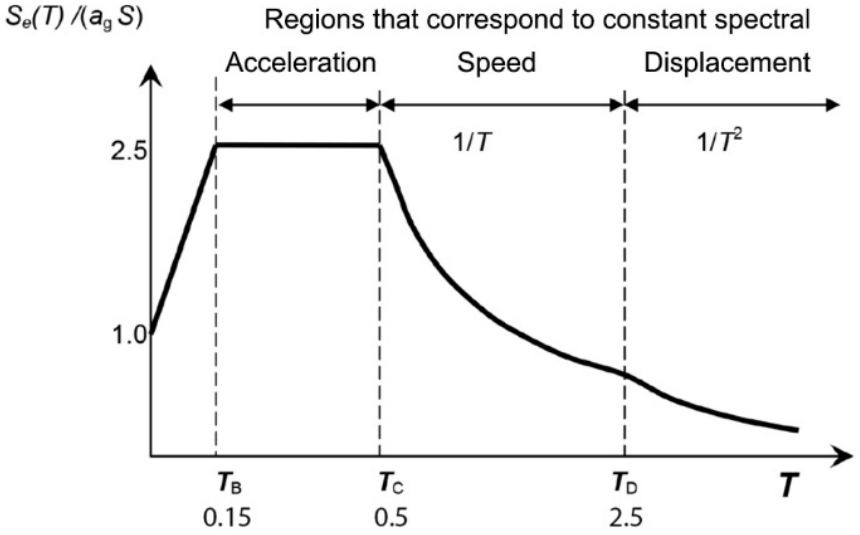


**Fig. 2.** Elastic Spectrum

## 2.2 Dynamic Properties

The period, $T$ (Empirical period) of the building, when applying the methodology of the Second-degree pre-earthquake inspection was determined according to the approximate equation of the Greek Code of Structural Interventions - *KANEPE* [3] from Eq.1:

$$T = C_t \, H^{0.9} \tag{1}$$

where $C_t$ is equal to 0.052 and $H$ is the height of the building equal to 9.90 m.

When conducting the non-linear static analysis (analysis period), the period $T$ was determined according to the direction and distribution of the seismic loading and the structural properties of the buildings. The results obtained from the two methods are shown in Table 3. The indication "No Infill Walls" stands for case of the buildings $\mathrm{A_n}$ and $B_\mathrm{n}$.

**Table 3.** Empirical and Analysis Periods $T$.

| | EMPIRICAL | ANALYSIS | | | | | |
|---|---|---|---|---|---|---|---|
| | | A | B | $A_s$ | $B_s$ | $A_p$ | $B_p$ |
| No Inf. Wall | 0.41 | 1.36 | 1.32 | - | - | - | - |
| Inf. Wall.g | 0.41 | 0.71 | 0.75 | 0.63 | 0.82 | 0.99 | 0.96 |
| Inf. Wall.p | 0.41 | 1.06 | 0.78 | 0.71 | 0.71 | 1.17 | 1.02 |

Similar to [5], the period $T$ obtained by the approximate equation from *KANEPE* [3], is equal for both structures with values much smaller than those resulting by the non-linear static analysis (pushover analysis). In the analysis, the periods $T$ in all examined cases correspond to values higher than $T_c = 0.50s$, i.e. they are in the descending branch of the spectrum. Consequently, a lower demand is expected compared to the one Second-degree pre-earthquake inspection predicts, where the period of the structure is between the $T_B$ and $T_c$ periods of the spectrum and therefore, corresponds to the plateau of the spectrum ($T < T_c$) (Fig. 2).

High values of the periods $T$ of pushover analysis of the six building categories that were examined and are given in Table 3 are due to the fact that the effective stiffness of the members is obtained at the guilt point of the section using Eq.2 of *KANEPE* §7.2.3 [3]. As a result, the effective stiffness values of pushover analysis are significantly low for all examined buildings compared to the ones of the uncracked section. This is further demonstrated by Table 4, where the effective stiffness of the ground floor column C5 of building A is presented as a percentage of the respective uncracked section, for primary loading direction 90°. The same values of the effective stiffness arise for the rest of the primary loading directions (0°, 180° and 270°). As observed, the effective stiffness ($EI_{eff}$) has a low percentage ranging from 8.7% to 19.1% of the uncracked section stiffness ($EI_{gross}$). These values cannot exceed 25% of the uncracked section stiffness as dictated by *KANEPE* §7.1.2.2 [3]. This has been concluded in an earlier study of Bardakis and Dritsos [8] where the procedures of *FEMA 356* [9] and *KANEPE* [3] are compared. In the procedure of *FEMA 356* [9], high values of effective stiffness are used, as is also in the Second-degree pre-earthquake inspection examined in the present study.

**Table 4.** Correlation between effective stiffness and uncracked section stiffness for C5.

| Angle (deg) | $EI_{eff}/EI_{gross}$ |
|---|---|
| 90 | 8.7% |
| | 14.3% |
| | 14.6% |
| | 17.8% |
| | 19.1% |

# 3 Application of the approximate method

Analysis is performed for the "Significant Damage Performance" level (Level B) [3]. The behavior factor $q$, for all buildings is taken $q = 2.00$ according to Table 4 of the methodology of the Second-degree pre-earthquake inspection [1]. For the case of buildings with a soft storey, an additional investigation is performed considering a $q = 1.5$, as they could reasonably be characterized as buildings with unfavorable presence of masonry infill walls.

The basic seismic resistance ($V_{R0}$), of the building of the critical floor (generally the ground floor) is determined (see also [5]) by Eq.2:

$$V_{R0} = \alpha_1 \sum V_{Ri}^{columns} + \alpha_2 \sum V_{Ri}^{walls} + \alpha_3 \sum V_{Ri}^{short\ columns} + \sum V_{Ri}^{infill\ walls} \quad (2)$$

where $V_{Ri}^{columns}$ is the seismic resistance of each column, $V_{Ri}^{walls}$ is the seismic resistance of each wall, $V_{Ri}^{short\ columns}$ is the seismic resistance of each short column, $V_{Ri}^{infill\ walls}$ is the seismic resistance of each infill wall and $\alpha_1, \alpha_2$ and $\alpha_3$ are values that can be taken according to the proposed method [1].

For the examined cases (frame structural system with RC columns) the values for reference buildings $(\mathrm{A}, \mathrm{B})$ and buildings with soft storey $(\mathrm{A_p}, \mathrm{B_p})$ are taken according to the proposed method as $\alpha_1 = 0.85$ and $\alpha_2 = \alpha_3 = 0$. For the case of buildings with short columns $(\mathrm{A_s}, \mathrm{B_s})$, the corresponding values are $\alpha_1 = 0.70$, $\alpha_2 = 0$, $\alpha_3 = 0.85$.

The shear resistance of the masonry infill walls $V_{Ri}^{infill\ walls}$ is calculated by the following Eq.3:

$$V_{Ri}^{infill\ walls} = 0.3\ f_{wc,s}\ t_w\ b_w\ \left(\frac{l}{L}\right) \quad (3)$$

where $f_{wc,s}$ is the compressive strength of the infill walls in the diagonal direction and can be obtained from Table 3 of Appendix D [1], whereas $t_w, b_w$ stands for the thickness and the effective width of the infill wall respectively. The contribution of infill walls in the resistance of the structure is governed by *KANEPE* §7.4.1 [3]. Approximately, $b_w$ can be considered as $b_w \approx L \cdot (f_{wv}/f_{wc,s})$, where $f_{wv}$ is the strength in diagonal cracking [3].

According to the methodology of the approximate method of the Second-degree pre-earthquake inspection, the maximum shear force that the vertical elements can withstand is calculated based on the existing reinforcements, by checking the expected failure mechanism (flexural or shear) as per $V_{R,i} = min\ (V_{Rd}, V_M)$. The flexural strength $(V_M)$ is equal to $V_M = M_R/L_s$, where $L_s$ is obtained by *KANEPE* [3].

In cases where reinforcement data is not available, there is the option for an approximate estimation of lower accuracy to be performed, considering only the shear strength of the vertical elements $(V_{Rd})$, without checking their flexural capacity. The method is applied by assuming that $V_{R,i} = V_{Rd}$. In this last case, the results are obtained by assuming that, in the examined cases, the height of the compression zone $x$ is equal to $0.35d$,

and the ductility index $\mu_\theta^{pl}$ is equal to 2.5. The justification for these assumptions can be found in [5]. The value of $V_{Rd}$ is determined based on the expression of *KANEPE* Appendix 7C [3]. The shear resistance of the structural elements has been determined using the Eq. C1 *KANEPE* of the aforementioned Appendix [3].

However, for short columns, the shear strength cannot exceed the limit value $V_{R,max}$, corresponding to web failure due to inclined compression, as given by Eq. C5 *KANEPE* of the same Appendix [3]. In particular, in the case of buildings ($A_s, B_s$), when reinforcement data is available the shear strength of vertical members *($V_{R,i}$)* is obtained by $V_{R,i} = min\,[(V_{Rd}, V_{R,max}), V_M]$, otherwise when reinforcement data in not available, by $V_{R,i} = min\,(V_{Rd}, V_{R,max})$.

In Table 5, the results of the shear strength of the columns of buildings (A & $A_p$) and (B & $B_p$) are presented, applying the Eq. C1 *KANEPE* of Appendix 7C [3]. The values of shear strength for building A and building with soft storey $A_p$ are the same, similarly for buildings B and $B_p$, as the height of the cross section does not change according to the Eq. C1 *KANEPE* of Appendix 7C [3]. As observed, the critical failure mechanism for all cases of building's columns was the flexural failure *($V_M$)*, except for the buildings with short columns. In Table 6, the results of the shear strength of the columns for buildings with short columns are presented, applying the Equations C1 and C5 *KANEPE* of Appendix 7C [3]. As observed, the critical failure mechanism in shear for all cases of short columns was the failure in inclined compression *($V_{R,max}$)*.

**Table 5.** Shear resistance of RC columns – Approximate and Precise values for Buildings A & $A_p$ , B & $B_p$

| Second degree pre-earthquake Insp. | BUILDINGS A & $A_p$ | | | BUILDINGS B & $B_p$ | | |
|---|---|---|---|---|---|---|
| | Reinf. Data | | No Reinf. Data | Reinf. Data | | No Reinf. Data |
| COLUMNS | $V_{Rd}$ (KN) Eq.C1 | $V_M$ (KN) | $V_{Rd}$ (KN) $x = 0.35d$ $\mu_\theta^{pl} = 2.5$ Eq.C1 | $V_{Rd}$ (KN) Eq.C1 | $V_M$ (KN) | $V_{Rd}$ (KN) $x = 0.35d$ $\mu_\theta^{pl} = 2.5$ Eq.C1 |
| 1 | 107.31 | 92.44 | 108.35 | 107.31 | 92.44 | 108.35 |
| 2 | 126.11 | 101.80 | 133.52 | 126.50 | 101.88 | 134.32 |
| 3 | 100.40 | 85.58 | 101.94 | 104.75 | 89.87 | 105.94 |
| 4 | 126.22 | 101.82 | 133.76 | 126.70 | 101.92 | 134.73 |
| 5 | 185.46 | 158.41 | 173.30 | 177.57 | 157.52 | 181.45 |
| 6 | 122.10 | 101.19 | 126.27 | 98.06 | 83.30 | 99.84 |
| 7 | 109.16 | 94.31 | 110.12 | 115.09 | 100.41 | 115.93 |
| 8 | 127.11 | 102.00 | 135.58 | 108.05 | 93.19 | 109.06 |
| 9 | 102.13 | 87.27 | 103.52 | – | – | – |

**Table 6.** Shear resistance of RC columns – Approximate and Precise values for building $A_s$-$B_s$

| Second-degree pre-earthquake Insp. | BUILDING $A_s$ | | | | |
|---|---|---|---|---|---|
| | Reinf. Data | | | No Reinf. Data | |
| COLUMNS | $V_{Rd}$ (KN) Eq.C1 | $V_{R,max}$ (KN) Eq.C5 | $V_M$ (KN) | $V_{Rd}$ (KN) $x = 0.35d$ $\mu_\theta^{pl} = 2.5$ Eq.C1 | $V_{R,max}$ (KN $\mu_\theta^{pl} = 2.5$ Eq.C5 |
| 1 | 275.74 | 111.17 | 459.10 | 267.26 | 108.34 |
| 2 | 367.65 | 131.57 | 508.73 | 393.10 | 127.65 |
| 3 | 245.73 | 105.83 | 424.74 | 235.22 | 103.42 |
| 4 | 368.28 | 131.76 | 508.84 | 394.28 | 127.83 |
| 5 | 185.47 | - | 158.42 | 195.64 | - |
| 6 | 346.56 | 125.77 | 505.77 | 356.84 | 122.09 |
| 7 | 283.81 | 112.64 | 468.49 | 276.11 | 109.70 |
| 8 | 372.96 | 133.23 | 509.72 | 403.43 | 129.23 |
| 9 | 253.22 | 107.14 | 433.24 | 243.10 | 104.63 |
| Second-degree pre-earthquake Insp. | BUILDING $B_s$ | | | | |
| | Reinf. Data | | | No Reinf. Data | |
| COLUMNS | $V_{Rd}$ (KN) Eq.C1 | $V_{R,max}$ (KN) Eq.C5 | $V_M$ (KN) | $V_{Rd}$ (KN) $x = 0.35d$ $\mu_\theta^{pl} = 2.5$ Eq.C1 | $V_{R,max}$ (KN) $\mu_\theta^{pl} = 2.5$ Eq.C5 |
| 1 | 275.74 | 111.17 | 459.10 | 267.26 | 108.34 |
| 2 | 369.75 | 132.22 | 509.11 | 397.10 | 128.26 |
| 3 | 264.59 | 109.15 | 446.23 | 255.19 | 106.49 |
| 4 | 370.81 | 132.55 | 509.31 | 399.17 | 128.58 |
| 5 | 536.15 | 140.75 | 850.37 | 553.54 | 135.69 |
| 6 | 235.61 | 104.08 | 413.35 | 224.72 | 101.81 |
| 7 | 309.70 | 117.49 | 499.03 | 305.17 | 114.16 |
| 8 | 278.98 | 111.76 | 462.86 | 270.80 | 108.88 |

The final seismic resistance $V_R$, is determined for each direction by Eq.4:

$$V_R = \beta \times V_{R0} \tag{4}$$

where $\beta$ is the reduction factor determined according to 13 criteria which are used to assess the vulnerability of a structure, as described in the methodology [1], and evaluated with a value of 1 to 5, where 1 corresponds to the highest reduction.

In the case of building with short columns, all criteria were graded with 5 for both buildings, except for criterion 3 (Normalized axial load), which resulted in $\beta_3 = 2$ for building A and $\beta_3 = 3$ for building B. These values were obtained taking into consideration the average value of the normalized axial load of the vertical elements which were $0.35 \leq v_d = 0.39 < 0.45$ for building A and $0.25 \leq v_d = 0.34 < 0.35$ for building B. In criterion 7 (Stiffness distribution in elevation) both buildings were graded equal to $\beta_7 = 1$, given that the ductility of the ground floor exceeds the ductility of the first floor with a value of $462\% > 150\%$ in the x direction and $548\% > 150\%$ in the y direction for building A and $506\% > 150\%$ in the x direction and $491\% > 150\%$ in the y direction for building B. In criterion 9 (Short columns), according to the calibration of the criterion using the value of the quantity $l/h$ of the supports and the gravity factor corresponding to it, the grade is equal to $\beta_9 = 1$ for building A and $\beta_9 = 1.67$ for building B. Only in building B, criterion 5 (Stiffness distribution in plan – torsion) is differentiated in the x direction, where the normalized eccentricity is $\varepsilon_x = 0.076 > 0.05$, corresponding to a grade equal to $\beta_5 = 4$. Consequently, the values of the reduction factor $\beta$ for building $A_s$ and $B_s$ in the two main directions were $\beta_x = \beta_y = 0.76$ and $\beta_x = 0.74$, $\beta_y = 0.77$ respectively.

In the case of buildings with a soft storey (pilotis), Criterion 3 (Normalized axial load), was graded the same as in the reference buildings (see [5]), equal to $\beta_3 = 3$ for both buildings A and B. Criterion 7 (Stiffness distribution in elevation), was graded equal to $\beta_7 = 1$, for both buildings, as the stiffness of the first floor exceeds the one of the ground floor with values of $245\% > 150\%$ in the x direction and $269\% > 150\%$ in the y direction for building A, and $277\% > 150\%$ in the x direction and $303\% > 150\%$ in the y direction for building B. Criterion 5 (stiffness distribution in plan – torsion), was graded equal to $\beta_5 = 4$, as the eccentricity in the loading direction x was found to be $\varepsilon_x = 0.067 > 0.05$. As a result, the values of the reduction factor $\beta$ for buildings $A_p$ and $B_p$ in the two main directions were $\beta_x = \beta_y = 0.86$ and $\beta_x = 0.84$, $\beta_y = 0.86$ respectively.

It is noted that values of the reduction factor $\beta$ for the reference buildings A and B have been derived in [5] and are $\beta_x = \beta_y = 0.98$ and $\beta_x = 0.96$, $\beta_y = 0.98$ respectively.

The failure index $\lambda$ of the structure for each main direction x and y is determined considering the available seismic resistance and the seismic demand according to Eq.5 as follows:

$$\lambda_x = \frac{V_{req,x} + 0.30V_{req,y}}{V_{R,x} + 0.30V_{R,y}} \ , \ \lambda_y = \frac{V_{req,y} + 0.30V_{req,x}}{V_{R,y} + 0.30V_{R,x}} \tag{5}$$

The classification of the building into a seismic category of Second-degree pre-earthquake inspection is done based on the capacity factor $\delta$, as follows according to Eq.6:

$$\delta = min\left\{\frac{1}{\lambda_x}, \frac{1}{\lambda_y}\right\} \tag{6}$$

Further information on this matter can be found in [10].

# 4 Application of the Non-linear static analysis method

A non-linear static analysis (pushover analysis) method is also employed, in accordance with the provisions of *KANEPE* [3] for a "performance level B". As described in [5], the failure indices $\lambda$ of the buildings are defined in two ways: a) based on the minimum horizontal ground acceleration $a_g$ for which the first failure of a vertical member of the building occurs for an acceptable "performance level B", as defined in Eq.7, and b) through the maximum failure index $\lambda_{max}$ of the vertical elements of the structure for a "performance level B1" and for all possible loading combinations.

$$\lambda_{ag} = \frac{a_{g,ref}}{\alpha_g} \tag{7}$$

where $a_{g,ref}$ is the reference horizontal ground acceleration, with a probability of exceeding the seismic action of 10% in the structure's intended life span, which equals to 50 years for ordinary structures. In this case of the study, the reference horizontal ground acceleration equals to $0.24g$.

The seismic category of the building is determined according to *KANEPE* [3] based on the ratio $a_g \,/a_{g,ref}$, i.e., the quantity $1 \,/\, \lambda_{ag}$ and is defined as the maximum target for assessment or redesign that a building can achieve for a selected "performance level B". More details on this matter are presented in [10].

The pushover analysis was conducted utilizing the commercial software *FESPA* of LH Logismiki [11]. The structural system is a three-dimensional concrete frame. The beam elements used in the analysis are considered as 3D beam-column elements with concentrated plasticity in both edges. It is a displacement-based beam element, where plastic penetration is taken into account. The flexural plastic hinges have been defined using the cord rotation equations provided by *KANEPE* [3]. The model has been checked for both flexure and shear plastic hinges. For shear, the provisions of Chapter 7 *KANEPE* §7.2.4.2 and §7.2.5 [3] are followed. The displacement-based control, that has been used was the multi-control point. The minimum number of steps (static analysis) to be performed in each pushover analysis with incrementally increasing load until the end of the analysis, which is defined as the exceedance of the given maximum displacement for the "performance level B", is equal to 120. The displacement control arises from the minimum number of steps, and the maximum displacement is 3% of the building's height.

The mechanic behaviour of a structural element, or of a critical region of a structural element is described through a diagram of force "$F$" versus deformation "$\delta$". In the present study the choice of $F$ and $\delta$ are moment "$M$" and chord rotation "$\theta$" at the ends of the element, where $\theta$ incorporates the sum of flexural and shear deformations, as well as the rotation of member ends due to reinforcement slip [3].

The non-linear laws of the reinforced concrete sections that were used to the non-linear analysis are defined in terms of $M - \theta$, where a) the deformation in yielding, is determined by the chord rotation $\theta_y$, using the Eq. S.2a *KANEPE* §7.2.2 [3], b) the deformation in failure, is determined by the mean value of chord rotation at failure $\theta_{um}$, using the Eq. S.11a *KANEPE* §7.2.4.1 [3] and c) the yielding moment, $M_y = M_u$ is

determined by the Eq. A.6a *KANEPE* of Appendix 7.A [3]. An indicative representation of the relation of moment "$M$" as a function of chord rotation "$\theta$" is presented in Fig.3 for "performance level B" of the ground floor column C5 of building A.

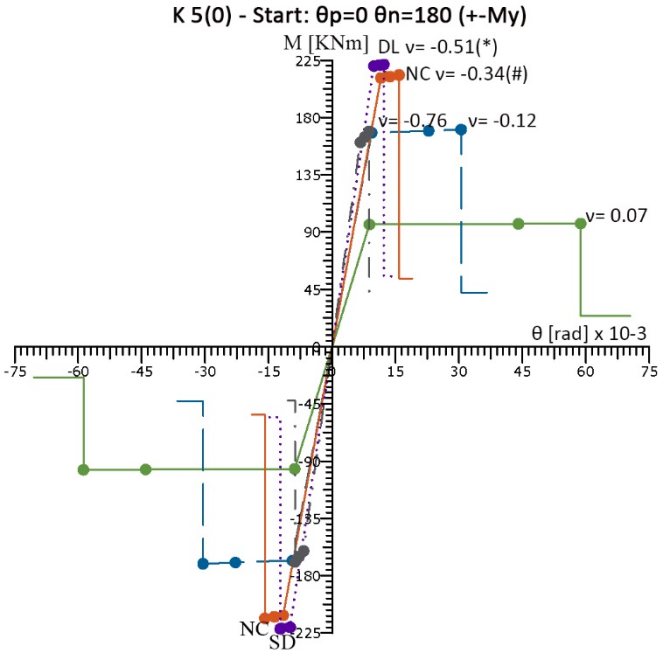


**Fig. 3.** Moment "$M$" as a function of chord rotation "$\theta$"

Pushover analysis significantly evaluates the expected performance level of the structural system by the building's capacity curve. Based on this capacity curve, the target displacement expected to occur during the earthquake is estimated. Fig. 4 presents the capacity curves for a "performance level B" for the direction $(90° + 30\% \cdot 0° + eX)$ for the column C5 of the ground floor of the buildings A, $A_s$ and $A_p$ respectively for good construction detailing and wedging of masonry infill walls considering the presence of openings. Moreover, the acceleration displacement response spectrum is also evident. In Fig. 4(a) and Fig. 4(b) the dashed blue line (SD) is located to the left of the target displacement, indicating that column C5 fails in flexure. In Fig. 4(c) the same column fails in shear, as the dashed blue line (SD) is located to the right of the target displacement, and the dashed orange line (VR) precedes the target displacement. The yellow line represents the capacity curves. The blue line represents the elastic spectrum $\mu(el) = 1.00$ and the green line represents the inelastic spectrum arising from the transformations of Eq. 6a and Eq. 6b *KANEPE* §7.2.6.2 [3]. The $T^*$ is the period of an elastic single degree of freedom system.

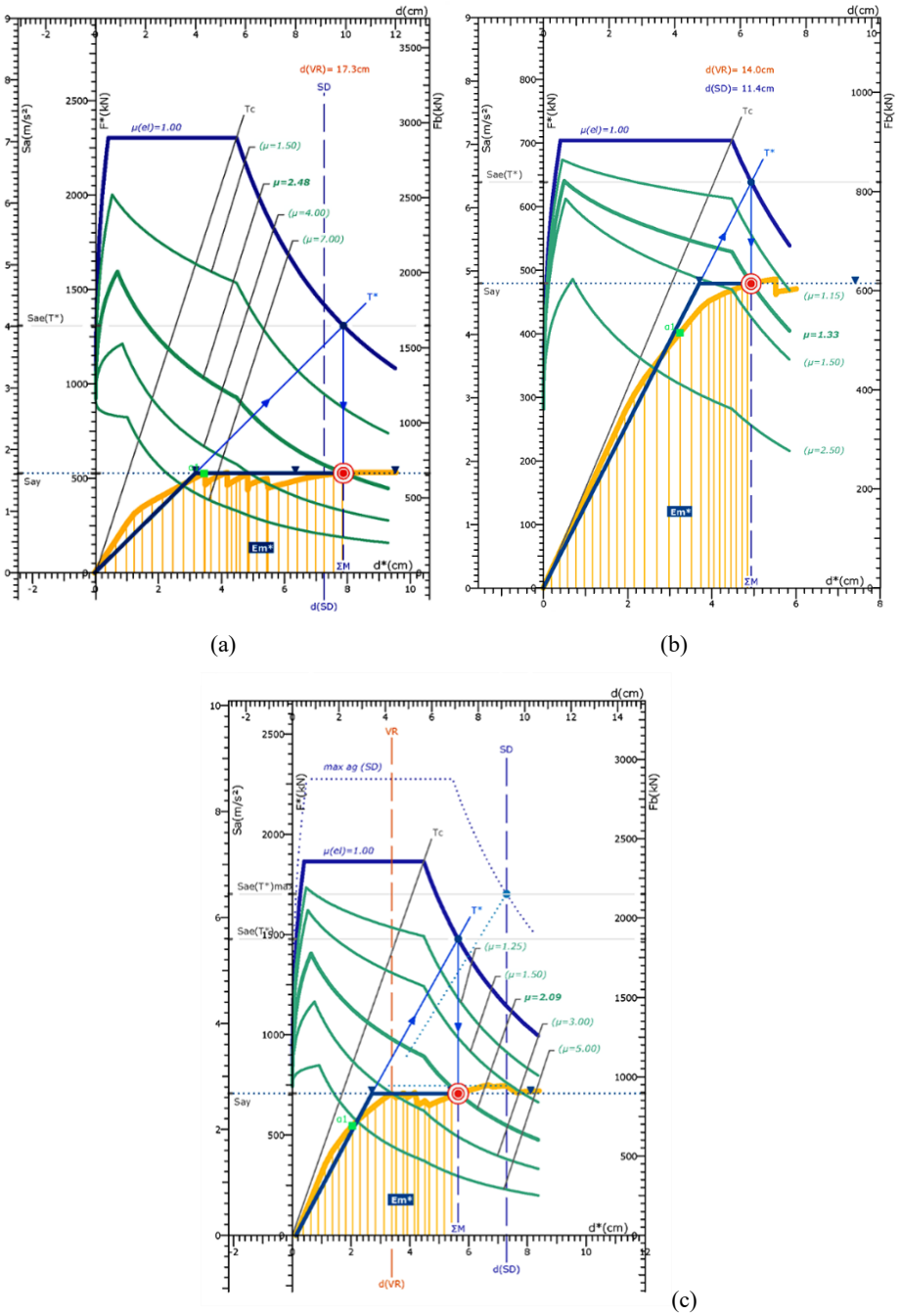


**Fig. 4.** Capacity curves for column C5 for building A (a) reference (b) soft storey and (c) short columns

# 5 Results and Discussion

## 5.1 Determination of seismic resistance of Second-degree pre-earthquake inspection and Non-linear static analysis

In Table 7, the results of seismic resistance, in terms of base shear force for the reference buildings, those with short columns, and those with soft storey (pilotis) are presented. Fig. 5 presents, the results of shear forces considering good and poor construction detailing and wedging of masonry infill walls on the two upper floors. The results from the application of the methodology of the Second-degree pre-earthquake inspection are presented for both cases previously mentioned above, i.e. when data about reinforcement amounts of the vertical elements are available and when they are not available. Regarding the non-linear static analysis (pushover analysis), the value of the shear force presented in Table 7 is the maximum value obtained by the capacity curve of the structure, which appears before or during the point when the structure reaches "performance level B". The failure mechanism determined by applying the Second-degree pre-earthquake inspection with known reinforcement data, was found to be flexural for the case of reference buildings and pilotis, while for the case of buildings with short columns, it was found to be shear, in full agreement with the analysis results for both buildings. The values of the seismic resistance obtained when the Second-degree pre-earthquake inspection was applied without reinforcement data were higher than those obtained using reinforcement data. This is reasonable considering that, for this case, only the shear strength of the members is taken into account.

**Table 7.** Maximum Seismic Resistance

| | BUILDING A | | | BUILDING B | | |
|---|---|---|---|---|---|---|
| | Second degree pre-earthquake Insp. | | Non-linear Static Analysis | Second degree pre-earthquake Insp. | | Non-linear Static Analysis |
| | Reinf. data | No Reinf. data | | Reinf. data | No Reinf. data. | |
| REFERENCE BUILDINGS | | | | | | |
| No Infill Walls | 770.39 | 938.26 | 620.75 | 669.54 | 807.53 | 499.91 |
| Inf. W.g | 1064.42 | 1232.29 | 660.62 | 997.10 | 1095.20 | 64.47 |
| Inf. W.p | 878.70 | 1046.57 | 654.40 | 808.74 | 914.38 | 528.94 |
| BUILDINGS WITH SHORT COLUMNS | | | | | | |
| Inf. W.g | 642.57 | 625.47 | 854.00 | 423.94 | 412.60 | 865.00 |
| Inf. W.p | 642.57 | 625.47 | 848.00 | 423.94 | 412.60 | 849.00 |
| BUILDINGS WITH SOFT STOREY | | | | | | |
| Inf. W.g | 676.06 | 823.37 | 634.95 | 585.85 | 706.59 | 544.07 |
| Inf. W.p | 676.06 | 823.37 | 629.33 | 585.85 | 706.59 | 529.74 |

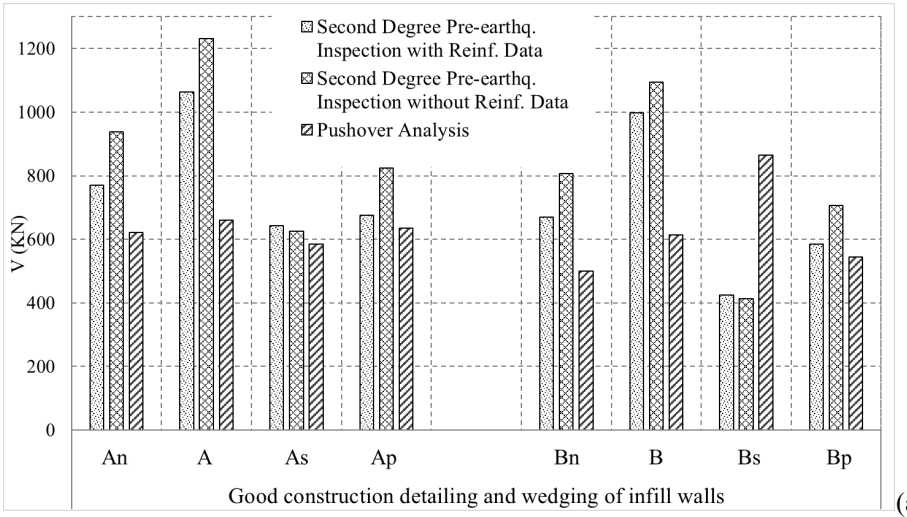


(a)

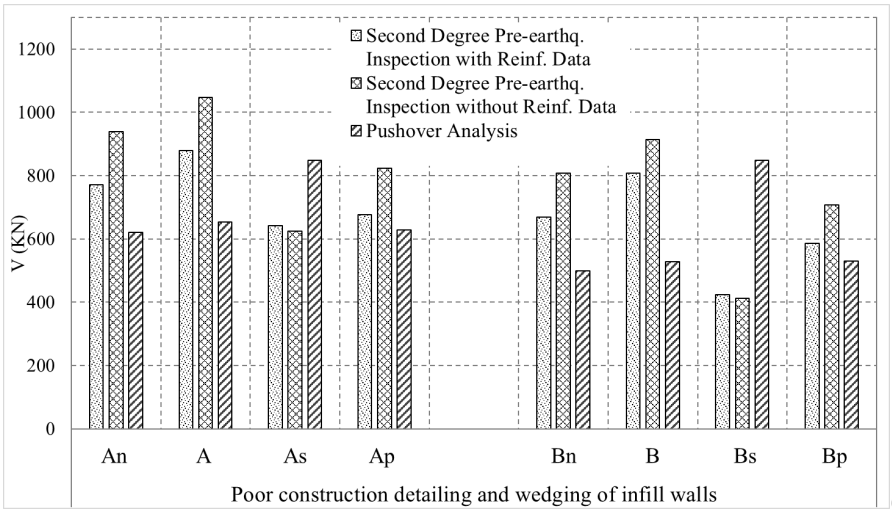


(b)

**Fig. 5.** Earthquake resistance obtained by Second degree pre-earthquake inspection (with and without considering reinforcement data) and Non-linear static analysis for (a) Good and (b) Poor construction detailing and wedging of infill walls

## 5.2 Determination of the failure indices by Second-degree pre-earthquake inspection and Non-linear static analysis

Fig. 6 and Fig. 7 demonstrate the values of failure indices ($\boldsymbol{\lambda_{Sec.}}$) related to the Second- degree pre-earthquake inspection [1], for both the cases of available, and unavailable ($\boldsymbol{\lambda_{Sec.,v}}$) reinforcement data. The corresponding values obtained by the non-linear static analysis (pushover analysis) for the failure index in terms of base acceleration ($\boldsymbol{\lambda_{ag}}$) and in terms of maximum failure index ($\boldsymbol{\lambda_{max}}$) are also presented for good and poor construction detailing and wedging of masonry infill walls. The dashed line

indicates the value corresponding to the adoption of the behavior factor $\boldsymbol{q = 2.0}$ in the case of buildings with a soft storey (pilotis).

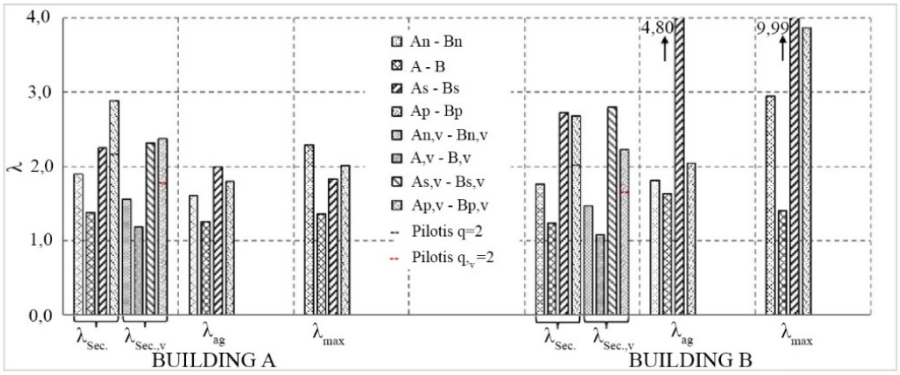


**Fig. 6.** Failure indices obtained by Second-degree pre-earthquake inspection and Non-linear static analysis for good construction detailing and wedging of infill walls

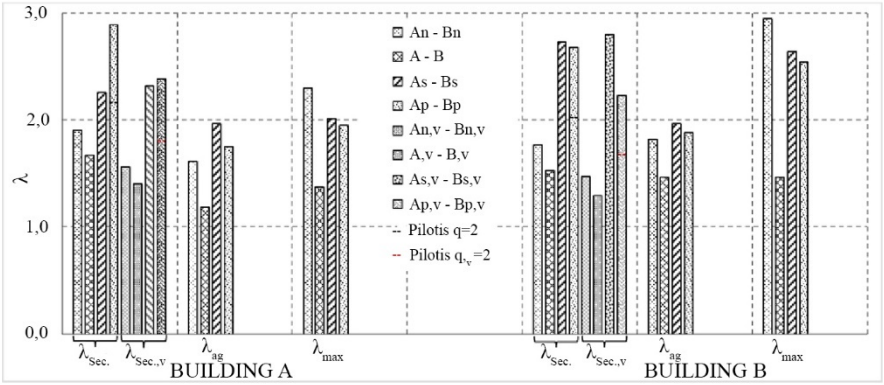


**Fig. 7.** Failure indices obtained by Second-degree pre-earthquake inspection and Non-linear static analysis for poor construction detailing and wedging of infill walls

As can be observed from Fig. 6 and Fig. 7, failure indices $\lambda_{Sec.}$ are in very good agreement with $\lambda_{ag}$ in comparison to the failure indices $\lambda_{max}$ of the columns. This can be explained considering that the failure indices $\lambda_{max}$ represent local member deficiencies that can lead to incorrect conclusions about the overall behavior of the structure.

**Table 8.** Failure indices $\lambda$

| Buildings | Categories of Infill Walls | Second-degree pre-earthquake inspection | | | | Non-linear Static Analysis | |
|---|---|---|---|---|---|---|---|
| | | v.2022 - Reinf. data | v.2022 - No Reinf. data | v.2018 - Reinf. data | v.2018 - No Reinf. data | $\lambda_{max}$ | $\lambda_{ag}$ |
| REFERENCE BUILDINGS | | | | | | | |
| A | No Infill Walls | 1.90 | 1.56 | 2.24 | 1.84 | 2.30 | 1.61 |
| | Inf. Wall.g | 1.38 | 1.19 | 2.24 | 1.84 | 1.37 | 1.26 |
| | Inf. Wall.p | 1.67 | 1.40 | 2.24 | 1.84 | 1.37 | 1.18 |
| B | No Infill Walls | 1.76 | 1.46 | 2.07 | 1.72 | 2.95 | 1.82 |
| | Inf. Wall.g | 1.23 | 1.08 | 2.07 | 1.72 | 1.41 | 1.63 |
| | Inf. Wall.p | 1.52 | 1.29 | 2.07 | 1.72 | 1.31 | 1.47 |
| BUILDINGS WITH SHORT COLUMNS | | | | | | | |
| A | Inf. Wall.g | 2.25 | 2.32 | 2.51 | 2.58 | 1.83 | 2.00 |
| | Inf. Wall.p | 2.25 | 2.32 | 2.51 | 2.58 | 2.01 | 1.97 |
| B | Inf. Wall.g | 2.73 | 2.80 | 3.21 | 3.30 | 9.99 | 4.80 |
| | Inf. Wall.p | 2.73 | 2.80 | 3.21 | 3.30 | 2.64 | 1.97 |
| BUILDINGS WITH SOFT STOREY | | | | | | | |
| | $q$ | 2.0 | 1.5 | 2.0 | 1.5 | 1.7 | 1.3 | 1.7 | 1.3 | - | - |
| A | Inf. Wall.g | 2.17 | 2.89 | 1.78 | 2.37 | 2.55 | 3.33 | 2.09 | 2.74 | 2.01 | 1.80 |
| | Inf. Wall.p | 2.17 | 2.89 | 1.78 | 2.37 | 2.55 | 3.33 | 2.09 | 2.74 | 1.95 | 1.75 |
| B | Inf. Wall.g | 2.01 | 2.68 | 1.67 | 2.22 | 2.36 | 3.09 | 1.96 | 2.56 | 3.87 | 2.05 |
| | Inf. Wall.p | 2.01 | 2.68 | 1.67 | 2.22 | 2.36 | 3.09 | 1.96 | 2.56 | 2.54 | 1.88 |

Similar results are presented in Table 8 to evaluate the influence of the recent changes in the Secon-degree pre-earthquake inspection guidelines [1], showing the values of failure indices according to both versions of the provisions [1-2] along with the corresponding results from the non-linear static analysis (pushover analysis). As observed, the values of failure indices according to the methodology of the pre-revised version [2] are consistently higher than those from the revised version [1], are independent of the presence of masonry infill walls, and deviate more from the corresponding results of the non-linear static analysis (pushover analysis). The main reason for these differences is that in the pre-revised version [2]: a) lower values are adopted for the available behavior factor $q$ (which for the cases examined is considered equal to $\boldsymbol{q = 1.7}$ instead of $\boldsymbol{q = 2.0}$ that is dictated by the revised version [1]) and b) the contribution of masonry infill walls to the seismic resistance of the structure is disregarded.

It is observed that the failure indices are significantly higher for buildings with short columns and soft storey compared to the reference buildings in both the Second-degree pre-earthquake inspection and the non-linear static analysis (pushover analysis), for both types of masonry infill walls (Inf. Wall.g, Inf. Wall.p). For buildings with pilotis, the results from the Second-degree pre-earthquake inspection and the analysis converge more for a value of the behavior factor $q = 2.0$ compared to the ones when the value $q = 1.5$ is used. Therefore, it is considered reasonable to adopt the value $q = 2.0$ for the Second-degree pre-earthquake inspection for buildings with soft storey (pilotis). This could be interpreted considering that the deficiency of the soft storey, due to the non-uniform distribution of masonry infill walls along the height of the building, is already being considered through the vulnerability factor $\beta$.

### 5.3 Categorization of buildings into Seismic Categories via the method of the Second-degree pre-earthquake inspection and Seismic Classifications as defined by KANEPE

In Table 9, the results of the classification of buildings into seismic categories according to the Second-degree pre-earthquake inspection and seismic classes according to the approximate equation of the Greek Code of Structural Interventions - *KANEPE* [3] are presented. In all cases, the classification is being done according to the capacity factor $\boldsymbol{\delta = 1/\lambda}$, where for seismic classes $\boldsymbol{\delta = 1/\lambda = a_g/a_{g,ref}}$. The results of the Second-degree pre-earthquake inspection are presented for both the cases of known and unknown reinforcement amounts of the vertical elements (Second degree pre-earthquake inspection with / without reinforcement data respectively).

**Table 9.** Seismic Categories of Structures

| Buildings | Infill Walls | Second-degree pre-earthquake inspection | | | | Non-linear Static Analysis | |
|---|---|---|---|---|---|---|---|
| | | Reinf. Data $\delta = 1/\lambda$ | Seismic Category-Reinf. Data | No Reinf. Data $\delta = 1/\lambda$ | Seismic category-No Reinf. Data | $\frac{a_g}{a_{g,ref}}$ | Seismic Classes by *KANEPE* |
| REFERENCE BUILDINGS | | | | | | | |
| A | Inf. W.g | 1/1.38=0.72 | K2 | 1/1.19=0.84 | $K2^+$ | 1/1.2= 0.79 | $B2^+$ |
| | Inf. W.p | 1/1.67=0.60 | K2 | 1/1.40=0.71 | K2 | 1/1.1= 0.85 | $B2^+$ |
| B | Inf. W.g | 1/1.23=0.81 | $K2^+$ | 1/1.08=0.93 | $K2^+$ | 1/1.6= 0.61 | B2 |
| | Inf. W.p | 1/1.52=0.66 | K2 | 1/1.29=0.78 | $K2^+$ | 1/1.4= 0.68 | B2 |
| BUILDINGS WITH SHORT COLUMNS | | | | | | | |
| A | Inf. W.g | 1/2.25=0.44 | K3 | 1/2.32=0.43 | K3 | 1/2.00= 0.50 | $B3^+$ |
| | Inf. W.p | 1/2.25=0.44 | K3 | 1/2.32=0.43 | K3 | 1/1.97= 0.51 | $B3^+$ |
| B | Inf. W.g | 1/2.73=0.37 | K3 | 1/2.80=0.36 | K3 | 1/4.80= 0.21 | B4 |
| | Inf. W.p | 1/2.73=0.37 | K3 | 1/2.80=0.36 | K3 | 1/1.97= 0.51 | $B3^+$ |
| BUILDINGS WITH SOFT STOREY | | | | | | | |
| A | Inf. W.g | 1/2.17=0.46 | $K3^+$ | 1/1.78=0.56 | $K3^+$ | 1/1.80= 0.56 | $B3^+$ |
| | Inf. W.p | 1/2.17=0.46 | $K3^+$ | 1/1.79=0.56 | $K3^+$ | 1/1.75= 0.57 | $B3^+$ |
| B | Inf. W.g | 1/2.01=0.50 | $K3^+$ | 1/1.67=0.60 | K2 | 1/2.05= 0.49 | $B3^+$ |
| | Inf. W.p | 1/2.01=0.50 | $K3^+$ | 1/1.67=0.60 | K2 | 1/1.88= 0.53 | $B3^+$ |

It is observed that a great convergence exists between the seismic categories derived from the Second-degree pre-earthquake inspection and the corresponding seismic classifications outlined in *KANEPE* [3]. This convergence is particularly conspicuous in

cases where precise information regarding reinforcement amounts of the vertical elements was available.

# 6 Conclusions

In this present study, the reference buildings described in [5] were examined but considering the present of short columns and soft storey (pilotis) on the ground floor. The assessment of their seismic capacity was done by applying the approximate methodology of Second-degree pre-earthquake inspection and results were validated by comparison with the corresponding ones of a non-linear static analysis (pushover analysis). Subsequently, failure indices were determined, leading to the structural categorization of the buildings into seismic categories as defined by the Second-degree pre-earthquake inspection and seismic classifications as derived by *KANEPE* [3]. The outcomes derived from the examined buildings in this study lead to the following conclusions. It is evident that further research is imperative, involving a more extensive examination of diverse building cases, to establish comprehensive and reliable conclusions applicable to a broader spectrum of structures:

- The failure mechanism determined by the Second-degree pre-earthquake inspection with available reinforcement data for vertical elements, was found to be flexural in the reference buildings and in buildings with a soft storey on the ground floor. In contrast, structures with short columns exhibited shear failures, notably attributed to the exceedance of the web's resistance in inclined compression. These findings were confirmed by the results derived from the non-linear static analysis (pushover analysis).
- The buildings which were examined, with or without the existence of a soft storey or short columns, the failure indices ($\lambda$) and corresponding seismic categories obtained when applying the Second-degree pre-earthquake inspection, were, in most case, in great convergence with the corresponding results of the non-linear static analysis (pushover analysis). In the analysis, failure indices are given in terms of acceleration ($\lambda_{ag}$) and seismic classifications are considered as defined in *KANEPE* [3]. The convergence between the values of the failure indices was lower for the case where reinforcement data were unavailable but as good regarding seismic classifications. However, it is imperative to underscore that, under no circumstances, does this observation permit a direct correspondence between the seismic classifications according to *KANEPE* [3] and the corresponding seismic categories determined by the Second-degree pre-earthquake inspection.
- The seismic vulnerability of buildings with soft storey or short columns, compared to the reference buildings, was confirmed in both methods in an equivalent manner.
- For the assessment of buildings with soft storey, using the methodology of the Second-degree pre-earthquake inspection, it is reasonable to use a behavior factor equal to $q = 2.0$, rather than using the value of $q = 1.5$.

# References


1. EPPO, Second level pre-earthquake assessment of RC buildings, Earthquake Planning and Protection Organization of Greece (EPPO), Greek Ministry for Environmental Planning and Public Works, Athens, Greece (1st Revision 2022)
2. EPPO, Second level pre-earthquake assessment of RC buildings, Earthquake Planning and Protection Organization of Greece (EPPO), Greek Ministry for Environmental Planning and Public Works, Athens, Greece (2018)
3. KANEPE, Greek code for structural interventions. Earthquake Planning and Protection Organization of Greece (EPPO), Greek Ministry for Environmental Planning and Public Works, Athens, Greece (2017)
4. KADET, Greek code for the assessment and structural interventions of masonry structures. Earthquake Planning and Protection Organization of Greece (EPPO), Greek Ministry for Environmental Planning and Public Works, Plan 2021, Athens, Greece (2021)
5. Zochiou L., Panagopoulou M., Dritsos S.: An approximate method to assess the seismic capacity of existing RC buildings. In: 5th ΠΣΑΜΤΣ, Athens, 20-22 October (2022)
6. Vasileiadi M., Dritsos S.: An approximate method to assess the seismic capacity of existing RC buildings. 7th ECCOMAS Thematic Conference on Computational Methods in Structural Dynamics and Earthquake Engineering, Crete, Greece, 24–26 June (2019)
7. EC8, Eurocode 8 Part 3, Design of structures for earthquake resistance: Assessment and retrofitting of buildings. European Standard EN 1988-3, European Committee for Standardization (CEN), Brussels (2005)
8. Bardakis V.G., Dritsos S.E.: Evaluating assumptions for seismic assessment of existing buildings. Soil Dynamics and Earthquake Engineering 27 (2007) 223-233. Elsevier
9. FEMA 356, Prestandard and Commentary for the Seismic Rehabilitation of Buildings, Federal Emergency Management Agency, American Society of Civil Engineers (ASCE), Washington, D.C. (2000)
10. Apostolidi E., Dritsos S.: Seismic categories and seismic classifications – Comparisons. In: 5th ΠΣΑΜΤΣ, Athens, 20-22 October (2022)
11. FESPA, LH LOGISMIKI, High Performance Software, Version 1.2.82, Athens, Greece (2016)

# Earthquake Engineering

# Preliminary evaluation of predictions from compressive strength models for masonry

Lampros Kouzelis[0009-0007-3913-7193] and Marina L. Moretti[0000-0003-2082-5571]

National Technical University of Athens 42, Patission st., 10682 Athens, Greece
kouzelis@mail.ntua.gr, moretti@central.ntua.gr

**Abstract.** Compressive strength is the most essential design parameter of load-bearing masonry structures. The performance of masonry under compression depends on numerous parameters and is linked to the properties of its component materials, which enclose high variability, and to its geometrical characteristics and interlocking arrangement. Available predictive models are usually based only on few variables and therefore their estimates are liable to uncertainties. In this paper, the performance of four existing models for the estimation of the compressive strength of masonry made of solid units, is evaluated. To this end, experimental data from tests on single-layered specimens made of solid clay bricks, and subjected to monotonic compression, were collected from the literature. The predictions of the four models are compared to the experimental strength of the masonry specimens. The performance of each model is assessed through statistical analysis indices. From the analysis, it is concluded that the examined predictive models overestimate the masonry specimens with experimental strength less than 5 MPa.

**Keywords:** masonry, compression, models

## 1 Introduction

Load-bearing masonry systems comprise a significant part of the building stock mainly in rural areas, but also in large urban centers around the world. Moreover, masonry structures represent the main method of construction of architecturally noteworthy structures of the world's cultural heritage. Even today, use of masonry remains a popular option for satisfying housing needs. The layout of load-bearing masonry buildings is realized with various structural configurations and numerous materials, such as natural or artificial masonry units (solid, perforated or frogged) and binding mortars of different composition, depending on the design requirements, the traditional construction practice and the local materials of each region.

The primary mechanical property of load-bearing masonry in structural design is its compressive strength. As a consequence, research on the compressive behavior of masonry has been very popular among researchers for the past decades. The complexity of the stress transfer mechanisms developed in masonry subjected to compression and

the numerous factors that affect its ultimate failure stress, have been discussed since early 1900's.

The principal factors that have been determined to affect the masonry compressive behavior are the mechanical properties of its components [1 – 4], the thickness of the mortar joints [5, 6], the ratio with which the two materials participate in the masonry [7], and the bond properties between the two materials [8]. Also, the role of the slenderness ratio of the masonry, (h/t), the quality of construction and the interlocking arrangement of its units in compressive strength are also emphasized in several studies.

However, available models for estimating the compressive strength of masonry are expressed as a function, mainly, of the compressive strength of the units and mortar. Consequently, a large scatter in their predictions is typically observed. In the following sections, a preliminary assessment of the reliability of four predictive models proposed in Standards and by researchers is carried out, based on experimental results from compression tests available in the published literature.

## 2 Experimental Data

To evaluate the models, results were collected from compression tests under monotonic loading, on rectangular and square single-layered masonry prisms and rectangular single-layered wallettes, made of solid clay bricks and mortars of different composition (Figure 1). In total, 57 datasets of prism specimens and 29 datasets of wallette specimens that failed in compression, were gathered and analyzed. Each dataset consists of 3 or more specimens with the same characteristics. The datasets are derived from four experimental studies [7, 9 – 11], in which 234 prism and 92 wallette specimens, were constructed.

**Constituent Materials.** The dimensions of the clay bricks used to construct the masonry specimens range from 100 to 228 mm in length, 96 to 112 mm in width, and 50 to 78 mm in height, while the joint thicknesses range from 10 to 18 mm for horizontal joints and from 10 to 12 mm for the vertical.

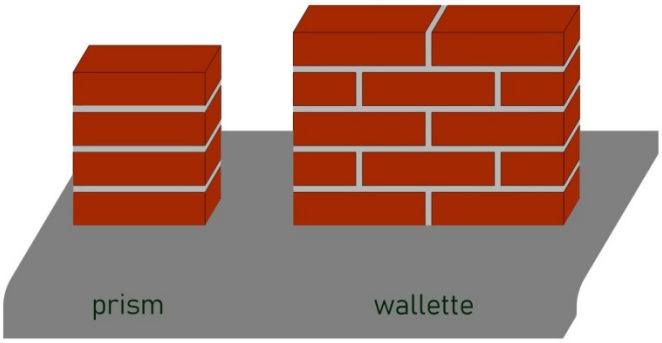


**Fig. 1.** Schematic illustration of prisms and wallettes

As binding material cement mortars, cement-lime mortars and lime mortars, with different composition proportions and a wide range of compressive strength were applied. Specifically, the compressive strength of the two components in the research programs considered range from 6.68 to 120.00 MPa for the clay bricks and from 0.69 to 48.00 MPa for the mortar, as shown per type of specimen in Table 1. Table 2 displays the number of datasets divided in sub-ranges of compressive strengths for the units and mortar of the collected database.

**Table 1.** Range of compressive strength of units and mortars per type of specimen

| Component | | Prisms | Wallettes |
|---|---|---|---|
| | | Compressive Strength (MPa) | |
| Units | min | 6.68 | |
| | max | 120.00 | |
| Mortars | min | 0.69 | 4.00 |
| | max | 48.00 | 48.00 |

**Table 2.** Datasets categorized by compressive strength of each material

| | | Compressive Strength of Units (MPa) | | | |
|---|---|---|---|---|---|
| Type of specimen | | ≤ 25 | > 25, ≤ 50 | > 50, ≤ 75 | > 75 |
| Prism | Number of datasets | 31 | 12 | 10 | 4 |
| Wallette | | 18 | 4 | 5 | 2 |
| | | Compressive Strength of Mortar (MPa) | | | |
| Type of specimen | | ≤ 5 | > 5, ≤ 15 | > 15, ≤ 30 | > 30 |
| Prism | Number of datasets | 12 | 23 | 11 | 11 |
| Wallette | | 4 | 12 | 6 | 7 |

**Masonry Specimens.** The masonry specimens consist of 2 to 8 and 2 to 6 layers of clay bricks in height, for the prisms and wallettes, respectively, assembled with full mortar joints. Their height-to-thickness ratios (h/t) range from 1.15 to 5.00 for the prism specimens and from 1.15 to 3.65 for the wallettes. Table 3 illustrates the ranges of strength and geometrical characteristics of the two types of masonry specimens included in the collected experimental data.

**Table 3.** Range of strength and geometrical characteristics of masonry specimens

| Property | | Prisms | Wallettes |
|---|---|---|---|
| Compressive Strength (MPa) | min | 1.22 | 1.10 |
| | max | 39.80 | 46.70 |
| Length (mm) | min | 100 | 210 |
| | max | 228 | 430 |
| Thickness (mm) | min | 96 | 96 |
| | max | 112 | 100 |
| Height (mm) | min | 110 | 110 |
| | max | 500 | 350 |

# 3 Predictive Models

In this section, are presented the equations included in the European (EN 1996–1–1) [12] and American (TMS 602 – 11/ACI 530.1 – 11/ASCE 6 – 11) [13] Standard, as well as two more models which have been proposed by T.P. Tassios [14] and G. Rossi [15]. It is further stated that the model of T.P. Tassios [14], is also adopted by the Greek Code for the assessment and structural interventions of masonry structures [16].

**European Standard EN 1996-1-1** [12]. The model is utilized for the design of masonry structures with binding material mainly of cement mortars, in which the arrangement of the units in height is implemented in regular layers. For masonries constructed from solid unit blocks with general-purpose mortar, the compressive strength results from equation (1):

$$f_{\mathrm{mod}} = 0.55 \cdot f_b^{0.7} \cdot f_m^{0.3} \tag{1}$$

where $f_{\mathrm{mod}}$ is the compressive strength of masonry [MPa], $f_b$ is the compressive strength of units [MPa] and $f_m$ is the compressive strength of mortar [MPa].

**American Standard** [13]. The equation provided by the American Standard TMS 602 – 11/ACI 530.1 – 11/ASCE 6 – 11 (TMS/ACI/ASCE) for predicting the compressive strength of masonry, is based on the compressive strength of units and the type of mortar applied. According to this model, the compressive strength of the masonry is calculated as follows:

$$f_{\mathrm{mod}} = A \cdot (400 + B \cdot f_b) \tag{2}$$

where $f_{\text{mod}}$ is the compressive strength of masonry [psi], $f_b$ is the compressive strength of units [psi], $A$ is a factor equal to 1 for masonry constructed under supervision and $B$ is a factor equal to 0.2 for lime-cement mortar type N and 0.25 for lime-cement mortar type S or M, as defined in the Standard. For the mortars of the specimens of this paper, type S/M is assumed for mortar's compressive strength equal to or greater than 10 MPa and type N for compressive strength less than 10 MPa. It is recalled that 1 psi is equal to 0.0068947573 MPa.

**Model T.P. Tassios** [14]. The proposed relationship links the compressive strength of the masonry, with the ratio of the joint thickness to the height of the units, the compressive strength of the units and, if applicable, the compressive strength of the mortar. The strength of masonry is calculated from equation (3):

$$f_{\text{mod}} = \begin{cases} [f_m + 0.40 \cdot (f_b - f_m)] \cdot (1 - 0.8 \cdot \sqrt[3]{\alpha}), \text{ for } f_b \succ f_m \\ f_b \cdot (1 - 0.8 \cdot \sqrt[3]{\alpha}), \text{ for } f_b \prec f_m \end{cases} \quad (3)$$

where $f_{\text{mod}}$ is the compressive strength of masonry [MPa], $f_b$ is the compressive strength of units [MPa], $f_m$ is the compressive strength of mortar [MPa] and $\alpha$ is the ratio of the horizontal mortar joints thickness to the height of the units.

**Model G. Rossi** [15]. Guido Rossi proposes a logarithmic relationship to predict the compressive strength of masonry constructed with solid or perforated – with vertical or horizontal holes – units and different mortar arrangements. For masonry consisting of solid units and mortar of general application, the compressive strength is expressed by equation (4):

$$f_{\text{mod}} = \frac{S}{A} \cdot \frac{f_b}{\alpha} \cdot \log(10 \cdot f_m + 5) \quad (4)$$

where $f_{\text{mod}}$ is the compressive strength of masonry [MPa], $f_b$ is the compressive strength of units [MPa], $f_m$ is the compressive strength of mortar [MPa], $S$ is the total area of the units that is filled with the mortar of the horizontal joints [cm$^2$], $A$ is the total horizontal area of the units, resulting from the product of their width over their length, without removing potential holes [cm$^2$] and $\alpha$ is a factor as follows: $\alpha$ = 5 for solid units with compressive strength $f_b$ > 10 MPa, while $\alpha$ = 4 for $f_b$ < 10 MPa.

# 4 Statistical Analysis Indices

In this work statistical indices based on the ratio of the estimated, $f_{\text{mod}}$, to the experimental, $f_{\text{exp}}$, masonry strength ($f_{\text{mod}} / f_{\text{exp}}$) are used for the evaluation of the predictive models. More precisely, the statistical indices calculated are: the mean, the coefficient of variation and the average absolute error of estimation. The relationships of those indices are discussed in the next two subsections.

Mean and coefficient of variation. Mean, designates the average of the ratios $f_{\text{mod}} / f_{\text{exp}}$ as shown in equation (5). For mean values greater than unity the experimental strength is overestimated, which demonstrates that the model predictions are unsafe. For ratios $f_{\text{mod}} / f_{\text{exp}} < 1$, the model is safe. Too low values imply that the model tends to underestimate the actual compressive strength of the specimen.

The coefficient of variation, $COV$, is calculated from equation (6). It is noted that lower values of $COV$ indicate better predictive capacity of the model. The $mean$ and the coefficient of variation of the ratios of the two variables ($COV$), are calculated by the relations:

$$mean = \frac{1}{n} \cdot \sum_{i=1}^{n} (f_{\text{mod},i} / f_{\text{exp},i}) \tag{5}$$

$$COV = \frac{\sqrt{\frac{1}{n} \cdot \sum_{i=1}^{n} [(f_{\text{mod},i} / f_{\text{exp},i}) - \frac{1}{n} \cdot \sum_{i=1}^{n} (f_{\text{mod},i} / f_{\text{exp},i})]^2}}{\frac{1}{n} \cdot \sum_{i=1}^{n} (f_{\text{mod},i} / f_{\text{exp},i})} \tag{6}$$

where $mean$ is the average value of the ratios $f_{\text{mod},i} / f_{\text{exp},i}$ of a database with $n$ datasets, $f_{\text{mod},i}, f_{\text{exp},i}$ are the estimated and the experimental compressive strength, respectively, of a dataset with index $i$ and $COV$ is the coefficient of variation for the datasets considered.

**Average absolute error of estimation.** The index of average absolute error (Average Absolute Error – AAE) [17, 18], expresses – on average – the relative error between the estimated and experimental masonry compressive strength of a database, as a percentage of the experimental strength. The relation that provides the average absolute error of the estimation is defined as shown in equation (7):

$$AAE = \frac{\sum_{i=1}^{n} \left| \frac{f_{\mathrm{mod},i} - f_{\mathrm{exp},i}}{f_{\mathrm{exp},i}} \right|}{n} \tag{7}$$

where $AAE$ is the average absolute error of estimation, $f_{\mathrm{mod},i}$, $f_{\mathrm{exp},i}$ are the estimated and the experimental compressive strength, respectively, of an -$i$ dataset and $n$ is the number of datasets included in the database.

# 5 Results

The compressive performance of the two types of specimens is, as expected, different. The presence of vertical joints in the wallettes increases their horizontal deformation during compression and as a consequence reduces quite frequently their ability of resistance. For this reason, the evaluation of the design models is carried out separately for the two types of specimens.

Figure 2 demonstrates the comparison between experimental strengths, $f_{\mathrm{exp}}$, and estimated strengths, $f_{\mathrm{mod}}$. The circular points represent the prism specimens and the diamonds the wallettes. The points on the bisector correspond to $f_{\mathrm{mod}} = f_{\mathrm{exp}}$. The points in the diagrams included between the bisector and the upper dashed line correspond to overestimation of the model up to 20%. Similarly, the points included below the bisector and between the lower dashed line indicate that the model underestimates up to 20% the experimental strength of specimens.

Table 4 presents the results of the statistical analysis indices shown in section 4, which qualitatively capture the degree of reliability of the predictions of the models of section 3, for the two types of specimens.

As demonstrated in Fig. 2, the predictive models tend to overestimate the compressive strength of prisms and wallettes with experimental strength lower than 5 MPa. For greater experimental strengths, EN 1996-1-1 estimations are better for wallettes in comparison to prism specimens.

For this range of compressive strengths, the predictions of TMS 602 model are, mainly, conservative. The model significantly underestimates the experimental strengths of both types of specimens constructed with units and mortars of very high compressive strength. That is probably due to the equation of the American Standard which ignores the compressive strength of mortar and its contribution to masonry's strength.

In contrast, specifically for prism and wallette specimens which are constructed with masonry units of very high compressive strength, the estimations of the Rossi model are in general much higher from experimental strengths.

The model Tassios, results quite good estimated strengths for both types of wall

specimens, as shown from the diagrams of Fig. 2 and the statistical indices in Table 4.

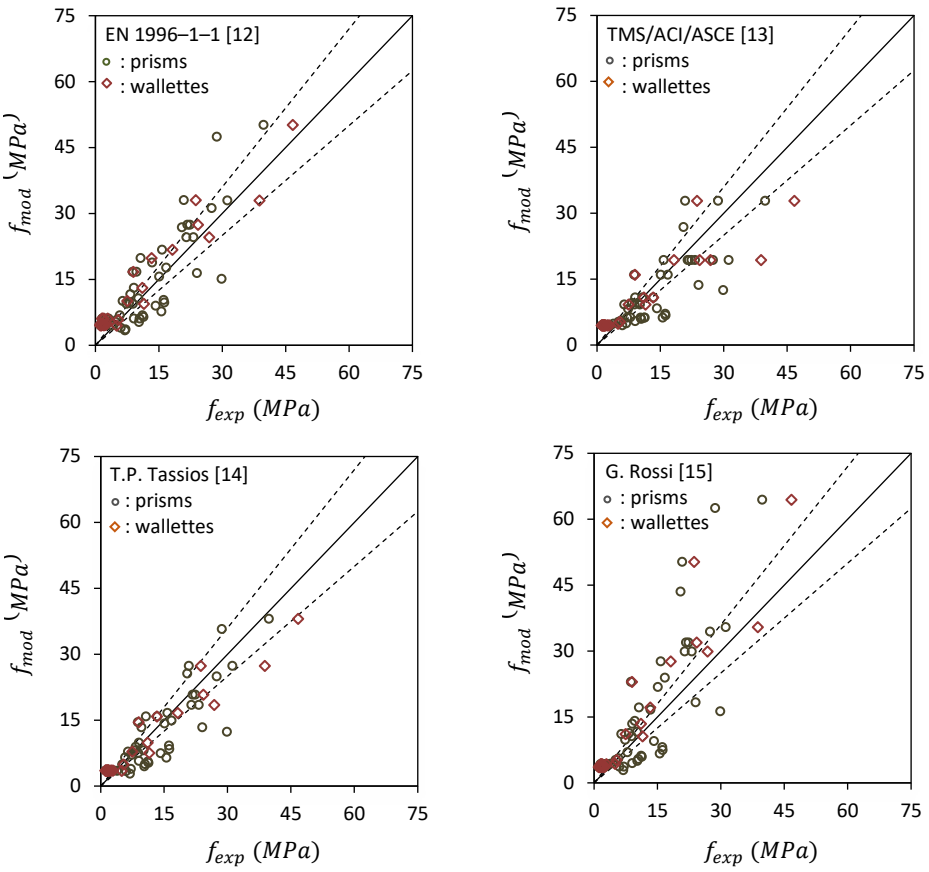


**Fig. 2**. Comprarison between experimental strengths $f_{\exp}$ and estimated strengths $f_{\mathrm{mod}}$

**Table 4.** Statistical indices for the database per type of specimen (P: Prisms, W: Wallettes)

| Models | $\sum_{i=1}^{n}(f_{\mathrm{mod},i} / f_{\mathrm{exp},i})$ | | | | $AAE$ | |
|---|---|---|---|---|---|---|
| | $mean$ | | $COV$ | | | |
| | P | W | P | W | P | W |
| EN 1996–1–1 [12] | 1.54 | 2.20 | 0.59 | 0.49 | 0.75 | 1.24 |
| TMS/ACI/ASCE [13] | 1.33 | 1.93 | 0.63 | 0.53 | 0.61 | 1.06 |
| T.P. Tassios [14] | 1.18 | 1.62 | 0.54 | 0.47 | 0.48 | 0.75 |
| G. Rossi [15] | 1.42 | 1.89 | 0.49 | 0.37 | 0.66 | 0.91 |

# 6 Conclusions

In this paper the reliability of four models to predict the compressive strength of masonry specimens consisting of solid clay bricks and different types of mortars, is examined. For that purpose an experimental database of compression tests, under monotonic loading, on prism and wallette specimens, was assembled.

The processing of the data was carried out by type of specimen. From the analysis of the results the following conclusions are drawn for the sample of the database presented in this paper:

- The predictive models significantly overestimate the compressive strength of masonry specimens with experimental strength lower than 5 MPa for both types of specimens
- The estimated strengths of the model calculated according to EN 1996–1–1, for the masonry specimens with experimental strength greater than 5 MPa, are placed better in the comparison diagrams for the wallettes than for the prism specimens.
- The predictions of TMS 602 model, for the specimens with experimental strength greater than 5 MPa, are in general conservative
- The estimations of Tassios model result in quite good estimated strengths and statistical indices for both types of wall specimens
- The model proposed by Rossi mainly overestimates the experimental strengths of both prism and wallette specimens

## References

1. Ciblac, T., Morel, JC.: Sustainable Masonry: Stability and Behavior of Structures. ISTE Ltd and John Wiley & Sons, Inc., (2014)
2. Fishburn, CC.: Effect of mortar properties on strength of masonry. United States Department of Commerce, National Bureau of Standards Monograph 36, (1961)

3. Singh, SB., Munjal, P.: Bond strength and compressive stress - strain characteristics of brick masonry. Journal of Building Engineering 9, 10–16 (2017)
4. Zucchini, A., Lourenço, PB.: Mechanics of masonry in compression: Results from a homogenisation approach. Computers & Structures 85, 193–204 (2007)
5. Francis, AJ., Horman, CB., Jerrems, LE.: The effect of joint thickness and other factors on the compressive strength of brickwork. In: Proceedings of the 2th International Brick and Block Masonry Conference, Stoke-on-Trent, United Kingdom (1971)
6. Monteagudo, SM., Casati, MJ., Gálvez, JC.: Influence of the bed joint thickness on the bearing capacity of the brick masonry under compression loading: an ultrasound assessment. Journal of Construction 14(1), 9–15 (2015)
7. Thaickavil, NN., Thomas, J.: Behaviour and strength assessment of masonry prisms. Case Studies in Construction Materials 8, 23–38 (2018)
8. Costigan, A., Pavía, S.: Influence of the mechanical properties of lime mortar on the strength of brick masonry. Historic mortars: characterization, assessment and repair, RILEM book series 7, 359–372 (2012)
9. Lumantarna, R., Biggs, DT., Ingham, JM.: Uniaxial compressive strength and stiffness of field extracted and laboratory constructed masonry prisms. Journal of Materials in Civil Engineering 26(4), 567–575 (2014)
10. Ravula, MB., Subramaniam, KVL.: Experimental investigation of compressive failure in masonry brick assemblages made with soft brick. Materials and Structures 50(19), 1–11 (2017)
11. Vermeltfoort, AT.: Compression properties of masonry and its components. In: Proceedings of the 10th International Brick and Block Masonry Conference, Calgary, Alberta, Canada, 1433–1442 (1994)
12. European Standard EN 1996-1-1. Eurocode 6: Design of masonry structures, Part 1-1: General rules for reinforced and unreinforced masonry structures. European Committee for Standardization, Brussels, Belgium (2005)
13. American Standards TMS 402-11/ACI 530-11/ASCE 5-11, TMS 602-11/ACI 530.1-11/ASCE 6-11. Building Code Requirements and Specification for Masonry Structures. Masonry Standards Joint Committee (MSJC), United States of America (2011)
14. Tassios, TP.: Mechanics of masonry (under static and seismic conditions), National Technical University of Athens, Reinforced Concrete Laboratory. Symmetria Publications, Greece (1992). (In Greek)
15. Rossi, G.: Compressive Strength of masonry: Proposal of a formula on experimental bases valid also for elements with "irregular holes" and/or discontinued mortar joints. In: Proceedings of the 6th International brick masonry conference, Rome, Italy, 364–375 (1982). (In Italian)
16. Greek Code for the assessment and structural interventions of masonry structures. Government Gazette, Greece (2023). (In Greek)
17. Moretti, ML., Kono, S., Obara, T.: On the shear strength of reinforced concrete walls. ACI Structural Journal 117(4), 293–304 (2020)
18. Ozbakkaloglu, T., Lim, JC., Vincent, T.: FRP - confined concrete in circular sections: Review and assessment of stress - strain models. Engineering Structures 49, 1068–1088 (2013)

# Can we quickly retrieve Seismic Source Spectrum characteristics after a large magnitude earthquake? Implementation of an approach based on coda wave analysis

Grendas, I.[1][0000-0003-4142-1795], Theodoulidis, N.[1][0000-0002-0169-9197], Hollender, F.[2][0000-0003-1440-6389] and Hatzidimitriou, P.[3][000-0002-9366-1187]

[1]Institute of Engineering Seismology and Earthquake Engineering, Greece
[2]Atomic Energy and Alternative Energies Commission (CEA), France
[3]Aristotle University of Thessaloniki, Greece
grendasioannis@gmail.com, ntheo@itsak.gr, fabrice.hollender@cea.fr, chdimitr@geo.auth.gr

**Abstract.** After a large magnitude earthquake event, the direct estimation of its Seismic Source Spectrum (SSS) is important to estimate the energy content of the seismic source in broad-band frequency range. This direct knowledge of the SSS, except for the fact that can directly provide information about the Moment Magnitude of the earthquake, constitutes also, in frequency domain, that information, which is required to the Fourier Amplitude Spectra (FAS) simulation of the real-input seismic motion, in several target sites close to the source for which no earthquake recordings exist. In this study, the computation of the SSS of an earthquake is based on a single-station analysis algorithm by applying the spectral factorization method on the coda wave part of a seismic record. An application of this algo-rithm is implemented here for the Mw = 6.1 Cephalonia Island earthquake of 26/01/2014. The corresponding SSS, computed for several stations away from the source, are compared with the average SSS retrieved by standard applied method. The comparison results strongly encourage application and development of this SSS computation approach.

**Keywords:** Seismic Source Spectrum, Coda waves, Near-field motion estimation

## 1 Introduction

Simulation of seismic ground motion or its Fourier Amplitude Spectrum (FAS) at specific sites close to a seismic fault, is significant in understanding the amount of energy that affected the nearby constructions. Realistic simulation is directly related to the knowledge of fault rupture, or in other words of its Source Time Function (STF). In most of large magnitude earthquakes ($M \geq 6.0$), the STF estimation is achieved through relevant time-consuming processes (e.g. the method of Empirical Green's Functions, [1], [2], [3]) that requires selection and combination of several earthquake records quite close to the seismic source, so as to converge to a single-accepted STF solution. In other

cases, the STF estimation is impossible to be extracted, since not enough number of earthquake records exist close to the seismic source due to the lack of installed stations. For this reason, to estimate a STF, proper use of remote stations with respect to seismic source, is an issue that requires further research.

In this short study the applied methodology that uses the coda waves part of an earthquake recording, based on a particular property related to their "generation" natural mechanism, as firstly studied in [4], [5], and [6], seems that can provide Seismic Source characteristic by using remote stations with respect to the Source. Moreover, this methodology can be directly applied to a single earthquake-station record, without requiring the combination of several records of the same earthquake, being also feasible to make the computation in real time, after a few minutes of the earthquake occurrence and its origin time determination.

Except for the STF, its Fourier Amplitude Spectrum (FAS) is an essential information about the characteristics of the amount of seismic source energy releasement per each frequency, albeit it does not directly provide the time domain characteristics of the fault rupture. A methodology where the FAS of an earthquake can be estimated based on a single station analysis, by using the coda wave part of an earthquake record has been introduced in [7]. Moreover, based on this study ([7]), the unique produced wavelet, which corresponds to the minimum phase scenario of the extracted FAS, is similar to the real STF, which is general considered as a simple pulse, corresponding to a point source for low magnitude earthquakes. In large magnitude earthquakes the point source scenario is generally not the expected one, considering that the fault rupture is a relevant complicated function of space and time.

In this study an effort in retrieving the FAS of a large earthquake (Mw = ~6.1), based on this coda wave analysis [7], was implemented using the modified coda wave analysis algorithm developed in [8]. The examined earthquake is the one occurred in western Greece, on Cephalonia Island and it was chosen since its source characteristics were known by other studies and could validate the results extracted by the present research study.

It's worth noting that the coda wave analysis was applied to stations located on non-reference sites after removing their corresponding Site Amplifications Factor, as they were determined by [8], since no records were available by accelerographs located on rock site.

## 2 Methodology

Computation of the Fourier Amplitude Spectrum (FAS) of a seismic source, is based on a single station analysis proposed in [7], applied on the coda waveform of an earthquake record (e.g. Fig.1.). This analysis can be applied in 7 steps (Fig.2.), as defined in [8], plus one more aiming to scale the corresponding FAS of the seismic source. The analysis is based on the following fundamental equation (1) that relates the Power Spectral Density (PSD), $R_{ij}(f, t')$ of a coda wave window, centred at travel time, $t'$, with the corresponding PSD of the Seismic Source, $W_i(f)$, of $E_c$, coda excitation factor, of

Attenuation Path, $|A_C(f,t')|^2$ and of Site Amplification Factor (SAF(f)2 = N_j (f)), at a station, j and a source, i ([4], [5], [6]):

$$R_{ij}(f,t') = W_i(f) \cdot E_c \cdot |A_C(f,t')|^2 \cdot N_j(f) \quad (1)$$

where:

$$|A_c(f,t')|^2 = \frac{1}{(v_s \cdot t')^2} e^{-\frac{2\pi f t'}{Q_c(f)}} \quad (2)$$

and

$$W_i(f) = \frac{\left|\dot{\Omega}_i(f)\right|^2}{10\pi\rho\beta^5} \quad (3)$$

following the source model given in [9].

The attenuation factor (Eq. (2), [5], [6], [10]), except for the travel time, $t'$, is controlled by the average shear wave velocity, $v_s$ of the total examined area, as well as by the frequency dependent quality factor, $Q_c(f)$ of the coda waves. The PSD of the seismic source, $W_i(f)$, is controlled by its corresponding FAS, $\dot{\Omega}_i(f)$ and is scaled by the average shear wave velocity, $\beta$ and density, $\rho$ close to the fault.

The $R_{ij}(f,t')$ is also controlled by the coda wave excitation factor, $E_c$ ([11]) as following:

$$E_c = \frac{1}{\pi \cdot l} \quad (4)$$

where, $l$ (in meters) is the mean free path factor ([6]), expressing the fractional loss of energy per unit travel distance of the shear waves from the source to the receiver, due to the wave scattering by the lithosphere heterogeneities ([12]). All those scattered waves arrive late in time, after the main seismic motion of the direct P and S-waves, with reduced amplitudes in time, due to the longer travel distances and they actually form the "tail" of the seismograms (e.g. Fig.1.).

The first two steps of the coda wave analysis, refer to the signal pre-processing corrections related to the instrument characteristics, as well as to a suitable Signal to Noise Ratio (SNR) analysis determined in [8], so as to detect the good quality coda wave record which is able to extract the reliable FAS of the seismic source.

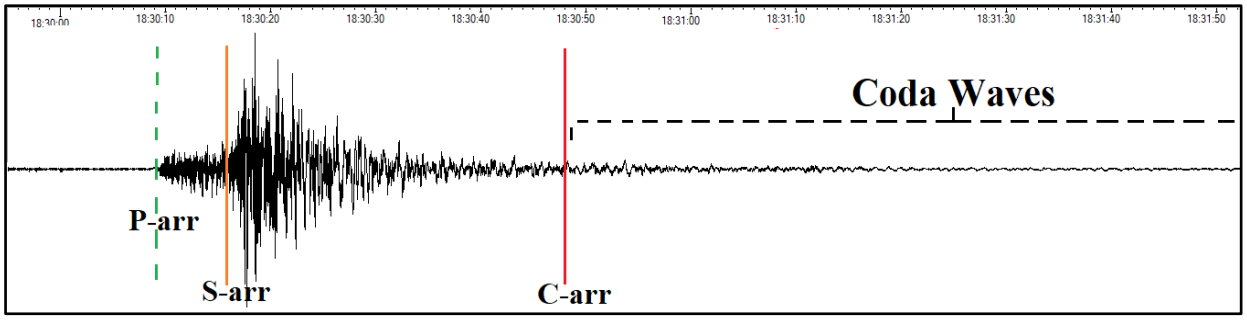


**Fig. 1.** An example of an earthquake record, where the P, S and Coda wave arrival times are depicted, in green, orange and red vertical lines, respectively

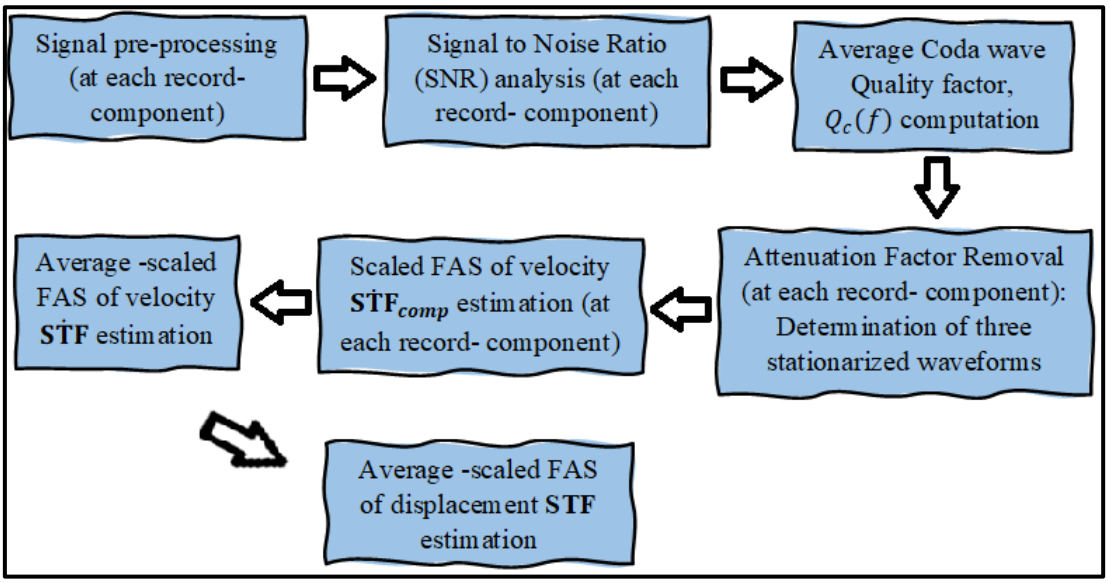


**Fig. 2.** The flowchart of the 7 steps applied by the examined coda wave analysis, for the estimation of the average – scaled by the mean free path factor, $FAS[\mathrm{STF}^{sc}]$ (in displacement) (modified by [8])

In the third step the common for the three components (EW, NS and vertical one) frequency dependent coda wave Quality factor, $Q_c(f)$ is estimated, as well as its standard deviation, based on the process introduced in [5] and analytically explained in [13]. In the fourth step the frequency dependent and distance dependent attenuation factor is removed in time domain by each component of the source-site coda wave record, based on the deconvolution ([14]) of all the progressive in time, $t'$ minimum phase wavelets, $A_C(t,t')^{min}$ (Eq. (2)), as analytically explained in [8]. By this way the three component coda wave records (e.g. Fig.3., top) are "corrected" for the attenuation factor and three stationarized waveforms are "created" (e.g. Figure 3, bottom). These three waveforms

are directly reduced to the source, but they are still scaled by the constant mean free path factor (Eq. (1) and (4)).

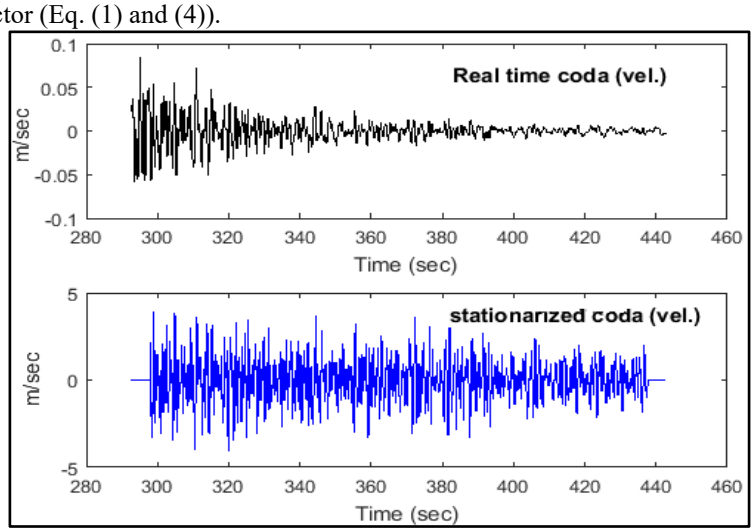


**Fig. 3.** An example of a real coda waveform (top) and of the corresponding corrected for the attenuation factor, stationarized coda waveform (bottom)

In the fifth step of the coda wave analysis algorithm (Figure 2) the scaled FAS of the $S\dot{T}F$ (in velocity) at each horizontal component $FAS[S\dot{T}F^{sc}_{comp}]$) is extracted (e.g. Figure 4a), being uncorrected for the low frequency noise effect, related to the SNR process. Finally, at the sixth step the two horizontal components STF (in velocity) are cumulatively combined in terms of energy according to the following formula:

$$FAS[S\dot{T}F^{sc}] = \sqrt{FAS[S\dot{T}F^{sc}_{EW}]^2 + FAS[S\dot{T}F^{sc}_{NS}]^2} \quad (5)$$

concluding to the average, scaled by the mean free path factor, $FAS[S\dot{T}F^{sc}]$ (in velocity). It's worth noting that the standard deviation of each $FAS[S\dot{T}F^{sc}_{comp}]$), is considered in the average $FAS\left[S\dot{T}F^{sc}\right]$ computation, based on the propagation error method.

In the seventh step (Fig.2.), the average, scaled by the mean free path factor, $FAS[\mathrm{STF}^{sc}]$ in displacement is determined after dividing by the frequency dependent, $2\pi f$, factor ($f \neq 0$) (e.g. Fig.4b). Here it must be clarified that this $FAS[\mathrm{STF}^{sc}]$ refers to the good quality part of the coda waves in frequency domain defined after the suitable Signal to Noise Ration process and it is still affected by the low frequency noise. In general, in case that the minimum phase wavelet corresponding to $FAS[\mathrm{STF}^{sc}]$ is wished to be computed, this low frequency noise effect must be corrected in an extra step, to a low frequency plateau (e.g. Fig.4b), as it is normally expected for the STF which must be a positive wavelet representing the moment rate in time.

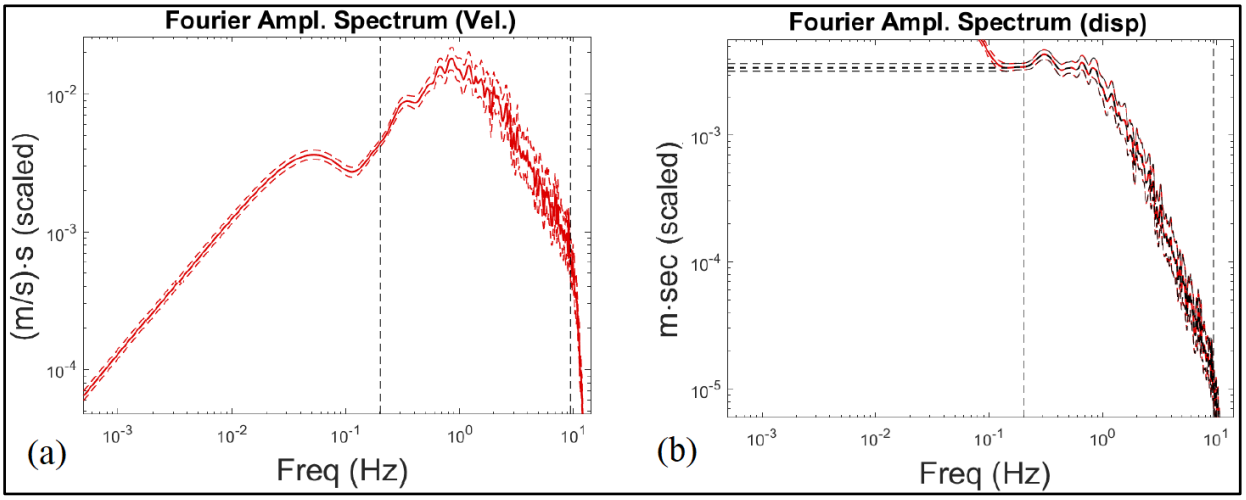


**Fig. 4.** (a) An example of a 〖FAS[(STF)˙〗 _comp^sc]) (Eq. (5)), in velocity (for the EW component) and of its standard deviation, for the ML = 4.3 earthquake of 20190117_214639. Between the vertical dashed lines, the reliable frequency range is defined based on the already applied SNR process (b) An example of a FAS[(STF)¨^sc] (in displacement) (Eq. (5)). In horizontal black dashed line, the low frequency plateau correction on the non-reliable frequency part, is depicted

## 3 Data

The data used in this study refer to the coda wave part (e.g. Fig.1.) of five, 3-component, seismic records, corresponding to the $M_w$ = 6.1 (±0.2) ($M_L$ = 5.8) earthquake occurred in western Greece (Cephalonia island, 26/1/2014, GMT: 13:55:43, Lat: 38.1522o, Long: 20.3912o, Depth: ~15 km, as given by the Seismological Station of Aristotle University of Thessaloniki and confirmed in [15]) (Fig.5.). The examined earthquake records correspond to the accelerograph stations: PRE2, MSL1, PAT4, KAC1 and ZAK2, which belong to the Institute of Engineering Seismology and Earthquake Engineering (ITSAK). These recordings were selected in this study, since they were the only ones that included coda wave records appropriate to be analyzed and were not interrupted by the occurrence of other local earthquake recordings. Regarding the characteristic of the examined Seismic Source of the Cephalonia earthquake the fault process of this earthquake was related to the Cephalonia Transform Fault zone ([16]), as it is indicated in [17] and was dominated mainly by a dextral strike slip motion (Figure 5). Also, based on the rupture process study of this earthquake which was carried out in [15], the fault strike lies on NNE-SSW direction, and its plane is steeply dipped to the East (Fig.5.).

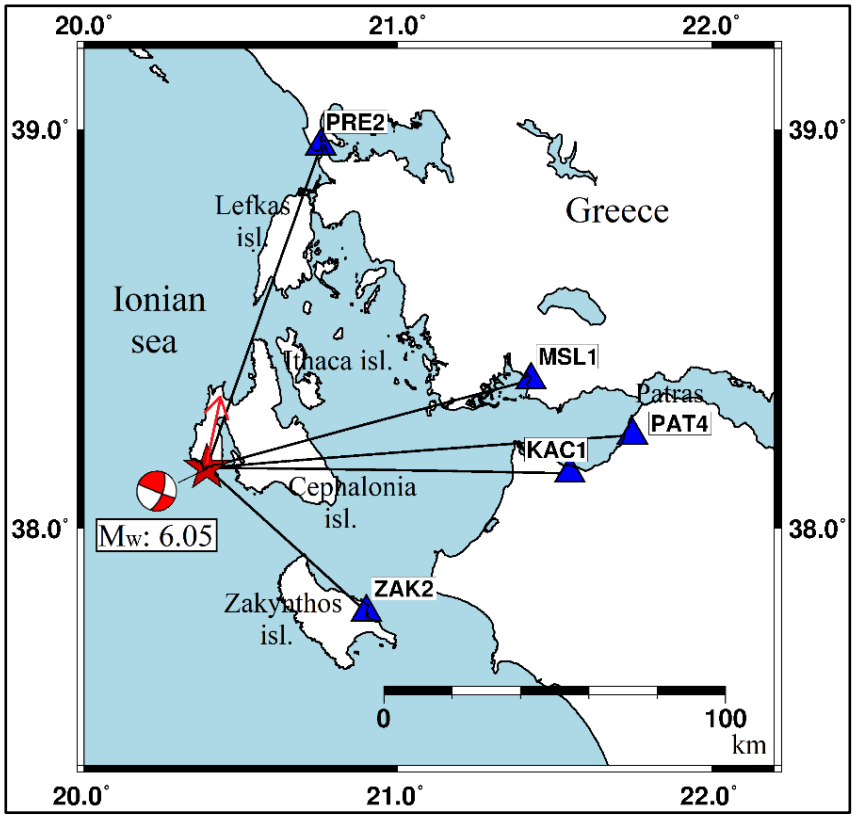


**Fig. 5.** The examined area (western Greece). In red asterisk the location of the Cephalonia earthquake is depicted ([15] and Seismological Station of Aristotle University of Thessaloniki), as well as its focal mechanism ([17]) and the rupture direction (red arrow). The location of the five examined stations (Institute of Engineering Seismology and Earthquake Engineering), are presented in blue triangles

## 4 Results

Based on the coda wave analysis mentioned above, the scaled Fourier Amplitude Spectra, $FAS[\dot{STF}^{sc}]$ (Eq. (5), e.g. Figure 4a), in velocity, of the $M_w$ = 6.1, Cephalonia earthquake, for the horizontal component, were determined for the five examined stations (Fig.5.). Then the corresponding scaled $FAS[\mathrm{STF}^{sc}]$ in displacement were computed by dividing the $FAS[\dot{STF}^{sc}]$ ], with $2\pi f$ ($f \neq 0$). Finally, these $FAS[\mathrm{STF}^{sc}]$ results were divided by the coda excitation factor, $E_c$ (Eq. (4)), based on Eq. (1), so as to be scaled. The mean free path value, $l$ (Eq. (4)) was considered equal to 253 km, as it was determined in [8], examining plethora of low to moderate magnitude earthquakes in this area (western Greece) and scaling the computed $FAS[\mathrm{STF}^{sc}]$ with the extracted ones by a Generalized Inversion Technique application for the same dataset ([18]). Except for the average value of $l$, its standard deviation range, in logarithmic scale (88 km

– 727 km), which was also determined in [8], was considered in order to take into account the statistical uncertainties at the $FAS$[STF] estimation. In Figure 6 the unscaled $FAS$[STF] results of the examined earthquake, for the five examined station, are presented. It's worth noting that these $FAS$[STF] are also corrected for the corresponding known frequency dependent average Site Amplification Factors (SAF(f)), as they were computed in [8]. The correction was achieved in frequency domain by dividing the $FAS$[STF] with the corresponding SAF(f).

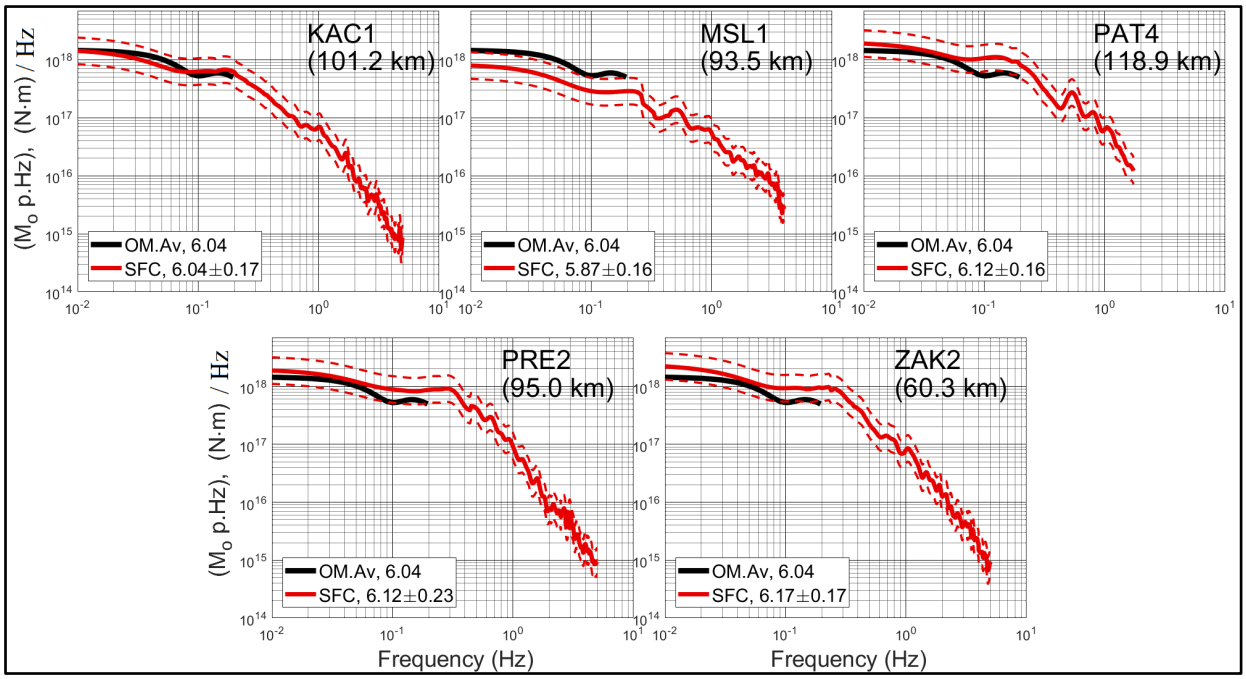


**Fig. 6.** The examined area (western Greece). In red asterisk the location of the Cephalonia earthquake is depicted ([15] and Seismological Station of Aristotle University of Thessaloniki), as well as its focal mechanism ([17]) and the rupture direction (red arrow). The location of the five examined stations (Institute of Engineering Seismology and Earthquake Engineering), are presented in blue triangles

The moment magnitudes, $M_w$, separately extracted by each one $FAS$[STF] (Figure 6), are quite close to the $M_w$ = 6.04±0.20, determined in [15], [17] and by the Seismological Station of Aristotle University of Thessaloniki, while their average, $M_w$= 6.08±0.20 (Figure 7a) and its standard deviation indicate reliable results regarding the scaling of the $FAS$[STF]. Moreover, a quite good agreement is presented between all the $FAS$[STF] and their standard deviation range at each station, with respect to the corresponding average $FAS$[STF] extracted by an alternative methodology performed in [15], up to 0.2 Hz, which is the higher frequency limit of their computation. Also, the results by the coda wave analysis gave Fourier Amplitude information in higher frequencies up to ~5 Hz, where in Figure 7a, it seems that they satisfactorily agree between each other. This result also supports reliability of the examined $FAS$[STF]

estimation approach, although corresponding information in higher frequencies do not exist by other methodologies to compare.

Finally, in this study an effort was made in retrieving the Source Time Function wavelets, of the examined earthquake, at each station, based on the computed $FAS$[STF] (Fig.6.) and on the minimum phase scenario, as proposed in [7]. The results presented in Fig.7b, confirm that the minimum phase scenario in large magnitude earthquake like the examined one, ($M_w$ = ~6.1) does not satisfactory simulate how the energy releases in time (Fig.7c). However, as it is presented in Fig.7d, based on the total energy release computations of Fig.7c, the 95% of the total energy release by the minimum phase STF wavelets (average ~12.5 sec), is in good agreement with the actual fault-rupture duration (~12.1 sec) estimated in [15]. This indicates that the minimum phase scenario could reveal this important information of the seismic source.

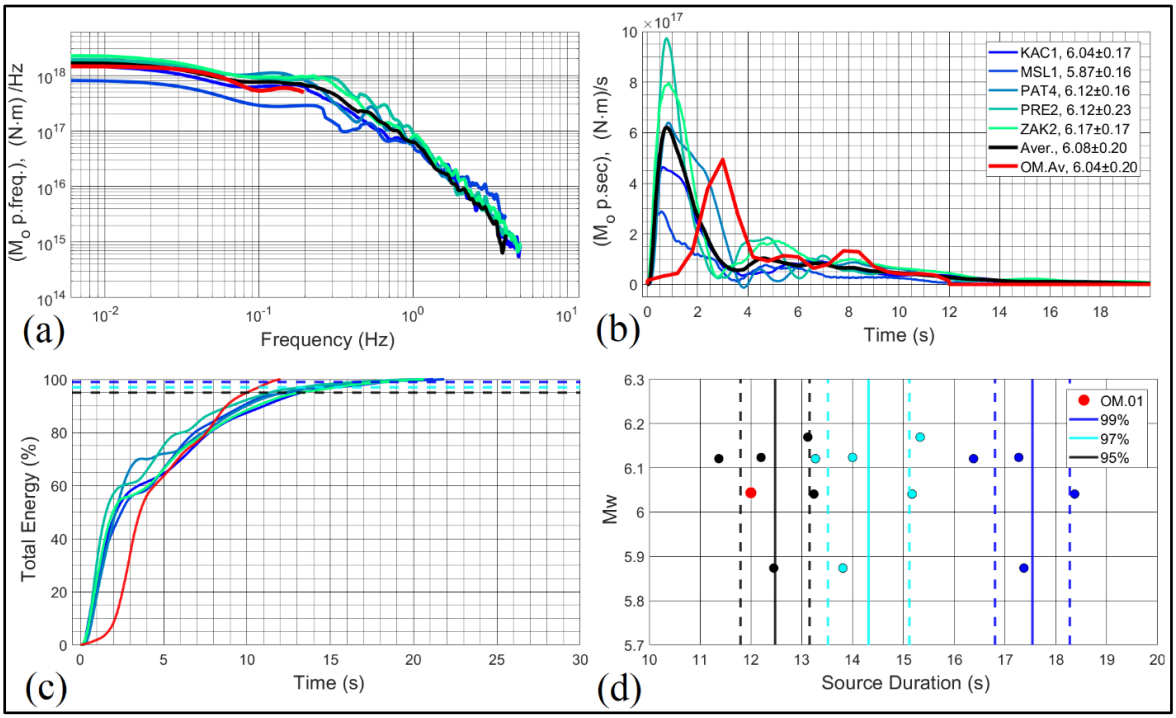


**Fig. 7.** (a) The $FAS$[STF] of the examined earthquake computed in this study (Fig.6.), for each one of the five stations (multi-color lines), their average one (black line) and the $FAS$[STF] (red line) computed by [15], using Other Methodology (O.M.). (b) The corresponding to each $FAS$[STF] of Figure 7a, minimum phase wavelets (c) The total energy release of each minimum phase wavelet of Figure 7b (d) The duration of each minimum phase wavelet of Fig.7b, corresponding to 95%, 97% and 99% of the total energy release of Fig.7c

# 5 Conclusions

In this study an application of the Spectral Factorization of Coda waves (SFC) methodology, proposed in [7], was applied for a large magnitude earthquake, Mw = ~6.1, in Cephalonia Island 9 (26/1/2014), aiming at retrieving the Fourier Amplitude Spectrum (FAS) of its Source Time Function (STF). Five FAS[STF]s were computed for five accelerograph stations located in western Greece, recorded the earthquake in epicentral distances from ~60 km to 120 km. These FAS[STF]s results are in satisfactory agreement with the corresponding FAS[STF]s determined in [15] at least up to ~0.2 Hz, the upper frequency limit of the latter. Moreover, the computed seismic moment magnitudes determined separately by these FAS[STF]s, as well as their average ($M$w= 6.08□}0.20), are in very good agreement with the corresponding magnitude determined in [15], [17] and by the Seismological Station of Aristotle University of Thessaloniki. In general, the FAS[STF]s of this study exhibits a satisfactory agreement between each other, providing information up to ~5 Hz. This agreement and stability of the results is encouraging to assessing reliably and rapidly seismic source properties based on coda waves.

Finally, an effort in retrieving the minimum phases STF wavelets was implemented. Based on the results it can be concluded that the minimum phase scenario does not satisfactorily agree with the STF estimated in [15]. Consequently, it seems that the methodology applied in this study cannot accurately estimate STF of complex seismic sources (e.g. M ≥ 6.0). However, based on the estimated minimum phase STF wavelets, it results that their duration which corresponds to 95% of the total energy release (11.5-13.1 sec), is in very good agreement with the respective STF duration (~12.1 sec) estimated in [15]. After all, it can be concluded that the methodology applied in this study can reliably and quickly estimate important properties of the seismic source, even for large magnitude earthquakes. Consequently, estimation of strong ground motion in the near field can be greatly supported by the methodology applied in this work.

# Acknowledgments

This work was funded by the SIREAT (KE 2.027) project. Pr. Pierre-Yves Bard has greatly contributed to understanding the theoretical background of the applied methodology.

# References

1. Courboulex F, Santoyo MA, Pacheco JF, Singh SK. The 14 September 1995 (M = 7.3) Copala, Mexico, earthquake: a source study using teleseismic, regional, and local data. Bull Seism Soc Am 1997;87–4:999–1010
2. Roumelioti Z, Benetatos C, Kiratzi A. The 14 February 2008 earthquake (M6.7) sequence offshore south Peloponnese (Greece): source models of the three strongest events. Tectonophysics 2009;471–3:272–284
3. Vallée M. Stabilizing the empirical Green function analysis: development of the

projected Landweber method. Bull Seism Soc Am 2004;94–2:394–409
4. Aki K. Analysis of the Seismic Coda of Local Earthquakes as Scattered Waves. J Geophys Res 1969;74:615–31
5. Aki K, Chouet B. Origin of coda waves: Source, attenuation, and scattering effects. J Geophys Res 1975;80:3322–42. https://doi.org/10.1029/JB080i023p03322
6. Sato H. Energy propagation including scattering effects single isotropic scattering approximation. J Phys Earth 1977;25:27–41. https://doi.org/10.4294/jpe1952.25.27
7. Sèbe O, Guilbert J, Bard P-Y. Spectral factorization of the source time function of an earthquake from coda waves, application to the 2003 rambervillers, France, earthquake. Bull Seismol Soc Am 2018;108:2521–42. https://doi.org/10.1785/0120170038
8. Grendas I, Theodoulidis N, Bard PY, Perron V, Hatzidimitriou, P., Hollender F. Can site effects be estimated with respect to a distant reference station? Performance of the spectral factorization of coda waves. Geophys J Int 2022;230:1–28
9. Vassiliou MS, Kanamori H. The energy release in earthquakes. Bull Seismol Soc Am 1982;72:371–87
10. Sato H, Fehler MC, Maeda T. Seismic wave propagation and scattering in the heterogeneous earth. Vol. (496). Berlin: Springer; 2012
11. Herraiz M, Espinosa AF. Coda waves: A review. Pure Appl Geophys PAGEOPH 1987;125:499–577. https://doi.org/10.1007/BF00879572
12. Aki K. Scattering and attenuation of shear waves in the lithosphere. J Geophys Res 1980;85:6496–504. https://doi.org/10.1029/JB085iB11p06496
13. Margerin L, Campillo M, Shapiro NM, Van Tiggelen B. Residence time of diffuse waves in the crust as a physical interpretation of coda Q: Application to seismograms recorded in Mexico. Geophys J Int 1999;138:343–52. https://doi.org/10.1046/j.1365-246X.1999.00897.x
14. Margrave GF. Theory of nonstationary linear filtering in the Fourier domain with application to time-variant filtering. Geophysics 1998;63:244–59. https://doi.org/10.1190/1.1444318
15. Sokos E, Kiratzi A, Gallovič F, Zahradník J, Serpetsidaki A, Plicka V, et al. Rupture process of the 2014 Cephalonia, Greece, earthquake doublet (Mw6) as inferred from regional and local seismic data. Tectonophysics 2015;656:131–41. https://doi.org/10.1016/j.tecto.2015.06.013
16. Scordilis EM, Karakaisis GF, Karacostas BG, Panagiotopoulos DG, Comninakis PE, Papazachos BC. Evidence for transform faulting in the Ionian sea: The Cephalonia island earthquake sequence of 1983. Pure Appl Geophys PAGEOPH 1985;123:388–97. https://doi.org/10.1007/BF00880738
17. Karakostas V, Papadimitriou E, Mesimeri M, Gkarlaouni C, Paradisopoulou P. The 2014 Kefalonia Doublet (Mw6.1 and Mw6.0), central Ionian Islands, Greece: Seismotectonic implications along the Kefalonia transform fault zone. Acta Geophys 2015;63:1–16. https://doi.org/10.2478/s11600-014-0227-4
18. Grendas I, Hollender F, Theodoulidis N, Hatzidimitriou P. Spectral decomposition of S - waves in investigating regional dependent attenuation and improving site amplification factors: A case study in western Greece. Bull Earthq Eng 2022:1–25. https://doi.org/10.1007/s10518-022-01459-z

# Seismic Assessment and Proposal for Interventions of a Historical Masonry Building in Rhodes

Andromachi Eleftheriou[1], Aristidis Papachristidis[2] and Constantinos Repapis[1]

[1]University of West Attica, 250 Thivon & P. Ralli str., 12244, Athens, Greece
[2]3DR Engineering Software
andromahi.elef@gmail.com, crepapis@uniwa.gr
aristidi@3dr.eu

**Abstract.** The aim of this study is the seismic assessment of a historical two-storey masonry building, located in the city of Rhodes and the investigation of intervention ways to strengthen the building and improve the mechanical characteristics of its materials. The 3DR.PESSOS software was used for the simulation and analysis of the structure. For the evaluation of the seismic behaviour of the building, an elastic static analysis (lateral force analysis) was carried out based on the Greek Code for Structural Interventions of Masonry Structures. Elastic static analysis methods with global behaviour factor ($q$) or local ductility indices ($m$) were applied for performance levels B1 and B2. From the analyses and the code checks it was concluded that the building is vulnerable to in-plane and out-of-plane actions. For this reason, methods of intervention are being investigated to increase the diaphragm function of the building and to improve the mechanical characteristics of the masonry.

**Keywords:** Seismic Assessment, Historical Building, Unreinforced Masonry

## 1 Introduction

Masonry buildings until the mid-19th century constituted the majority of the built environment not only in Greece but all over the world. Despite the fact that it was one of the oldest materials, knowledge regarding its mechanical behaviour was limited. In the 1970's, an intense research interest began, which continues to this day, mainly due to the need to preserve old structures that constitute cultural heritage monuments. It had been proven that the methods of preservation and strengthening that had been used in the past were ineffective and sometimes even dangerous [1].

The seismic codes currently in force for the assessment and retrofitting of masonry buildings are Eurocode 8 - Part 3 [2] and the more recent Greek Code for Structural Interventions of Masonry Structures [3], which has been in force since 2023. The purpose of the Greek Code for Structural Interventions of Masonry Structures is to establish criteria for the assessment of the load-bearing capacity of existing masonry structures and their redesign after possible interventions (repairs, retrofits). Other methodologies have been proposed that lead to interventions with respect for the cultural and

archaeological characteristics of the structure [4]. Examples of strengthening schemes on cultural structures or bridges are presented in [5,6] while the application of non-destructive techniques for the investigation and rehabilitation of historical masonry structures or monuments are presented in [7-9]. Papanicolaou et al. [10] experimentally investigated the effectiveness of textile reinforced mortar (TRM) as strengthening material of unreinforced masonry walls subjected to out-of-plane cyclic loading, and it was concluded that TRM jacketing provides a substantial gain in strength and deformability.

In this study, an evaluation of a historical masonry building, located in Rhodes, is carried out based on the Greek Code for Structural Interventions of Masonry Structures. Specifically, it is checked whether the minimum requirements of its load-bearing capacity are met both during the assessment and during its redesign, after the proposed interventions. Under certain conditions, the minimum load-bearing capacity requirements for the assessment and redesign of an existing structure may be reduced compared to the provisions of the current design codes for new structures.

# 2 Case Study

## 2.1 Historical data – Building location

In 1522, when Rhodes was occupied by the Ottomans, the decisive measure in forming the new living conditions for the next 400 years was the removal of the Greeks from the walled city. Thus, in order to meet the needs of the persecuted population, new residential nuclei, the "Marasia", were created. This form of "Marasias" was maintained until 1925, when the Italian buildings began to be built. The Marasias thus expanded and, with the new urban organisation, especially towards the end of the Italian period, were integrated for the first time into a single urban fabric. Despite the alterations brought by the construction activity of recent years in the city of Rhodes, the urban fabric of Marasia is still preserved, while several buildings of the late 19$^{th}$ and early 20$^{th}$ century are still standing, thanks to their designation as preserved buildings by the Ministry of Culture and the Ministry of Environment, Physical Planning and Public Works. Although no building within the urban fabric of Marasi can be considered to be earlier than the end of the 18$^{th}$ century, we can assume that the type of housing in Marasia was formed in the early years of the Ottoman period and was maintained unchanged with minor variations until the end of the 19$^{th}$ century [11].

The building under consideration is located southeast of the Medieval City, within the urban plan of the city of Rhodes and specifically in the residential unit “Marasi Ag. Nikolaos”, where according to the ministerial decision of the Ministry of Culture [12] it is classified as a “Historic Site”. The building is also owned by the Archaeological Receipts and Expropriations Fund and since 1948 [13], it has been designated as a historical monument and is probably the earliest surviving example of a Marasio house.

## 2.2 Geometry, materials, loads

The masonry structure under investigation is constructed with two-leaf stone masonry of local Rhodesian porous stone, 50 cm and 55 cm thick. The structure is rectangular in plan, with three rooms and average external dimensions of 5.55 m wide and 24.60 m long. It consists of the ground floor, the mezzanine floor, which occupies 2/3 of the building, and the roof. The mezzanine consists of timber floorboard on wooden beams with dimensions of 10 cm x 15 cm at 50 cm spacing, while the roof consists of timber floorboard on wooden beams with dimensions of 15 cm x 20 cm at 50 cm spacing, covered with a light reinforced concrete slab. The height of the ground floor is 5.80 m and 3.25 m, while the height of the first floor is 2.55 m. Fig. 1. shows the ground floor plan and upper floor plan of the building.

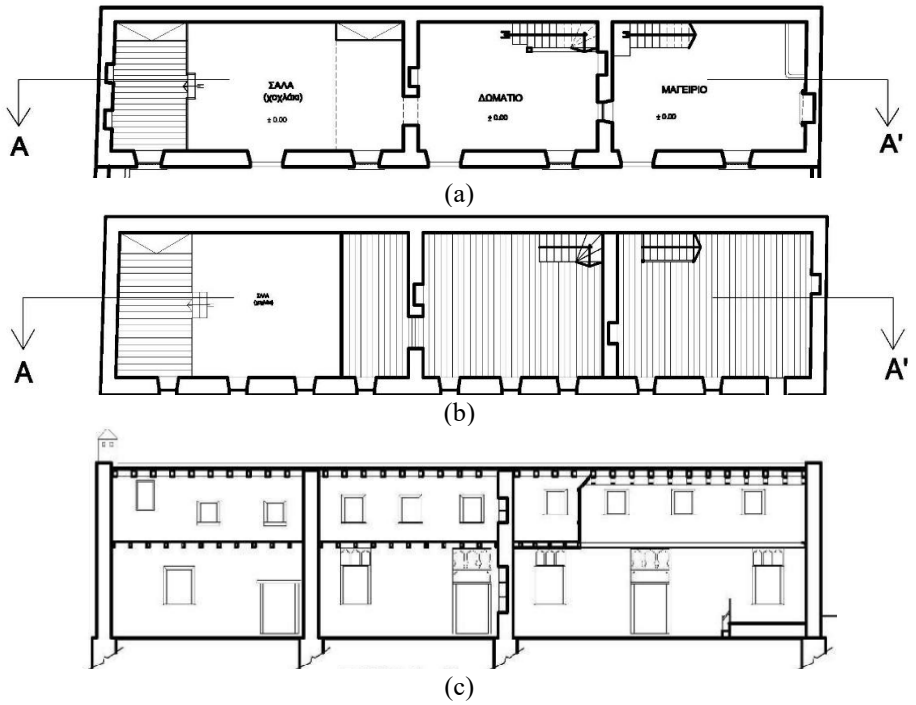


**Fig. 1.** (a) Ground floor plan, (b) first floor plan and (c) longitudinal section A-A' [14]

For the materials, properties were taken from experimental data for similar buildings. Thus, the compressive strength of the stone $f_{bc}$ was obtained equal to 30 MPa and the average compressive strength of the mortar $f_{mc}$ equal to 1.0 MPa. The compressive strength of masonry $f_{wc}$ which was calculated from Equation (1) [3, 15], was taken equal to 2.0 MPa.

$$f_{wc} = \xi \left[ \left( \frac{2}{3} \sqrt{f_{bc}} - f_0 \right) + \lambda \, f_{mc} \right] = 0.74 \left[ \left( \frac{2}{3} \sqrt{30} - 1.50 \right) + 0.50 \cdot 1.0 \right] = 2.0 \, MPa \quad (1)$$

where $\xi$ = 1 / [1 +3.5 ($k$ - $k_o$)] = 0.74, a coefficient which takes into account the adverse influence of the thickness of mortar joints, $k$ is the percentage by volume of mortar in the masonry, equal to 0.40, $k_o$ the maximum percentage of mortar considered not to cause a reduction in the strength of the wall, equal to 0.3, $f_o$ the coefficient which takes into account the degree of carving of the stones, equal to 1.50, $\lambda$ the coefficient of bonding between stone and mortar, equal to 0.5 for stone masonry.

The tensile strength of the masonry, $f_{wt}$, based on paragraph 6.5 of the Greek Code for Structural Interventions of Masonry Structures [3], was taken equal to 0.10 MPa and the mean characteristic initial shear strength of the masonry, $f_{vk0}$, based on Table 3.5 of EC6-1-1 [16], for natural stones, equal to 0.10 MPa. The self-weight of the masonry equal to 21 kN/m$^3$ and the material safety factor $\gamma_m$ equal to 1.35 based on paragraph 4.5.3.1 of the Greek Code for Structural Interventions of Masonry Structures [3]. The modulus of elasticity $E$ was calculated from the equation of Tasios [17], $E = \alpha f_{wc}$ =1600 MPa, where $\alpha$ = 800. According to EC8-1 [11] and EC8-3 [2], the stiffness is estimated as half of that for non-cracked elements, thus, the masonry modulus of elasticity was taken equal to 800 MPa. The shear modulus $G$ was taken equal to 315 MPa and the Poisson's ratio equal to 0.30.

A live load equal to 2.0 kN/m$^2$ and a permanent load equal to 1.0 kN/m$^2$ was taken on all the slabs of the first floor and the roof. The building is located in an area with seismic hazard zone II (reference peak ground acceleration on type A ground $a_{gR}$ = 0.24g according to EC8-1-1), soil class B (soil factor $S$ = 1.20), importance class II ($\gamma_I$=1). For the geometric data and materials, the data reliability level was taken as "sufficient" (knowledge level *KL2*: normal knowledge according to EC8-3).

## 3 Numerical Analyses

The finite element method was used for the simulation of the building, where the masonry was modelled with 3319 quadrilateral shell elements in 3DR.PESSOS software [12], with a maximum dimension of 50 cm (Fig. 2.).

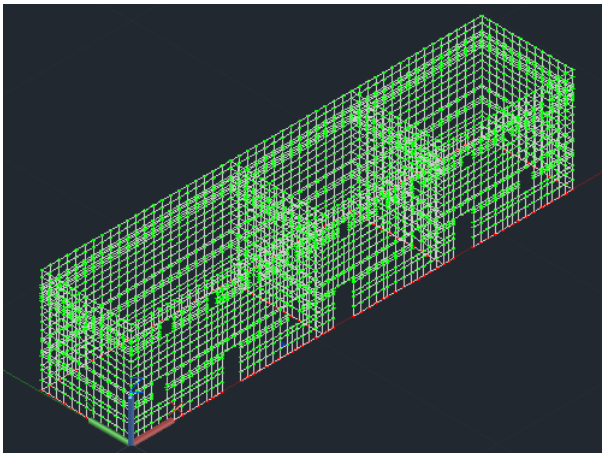

**Fig. 2.** 3D mathematical model of the building

The wooden floors were not simulated as static entities in the program. They were taken into account through their self-weight, dead and live loads, so that these loads were distributed to the perimeter walls.

For the determination of the building's stresses and deformations, an elastic (equivalent) static analysis (lateral force analysis) was carried out. Both elastic static analysis methods with global behaviour factor ($q$) and local ductility indices ($m$) were applied for performance levels B1 and B2, according to the Greek Code for Structural Interventions of Masonry Structures [3].

Figs. 3 and 4 show the distribution of moments $M_{xx}$ and $M_{yy}$ for the two basic seismic combinations $G + 0.30\,Q + E_x + 0.30\,E_y$ and $G + 0.30\,Q + 0.30\,E_x + E_y$ using the method of the global behaviour factor $q = 1.50$ and for performance level B1.

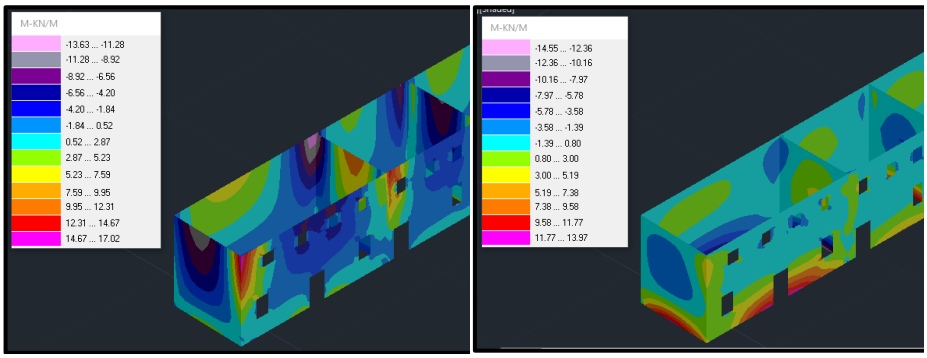


(a) Bending moment distribution $M_{xx}$. (b) Bending moment distribution $M_{yy}$.

**Fig. 3.** Bending moment distribution for the seismic load combination $G+0.30Q+E_x+0.30E_y$

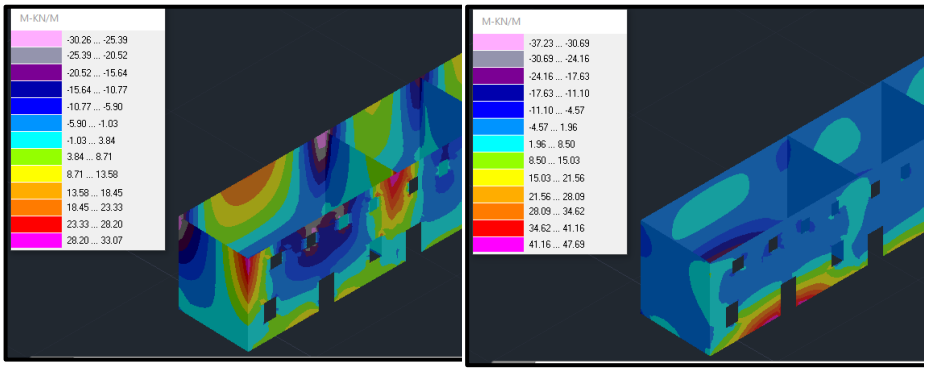


(a) Bending moment distribution $M_{xx}$. (b) Bending moment distribution $M_{yy}$.

**Fig.** 1**.** Bending moment distribution for the seismic load combination $G+0.30Q+0.30E_x+E_y$

It is observed that the largest values of out-of-plane bending moments about the vertical axis are developed at the connections with the transverse walls, while the largest values of out-of-plane bending moments about the horizontal axis are developed at the base of the walls.

# 4 Code Checks

In order to assess the seismic behaviour of the building, code checks were carried out. Elastic analysis methods were performed for the assessment. The following Tables present the results of the checks per wall, per pier and per level, with the highest value of the failure index λ. The values of the failure index are obtained from the analysis of the building using the elastic analysis method based on the global behaviour factor (q), for performance levels B1 and B2. Comparative results for each objective are presented below.

## 4.1 Results of elastic analysis method based on the global behaviour factor q = 1.5 and performance level B1

Table 1 presents the results of elastic analysis method based on the global behaviour factor q, for performance level B1 and q = 1.5 for level 1 (ground level) of the building, while Table 2 presents the corresponding results for performance level B2.

**Table 1.** Results of the code checks per wall, per pier for level 1, with the highest value of the failure index λ, *Green* (<=1.00): Adequacy, **Red** (>1.00): Inadequacy)

| Wall | Pier | In-plane shear | In-plane bending | Out-of-plane bending, plane of failure parallel to the bedjoints | Out-of-plane bending, plane of failure perpendicular to the bedjoints | Out-plane shear |
|---|---|---|---|---|---|---|
| | | λ | λ | λ | λ | λ |
| 1 | 1 | **2.75** | *0.95* | **1.17** | *0.45* | **1.01** |
| 2 | 2 | **1.12** | *0.19* | **4.38** | *0.01* | **2.23** |
| 3 | 3 | **2.61** | *0.82* | **1.27** | *0.46* | **1.79** |
| 4 | 4 | **10.00** | **1.31** | **107.47** | *0.75* | **76.99** |
| | 6 | **5.07** | *0.76* | **2.05** | *0.66* | *0.96* |
| 5 | 9 | **3.01** | *0.61* | *0.82* | *0.40* | *0.61* |
| 6 | 10 | **1.57** | *0.07* | **2.49** | *0.23* | **3.32** |
| 7 | 11 | **13.85** | **1.22** | **39.86** | **3.71** | **36.51** |
| | 13 | **4.63** | *0.63* | **2.95** | **1.66** | **1.24** |
| | 15 | **3.43** | *0.57* | **3.14** | **1.33** | **1.29** |
| | 17 | **10.00** | **5.96** | **48.15** | **3.60** | **7.89** |
| 8 | 18 | **2.98** | *0.59* | *0.81* | *0.40* | *0.59* |
| 9 | 19 | **15.63** | *0.95* | **135.56** | **1.18** | **244.34** |
| | 21 | **4.33** | *0.74* | **1.51** | *0.43* | **1.59** |
| 10 | 24 | **1.79** | *0.29* | **4.31** | *0.30* | **3.25** |

In Fig. 5a, the piers for which there is a deficiency are illustrated in red colour in the 3D model. Therefore, when evaluating the seismic behaviour of the building using the method of the global behaviour factor $q$ and taking as an assessment target the

performance level B1, it is concluded that the building is not sufficient and should be strengthened.

**Table 2.** Results of the code checks per wall, per pier for level 2, with the highest value of the failure index λ, *Green* (<=1.00): Adequacy, **Red** (>1.00): Inadequacy)

| Wall | Pier | In-plane bending | Out-of-plane bending, plane of failure parallel to the bedjoints | Out-of-plane bending, plane of failure perpendicular to the bedjoints |
|---|---|---|---|---|
| | | λ | λ | λ |
| 1 | 25 | *0.49* | *0.34* | **1.32** |
| 2 | 26 | *0.08* | *0.27* | **1.33** |
| 3 | 27 | *0.34* | *0.43* | **1.34** |
| 4 | 28 | *0.18* | *0.66* | **7.59** |
| | 30 | *0.89* | **1.02** | **5.29** |
| | 32 | *0.29* | *0.99* | **4.91** |
| | 34 | *0.89* | **1.17** | **8.83** |
| 5 | 54 | *0.24* | *0.27* | **1.22** |
| 6 | 35 | *0.04* | *0.44* | *0.99* |
| 8 | 36 | *0.29* | **1.97** | **8.30** |
| | 38 | *0.02* | *0.61* | **7.98** |
| | 40 | *0.67* | *0.96* | **6.92** |
| | 42 | *0.08* | *0.81* | **6.56** |
| | 44 | *0.33* | **1.52** | **6.69** |
| 8 | 45 | *0.21* | *0.31* | **1.22** |
| 9 | 46 | *0.43* | *0.77* | **4.13** |
| | 48 | *0.31* | *0.81* | **3.52** |
| | 50 | *0.57* | *0.85* | **3.17** |
| | 52 | *0.89* | **1.36** | **5.58** |
| 10 | 53 | *0.11* | *0.69* | **1.52** |

### 4.2 Results of elastic analysis method based on the global behaviour factor q = 1.5 and performance level B2

The influence of the performance level on the seismic assessment results of the building was then investigated. The performance level B2 was selected and new elastic analyses were carried out based on the global behaviour factor ($q$) for q = 1.5. Fig. 5b illustrates in colour the piers for which there is inadequacy, which are obviously less than in the analysis for performance level B1 (Fig. 5a). By adopting a less stringent performance objective, i.e. a 50% probability of exceeding the seismic action in 50 years, on the basis of which the seismic action is reduced by about 40%, the more favourable behaviour of the masonry is evident, mainly in out-of-plane bending.

However, in this case more frequent and more extensive damage are expected for the same earthquake.

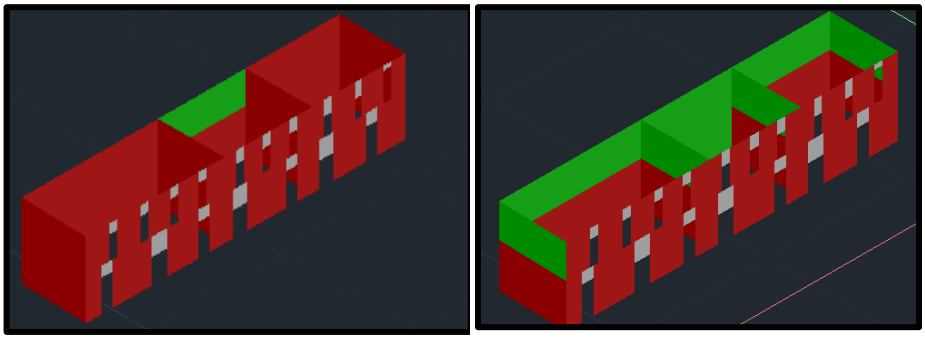

(a) Performance level B1 (b) Performance level B2

**Fig. 5.** Colour representation of inadequacies of the piers (green: adequacy, red: inadequacy)

# 5 Investigation of Interventions

The assessment of the seismic behaviour of the building according to the Greek Code for Structural Interventions of Masonry Structures [3] with the analysis method based on the global behaviour factor ($q$) and for the two performance levels, shows that the building has deficiencies and does not meet the required performance objective. For this reason, some interventions are being investigated which will improve the behaviour of the structure. Moreover, this is an elongated structure and the overturning check gives a failure index of 1.60, according to Equation 5.3.8a of the Greek Code for Structural Interventions of Masonry Structures [3]. In this case, it shall be ensured that the compressed parts of the walls can take up the whole of the horizontal and vertical loads.

Grout injection is an effective method for strengthening masonry walls. This technique involves low-pressure injection of fine hydraulic lime grout into cracks, voids, and cavities within the masonry, aiming to create a more homogenous structure. This method was initially investigated to increase the compressive strength of the masonry. The new compressive strength of the strengthened masonry was calculated based on equation 8.2 of the Greek Code for Structural Interventions of Masonry Structures [3],

$$f_{wc,f} = f_{wc,0} + \Delta f_0 + \lambda\, n\, f_{gc} = 2.0 + 0.75 + 0.50 \cdot 0.10 \cdot 5.0 = 3.0\ MPa \quad (2)$$

where $f_{wc,0}$ is the initial strength of the masonry, equal to 2.0 MPa, $n$ is the ratio of the volume of the grout to the total volume of the mortar, which, is taken to be equal to 0.10 because precise data are not available, $f_{gc}$ is the compressive strength of the grout equal to 5.0 MPa, $\lambda$ is the bond coefficient between stone unit and mortar, which is taken to be 0.50 for rough stones, $f_o$ is the coefficient (in MPa) which takes into account the degree of carving of the stones and takes a value of 1.50-2.50 MPa for clay mortar, depending on the building quality. In this study $f_o$ was assumed equal to 1.50 MPa, while due to the grout injections the irregularity and inhomogeneity of the building due

to the degree of carving of the stones is reduced and therefore a reduction of the $f_o$ coefficient is required according to the following equation:

$$\Delta f_0 = f_0 : \left(1 + \frac{1}{10\,n}\right) = 1.50 : (1 + 1) = 0.75 \quad (3)$$

Thus, the new compressive strength of the masonry after grout injection and homogenisation is equal to 3.0 MPa. The increase in shear strength of masonry depends strongly on the composition, application technique and consumption of grout [3]. In the present study, a 10% increase in strength was considered, therefore the shear strength in the absence of vertical load (cohesion), $f_{wv0}$, of the strengthened masonry was taken to be equal to 0.11 MPa.

The behaviour of the structure against earthquake can also be improved by strengthening the stiffness of the building's diaphragm. The construction of a perimeter ring beam and a reinforced concrete slab at the roof is investigated. The installation of a second additional floorboard in the mezzanine, oriented perpendicular to that of the existing floorboard, is being considered. In the analysis of the strengthened structure, according to the Greek Code for Structural Interventions of Masonry Structures, the behaviour factor ($q$) can be taken equal to 2.0.

The results of the checks of the strengthened building, for a behaviour factor $q$ = 2.0 and performance levels B1 and B2, are presented in the Tables and Figures below:

### 5.1 Results of elastic analysis method based on the global behaviour factor q' = 2.0 and performance level B1 for the strengthened building

Elastic analyses were carried out on the strengthened building for performance level B1. Table 3 shows the results of elastic analysis for in-plane action for level 1 and Table 4 for out-of-plane action. Table 5 shows the results of elastic analysis for out-of-plane action for level 2.

**Table 3.** Comparison of failure indices $\lambda$ of piers for level 1, for in-plane action before and after interventions

| Level 1 | | In-plane shear | | In-plane bending | |
|---|---|---|---|---|---|
| | | Before | After | Before | After |
| Wall | Pier | $\lambda$ | $\lambda$ | $\lambda$ | $\lambda$ |
| 1 | 1 | **2.75** | **2.37** | *0.95* | *0.70* |
| 2 | 2 | **1.12** | *0.86* | *0.19* | *0.19* |
| 3 | 3 | **2.61** | **2.15** | *0.82* | *0.63* |
| 4 | 4 | **10.00** | **3.67** | **1.31** | *0.51* |
| | 6 | **5.07** | **3.16** | *0.76* | *0.43* |
| 5 | 9 | **3.01** | **1.96** | *0.61* | *0.39* |
| 6 | 10 | **1.57** | **1.12** | *0.07* | *0.06* |
| 7 | 11 | **13.85** | **9.21** | **1.22** | *0.58* |
| | 13 | **4.63** | **2.92** | *0.63* | *0.47* |
| | 15 | **3.43** | **2.37** | *0.57* | *0.39* |
| | 17 | **10.00** | **7.25** | **5.96** | *0.71* |
| 8 | 18 | **2.98** | **2.02** | *0.59* | *0.39* |
| 9 | 19 | **15.63** | **8.82** | *0.95* | **0.53** |
| | 21 | **4.33** | **2.73** | *0.74* | **0.45** |
| 10 | 24 | **1.79** | **1.33** | *0.29* | **0.24** |

**Table 4.** Comparison of failure indices $\lambda$ of piers for level 1, for out-of-plane action before and after interventions

| Level 1 | | Out-of-plane bending, plane of failure parallel to the bedjoints | | Out-of-plane bending, plane of failure perpendicular to the bedjoints | | Out-of-plane shear | |
|---|---|---|---|---|---|---|---|
| | | Before | After | Before | After | Before | After |
| Wall | Pier | $\lambda$ | $\lambda$ | $\lambda$ | $\lambda$ | $\lambda$ | $\lambda$ |
| 1 | 1 | **1.17** | *0.66* | *0.45* | *0.26* | *1.01* | *0.87* |
| 2 | 2 | **4.38** | *1.89* | *0.01* | *0.03* | **2.23** | **2.34** |
| 3 | 3 | **1.27** | *0.65* | *0.46* | *0.29* | **1.79** | *0.96* |
| 4 | 4 | **107.47** | **4.66** | *0.75* | *0.27* | **76.99** | **7.09** |
| | 6 | **2.05** | **1.24** | *0.66* | *0.23* | *0.96* | **1.36** |
| 5 | 9 | *0.82* | *0.56* | *0.40* | *0.25* | *0.61* | *0.91* |
| 6 | 10 | **2.49** | **1.19** | *0.23* | *0.14* | **3.32** | **1.62** |
| 7 | 11 | **39.86** | **5.26** | **3.71** | **1.38** | **36.51** | **9.17** |
| | 13 | **2.95** | **1.27** | **1.66** | *0.62* | **1.24** | **1.36** |
| | 15 | **3.14** | **1.42** | **1.33** | *0.49* | **1.29** | **1.51** |
| | 17 | **48.15** | **23.32** | **3.60** | **1.34** | **7.89** | **25.31** |
| 8 | 18 | *0.81* | *0.56* | *0.40* | *0.26* | *0.59* | *0.92* |
| 9 | 19 | **135.56** | **2.36** | **1.18** | *0.62* | **244.34** | **4.03** |
| | 21 | **1.51** | *0.95* | *0.43* | *0.23* | **1.59** | **1.07** |
| 10 | 24 | **4.31** | **2.18** | *0.30* | *0.15* | **3.25** | **2.98** |

**Table 5.** Comparison of failure indices $\lambda$ of piers for level 2, for out-of-plane action before and after interventions

| Level 2 | | Out-of-plane bending, plane of failure parallel to the bedjoints | | Out-of-plane bending, plane of failure perpendicular to the bedjoints | |
|---|---|---|---|---|---|
| | | Before | After | Before | After |
| Wall | Pier | $\lambda$ | $\lambda$ | $\lambda$ | $\lambda$ |
| 1 | 25 | *0.34* | *0.52* | **1.32** | *0.37* |
| 2 | 26 | *0.27* | **1.56** | **1.33** | *0.20* |
| 3 | 27 | *0.43* | *0.58* | **1.34** | *0.39* |
| 4 | 28 | *0.66* | **1.89** | **7.59** | **1.57** |
| | 30 | **1.02** | **1.62** | **5.29** | **1.09** |
| | 32 | *0.99* | **1.65** | **4.91** | **1.01** |
| | 34 | **1.17** | *0.25* | **8.83** | **1.83** |
| 5 | 54 | *0.27* | *0.39* | **1.22** | *0.37* |
| 6 | 35 | *0.44* | *0.78* | *0.99* | *0.31* |
| 7 | 36 | **1.97** | *0.39* | **8.30** | **1.16** |
| | 38 | 0.61 | **1.54** | **7.98** | **1.11** |
| | 40 | 0.96 | **1.88** | **6.92** | *0.96* |
| | 42 | 0.81 | **1.93** | **6.56** | *0.91* |
| | 44 | **1.52** | **1.18** | **6.69** | *0.93* |
| 8 | 45 | *0.31* | *0.40* | **1.22** | *0.39* |
| | 46 | *0.77* | *0.19* | **4.13** | **1.12** |
| 9 | 48 | *0.81* | **1.10** | **3.52** | *0.95* |
| | 50 | *0.85* | **1.15** | **3.17** | *0.86* |
| | 52 | **1.36** | *0.11* | **5.58** | **1.51** |
| 10 | 53 | *0.69* | **1.36** | **1.52** | *0.35* |

Fig. 6 illustrates in red colour the piers that fail in the original and the strengthened structure, respectively, for performance level B1. From Tables 5 to 7 and Fig. 6, it is observed that the failure indices for in-plane shear action for most of the piers have been significantly reduced after the interventions, however, shear failures of masonry remain. The same conclusion is reached for the out-of-plane action.

Significantly improved behaviour of the masonry appears mainly in the crown of the walls and in particular in out-of-plane bending for plane of failure perpendicular to the bedjoints. This can be attributed to the strengthening of the diaphragm function of the roof. Overall, despite the significant improvement observed in the failure indices, the building still exhibits deficiencies.

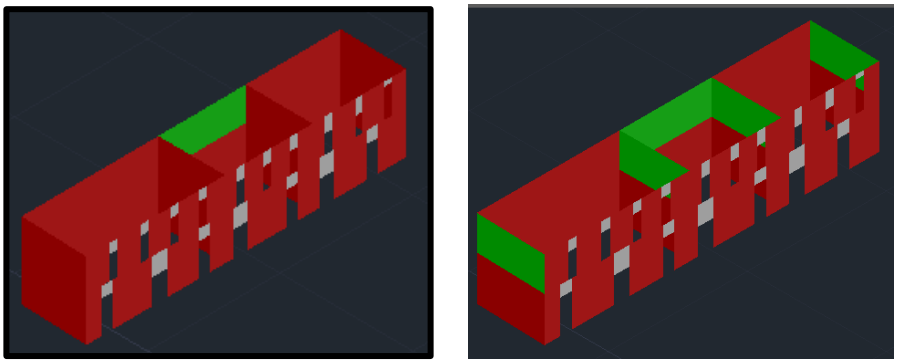

(a) Initial structure, $q$ = 1.5 0 and performance level B1.

(b) Strengthened structure, $q$ = 2.0 and performance level B1.

**Fig. 6.** Colour representation of failed piers (green: adequacy, red: inadequacy)

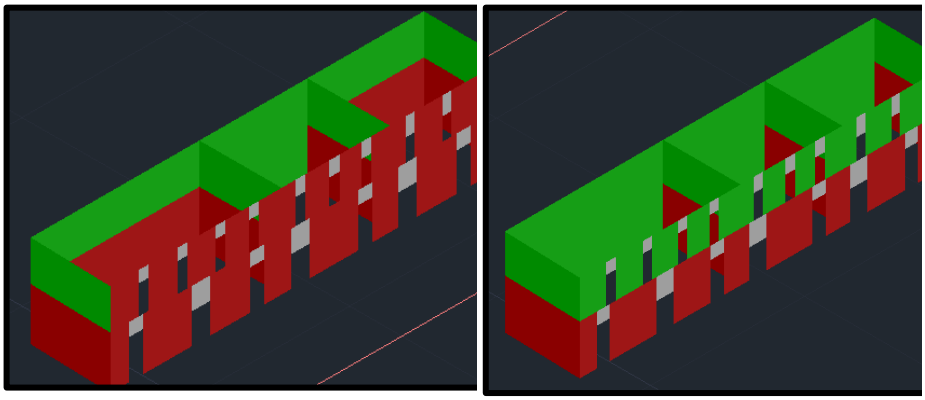

(a) Initial structure, $q$ = 1.5 0 and performance level B2.

(b) Strengthened structure, $q$ = 2.0 and performance level B2.

**Fig. 7.** Colour representation of failed piers (green: adequacy, red: inadequacy)

### 5.2 Results of elastic analysis method based on the global behaviour factor q' = 2.0 and performance level B2 for the strengthened building

As with the original building, the behaviour of the strengthened building was investigated for performance level B2, i.e. for an earthquake with a 50% probability of exceedance in 50 years. In Fig. 7, the piers that fail in the original and the strengthened structure, respectively, for performance level B2 are shown in colour in the 3D model.

As shown by the analysis of the strengthened building, for performance level B2, failure occurs only for in-plane shear actions, in the face piers and in the piers along the transverse direction (short side) of the building, only for the ground floor level. The favourable function of the diaphragm at the crown of the building is evident, where no pier shows deficiency in out-of-plane bending.

In conclusion, the method of homogenising the masonry mass with grout injections and increasing its compressive strength, in terms of in-plane shear action, does not achieve adequacy in all the piers of the structure, however, the seismic behaviour of the masonry is clearly improved. At the same time the contribution of the diaphragm at the crown level is decisive in out-of-plane flexural failure.

The strengthened structure is still inadequate regarding in-plane shear, even if grout injection and the diaphragm insertion improved the behaviour of the structure. Other methods that could be applied for strengthening of the structure could be the application of a layer of shotcrete with added reinforcement mesh to the walls which would increase both out-of-plane and in-plane strength, the application of fibre reinforced polymer sheets to the walls, or the application of fibre reinforced mortar jacketing. These methods would significantly increase the shear capacity of the walls, however, since the examined structure is a listed building, all of these methods should be approved and take listed building consent for repair works from the appropriate authorities.

# 6 Conclusions

In the present study, the seismic behaviour of a historical two-storey masonry building, located in the city of Rhodes, was evaluated. Subsequently, interventions were proposed to strengthen the structure and improve the mechanical characteristics of its materials. An elastic equivalent static analysis was carried out based on the Greek Code for Structural Interventions of Masonry Structures and the elastic dynamic analysis methods of global behaviour factor (q) and local ductility indices (m) were applied for performance levels B1 and B2. The analyses lead to the following conclusions:

- The original building shows significant deficiencies in both in-plane and out-of-plane action. The piers with deficiencies are significantly reduced when performance level B2 is chosen over B1. When performance level B1 is selected, only 3% of the piers are sufficient, whereas when performance level B2 is selected, the percentage of sufficient piers reaches 23%.
- Due to the inadequacy of the original structure, methods of interventions are being investigated in order to improve the diaphragm function of the building and upgrade the mechanical characteristics of masonry. The diaphragms of both the mezzanine and the roof of the building are strengthened, while the method of homogenising the masonry mass with grout injections is used to increase its compressive strength. The application of injections led to an increase in the compressive strength of the masonry by 50%, while also ensuring better bonding between mortar and natural stones.
- In the strengthened structure, in terms of in-plane shear, adequacy is not achieved in all the piers of the structure, but the seismic behaviour of the masonry is clearly improved. At the same time, the contribution of the diaphragm at the crown level is decisive in out-of-plane flexural failure.

# References


1. Karantoni, F.: Masonry Structures, Design and repairs. Papasotiriou Publishing, Athens (2004) (in Greek)
2. EN1998-3: Eurocode 8, Design of structures for earthquake resistance – Part 3: Assessment and retrofitting of buildings, European Committee for Standardization, Brussels (2005)
3. Earthquake Planning & Protection Organization (E.P.P.O.), Greek Code for Structural Interventions of Masonry (2023)
4. Spyrakos, C. C. (2018). Bridging performance based seismic design with restricted interventions on cultural heritage structures. Engineering Structures, 160, 34-43
5. Karantoni, F. V., & Dimakopoulou, D. (2022). Strengthening Measures for Upgrading the Seismic Response of Gazi Hasan Pasha Mosque, Kos Island. In Protection of Historical Constructions: Proceedings of PROHITECH 2021 4 (pp. 892-902). Springer International Publishing
6. Giannelos, C., & Vintzileou, E. (2022). The rehabilitation of the historical bridge of Konitsa: A documentation-based investigation of structural behaviour. In Protection of Historical Constructions: Proceedings of PROHITECH 2021 4 (pp. 711-726). Springer International Publishing
7. Vintzileou, E., Konteas, I., Manoledaki, A.-A., Palieraki, V., Miltiadou-Fezans, A.: The Katholikon of Osios Loucas Monastery: In: situ investigations. RILEM Symposium on Site Assessment of Concrete, Masonry and Timber Structures-SACoMaTiS 2008. RILEM Publications SARL (2008)
8. Palieraki, V., Adami, Ch.-E., Vintzileou, E.: In-situ measurements using radar and boroscopy techniques: case study -Hagia Sophia museum of Trabzon, Turkey. In: Proceedings of the Conference BH2013 (Built Heritage 2013, Monitoring Conservation Management), 18-20 November, Milan, Italy (2013)
9. Oikonomopoulou, E. C., Palieraki, V. A., Nikolopoulou, V. S., & Vintzileou, E. (2022). Application of non-destructive techniques for the investigation of old masonry structures. In Protection of Historical Constructions: Proceedings of PROHITECH 2021 4 (pp. 34-45). Springer International Publishing
10. Papanicolaou, C. G., Triantafillou, T. C., Papathanasiou, M., & Karlos, K. (2008). Textile reinforced mortar (TRM) versus FRP as strengthening material of URM walls: out-of-plane cyclic loading. Materials and structures, 41, 143-157
11. Veneris, P, Karidakis, G., Diakostamatiou, E., Eleftheriou, V, Anastasiadis, E., Kakakiou, K., Kaka, E., Moustaki, E., Tetti, M., Oikonomou, N. (2005). Rhodes. The city out of the walls 1522-1947. Architecture - Urban Planning (in Greek), Technical Chamber of Greece - Dodekanisa Department & Hellenic Ministry of Culture - Service of Modern Monuments and Technical Works of Dodecanese
12. Hellenic Ministry of Culture 2500/40, Decree 171/AAP/14-5-2008, Historical preservation of the area between the streets: Athinagora Patriarch A, Nav. Kodrington, Mitr. Papaioanou Apostoloy, Kanada, Antin. Damaskinou, Kapodistria, E. Bevin, at Marasia in the city of Rhodes (in Greek)
13. Ministerial Decision 23084/737/25-8-1948 – Decree of General Administration of Dodecanese 10/23-9-1948, About preserved historical monuments of Rhodes City (in Greek)
14. Karidakis, G.: Marasia, the Greek Rhodian neighbourhoods, Hellenic Ministry of Cultural, Service of Modern Monuments and Technical Works of Dodecanese (2017) (in Greek)

15. Tasios, T.P. & Chronopoulos, M.P.: Interventions, (repairs/ strengthening) in masonry buildings, National Technical University of Athens, Athens (1986) (in Greek)
16. EN1996-1-1: Eurocode 6: Design of masonry structures - Part 1-1: General rules for reinforced and unreinforced masonry structures, European Committee for Standardization, Brussels (2005)
17. Tasios, T.P.: Mechanics of Masonry, Symmetria Publishing, Athens (1992) (in Greek)
18. EN1998-1: Eurocode 8: Design of structures for earthquake resistance – Part 1: General rules, seismic actions and rules for buildings, European Committee for Standardization, Brussels (2004)
19. 3DR Engineering Software Ltd (2022). 3DR.PESSOS Manual

# Annex A – Detailed Calculations

Detailed calculations in vertical loads, in-plane and out-of-plane bending moment and shear check of piers 6 and 32 are presented below. Piers 6 and 32 are highlighted in yellow in Fig. 9.

## A.1 Vertical loads check

The maximum normal stress is calculated from the equation $\sigma_c = N_{sdmax}/A_w$, where $N_{sd,max}$ is the maximum axial force of each pier, resulting from the analysis of the building for the load combination 1.35G+1.50Q, and $A_w$ is the area of the pier at the control level. Pier 6 (Fig. 8) has length, $L$=2.425m, height $H$=3.20m and width $t$ = 0.55m.

For load combination 1.35G+1.50Q the maximum axial load is $N_{sdmax}$ = 261.95kN, so the maximum normal stress is: $\sigma_c = N_{sdmax}/A_w$,= 196.40 kPa,

The mean compressive strength of the masonry is $f_{mc}$= 2.0 MPa and the safety factor $\gamma_w$ = 1.35 for normal knowledge level (Greek Code for Structural Interventions of Masonry, 2021, §4.5.3.1). Therefore, the design compressive strength is:
$f_d = f_{mc}/\gamma_w$ = 2 MPa/1.35 = 1481.48 kPa

The failure index is $\lambda = \sigma_c / f_d$ = 0.13 < 1, meaning that the pier strength is adequate.

## A.2 In-plane checks

The in-plane shear check, according to the global behaviour factor method and for load combination G+0.30Q+Ex+0.30Ey, is presented in detail for pier 6 (Fig. 8).
The results at the bottom of Pier 6, from the lateral force analysis (linear) of the structure using the software 3DR.PESSOS 2022, for the q factor approach and for the load combination *G+0.30Q+Ex+0.30Ey*, are the following:

$F_x$ ($V_{sd}$) = 99.43 kN,
$F_y$ ($N_{sd}$) = 135.91 kN,
$F_z$ = 10.11 kN,
$M_x$ ($M_{sd,x}$) = 14.32 kNm,
$M_y$ ($M_{sd,y}$) = 1.63 kNm
$M_z$ ($M_{sd,z}$) = 79.29 kNm

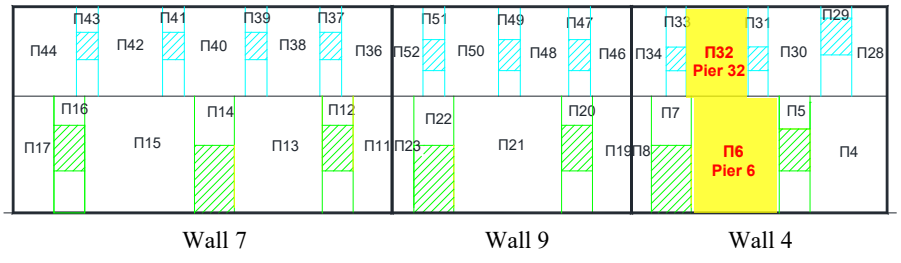


**Fig. 8.** Numerical representation of piers, for levels 1 and 2.

***Axial force and bending moment check***

The flexural design strength of the pier, considering an inactive area, is
$M_{Rd} = N_{sd}\ (1 - 1.15 v_{sd})\ L/2 = 151.76\ kNm$

The acting bending moment at the bottom of the pier (from analysis) is $M_{sd,z}$ = 79.29kNm.

Therfore, the failure index is $\lambda = M_{sd,z} / M_{Rd} = 0.52 < 1$, meaning that the pier strength is adequate.

***Shear check***

*Capacity design*

The shear strength according to the capacity design rule for Pier 6 in Wall 4, level 1, is calculated according to the following equation:

$$V_f = \frac{L\ N}{2H_0}(1 - 1.15 v_{sd}) = \frac{2.425\ m\ 135.91\ kN}{2 \cdot 5.47 m}(1 - 1.15 \cdot 0.0687) = \ 27.73\ kN$$

where $H_o$= 5.47 m is the shear length, that is the length between the two sections where the bending moment is maximum and zero respectively,

$L$= 2.425m is the length of the pier,
$t$= 0.55m is the width of the pier,
$N_{sd(G+0.30Q)}$= -135.91 kN is the acting axial load and
$v_{sd} = N_{sd} / (L \cdot t \cdot f_d) = 0.0687$ is the normalised axial load.

*Shear strength*

The in-plane shear strength of the wall is the minimum of the following two mechanisms for shear failure:

a) Due to diagonal tensile cracking, according to the Greek Code for Structural Interventions of Masonry, 2021, §7.2.2i

$$f_{vd,t} = \sqrt{f_{wtd} \cdot (f_{wtd} + v_{sd} \cdot f_d)} = 142.09\ kPa$$

where $f_{vd,t}$ is the shear strength of the masonry associated with diagonal tensile cracking and $f_{wtd}$ = 100 kN/m$^2$ is the mean tensile strength of the masonry.

b) Due to horizontal joint slipping, according to the Greek Code for Structural Interventions of Masonry, 2021, §7.2.2ii

The average shear strength of the masonry, $f_{vd,s}$, which takes into account the presence of the vertical load is:

$$f_{vd,s} = f_{vm0} + 0.4 \frac{N_{sd}}{L' t} = 135.69\ kPa \leq 0.065\ f_b = 1950\ kPa$$

where $f_{vmo}$ = 100 kN/m$^2$ is the shear strength of masonry in case of absence of vertical loads for natural carved stones,

$L'$ = 1.89 m is the length of the compressive area of the pier,
$f_b$ = 30 MPa is the normalised compressive strength of the stone unit, according to EN 1996-1-1.

Therefore, the in-plane shear strength of the wall is the minimum of the two:

$$f_{vd} = min(f_{vd,t}, f_{vd,s}) = 135.69\ kPa$$

and the shear strength of the pier is

$$V_v = f_{vd} \cdot L' \cdot t = 140.90\ kN$$

*Final shear check*

The design shear force $V_{sd}$ shall be compared with the minimum of the values of $V_v$ and $V_f$. If $V_v \leq V_f$, it is assumed that the shear force is critical for wall failure and the wall is controlled by shear, otherwise it is assumed that the moment is critical and the wall is controlled by bending (Greek Code for Structural Interventions of Masonry, 2021, §7.2.3). Because $V_v > V_f$, the bending moment is critical for failure of the pier by elastic forces. Therefore, the final shear capacity of the pier is:
$V_{Rd} = \min(V_f, V_V) = 27.73$ kN,

The acting shear force at the base of the pier is $V_{sd}$ = 99.43 kN, according to the results from analysis.
Therefore, the failure index is $\lambda = V_{sd} / V_{Rd} = 3.59 > 1$, that is the capacity of the pier is inadequate.

**A.3 Out-of-plane actions checks**

The out-of-plane check, according to the global behaviour factor method and for load combination *G+0.30Q+0.30Ex+Ey*, is presented in detail for Pier 32 of level 2 (Fig. 8). The length of Pier 32 is *L*=1.71 m, its height is *H*= 2.46 m and its width is *t* = 0.55m. The results at the bottom of Pier 32, from the lateral force analysis (linear) of the structure, for the *q* factor approach and for the load combination *G+0.30Q+0.30Ex+Ey*, are the following

$F_x$ ($V_{sd}$) = 0.079 kN,
$F_y$ ($N_{sd}$) = 35.22 kN,
$F_z$ = 1.34 kN,
$M_x$ ($M_{sd,x}$) = 5.61 kNm,
$M_y$ ($M_{sd,y}$) = 25.98 kNm
$M_z$ ($M_{sd,z}$) = 2.67 kNm

***Out-of-plane bending, plane of failure parallel to the bedjoints (Greek Code for Structural Interventions of Masonry, §7.3, Eq.7.6a)***

The bending moment capacity of the cross-section is

$$M_{Rd1,o} = \frac{1}{2}\ell t_w^2 \sigma_o \left(1 - \frac{\sigma_o}{f_d}\right) = 9.36\ kNm$$

where $\ell = L = 1.71$ m is the length of the pier,
$t_w = 0.55$ m is the width of the pier,
$N_{sd} = -35.22$ kN is the axial load,
$\sigma_o = N_{sd} / (\ell \cdot t_w) = 37.44$ kN/m$^2$ is the mean compressive stress due to axial load at the cross section and
$M_{sd,x}$=5.61kNm is the acting bending moment.

Therefore, the failure index is $\lambda = M_{sd,x} / M_{Rd1,o} = 0.60 < 1$, meaning that the pier strength is adequate.

***Out-of-plane bending, plane of failure perpendicular to the bedjoints (Greek Code for Structural Interventions of Masonry, §7.3, Eq.7.6b)***

The bending moment capacity of the cross-section is

$$M_{Rd2,o} = \frac{1}{6} f_{wt,d} t^2 \ell = 6.38\ kNm$$

where $f_{wt,d} = f_{wt} / \gamma_w = 100$ kN/m$^2$/ 1.35 = 74.07 kN/m$^2$ is the tensile strength of the wall and $\gamma_w = 1.35$ is the safety factor for normal knowledge level. The bending moment about the vertical axis at the base of the pier, from the elastic analysis, is $M_{sd,y} = 25.98$ kNm.

Therefore, the failure index is $\lambda = M_{sd,y} / M_{Rd2,o} = 4.07 > 1$, meaning that the capacity of the pier is not adequate.

# Substandard Reinforced Concrete Walls with Rectangular Cross-section: Assessment of Shear Resistance

Marina L. Moretti[0000-0003-2082-5571]

National Technical University of Athens 42, Patission st., 10682 Athens, Greece
moretti@central.ntua.gr

**Abstract.** Reinforced concrete walls in buildings constructed before 1990 possess low shear resistance and their reinforcement detailing differs considerably as compared to similar walls in modern buildings, designed according to modern code principles. Accurate estimation of shear resistance of existing RC walls is crucial for the seismic capacity assessment of older buildings. In this paper, a design model is presented for the assessment of shear resistance of RC walls with rectangular section, irrespective of reinforcement configuration. The model includes the contribution of all major mechanisms to shear resistance, namely: the longitudinal reinforcement of the confined regions at either end of the cross-section, the horizontal and vertical web reinforcement, the axial compressive force, and the concrete strut through a novel approach. The proposed equations have no restrictions in their applicability, in contrast to the majority of existing models, and proved to be the most effective in assessing the shear resistance of 129 tested RC walls, among 14 other design models considered, including existing design codes. Indicative case studies are presented to demonstrate the better predictive capacity of the proposed equations and the deficiency of four code provisions regarding the prediction of shear resistance of older RC walls with substandard reinforcement detailing.

**Keywords:** Shear Wall Resistance, Reinforced Concrete, Assessment, rectangular cross-section

## 1 Introduction

The contribution of reinforced concrete (RC) walls on the seismic behaviour of RC buildings has been investigated early on [1]. Research on the calculation of the shear resistance of reinforced concrete (RC) walls dates since the 1970's [2-4]. Different design approaches have been proposed to estimate the shear resistance of RC walls, including empirical formulas, e.g. [5], strut-and-tie models, e.g [6], truss models, e.g. [7], superposition of strut and truss mechanism, e.g. [8-9], as well as other approaches, e.g, [10]. However, it is well established that the estimation of shear resistance of RC walls is still considered an open issue [11, 12]. Further on, the predictions of available

models, including the respective code provisions, differ considerably between them. The discrepancy between predicted and actual shear resistance is particularly large in case of RC walls in older buildings, which do not possess the reinforcement detailing prescribed by modern codes, given that most design models presuppose the presence of certain detailing [11].

However, the knowledge of shear resistance of RC walls is essential for the assessment of the seismic capacity of RC walls. It is noted that particularly in case of buildings constructed according to older code principles, in which the behavior of RC walls is governed by shear resistance, an accurate estimation of shear resistance of RC walls is essential in the assessment of seismic capacity. This is especially important for the existing building stock in Greece. Reinforced concrete (RC) buildings in Greece constructed prior to 1990's are, generally, frame structural systems. Occasional RC shear walls have very different reinforcement detailing compared to that prescribed by modern codes, i.e. no confined regions in their cross-section and low amount of web reinforcement. As a result, they possess low shear resistance and are liable to fail in shear in the event of a major earthquake. Seismic design according to modern codes aims at safeguarding against collapse through ductile seismic performance of the structural elements. Shear failure results in brittle failure and abrupt decrease of the element's mechanical properties. In order to reduce the possibility of shear failure, in modern codes all structural elements should be designed so as have higher shear resistance, $V_R$, than the shear force corresponding to the flexural resistance of the cross-section $V(M_R)$, i.e. $V_R < V(M_R)$. This prerequisite falls within the concept of "capacity design", which is a practice that did not exist in older code principles.

This work stemmed from the practical need for a reliable design model to estimate the shear resistance of RC walls, irrespective of their reinforcement detailing. Based on the results of an extensive study, the current paper focusses on the prediction of shear resistance of RC walls with rectangular cross section, and reinforcement detailing different than that prescribed by modern code provisions.

A design model is proposed for the calculation of the shear strength of RC walls, which has no restrictions in its application regarding the values of individual characteristics of the wall, as happens with the majority of existing design models. The model proved to be the most effective among 14 other design models considered [11], based on a dataset of 129 tested RC walls. The model is compared to the performance of three other models from international codes: EN1998-1, DCM [13], EN1998-3 [14], and AIJ2016 [15], and of an empirical model include in the Greek code for RC, EKOS2000 [16]. The predictive performance of the five models is discussed based on three case-studies of tested RC walls that did not comply with modern reinforcement detailing. Shortcomings of the existing models are briefly discussed.

The better predictive performance of the proposed model, as compared to other available models, is attributed to the following:

- Inclusion of all the individual load transfer mechanisms with their contribution appropriately calibrated against a large database. The other models consider only some of the load transfer mechanisms
- Different design equations are provided for rectangular and barbell cross-sections, while most models do not make any distinction. It is experimentally verified that

RC walls with barbell cross-section have increased shear resistance. In this paper only the equations for rectangular sections are discussed

- A novel method is proposed to calculate the contribution of the concrete strut mechanism, which is the most significant contributor to shear resistance. The proposed equation stems from the strut contribution in infilled frames
- No upper limit for shear resistance is included. The upper limit in shear resistance in the majority of other models is based on the upper limit in the truss analogy aimed to exclude the occurrence of concrete crushing. However, in RC walls no such type of failure is observed, so this limit is not physically justified. The models apparently require an upper limit to guarantee safe predictions
- The model has no restrictions in its application. Other models are applicable only to RC walls with specific reinforcement detailing, the one prescribed by modern codes, as a rule, e.g. the existence of confined ends at the cross-section, minimum amount of web reinforcement, etc. Those prerequisites reduce the applicability of existing design models

# 2 Modelling the shear resistance of RC walls

## 2.1 General aspects affecting shear resistance

It is well established that the estimation of shear resistance of RC walls is still considered as on open issue [11, 12]. In modern codes, available equations for the calculation of shear resistance, $V_R$, of walls are intended to be used for RC walls that comply with modern reinforcement detailing. Among the prevalent factors that are known to affect shear behavior of RC walls is the value of the shear ratio, $\alpha_s = M/V \cdot L_w$, where $L_w$ is the larger dimension of the section, $V$ is the maximum shear force that acts at the base of the wall parallel to $L_w$, and $M$ is the corresponding bending moment.

(a) For walls with shear ratio $\alpha_s > 2$, the design equations for shear resistance proposed by the codes are similar to the equations for linear elements and are based on truss analogy. Shear capacity $V_R$ is calculated, as a rule, as the sum of the contribution, $V_w$, of the reinforcement parallel to shear force, and the contribution, $V_c$, of the other load transfer mechanisms, including concrete, dowel action, etc., e.g. EN1992-1-1 [17]. For adequate ductility, failure due to concrete crushing of the inclined struts of the Moersch-type truss should be excluded. To this end, an upper limit $V_{R,max}$, which is supposed to be the shear force that results in concrete crushing is introduced. Hence, shear resistance $V_R$ is, generally, calculated from Equation (1).

$$V_R = V_w + V_c < V_{R,max} \tag{1}$$

(b) For walls with shear ratio $\alpha_s < 2$ it is generally assumed that a large part of the shear force is carried by the mechanism of concrete strut. A similar assumption is made for other structural elements with low shear ratio, e.g. coupling beams of coupled shear walls [18] and short columns [19].

Figure 1 indicates the characteristics of a reinforced concrete (RC) wall with rectangular cross-section that contribute to shear resistance. The symbols are explained in section 2.2.

### 2.2 Proposed design model

**Research background.** The initial research on shear strength of RC walls, on which the present paper is based, had the following objectives (a) identify the major parameters that affect shear resistance, (b) assess the performance of existing design models regarding the estimation of shear capacity, and (c) proposal of an improved design model for the shear resistance of RC walls.

As a first step of the research, a broad database of 414 reinforced concrete (RC) wall specimens reported to have failed in shear has been assembled from the literature. Reinforcement and geometrical characteristics of the walls of the database are available in Moretti et al. 2019 [11]. Moreover, 14 different design models aiming at the estimation of shear strength of RC walls were collected and assessed in relation to their capacity to accurately predict the shear resistance of the wall of the database. Major differences were observed between the models, which led to discrepancies in the predictions of shear resistance for the same wall specimens. Increased differences in models' predictions were observed for walls with reinforcement characteristics not in accordance to modern code provisions. To address this issue, new empirical equations were proposed which consider all the wall characteristics that affect shear resistance of walls, namely: geometry, materials, axial force, horizontal and vertical web reinforcement, longitudinal reinforcement of the end parts of the cross-section, without any restrictions of applicability. Different sets of equations were proposed for rectangular section and for section H, i.e. barbell/flanged section with reduced web width, compared to the end parts where larger boundary elements are present. It was already established that shear resistance of walls is considerably influenced by the shape of the cross-section [6,12,20-21]. It is important to note that in the design equations proposed by the majority of codes and researchers, including the Eurocodes and the Greek codes, no distinction is made between different shapes of section.

In this paper design equations for shear resistance of rectangular wall section are presented, which is the section generally used in buildings in Greece. More detailed presentation and comments on the proposed design equations for both types of cross-sections, and comments on the performance of other design models may be found in [11,22-23].

In this paper the set of design equations proposed for walls with rectangular section are provided in equations 2 to 4.

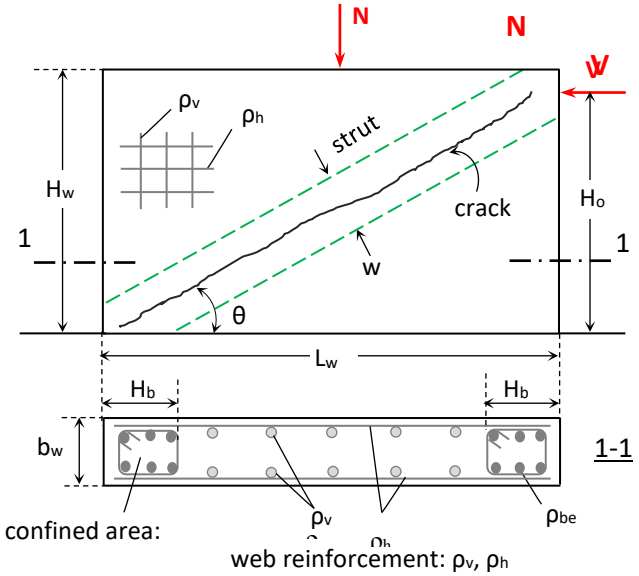


**Fig. 1.** Geometric and reinforcement characteristics that affect shear resistance of a reinforced concrete wall (RC) with rectangular section. Symbols are explained in section 2.2

**Design equations. Discussion on the contribution of the individual mechanisms.** In the proposed model, shear resistance, $V_u$, of a reinforced concrete wall with rectangular cross-section is calculated through equation (2) by summing up the contribution of five (5) individual constituents, calculated through equations (3a) to (4d). The effect of each component to the wall shear resistance is briefly discussed in the following.

Concrete contribution to shear resistance consists in the shear force carried by the diagonal strut mechanism, $V_{strut}$, and is calculated by equation (3a). Strut mechanism in more activated in structural elements with low shear ratio, e.g. [24]. Strut width, w, depends on the wall dimensions and the amount of longitudinal reinforcement at the end sections of the wall, and is calculated through equations (3a-1), (3a-2) and (4). It has been verified [11] that the contribution of strut mechanism is enhanced in walls (a) with larger cross-section width and (b) in the presence of higher amount of longitudinal reinforcement at the confined regions. The width of the diagonal strut, *w*, is calculated from equation (4) [25]. It is pointed out that the provisions of FEMA 306 [25], originally intended for the case of infilled frames, are applied for the first time for the calculation of shear resistance of RC walls. Appropriate modifications are proposed to better describe the strut contribution to shear in RC walls, namely the equations (3a-1), (3a-2) and (4d).

$$V_u = V_{strut} + V_h + V_v + V_{be} + V_N \tag{2}$$

$$V_{strut} = w \cdot b_w \cdot f_c^{'} \cdot (0.78 - \frac{f_c^{'}}{200}) \frac{1}{\sqrt{M / VL_w} + 0.18} \cos\theta \tag{3a}$$

$$w = \max(b_w; w_{FEMA}) \text{ for } b_w \geq 120 \text{ mm or } \rho_{be} \geq 0.018 \tag{3a-1}$$

$$w = \min(b_w; w_{FEMA}) \text{ for } b_w < 120 \text{ mm and } \rho_{be} < 0.018 \tag{3a-2}$$

$$V_h = 0.2 \cdot \rho_h \cdot b_w \cdot (0.8L_w - H_b) \tan\theta \cdot f_{yh} \tag{3b}$$

$$V_v = 0.3 \cdot \rho_v \cdot b_w \cdot (0.8L_w - H_b) \cdot f_{yv} / \sqrt{H_w / L_w} \tag{3c}$$

$$V_{be} = 0.25 \cdot \rho_{be} \cdot H_b \cdot b_w \cdot \min(f_{ybe}; 700MPa) / \sqrt{H_w / L_w} \tag{3d}$$

$$V_N = 0.15 \cdot N / \sqrt{M / V \cdot L_w} \tag{3e}$$

$$w_{FEMA} = 0.175(\lambda \cdot H_o)^{-0.4} \cdot r_{\inf} \tag{4}$$

$$\lambda = \left( \frac{b_w \cdot \sin 2\theta}{4 \cdot I_{bc} \cdot H_w} \right)^{0.25} \tag{4a}$$

$$r_{\inf} = \sqrt{L_w^2 + H_w^2} \tag{4b}$$

$$\theta = \arctan(H_w / L_w) \tag{4c}$$

$$\mathrm{I}_{bc} = b_w \cdot H_b^3 / 12 \tag{4d}$$

where:

$V_{strut}$ = shear force carried through the mechanism of diagonal strut
$V_h$ = contribution of horizontal web reinforcement to shear resistance
$V_v$ = contribution of vertical web reinforcement to shear resistance
$V_{be}$ = contribution of longitudinal reinforcement in the confined boundary elements
$V_N$ = contribution of compressive axial force, N, of the wall to shear resistance
$M$, $V$ = bending moment and respective shear force at the wall base
$b_w$ = width of wall cross-section
$L_w$ = length of wall cross-section
$H_w$ = height of wall
$r_{\inf}$ = length of diagonal strut
$w$ = width of diagonal strut

$\rho_{be}$ = geometric ratio of longitudinal reinforcement of confined end wall regions
$\rho_h$ = geometric ratio of horizontal web reinforcement
$\rho_v$ = geometric ratio of vertical web reinforcement
$H_o$ = distance between base of wall and horizontal force (see Fig. 1)
$H_b$ = length of confined regions.
$I_{bc}$ = moment of inertia of confined regions at the cross-section ends

For the calculation of strut width from equation (4), for $I_{be}$ in (4d):

$H_b = b_w / 2$ for $\rho_{be} > 0$ or

$H_b = b_w / 4$ for $\rho_{be} = 0$

The reinforcement in the wall is supposed to contribute to shear resistance in relation to the amount of reinforcement bars activated by the potential diagonal crack at an angle $\theta$, shown in Figure 1. The contribution to shear resistance of the web reinforcement is calculated from equations (3b) for the horizontal bars, and (3c) for the vertical bars. It is noted that the majority of existing design models consider only one of the two types of web reinforcement, as described in [11].

The contribution to shear resistance of the longitudinal bars in the confined regions is calculated from equation (3d). The presence of high percentage of longitudinal reinforcement, although neglected in many design models, proved to result in increased shear resistance [11]. For that reason, in the proposed design model the effect of the longitudinal reinforcement is considered both directly through equation (3d) and also indirectly by increasing the strut width, as described in the respective equations (3a-1), (3a-2) and (4).

The presence of higher compressive axial force in a wall results in increased shear resistance. The contribution of axial force in calculated by equation (3e) and is inversely proportionate to the magnitude of the wall shear ratio.

### 2.3 Code design provisions discussed

In this paper, besides the proposed equations presented in section 2.2, four design models from codes are applied, and their assumptions are briefly outlined, namely: (a) the equation of Eurocode 8 part 1 [13] intended for new structures, (b) the equation of Eurocode 8 part 3 [14] for the assessment of existing structures, (c) a Japanese model included in AIJ2016 [15], which resulted in the second best predictions among the 14 models considered, and (d) the equation for squat walls in EKOS2000 [16], the Greek code for the design of new RC structures. The criterion for selecting the two Eurocode models is their use in Greece rather than their predictive performance, which is deficient.

**(a) EN1998-1** [13], for medium ductility level (DCM). The code provisions address new structures. Shear resistance is calculated from a truss model formed by the potential inclined cracks at an angle θ as per the direction of the longitudinal axis of the wall. Angle θ is determined in such a way that the shear resistance of the concrete struts equals the shear resistance of the reinforcement parallel to the shear force, within the limits $0.4 \le \tan\theta \le 1$ (EN1992-1-1 [17]). For the application of the model the wall should

include reinforcement detailing that enables the formation of a truss at ultimate state, i.e. adequate horizontal web reinforcement and reinforcement at both ends of the section, i.e. in the upper and lower chord of the truss. It is noted that the above restrictions are not stated in the code, because they are guaranteed in new structures.

**(b) EN1998-3** [14]. The provisions are intended for the assessment of shear resistance of existing buildings. Empirical equations for the calculation of shear resistance of walls as well as for the maximum shear force, VR,max, that results in crushing of the concrete struts are provided. The contribution of horizontal web reinforcement, the total vertical web reinforcement, the axial force and the shear ratio are considered. The equations include the ductility factor $\mu_{\Delta}^{pl}(=\theta_{pl}/\theta_{y})$ which expresses the ratio of the plastic part of the chord rotation, θpl, to the chord rotation at yielding, θy, the estimation of which presents uncertainties, which increase for walls constructed according to older code principles. At application of the equations it was assumed that $\mu_{\Delta}^{pl}=0$. No restrictions for the values of the wall characteristics are included for the application of the design equations.

**(c) AIJ2016** [15]. It is an empirical model from the Japanese provisions, easy to apply, which may be used for all types of cross section (i.e. rectangular and barbell). The model expresses the contribution to shear resistance of horizontal web reinforcement, longitudinal reinforcement at the end confined regions, shear ratio and axial force. Prerequisite for the application is the existence of reinforcement at both ends of the cross-section and of horizontal web reinforcement. This design model is presented in detail in [11], and results in the second best predictions of shear resistance for the specimens of the database, among the 14 models originally applied from the literature.

**(d) EKOS2000** [16]. The Greek code for the design of reinforced concrete structures includes an empirical design equation for the shear resistance of RC walls with shear ratio $\alpha s \leq 1.30$, which considers the contribution of both horizontal and web reinforcement of the wall. The code is intended for the design of new structures, and therefore presupposes modern reinforcement detailing and minimum requirements for the amount of reinforcement. The model has been applied only on the three test specimens presented in Figures 2 to 4, and was not included in the original comparative research based on the whole database, the results of which are shown in Table 1.

# 3 Results

## 3.1 Comparative evaluation of predictive capacity of the design equations

The accuracy of the design models was assessed by their capacity to predict the experimental ultimate shear force of 129 walls with rectangular cross-section, from an assembled experimental database. The database is available in Moretti et al. (2019) [11]. In the evaluation process, nine code models and five other design models from the literature were compared. It is interesting to note that apart from the proposed model and the model of EN1988-3 [14], all the other design models have restrictions in their

applicability, related to the individual wall characteristics. Details on the predictive performance of all 14 models considered are available in [11] and [22].

The performance of the proposed model and the three international code equations herein discussed was assessed by their capacity to predict the experimental ultimate shear resistance of tested shear walls. For assessing the accuracy of the shear predictions, three statistic indices for the ratios $V_{mod}/V_{exp}$, where $V_{mod}$ is the predicted shear resistance by each model and $V_{exp}$ is the experimental peak shear strength for the same wall, were calculated: (a) the Covariance, COV(= STDEV/MEAN), (b) the average value $\overline{\Delta} = \left(\Sigma_{i=1}^{N}\Delta_i\right)/N \times 100(\ )$, where $\Delta_i = [(V_{exp,i}-V_{mod,i})/V_{exp,i}]<0$ of the model's overestimation of peak shear strength of –i specimen, and (c) the average absolute error of the model's prediction $AAE = \Sigma_{i=1}^{N}\left(\left|V_{\mathrm{mod},i} - V_{\mathrm{exp},i}\right|/V_{\mathrm{exp},i}\right)/N \times 100$ for each –i wall specimen, where N is the total number of specimens considered in each case.

Table 1 displays the statistical indices for the ratios $V_{mod}/V_{exp}$ for the four models. The number, N, of specimens on which each model was applied is also displayed on the Table. Only the proposed model and EN1998-3 could be applied to all 129 specimens of the database, as the specific models do not include any restrictions regarding the wall parameters.

According to Table 1, among the four models discussed, the worst predictions are those of EN1998-1, based on truss analogy, a load carrying shear mechanism not expected to be predominant for RC walls that fail in shear.

The performance of EN1998-3, which is supposed to be used for the assessment of existing structural elements, is not good either. Although the model has no restrictions in its application and could be applied on all 129 specimens of the database, a considerable scatter between calculated and estimated shear strength values is observed. Also, this model results in considerable amount of unsafe predictions, indicated by $\overline{\Delta}$ despite the fact that it was generally taken: $\mu_{\Delta}^{pl} = 0$.

AIJ model results in the second best predictions. More details on the model are available in [11].

The proposed design model results in the best predictions. It is noted that the undisputable better performance of the proposed model was also verified against 14 design models in a broader database of 414 RC walls, which included also barbell walls.

**Table 1.** Statistical indices for the ratio $V_{mod}/V_{exp}$ for walls with rectangular section

| Design equations | Number of specimens, N | COV | AAE (%) | $\overline{\Delta}<0$ (%) |
|---|---|---|---|---|
| Proposed model | 129 | 0.164 | 15.7 | 7.2 |
| EN1998-1, DCM [13] | 97 | 0.491 | 43.1 | 59.4 |
| EN1998-3 [14] | 129 | 0.423 | 32.1 | 26.5 |
| AIJ 2016 [11], [15] | 97 | 0.250 | 19.8 | 21.5 |

### 3.2 Case studies on the estimation of shear resistance of RC walls that do not comply to modern design provisions

In the following, some shortcomings typically encountered at the application of existing design equations for the assessment of shear resistance of RC walls with different reinforcement characteristics as compared to those prescribed by modern codes for new structures are discussed. Specific pertinent examples from tested shear walls are provided for RC walls with rectangular section, through comparison of their experimental peak shear strength to the predicted one.

In Figures 2 to 4 the performance of the design models shown in Table 1 is compared for wall specimens from the literature. Moreover, the respective predictions of the Greek code EKOS2000 [16] are also shown. The predictions of EN1998-3 are indicated as EC8-3, while the predictions of EN1998-1 are indicated as EC8-1.

On the Figures the value of the experimental peak shear strength, $V_{exp}$, is indicated with dashed line. When feasible, different symbols are used to mark the contribution of each shear transfer mechanism, i.e. types of reinforcement, concrete strut, axial force. In the EN1998-3 model the contributions of the individual carrying mechanisms cannot be unlinked, and therefore are not indicated separately. Similarly, in AIJ2016 the contribution of the longitudinal reinforcement of the confined regions is included within the concrete strut, therefore both are depicted as concrete strut (in Figure 4). On each figure the following characteristics of the wall specimens are indicated, as defined in Figure 1: the wall geometric characteristics, $b_w$, $L_w$, $H_w$, the shear ratio $\alpha_s$, the axial load ratio, $\nu$ (=$N/(L_w b_w f_c)$), the compressive strength of concrete, $f_c$, and the geometric reinforcement ratios of the longitudinal reinforcement of the confined regions, $\rho_{be}$, as well as the ratios of horizontal web reinforcement, $\rho_h$, and of vertical web reinforcement, $\rho_v$.

**Absence of longitudinal reinforcement in the end sections $\rho_{be}$=0**. Figure 2 shows the predictions of the five models for a large- scale wall with low shear ratio, $\alpha_s = 0.33$ and no axial force ($\nu = 0$). The wall has normal concrete strength, $f'_c = 26.2$ MPa. The web reinforcement ratio $\rho_h = \rho_v = 0.0033$ is larger than the minimum amount of web reinforcement required in the Greek code [16], which is: $\min(\rho_h, \rho_v) = 0.0025$. The specimen does not include reinforced confined areas at the ends of the section ($\rho_{be} = 0$). Hence truss-based models AIJ2016 and EN1998-1 cannot be applied for the estimation of shear strength, as the upper and lower chord of the truss cannot develop. This is indicated by symbol N.A. (=Not Applicable) on the X axis under the models' names. For comparison purposes, the predictions of the two models are also shown on Fig. 2. Models EN1998-3 and EKOS2000 underestimate peak shear strength. The proposed model estimates very well the peak shear strength of this specimen: $V_{mod}$ =1346 kN. According to the proposed model the major part of shear resistance is attributed to the concrete strut, i.e. $V_{strut}$ = 941 kN, followed by the contribution of the vertical web reinforcement, $V_v$ = 352 kN, and only minor contribution of the horizontal web reinforcement, $V_h$ = 53 kN. This behavior stems from the particularly small value of the shear ratio.

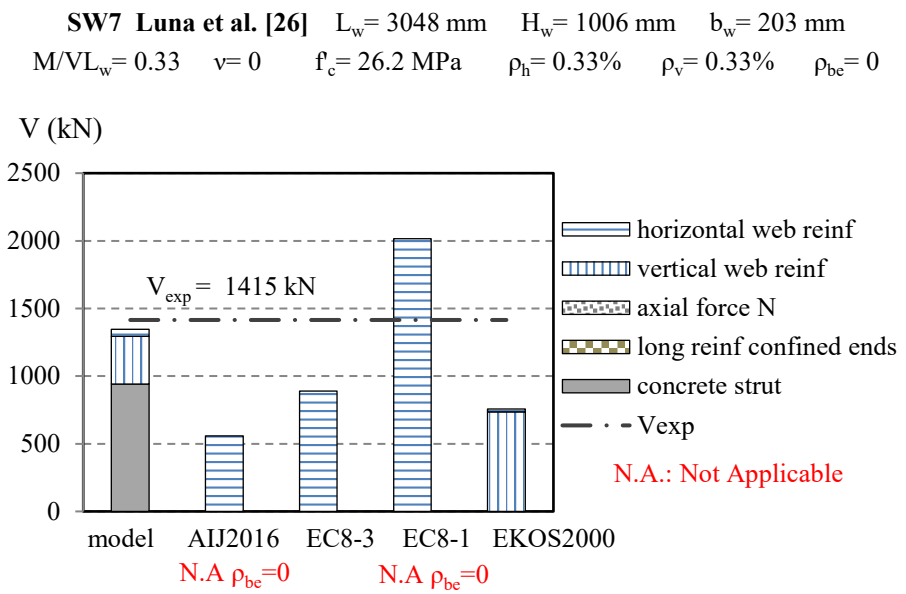


**Fig. 2.** Prediction of shear resistance, $V_R$, allocated to the shear resisting mechanisms considered by each model for a wall without without longitudinal reinforcement at the cross-section ends ($\rho_{be}$= 0)

**No web reinforcement $\rho_v$=$\rho_h$=0 - High longitudinal reinforcement at ends of cross-section.** Figure 3 displays the predictions for a wall with shear ratio $\alpha_s$ = 1.08 and no axial force (ν = 0). The wall has moderate to high concrete strength, $f'_c$ = 40.3 MPa and has no web reinforcement ($\rho_v$ = $\rho_h$ =0). High longitudinal reinforcement ratio at both ends of the cross-section is present, $\rho_{be}$ = 8.31%. It is noted that the longitudinal reinforcement ratio at either end of the section is higher than the maximum allowable reinforcement ratio, max $\rho_{be}$ = 4%, prescribed by EKOS2000 and EN1998-1. The models of EN1998-1 and EKOS2000 cannot be applied (N.A) because of the absence of the web reinforcement. AIJ2016 is also not applicable because the presence of horizontal web reinforcement is a prerequisite for the model, however the peak shear force calculated from the equation of AIJ from the mechanism of concrete strut and the longitudinal reinforcement at the end confined regions is indicated on Figure 3 for comparison purpose. Overestimation of AIJ2016 is simply attributed to the fact that it is not correct to apply the model when $\rho_h$ = 0. It is observed that EN1998-3 underestimates considerably the peak shear strength of the wall. The proposed model predicts exactly the peak shear strength of the specimen, $V_{mod}$ =307 kN, by considering the contribution of the concrete strut, $V_{strut}$ =172 kN, and the contribution of the longitudinal reinforcement at the confined regions $V_{be}$ =135 kN.

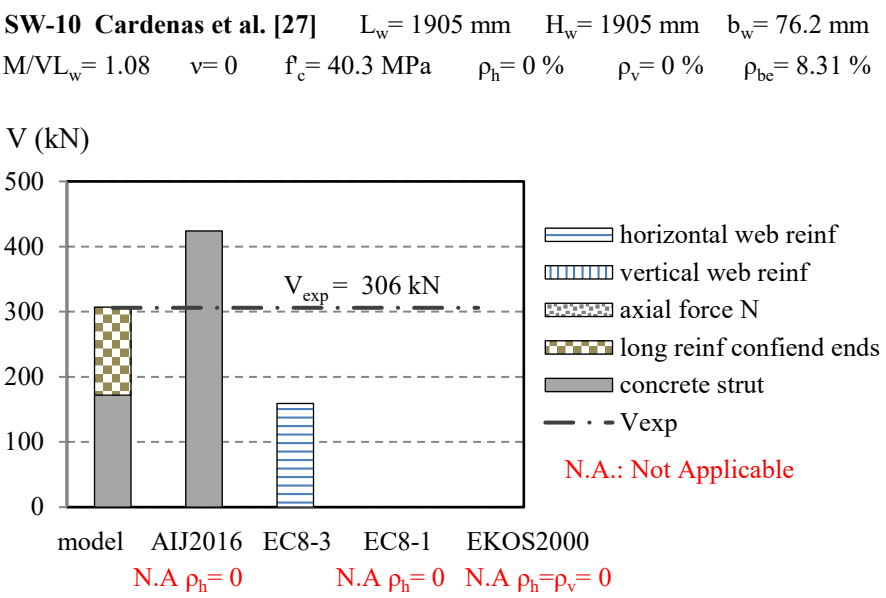


**Fig. 3.** Prediction of shear resistance, $V_R$, allocated to the shear resisting mechanisms considered by each model for a wall without web reinforcement ($\rho_h = \rho_v = 0$)

**High concrete strength-High longitudinal reinforcement at end section regions.** Figure 4 presents a wall with shear ratio $\alpha_s = 1.17$, axial load ratio $\nu = 0.07$, high concrete strength ($f_c$ = 70.3 MPa) and particularly high percentage of longitudinal reinforcement at the end regions $\rho_{be} = 9.57\%$, which is higher than the maximum allowable reinforcement ratio max $\rho_{be} = 4\%$, prescribed by EKOS2000 and EN1998-1. The web reinforcement ratio is more than twice the minimum amount prescribed by EN1998-1 and EKOS2000 (min ($\rho_v$, $\rho_h$) = 0.0025). The values of the reinforcement characteristics render all the models applicable. With the exception of EKOS2000 which underestimates the peak shear strength, the other four models result in good predictions of peak shear strength. AIJ2016 yields the best prediction, i.e. $V_{mod}$ = 2063 kN. The proposed model slightly overestimates shear strength, i.e. $V_{mod}$ = 2129 kN, with $V_{mod}$ / $V_{exp}$ = 1.02. EN1998-1 results in a slight underestimation, $V_{mod}$ / $V_{exp}$ = 0.97, while EKOS2000 in significant underestimation, $V_{mod}$ / $V_{exp}$ = 0.41. It is worth noting that EN1998-3 overestimates by 7% peak shear strength, i.e. $V_{mod}$ = 2229 kN, while the code equation serving as an upper limit (to safeguard against concrete crushing) results in even higher shear resistance, $V_{R,max}$ = 2676 kN.

Attention should be drawn on the importance of the contribution of each individual shear transfer mechanism included in the design equations. In case of wall specimen S3 depicted in Figure 4, in the four models that reach similar peak shear strength estimates, the equations are completely different. For example, comparing between AIJ2016 and the proposed model, it is interesting to note both models calculated similar total shear contribution of strut and longitudinal reinforcement, while the remaining part of shear transfer is attributed in AIJ2016 model to the horizontal web reinforcement and axial

load, while in the proposed model mainly to the axial force and vertical web reinforcement, and less to the horizontal web reinforcement.

Therefore, the appropriateness of a model should be judged by its capacity to predict well the shear resistance of a large number of specimens with different characteristics, as is the case of the models applied in the whole database shown in Table1.

Further on, it is worth mentioning that the introduction of an upper limit in shear resistance of RC walls is not apposite as it has been demonstrated [11,22-23]. This upper limit, although claimed to prevent from concrete crushing, similar to Moersch truss theory, in the case of RC walls it seems to serve exclusively towards safe predictions –which, in fact, did not happen for specimen S3 (Fig. 4).

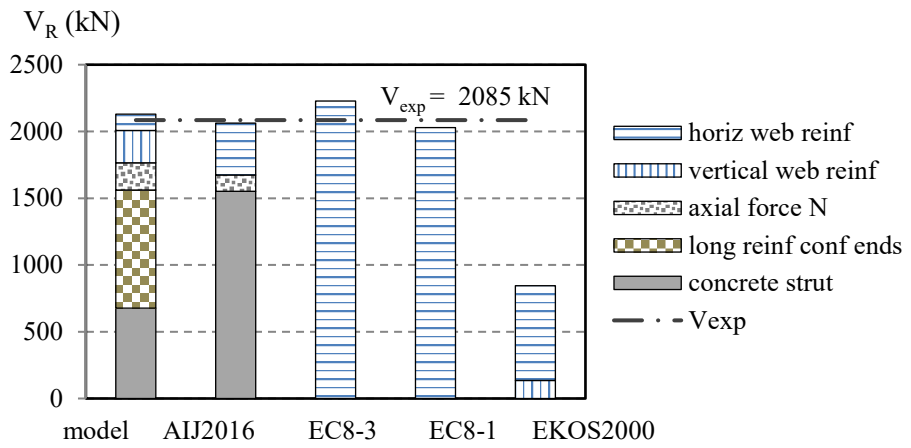


**Fig. 4.** Prediction of shear resistance, $V_R$, allocated to the shear resisting mechanisms considered by each model for a wall with high reinforcement ratios and high concrete strength

The good predictions of the proposed model, for the three walls discussed, are achieved through the correct estimation of the contribution of the individual mechanisms of load transfer to shear resistance, which have been determined over a broad range of values for the wall characteristics.

# 4 Conclusions

This paper addresses the prediction of peak shear strength of RC walls with rectangular cross-section, which is known to be still an open issue. The lack of a generally accepted design model for shear resistance of RC walls has a more pronounced impact in the assessment of shear strength of older RC walls, which do not comply with the minimum required reinforcement detailing prescribed by modern codes.

A set of design equations is proposed and presented in detail. The model has no restrictions in its application and is capable of reliably estimating the shear strength of RC walls, irrespective of the wall reinforcement characteristics. Besides the proposed model, the performance of four other design code-based models is discussed in relation to their ability to predict the experimental peak shear strength of tested RC walls. It is shown that in case of RC walls with reinforcement characteristics that do not comply with modern codes, existing models fail to accurately predict shear capacity.

The main problem of the existing design models is that they do not include all the individual characteristics of the RC walls which contribute to shear resistance. This shortcoming results in reduced predictive capacity, restrictions in applicability related to minimum reinforcement requirements, and also the need of introducing an upper limit in shear resistance, with no physical justification.

The design equations presented in this paper model all the RC wall parameters that contribute to shear resistance. They are easy to apply and have no restrictions of applicability in terms of reinforcement detailing and geometry. Given the model's superior performance, as compared to available design models, it is pertained that the proposed model could be used for the assessment of shear resistance of existing substandard RC walls in older structures.

# 5 Acknowledgements

Incentive for the research on shear resistance of RC walls, a part of which is presented in this paper, was the collaboration of the author with professor Susumu Kono and the researcher Taku Obara in Tokyo Institute of Technology (TIT), which was rendered possible owing to the financial support through a year scholarship form Laboratory of Materials and Structures, Institute of Innovative Research, TIT, for the years 2017-2018 and 2018-2019.

# References

1. Antebi, J., Utku, S., and Hansen, R.J.: The response of shear walls to dynamic loads. Department of Civil and Sanitary Engineering, Massachusetts Institute of Technology, Cambridge, MA., 312 pp. (1960)
2. Shiga, T., Shibata, A., and Takahashi, J.: Experimental study on dynamic properties of reinforced concrete shear walls. In: Proceedings, 5th World Conference on Earthquake Engineering, Rome, v.1, pp. 1157-1166 (1973)
3. Hirosawa, M.: Past experimental results on reinforced concrete shear walls and analysis on them. Kenchiku Kenkyu Shiryo, No. 2, Building Research Institute, Ministry of Construction, Tokyo, Japan, 279 pp. (in Japanese) (1975)
4. Sato, S., Ogata, Y., Yoshizaki, S., Kanata, K., Yamaguchi, T., Nakayama, T., Inada, Y., Kadoriku, J.: Behavior of shear walls using various yield strength of rebar, part 1: An experimental study. In: Proceedings, Tenth International Conference on Structural Mechanics in Reactor Technology, H09/01, Anaheim, C.A., pp. 233-238 (1989)
5. Carrillo, J., and Alcocer, S. M.: Shear strength of reinforced concrete walls for seismic design of low-rise housing. ACI Structural Journal, 110(3), 415-425 (2013)

6. Kassem, W.: Shear strength of squat walls: a strut-and-tie model and closed-form design formula. Engineering Structures, 84, 430-438 (2015)
7. Mau, S., T., Hsu, T., T., C.: Shear behavior of reinforced concrete framed wall panel with vertical loads. ACI Structural Journal, 84(3), 228-234 (1987)
8. Architectural Institute of Japan: Design guidelines for earthquake resistant reinforced concrete buildings based on inelastic displacement concept (1999)
9. Krolicki, J., Maffei, J., and Calvi, G. M.: Shear strength of reinforced concrete walls subjected to cyclic loading. Journal of Earthquake Engineering, 15(S1), 30-71 (2011)
10. Wood, S. L.: Shear strength of low-rise reinforced concrete walls with boundary elements. ACI Structural Journal, 87(1), 99-107 (1990)
11. Moretti, M.L., Kono, S., Obara, T.: On the shear strength of reinforced concrete walls. ACI Structural Journal 117(4), 293-304 (2021)
12. Gulec, C.K., Whittaker, A.S. Empirical equations for peak shear strength of low aspect ratio reinforced concrete walls. ACI Structural Journal 108(1), 80-89, (2011)
13. EN 1998-1:2004, Eurocode 8: Design of structures for earthquake resistance, part 1: General rules, seismic action and rules for buildings. European Committee for Standardization, Brussels, Belgium (2004)
14. EN 1998-3, Eurocode 8: Design of structures for earthquake resistance, part 3: Assessment and retrofitting of buildings. European Committee for Standardization, Brussels, Belgium (2005)
15. Architectural Institute of Japan. AIJ Standard for Lateral Load-Carrying Capacity Calculation of Reinforced Concrete Structures (Draft), Tokyo, Japan, (2016)
16. Greek Code for Reinforced Concrete, EKOS2000, in Greek (2000)
17. EN 1992-1-1. Eurocode 2: Design of concrete structures - Part 1-1: General rules and rules and rules for buildings. European Committee for Standardization, Brussels, Belgium (2004)
18. Tassios, T.P., Moretti, M., Bezas, A. On the behavior and ductility of reinforced concrete coupling beams of shear walls. ACI Structural Journal, 93(6), 711-720 (1996)
19. Moretti, M., Tassios, T.P. Behaviour of short columns subjected to cyclic shear displacements: Experimental results. Engineering Structures, 29(8), 2018-2029 (2007)
20. Barda, F., Hanson, J.M., Corley, W.G. Shear strength of low-rise walls with boundary elements. Reinforced Concrete Structures in Seismic Zones, SP-53, Hawkins, N.M., Mitchell, D. (eds.), American Concrete Institute, Farmington Hills, MI, pp. 149-202 (1977)
21. ASCE/SEI 43-05. Seismic Design Criteria for Structures, Systems and Components in Nuclear Facilities. American Society of Civil Engineers, Reston, VA (2005)
22. Moretti, M.L., Kono, S., Obara, T. Design equations for ultimate shear capacity of reinforced concrete walls. 17th World Conference on Earthquake Engineering, 17WCEE, Sendai, Japan, 13-18 September (2020)
23. Moretti, M.L. Assessment of shear strength of reinforced concrete walls: Is an upper limit apposite? A. Ilki et al. (Eds.): fib Symposium 2023, LNCE 350, pp. 1300-1309 (2023)
24. Moretti, M., Tassios, T.P. Behavior and ductility of reinforced concrete short columns using global truss model. ACI Structural Journal, 103(3), 319-327 (2006)
25. FEMA 306. Evaluation of Earthquake Damaged Concrete and Masonry Wall Buildings: Basic Procedures Manual. Prestandard and Commentary for the Seismic Rehabilitation of Buildings, Federal Emergency Management Agency, Washington, DC (1999)
26. Luna, B.N., Rivera, J.P., Whittaker, A.S. Seismic behavior of low-aspect-ratio reinforced concrete shear walls. ACI Structural Journal, 112(5), 593-603 (2015)

27. Cardenas, A.E., Russel, H.G., Corley, W.G. Strength of low-rise structural walls. Reinforced Concrete Structures Subjected to Wind and Earthquake Forces, SP-63, American Concrete Institute, Farmington Hills, MI, pp. 221-241 (1980)
28. Park, H.G., Baek, J.-W., Lee, J.-H., Shin, H.-M. Cyclic loading tests for shear strength of low-rise reinforced concrete walls with grade 550 MPa bars. ACI Structural Journal 112(3), 299-310 (2015)

# Seasonal Variation of $V_S$ at Shallow Depth and Nonlinear Behavior of Soil Based on the ARGONET Vertical Array Data

Zafeiria Roumelioti[1][0000-0001-5038-3052] and Fabrice Hollender[2][0000-0003-1440-6389]

[1]Department of Geology, University of Patras, 26504 Rio, Patras, Greece
[2]CEA DES, DIMP, DCET, SESN, Cadarache, 13108 Saint-Paul-lez-Durance, France / UGA, USMB, CNRS, IRD, UGE, ISTerre, 38000 Grenoble, France
zroumelioti@upatras.gr, fabrice.hollender@cea.fr

**Abstract.** Ground acceleration time histories from earthquakes recorded by the ARGONET vertical array in Cephalonia, Greece, in the period from July 2016 to April 2022, are analyzed seeking evidence for nonlinear behavior of the shallow soil layers. Shear waves velocity, $V_S$, between the shallowest sensor pair of the vertical array, i.e., within the top 5.6 m of the soil column, is derived for each earthquake record using the method of interferometry by deconvolution. The temporal variation of $V_S$ values is compared with indicators related to soil moisture and this leads to the identification of a clear difference in the level of the measured values between periods of intense rainfall and the dry summer months. Lower velocities, even lower than the level of $V_S$ during rainy periods (7-13% of the annual average), are obtained based on the strongest records of the analyzed sample. These low velocities are considered as indicators of nonlinear soil behavior, the threshold onset of which is difficult to determine without prior correction for the seasonal variation. The applied method can provide a detailed description of $V_S$ changes even during a single earthquake. Examples are provided on how nonlinear soil behavior may be manifested by a sudden $V_S$ value drop at the arrival of the strongest seismic phases.

**Keywords:** shear-wave velocity, interferometry, soil response

## 1 Introduction

The phenomenon of nonlinear soil behavior during strong seismic shaking has been recognized for decades, initially through laboratory experiments and later directly in seismic recordings (e.g. [1],[2],[3],[4],[5]). In seismic recordings, evidence of the phenomenon is usually sought through the comparative study of spectral ratios from recordings of strong and weaker earthquakes (e.g., a mainshock and its pre- and aftershocks) in the vicinity of a seismogenic fault. The nonlinear ground behavior is often imprinted as a "distortion" of the earthquake spectrum with energy shifting from higher to lower frequencies and a simultaneous reduction of spectral amplitudes in the natural frequency range of the ground column at the site (e.g. [6],[7]).

In the present study, the phenomenon of nonlinear soil behavior is investigated in changes of the shear wave velocity, $V_S$, in the shallowest meters of the soil column (upper 5.6 m) at the location of the ARGONET vertical accelerometer array in Argostoli, Cephalonia. The method applied is seismic interferometry by deconvolution and the aim is to identify unusually low $V_S$ values that could be used as indicators for further analysis of the recordings in terms of their correlation with nonlinear soil behavior phenomena.

# 2 Data

## 2.1 The ARGONET Vertical Array of Accelerometers

The data set analyzed was obtained from the vertical accelerometer array of the ARGONET infrastructure in Argostoli, Cephalonia [8]. The array was installed in July 2015, initially comprising a surface accelerometer (CK00) mounted on a small concrete slab within a specially constructed wooden shelter and three borehole accelerometers at depths of 15.5, 40.1 and 83.4 m (CK15, CK40 and CK83, respectively). All accelerometers are of the Episensor Force Balance type from Kinemetrics. One year after the launching of the array (July 2016), another accelerometer was added in a 5.6 m deep borehole (CK06). Since their installation, the accelerometers have been continuously recording (with only short interruption intervals for individual instruments due to various technical problems) the ground motion at a rate of 200 samples per second. More information on the installation and geotechnical details of the site are provided in [8]. The ARGONET infrastructure database is open access and available through the website https://argonet-kefalonia.org/data/argonet_data/.

The data analyzed in this work are from the shallowest pair of accelerometers in the array, i.e. CK00 (0 m) and CK06 (5.6 m). Based on the available geological and geotechnical data, the medium between the two accelerometer locations consists of artificial fill (sandy-silty gravel, occasional large stones) to a depth of ~2 m, which overlies a ~6 m thick horizon of lake sediments (silty sand, sandy silt and clay). At greater depths, alternations of clay, silt and marl are encountered, which gradually transition to sandy-marly limestones, whereas at 83.5 m the Cretaceous limestone, considered the geotechnical bedrock of the area, occurs.

## 2.2 Description of Data – Initial Processing

The analyzed dataset includes 1524 horizontal ground acceleration component pairs (North-South and East-West directions, as available in the ARGONET database) corresponding to 762 earthquakes that occurred in the period July 2016 - April 2022, with local magnitude $M_L$=1.4-6.6 and epicentral distances $R$=2-180 km. Most records are of weak seismic motion, with only 5 of them exceeding 100 cm/s$^2$ at the surface station CK00. The main parameters of these recordings and the earthquakes that caused them are summarized in Table 1. The focal parameters of the examined earthquakes were taken from the catalogue of the Geodynamic Institute of the National Observatory of Athens (https://bbnet.gein.noa.gr/HL/databases/database).

**Table 1.** Basic parameters of the strongest strong ground motion records included in the analysis and of their causative earthquakes (in increasing PGA at the surface station CK00)

| Date_Time | Lat | Lon | h(km) | $M_L$ | R | PGA_CK00 | PGA_CK06 |
|---|---|---|---|---|---|---|---|
| 20170501_110241 | 38.224 | 20.548 | 4.1 | 3.7 | 8 | 169.2 | 116.5 |
| 20181025_225449 | 37.341 | 20.512 | 9.9 | 6.6 | 91 | 149.7 | 107.4 |
| 20160919_035945 | 38.112 | 20.363 | 21.6 | 4.4 | 14 | 139.8 | 118.6 |
| 20200119_025209 | 38.168 | 20.748 | 6.9 | 4.8 | 21 | 119.4 | 58.1 |
| 20211119_132704 | 38.209 | 20.294 | 15.5 | 4.8 | 19 | 107.1 | 92.8 |

The set of horizontal recordings of stations CK00 and CK06 analyzed were corrected for base level and to remove possible linear trends over their entire duration. Then, a portion of each record with a duration up to the time when 75% of the Arias intensity is observed was automatically selected. In this way, part of the surface and coda waves were cut off, retaining most of the S waves [9], to avoid cases of highly energetic surface waves that could lead to surface wave velocity measurements instead of the requested $V_S$. Finally, a 2nd order Butterworth-type band-pass filter was applied in the frequency range 0.5-20 Hz, where the signal-to-noise ratio is sufficient to lead to reliable results even in the weaker recordings considered. The values of the signal-to-noise ratio in different frequency intervals are provided in the metadata file accompanying the recordings data (https://argonet-kefalonia.org/data/argonet_data/).

# 3 VS Velocity Using Interferometry by Deconvolution

## 3.1 Method

The method that was used to determine $V_S$ within the top 5.6 m at the ARGONET site is the interferometry by deconvolution ([5],[10],[11],[12]). Through the deconvolution of the borehole seismic recording from the surface one, it is possible to determine the travel velocity of the seismic waves pulse in the between the two stations distance. This velocity corresponds to the dominating in terms of energy/amplitude seismic phase, which in the selected parts of the seismic recordings is expected to be the S-wave phase. The mathematical description of the result of the deconvolution of the recording at the location of a station *j* to that of a station *i* is:

$$D_{j-i}(t) = FT^{-1}\left\{\frac{A_j(\omega)}{max\left\{A_i(\omega),\ k\left(|A_i(\omega)|,\ \frac{A_i(\omega)}{|A_i(\omega)|}\right)_{max}\right\}}\right\} \quad (1)$$

where $\omega$ is the angular frequency, $A_j(\omega)$ the Fourier transform of the recording at station *j*, $A_i(\omega)$ the Fourier transform of the «reference» *i* station and *k* a parameter that stabilizes the deconvolution procedure in the frequency domain by defining a minimum frequency amplitude, which in our application was set to 10% of the mean spectral amplitude [13].

The result of the deconvolution through Equation (1) is the required pulse, which is then used, for example through its peak value, to measure its travel time from the location of accelerometer j to that of accelerometer i. Knowing the distance between the

two accelerometers, the time measurement is converted into a measurement of the velocity $V_S$ in the intervening material. To avoid cases of erroneous measurements due to e.g. double earthquakes or noisy interferograms, a quality criterion was set that the pulse peak should be at least 1.5 times larger than the next in amplitude peak appearing in the interferogram. In addition, all interferograms were visually inspected to ensure the quality of the measurements.

An example of the process of measuring the seismic wave pulse velocity is shown in Figure 1. In this example, the results have been obtained from the recordings of an M3.9 earthquake, the epicenter of which was located 45 km from the ARGONET location (01/02/2019, 05:02GMT). The bottom part of Figure 1 clearly shows the pulse of the waves propagating towards the surface (upward pulse; negative part of x-axis), but also that of the waves reflected at the ground surface and returning propagating downward (downward pulse; positive part of x-axis). The measurements in this study were based on the upward propagating waves and the points considered for measuring the pulse travel time are marked in the example in Figure 1 with red circular symbols.

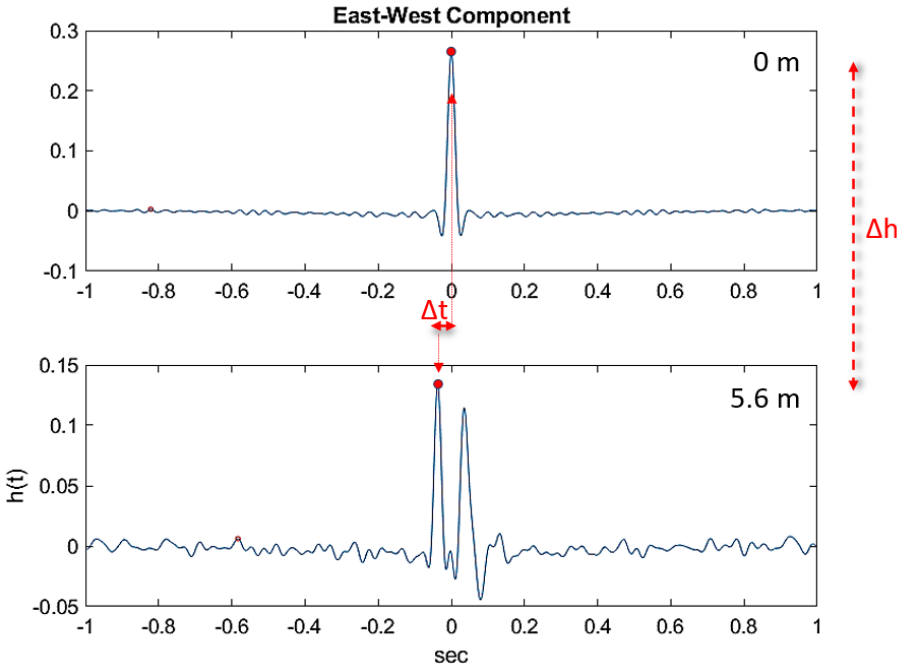


**Fig. 1.** Example results of the interferometry by deconvolution method using the recordings of a M3.9 earthquake (February 01, 2019, 05:02GMT) at epicentral distance of 45 km from the ARGONET site. Red circular symbols denote the pulse peaks that have been used to measure the travel velocity of the seismic waves pulse, $\Delta t$, for the distance $\Delta h$ and ultimately of $V_S$

### 3.2 Application and Results

Of the total 1524 pairs of records examined, 1318, corresponding to 659 earthquakes, met the quality criteria mentioned in the previous section. These values, as calculated

for the East-West component are presented in Figure 2. The results for the North-South component are not presented for reasons of space economy, but it has been checked and confirmed that they lead to the same conclusions as described below.

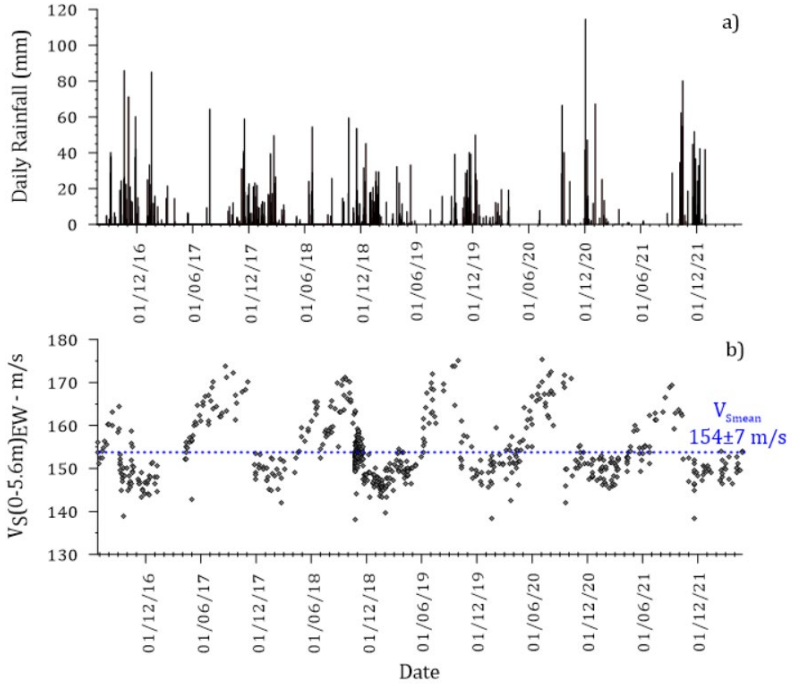


**Fig. 2.** Temporal variation of a) the daily precipitation height at a station of the Hellenic National Meteorological Service in Argostoli and b) the $V_S$ values measured by seismic interferometry. The dotted blue line indicates the average $V_S$ value calculated for the location of the ARGONET array

The main conclusion from observing the results in Figure 2 is that the measured quantity ($V_S$) in the upper 5.6 m of the soil column in ARGONET shows significant variation with time. The mapped values vary between 138 and 175 m/s, around the mean value of 154 m/s. The temporal variation is not random but shows repeatability with a period of one year. In a previous work [12], a correlation of these discrete periods with precipitation and indirectly with the moisture content of the shallow subsurface was found. In Figure 2 we contrast the $V_S$ results with daily precipitation data provided by the Hellenic National Meteorological Service (http://www.hnms.gr) for its permanent station in the Argostoli area. The comparison of the two distributions confirms over almost 6 hydrological cycles the existence of the previously mentioned correlation, with the lowest $V_S$ values occurring abruptly after the onset of intensive rainfall of each hydrological cycle, and the highest during the dry summer months.

The observation of the correlation between the variations of $V_S$ values and the hydrological cycle led to the decision to reinforce the ARGONET infrastructure with a meteorological station and a soil moisture meter. The ARGONET meteorological

station, installed at the Ionian University premises, at ~1 km from the vertical accelerometer array, and the soil moisture meter (type SoilVUE10 - 1 m, Campbell Scientific), installed at the vertical array site, have been operating with continuous recording since July 2021. Figure 3 compares the $V_S$ values corresponding to earthquakes in the period July 2021-April 2022, the rainfall data from the ARGONET meteorological station (hourly measurements) and the soil moisture measurements (% of volume) at 0.75 m depth for the corresponding period. The vertical dashed line marks the abrupt change in the level of measured $V_S$ values, which coincides with a sharp increase in soil moisture after the first heavy rainfall in October 2021.

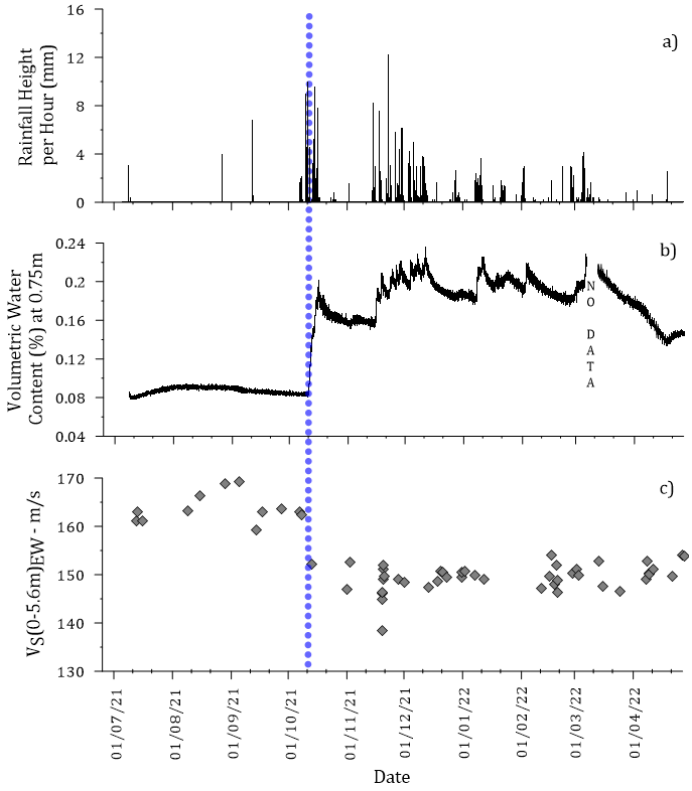


**Fig. 3.** Comparison of a) the precipitation height (hourly measurements) recorded at the newly installed ARGONET meteorological station, at ~1 km from the location of the accelerometer array, with b) soil moisture measurements at the ARGONET site at 0.75 m depth and c) the temporal variation of $V_S$ values calculated from earthquake data in the period July 2021 - April 2022. The vertical dashed line marks the time of the abrupt change in the level of measured $V_S$ values, which coincides with the onset of the strong and prolonged rainfall of the hydrological cycle and the consequent increase in soil moisture

A second observation with respect to Figure 2 is the presence of some $V_S$ values at levels even lower than the lowest of seasonal variation. These values are found to be associated with the strongest (in terms of PGA) records of the analysed sample. In

Figure 4, the $V_S$ values obtained from the five waveforms of the sample with PGA at the surface stations CK00 >100 cm/s$^2$ are marked with red triangular symbols. The correlation of these $V_S$ values with the intensity of ground vibration indicates a decrease in $V_S$ due to non-linear soil behavior.

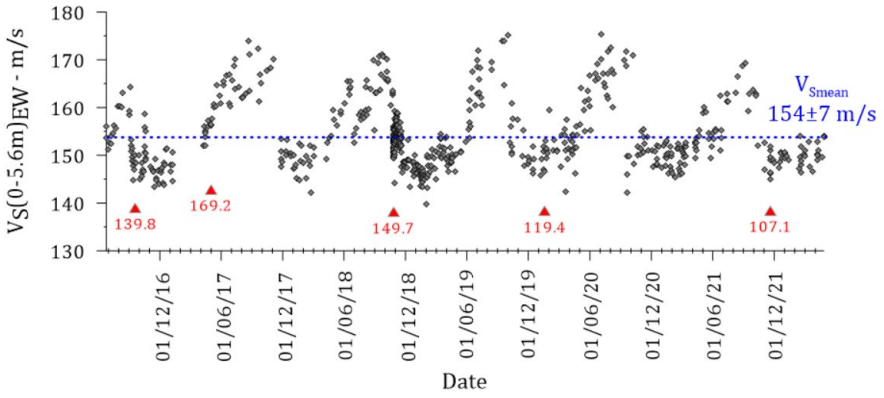


**Fig. 4.** Temporal variation of $V_S$ calculated by the interferometry method (as in Figure 2b) where red triangular symbols indicate the values obtained based on the 5 strongest records of the studied dataset (Table 1, PGA at surface station CK00 > 100 cm/s$^2$). The corresponding PGA value at station CK00 (in cm/s$^2$) is noted below the individual symbols

The five earthquakes corresponding to the red symbols in Figure 4 were further analysed through seismic interferometry, performing calculations in different time windows in order to obtain the time history of the VS variation during the individual events. The calculations were initially performed with a time window of 3s duration, starting at the beginning of each recording. In subsequent steps, the duration of the window was gradually increased (with a step of 0.1s) until the duration of the strong ground motion was exceeded. The results of this analysis are mapped as red curves in Figure 5 for 2 example events. The top of each plot shows the accelerogram at station CK00. The black curves in the plot of VS values with time correspond to the results obtained when instead of a time window of steadily increasing duration, a window of constant duration (3s) was used, which, however, was shifted with a constant step (0.1s) to the right of the time axis. The results of the two approaches in the plots in Figure 5 are comparable up to the region where VS takes the lowest values (~10s in 5a and at 5-7s in 5b). From there on, the increasing duration window maintains the low value, which proves that the effect of the applied method is modulated by the more active seismic phase. In contrast, the shifting but constant-duration window gradually enters the region of the coda waves and the level of the measured VS starts to rise, indicating the return of the ground behavior to the linear region. The VS drop for the 5 earthquakes studied was found to be of the order of 10-20 cm/s2 for the sediment thickness (5.6 m) studied, i.e. ~7-13% of the annual average VS value.

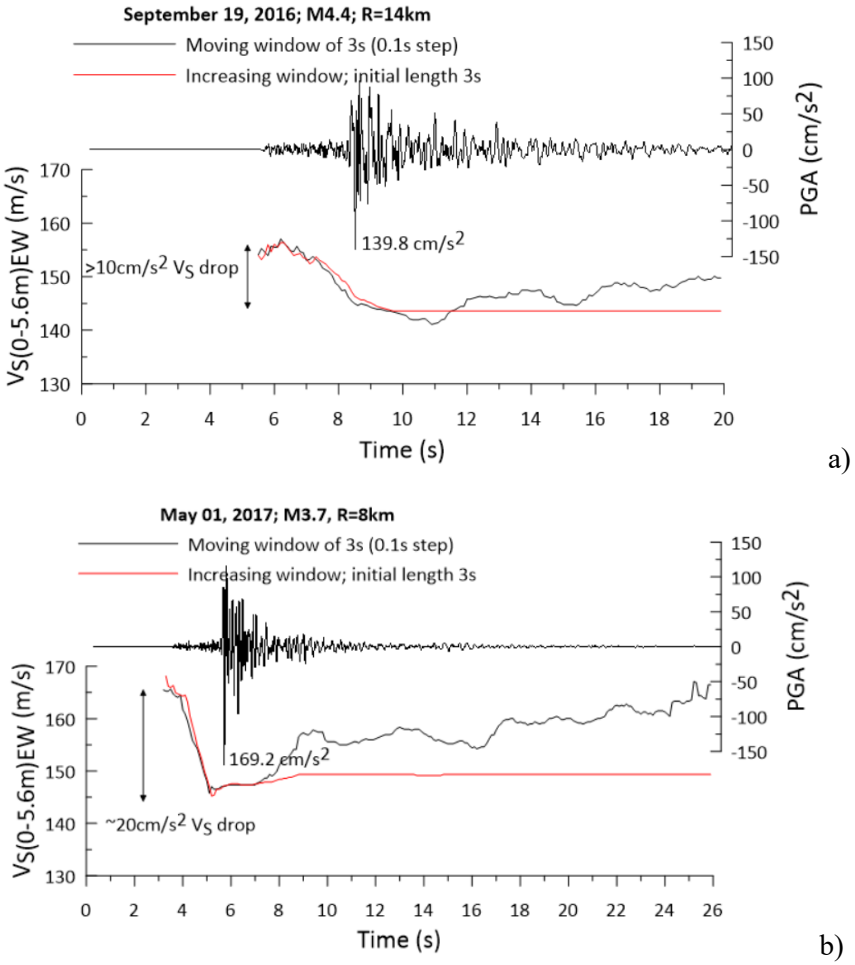


**Fig. 5.** Examples of $V_S$ variation analysis during individual earthquakes, namely a) the M4.4 earthquake that occurred at a distance of ~14 km from ARGONET on 19/09/2016 and b) the M3.7 earthquake that occurred at a distance of ~8 km on 01/05/2017. The top panel maps the time history of the ground acceleration in the East-West component of CK00, whereas the bottom panel maps the $V_S$ variation with time. The interferometry was applied to individual time windows that either gradually increased in duration starting from a minimum duration of 3s at the beginning of the record and including a progressively longer part of it (red curves), or were of fixed duration (3s) but moving at steps of 0.1s to the right (black curves)

# 4 Conclusions

In this paper, the ground acceleration records of 659 earthquakes obtained at the surface and the 5.6m-deep borehole station of the ARGONET vertical array in Argostoli, Cephalonia, during the period July 2016 - April 2017 were analysed. The aim

was to apply the seismic interferometry by deconvolution method to calculate the shear wave velocities in the upper 5.6 m of the soil column at the recording site and to investigate possible velocity variations that could indicate non-linear soil behaviour. The analysis revealed a significant seasonal variation in the measured values, clearly correlated with the variation in rainfall and soil moisture. At least 5 cases of $V_S$ values at a level lower than even the lower limit of the seasonal variation were identified in the analysed data set. These values correspond to the 5 strongest records in the sample (PGA = 107.1-169.2 cm/s2), which were further studied in terms of VS variation over their duration. A detailed analysis of the $V_S$ time history reveals a clear decrease in its value during the passage of the strongest shear waves, which in the analysed data reached up to 13% of the annual average $V_S$ value at the ARGONET site. This drop is attributed to effects of non-linear soil behaviour.

In the international literature one can find several different estimates of the value of PGA that defines the onset of non-linear soil behaviour. Indicative values are 100-200 cm/s$^2$ [6], ~60 cm/s$^2$ [14], 50 cm/s$^2$ [4], 35 cm/s$^2$ [3]. The results of the present study highlight the need to understand and correct the effect of the seasonal variation of $V_S$ in order to establish the true threshold of the onset of nonlinear soil behaviour. Although at the strongest records the effect is strong enough to be detected, at lower levels of ground shaking it may be obscured by the effect of seasonal variation of $V_S$ and become undetectable. In addition, it is of interest to investigate the role of $V_S$ level at the onset of nonlinear behavior, e.g., if the margin for nonlinear behavior is greater during dry months, when $V_S$ levels are at their maximum.

The aim of future research is the physical interpretation of the phenomenon of seasonal variation in VS, and the study of its effects on the amplitudes and frequency content of ground motion. By removing the seasonal variation from the measured values, it is expected to better highlight the low VS values that, according to this work, indicate non-linear soil behaviour. With the continued operation of the ARGONET infrastructure and the ongoing recording of numerous data, it will be possible to quantify the phenomenon even at low levels of ground vibration.

# Acknowledgments

The research project was supported by the Hellenic Foundation for Research and Innovation (H.F.R.I.) under the "2nd Call for H.F.R.I. Research Projects to support Faculty Members & Researchers (Project Number: 2724). The Hellenic National Metereological Service (http://www.hnms.gr) is gratefully acknowledged for providing data of the meteorological station of Argostoli.

# References

1. Field, E.H., Johnson, P.A., Beresnev, I.A., Zeng, Y.: Nonlinear ground-motion amplification by sediments during the 1994 Northridge earthquake. Nature 390, 599–602 (1997)
2. Lee, W.H.K., Shin, T.C., Kuo, K.W., Chen, K.C., Fu, C.F.: CWB free-field strong-motion data from the 21 September Chi-Chi, Taiwan, earthquake. Bull. Seism. Soc. Am. 91,

1370–1376 (2001)
3. Rubinstein, J.L.: Nonlinear site response in medium magnitude earthquakes near Parkfield, California. Bull. Seism. Soc. Am. 101(1), 275-286 (2011)
4. Régnier, J., Cadet, H., Bonilla, L.F., Bertrand, E., Semblat, J.F.: Assessing nonlinear behav-ior of soils in seismic site response: statistical analysis on KiK-net strong-motion data. Bull. Seism. Soc. Am. 103(3), 1750-1770 (2013)
5. Chandra, J., Guéguen, Ph., Bonilla. L.F.: PGA-PGV/VS considered as a stress-strain proxy for predicting nonlinear soil response. Soil Dyn. Earthq. Eng. 85, 146-160 (2016)
6. Beresnev, I.A., Wen, K.L.: Nonlinear soil response – a reality. Bull. Seism. Soc. Am. 86(6), 1964-1978 (1996)
7. Assimaki, D., Li, W., Steidl, J.H., Schmedes, J.: Quantifying nonlinearity susceptibility via site-response modeling uncertainty at three sites in the Los Angeles Basin. Bull. Seism. Soc. Am. 98(5), 2364-2390 (2008)
8. Theodoulidis, N., Hollender, F., Mariscal, A., Moiriat, D., Bard, P.-Y., Konidaris, A., Cushing, M., Konstantinidou, K., Roumelioti, Z.: The ARGONET (Greece) seismic observatory: An accelerometric vertical array and associated data. Seism. Res. Lett. 89(4), 1555–1565 (2018)
9. Abrahamson, N.A.: Program on Technology Innovation: Effects of Spatial Incoherence on Seismic Ground Motions. EPRI, Palo Alto, California, (2007)
10. Mehta, K., Snieder, R., Graizer, V.: Downhole receiver function: A case study. Bull. Seism. Soc. Am. 97(5), 1396–1403 (2007)
11. Guéguen, Ph.: Predicting nonlinear site response using spectral acceleration VS PGV/VS30: A case history using the Volvi-Test site. Pure Appl. Geophys. 173(6), 2047–2063 (2016)
12. Roumelioti, Z., Hollender, F., Guéguen, Ph.: Rainfall-induced variation of seismic waves ve-locity in soil and implications for soil response: what the ARGONET (Cephalonia, Greece) vertical array data reveal. Bull. Seism. Soc. Am. 110(2), 441-451 (2020)
13. Clayton, R.W., Wiggins, R.A.: Source shape estimation and deconvolution of teleseismic bodywaves. Geophys. J. Roy. Astron. Soc. 47, 151–177 (1976)
14. Wu, C.Q., Peng, Z.G., Ben-Zion, Y.: Refined thresholds for non-linear ground motion and temporal changes of site response associated with medium-size earthquakes. Geophys. J. Int. 182, 1567-1576 (2010)

# Investigation of the ANNs' potential for reliable assessment of r/c frame's seismic damage using different performance evaluation metrics

Ntovas Aggelos[1] and Kostinakis Konstantinos[2]

[1]Aristotle University of Thessaloniki, University Campus, 54124 Thessaloniki, Greece
[2]Aristotle University of Thessaloniki, University Campus, 54124 Thessaloniki, Greece
akntovas@civil.auth.gr, kkostina@civil.auth.gr

**Abstract**. The development of a reliable method for the rapid assessment of the expected level of seismic damage of buildings constructed in countries with high seismicity areas is one of the crucial issues of current research, so that the authorities can take the necessary decisions for their rehabilitation or retrofit. A new approach to the problem is the application of methods that fall within the field of Artificial Neural Networks (ANNs). In this paper, an application of ANNs is attempted to predict the level of seismic damage in reinforced concrete frames. For this purpose, 27 frames with different structural characteristics were selected, designed and analyzed by nonlinear dynamic analysis. Then, ANNs were used to test their ability to reliably predict the level of seismic damage. The parameters that configure the networks were also investigated and their performance was evaluated using a number of metrics. The results showed that the optimal network can estimate the seismic damage level with significant reliability, provided that the training sample and the network modeling parameters are properly selected through a testing procedure.

**Keywords:** Seismic Damage Assessment, Artificial Neural Networks, Machine Learning, Reinforced Concrete Buildings

## 1 Introduction

One of the most important and topical scientific issues in the field of seismic engineering is the assessment of the structural response of buildings subjected to seismic excitations. To date, a large number of researchers have addressed this issue and several different methods have been proposed for the seismic assessment of structures. Many of these methods focus on the rapid estimation of seismic damage and seismic vulnerability of buildings without the requirement of performing time-consuming nonlinear analyses (e.g. [1-4]). These methods, which use practices based on the application of statistical theory, have two main drawbacks: they cannot always reliably account for complex nonlinear relationships between the parameters describing the problem and

they are unable to adequately solve complex problems involving a large number of variables. In recent decades, the increase in computer power has led to the development of modern statistical methods based on the adoption of artificial intelligence and machine learning algorithms. These algorithms achieve seismic response estimation by extracting patterns from data collected or generated through measurements or analyses. Modern research on these methods has revealed that they can provide a fast, reliable and computationally easy way to evaluate buildings' seismic damage and that they can be used as an effective alternative to conducting demanding and time-consuming analyses (e.g. [5-6]).

A significant number of published research papers have focused on predicting the level of seismic damage of buildings by applying machine learning methods, especially Artificial Neural Networks (ANNs). A detailed literature review of the most important works in the field of applying machine learning methods for structural damage assessment was carried out by Harirchian et. al [7], Xie et. al [8] and Sun et. al [9]. In the following, a brief review of some of the most important related research works is given. Molas and Yamazaki [10] were among the first researchers to study the ability of ANNs to accurately predict the seismic damage of wooden structures. Stephens and VanLuchene [11] trained ANNs to use them to estimate the damage level of reinforced concrete buildings expressed through Park and Ang's damage index. Latour and Omenzetter [12] investigated the ability of ANNs to reliably estimate the seismic damage of planar reinforced concrete frames using the results of nonlinear dynamic analyses. Rofooei et al. [13] used data from nonlinear dynamic analyses of reinforced concrete frames to investigate the effect of structural and seismic characteristics on the predictive ability of the ANNs. Kostinakis, Morfidis et al., in a series of research papers [14-20], attempted to assess the reliability of the ANNs in terms of estimating the seismic response of reinforced concrete buildings. In addition, they examined the optimal number and combination of input parameters through which the most accurate seismic damage prediction can be achieved, the influence of the parameters used for the design and training of the networks on the effectiveness of their predictions, and the effect of the presence of masonry infills on the results. From this work, it was generally concluded that ANNs have the potential for relatively reliable real-time predictions of the level of seismic damage of buildings, as long as a sufficiently large database is available to train them.

Thus, in the context of the present study, a pilot application of ANNs for the assessment of the seismic damage level of reinforced concrete (r/c) frames designed according to the provisions of EC2 [21] and EC8 [22] was attempted. For this purpose, 27 r/c frame buildings with different structural characteristics, such as the number of storeys and number and length of openings, are selected, designed and analysed using Nonlinear Time History Analysis (NTHA). These buildings were analysed for 65 seismic excitations obtained from relevant international databases. From the analyses, their global damage index in terms of Maximum Interstorey Drift Ratio (MIDR) was calculated. This created a large training database with 1755 records. Subsequently, based on the above training sample, perceptron-type ANNs were used to investigate their ability to reliably estimate the seismic damage levels. The problem was formulated as a pattern recognition problem, which means that the aim is to predict the classification of frame

to pre-defined seismic damage categories on the basis of the value of the MIDR. The parameters that configure the networks were also investigated and their performance was evaluated using a number of metrics. The results of the investigation showed that the optimal network can estimate the seismic damage level with significant reliability provided that the training sample, as well as the network configuration parameters, are properly selected through a process of testing and optimization.

## 2 Artificial Neural Networks (ANNs)

The Artificial Neural Networks (ANNs) are complex computational tools which are capable to handle problems using the general rules of the human brain functions. Thus, using ANNs it is possible to approximate the solution of problems such as the pattern recognition and the function approximation problem. The ANNs' function is based on the combined action of interconnected processing units that are called artificial neurons (Fig. 1(a)). The artificial neuron receives input signals ($x_1$, $x_2$,…., $x_m$) and transform them to an output signal ($y_k$) through the use of an adder (which adds the products of the input signals by the respective synaptic weights ($w_{k1}$, $w_{k2}$,…., $w_{km}$) of neuron's synapses) and the use of an activation function (which has as argument the $u_k$ that results from the adder and transforms it to the output signal $y_k$). For details about the inputs and outputs of the present investigation see Section 3. Note that the problem was formulated as a pattern recognition problem, which means that the aim is to predict the classification of frames to pre-defined seismic damage categories on the basis of the value of the MIDR. In this case, the output is the classification of a r/c frame which is subjected to a seismic excitation into pre-defined seismic damage classes. Thus, the unknown function (which the ANNs have to approach) has as output a vector which is used for the mapping between the values of the global damage index in terms of MIDR and the predefined damage classes (see for example Fig. 2). Synaptic weights are numerical values that determine the strength and direction of the impact of one neuron on another. The activation function is a function that calculates the output of the network based on its individual inputs and their weights. Fig. 1(b) presents the typical configuration of a MFP type ANN with four layers of neurons (input layer, two hidden layers and output layer). The hidden layer is a series of artificial neurons that processes the inputs received from the input layers before passing them to the output layer. The solution of problems using ANNs is accomplished if they have been trained using the training algorithms. These algorithms are procedures which require a set of *n* input vectors **x** and the corresponding to them n output vectors **d** that called target vectors. The *n* pairs of vectors **x** and vectors **d** constitute the training dataset. During the training procedure the values of the synaptic weights (w) are successively altered until the error vector that is produced by the ANN is minimized.

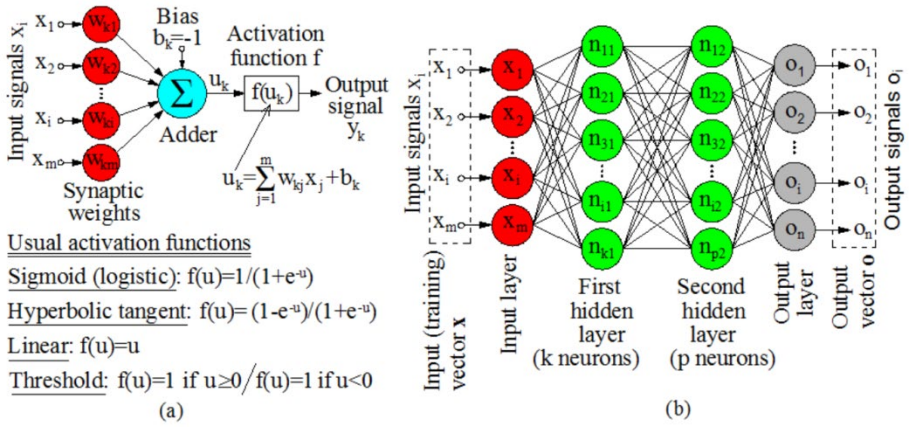


**Fig. 1.** The typical artificial neuron (a) and typical configuration of a Multilayer Feedforward Perceptron (MFP) network (b)

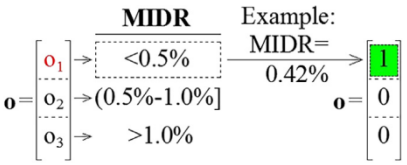


**Fig. 2.** General form of output vectors o (three damage classes)

# 3 Formulation of the Problem

## 3.1 Steps of the Methodology

The procedure adopted in order to formulate the problem in terms compatible with ANNs' methods consists of the following steps:

- Generation of the training dataset: selection of a sufficient number of representative r/c frames, design and modeling of the inelastic properties of the buildings and selection of seismic records.
- Selection of the input parameters of the problem (structural and seismic parameters).
- Conduction of NTHA, in which the buildings are analysed for the selected seismic records and the level of the seismic damage is determined in terms of an appropriate seismic damage index, which is selected as the output (target) parameter of the ANNs.

### 3.2 Generation of the Training Dataset

**Selection, design and modeling of the inelastic properties of the frame buildings**

For the generation of the training dataset, 27 r/c frames were chosen, which are differentiated from each other in terms of the following characteristics:

- Number of storeys (height of frame): 3, 5 and 7 storeys.
- Number of openings: 3, 5 and 7 openings.
- Opening length: 3.0, 4.5 and 6.0 m.

For the frames' modeling all basic recommendations of EC8 [22], such as the rigid zones in the joint regions of beams/columns and the values of flexural and shear stiffness corresponding to cracked r/c elements were taken into consideration. It also must be noted that the frames were considered to be fully fixed to the ground. The frames were designed considering static vertical as well as earthquake loads using the modal response spectrum analysis (for soil category C and PGA=0.24g), as described in EC8 [22]. The r/c structural elements were designed following the provisions of EC2 [21] and EC8 [22] and considering the following materials: concrete C20/25 and steel B500c. After the frames' design, the modeling of their inelastic properties was made with the aid of lumped plasticity models (plastic hinges) at the column and beam ends.

**Earthquake Records**

A suite of 65 pairs of horizontal earthquake excitations obtained from the European [23] and the PEER [24] strong motion databases was used as input ground motion for the analyses which were performed in order to generate the networks' training dataset. The seismic excitations, which have been chosen from worldwide well known sites with strong seismic activity, were recorded on Soil Type C according to EC8 [22]. The ground motion set employed was intended to cover a variety of conditions regarding tectonic environment, modified Mercalli intensity and closest distance to fault rapture, thus representing a wide range of intensities and frequency content. The elastic spectra of the ground motions are shown in Fig. 3.

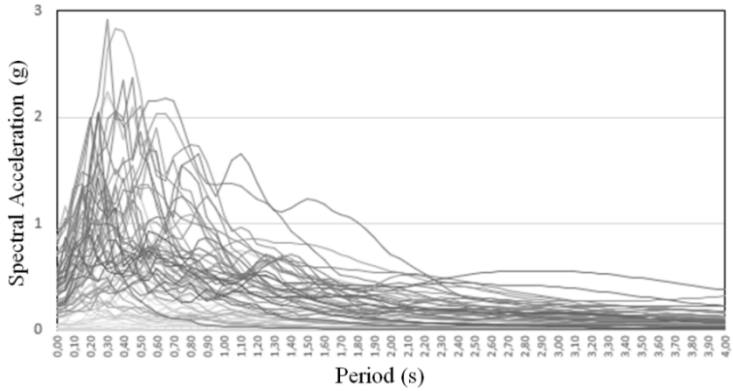


**Fig. 3.** Elastic spectra of the seismic motions

### 3.3 Inputs

The parameters which describe the problem of the assessment of the r/c buildings' seismic damage can be categorized in two classes: the structural parameters and the seismic parameters.

**Structural Parameters**

The response of r/c structures to seismic excitations and, therefore, the assessment of the expected level of structural damage, is a multiparametric problem which depends on an extremely large number of structural parameters. Thus, the problem of selecting the appropriate structural parameters that most influence the behaviour of a building under seismic excitation has no single solution. The use of ANNs gives a greater flexibility, as it is possible to use any number of structural parameters that is desired (see e.g. [12]). In the context of this paper, three structural parameters with three different values each (total number of frames: 3⊕3⊕3=27) were considered as an approach to solve the problem:

- Number of storeys (height of frame): 3, 5 and 7 storeys.
- Number of openings: 3, 5 and 7 openings.
- Opening length: 3.0, 4.5 and 6.0 m.

**Seismic Parameters**

As regards the seismic parameters which are used to describe the seismic excitations and their impact to structures, there are many definitions which are resulted from the analysis of accelerograms records (see e.g.[25]). These parameters can be classified into: (a) seismic parameters determined from the time histories of the records and (b) seismic parameters determined from the response spectra of the records. The reasons for the proposal of the large number of seismic parameters are the complexity of both the earthquake phenomenon and the complexity of the response of structures to seismic excitations. At this point, it is worth emphasizing the fact that the possibility of the ANNs to consider large numbers of parameters as inputs relieves the need to select only one specific seismic parameter, which may not be the most appropriate for the optimal correlation of the seismic intensity to the level of buildings' structural damage. For the investigation conducted in the present study, the seven seismic parameters presented in Table 1 have been chosen. These parameters have been widely used in scientific literature for the quantification of strong motions' intensity.

**Table 1.** Seismic parameters

| Ground Motion Parameter | Calculation procedure | Remarks |
|---|---|---|
| Peak Ground Acceleration: **PGA** | max\|a(t)\| | a(t), v(t) and d(t): acceleration, velocity and displacement time history<br>$t_{tot}$: total duration of the ground motion<br>$S_a$: acceleration spectrum<br>PSV: pseudovelocity spectrum<br>$\xi$: damping ratio |
| Peak Ground Velocity: **PGV** | max\|v(t)\| | |
| Peak Ground Displacement: **PGD** | max\|d(t)\| | |
| Arias Intensity: $\mathbf{I_a}$ | $I_a = \left(\frac{\pi}{2g}\right) \cdot \int_0^{t_{tot}} [a(t)]^2 dt$ | |
| Cumulative Absolute Velocity: **CAV** | $CAV = \int_0^{t_{tot}} \|a(t)\| dt$ | |
| Acceleration Spectrum Intensity: **ASI** | $ASI = \int_{0.1}^{0.5} S_a(\xi = 0.05, T) dT$ | |
| Housner Intensity: **HI** | $HI = \int_{0.1}^{2.5} PSV(\xi = 0.05, T) dT$ | |

### 3.4 Conduction of Analyses and Computation of the Seismic Damage (ANNs' Output)

It is well-known that the damage indices are used for the numerical modeling of the damage level in the vulnerability assessment of structures and can be grouped into categories based on whether they are local or global, deterministic or probabilistic, structural or financial. In the present study, the seismic damage of r/c buildings was expressed in terms of the Maximum Interstorey Drift Ratio (MIDR). The MIDR, which is generally considered an effective indicator of global structural and nonstructural damage of r/c buildings (e.g. [26]), corresponds to the maximum drift among the frame storeys. The relation between the MIDR values and the description of the seismic damage state of r/c frames which was used in the present study is illustrated in Table 2 [27]. According to this classification, the number of damage categories/levels (three) is consistent with the widely used seismic damage classification logic of light (green), moderate (yellow) and heavy (red) damage states used in the case of rapid seismic assessment of buildings after strong earthquake events. In order to generate the dataset required for the training of the ANNs, the selected buildings were analyzed by means of NTHA for each one of the 65 earthquake ground motion pairs presented in section 3.2. Thus, a total of 1755 NTHA (27 buildings x 65 earthquake records) were performed.

For each one of the 1755 analyses, the required data for the MIDR calculation were exported.

**Table 2.** Relation between MIDR and damage state

| **MIDR (%)** | <0.50 | 0.50-1.00 | >1.00 |
|---|---|---|---|
| **Degree of Damage** | Slight Damage | Moderate Damage | Heavy damage |

# 4 ANNs' Configuration and Training Algorithms

The solution of any problem using ANNs requires defining the parameters with the aid of which they will be designed/configured and trained. Determining these parameters is not straightforward, but requires a time-consuming testing process, where in each case the performance of the networks is examined using specific metrics. In the context of this study, the following choices were made for the configuration parameters of the ANNs:

- Number of Inputs: The number of inputs of each ANN equals the number of parameters that enter the problem to be solved. Thus, as mentioned above, the number of inputs was set equal to 10, i.e. the sum of the three structural parameters and the seven seismic parameters.
- Number of Outputs: In the present case the number of outputs equals to one and corresponds to the global damage index MIDR.
- Number of the hidden layers: Networks with a single hidden layer were selected. This choice was based on the fact that the efficiency of such an ANN has been well-documented in numerous relevant research studies (e.g. [12]).
- Number of neurons in hidden layers: The optimum number of neurons in hidden layers is not uniquely defined for all problems. In the context of the present study, an investigation for the determination of the optimum number of neurons in the hidden layer was conducted. More specifically, networks with a number of neurons in hidden layer that ranges between 10 and 100 were configured.
- Parameter Alpha: This parameter controls overfitting, limiting the values of synaptic weights. The values of Alpha that were adopted in this study range between $10^{-5}$ and 0.01.
- Activation functions of neurons: Two different types of activation functions for neurons of the hidden layer were used: the sigmoid function (logistic) and the hyperbolic tangent function (Fig 1(a)). These functions introduce nonlinearity into the behaviour of networks, making them more efficient.
- Partition of the dataset: In order to avoid the overfitting effect, the Cross-Validation procedure was used, which gives a more generalized solution. In this case, the initial training sample is first divided into a training sample (75%) and a control sample (25%). Then the 75% is divided into five equal parts and each time one fifth (20%) is used for control and the remaining 80% for training. The algorithm trains each time for 80%, concludes a function, tests with the remaining 20% and calculates a performance value. The same process is done by

selecting a different one of the five parts each time the training sample is split and finally the average value of the network performance metric is calculated from the five cases.

Finally, it should be noted that the procedures for generating, optimizing and training the ANNs used in this paper were implemented using the Python programming language [28].

# 5 ANNs' Performance Evaluation Metrics

The performance of the ANNs, i.e. the total error produced by the networks in estimating the level of seismic damage, can be quantified (measured) by a number of parameters. The selection of the correct performance metrics is a key part of the solution. The Accuracy metric is the most basic performance metric of an ANN and is defined as the ratio of correct predictions to the total number of predictions made. However, there are cases where Accuracy can lead to incorrect estimates, so a number of other metrics have been defined that can also quantify the performance of an ANN. Such metrics used in this paper are Precision, Recall, F1-Score, Micro Average F1 and Macro Average F1. Note that the Precision, Recall and F1-Score metrics are calculated separately for each level of seismic damage, while for the Accuracy, Micro Average F1 and Macro Average F1 metrics an overall value is calculated for all three damage categories. Also, the values of all metrics are assigned values from 0 (zero network performance) to 1 (excellent network performance). A detailed presentation of the calculation of the above metrics is given in [29].

# 6 Results

Table 3 shows the performance evaluation metrics of the four optimal neural networks, as obtained from the iterative process of optimizing their configuration parameters presented in Section 4. The four optimal ANNs are as follows:

A. A hidden layer of 80 neurons with a tansig activation function
B. A hidden layer of 100 neurons with a logsig activation function
C. Two hidden layers of (90,90) neurons with tansig activation function
D. Two hidden layers of (100,100) neurons with logsig activation function

For each metric, the four ANNs are compared with each other and the most efficient in estimating the level of seismic damage is given a strong coloring. The table shows that the four optimal neural networks perform equally well since their metrics show small deviations. However, neural network B (a hidden layer of 100 neurons with an activation function logsig) performs better than the four, as for almost all metrics it obtains the maximum value. For this network the accuracy value is 86%, which demonstrates the ability of the ANNs to reliably predict the level of seismic damage, provided the training sample, as well as the network configuration parameters, are properly selected.

**Table 3.** ANNs' Performance Evaluation Metrics

| | PRECISION | | | | RECALL | | | | F1-SCORE | | | |
|---|---|---|---|---|---|---|---|---|---|---|---|---|
| | **A** | **B** | **C** | **D** | **A** | **B** | **C** | **D** | **A** | **B** | **C** | **D** |
| **Slight Damage** | 0.91 | 0.90 | 0.90 | 0.92 | 0.92 | 0.91 | 0.94 | 0.93 | 0.92 | 0.90 | 0.92 | 0.93 |
| **Moderate Damage** | 0.70 | 0.75 | 0.74 | 0.71 | 0.54 | 0.70 | 0.70 | 0.65 | 0.61 | 0.73 | 0.72 | 0.68 |
| **Heavy Damage** | 0.81 | 0.88 | 0.88 | 0.86 | 0.89 | 0.91 | 0.88 | 0.88 | 0.85 | 0.89 | 0.88 | 0.87 |

| ACCURACY | | | | MICRO AVG F1 | | | | MACRO AVG F1 | | | |
|---|---|---|---|---|---|---|---|---|---|---|---|
| **A** | **B** | **C** | **D** | **A** | **B** | **C** | **D** | **A** | **B** | **C** | **D** |
| 0.82 | 0.86 | 0.85 | 0.84 | 0.82 | 0.86 | 0.85 | 0.84 | 0.79 | 0.84 | 0.84 | 0.82 |

# 7 Conclusions

The present paper attempts a pilot application of the ANNs for the assessment of the structural damage level in case of r/c frames under seismic excitations. To this end, 27 frame buildings with different structural characteristics were selected and designed. The buildings were analysed by means of the nonlinear time history method for 65 seismic excitations obtained from relevant international databases. From these analyses, their global damage index in terms of maximum interstorey drift ratio was calculated. Subsequently, based on the above training database, perceptron-type ANNs were used to investigate their ability to reliably estimate the seismic damage levels. The parameters that configure the networks were also investigated and their performance was evaluated using a number of metrics. The results of the investigation revealed that the optimal network can estimate the seismic damage level with significant reliability (86% accuracy) provided that the training database, as well as the network configuration parameters, are properly selected through a process of testing and optimization.

# References

1. ASCE/SEI 41-13, Seismic Evaluation and Retrofit of Existing Buildings. American Society of Civil Engineers (ASCE), Reston, VA (2014)
2. ATC, Earthquake damage evaluation data for California, Redwood City, CA: Applied Technology Council, ATC-13 Report (1985)
3. FEMA-154, Rapid visual screening of buildings for potential seismic hazards: a handbook (FEMA-154), Washington, DC, 2nd Edition (2002)
4. Tsang, HH., Ray, KLSu, Nelson, TKLam, Lo, SH: Rapid assessment of seismic demand in existing building structures. Struct Des Tall Special Build 18(4), 427–39 (2009)
5. Cao, BT., Obel, M., Freitag, S., Mark, P., Meschke, G.: Artificial neural network surrogate modelling for real-time predictions and control of building damage during mechanised tunnelling. Advances in Engineering Software 149, 102869 (2020)

6. Khosravani, MR., Nasiri, S., Anders, D., Weinberg, K.: Prediction of dynamic properties of ultra-high performance concrete by an artificial intelligence approach. Advances in Engineering Software 127, 51-58 (2019)
7. Harirchian, E., Hosseini, SEA., Jadhav, K., Kumari, V., Rasulzade, S., Işık, E., Wasif, M., Lahmer, T.: A review on application of soft computing techniques for the rapid visual safety evaluation and damage classification of existing buildings. Journal of Building Engineering 43, 102536 (2021)
8. Xie, Y., Ebad Sichani, M., Padgett, JE., DesRoches, R.: The promise of implementing machine learning in earthquake engineering: A state-of-the-art review. Earthquake Spectra 36(4), 1769-1801 (2020)
9. Sun, H., Burton, HV., Huang, H.: Machine learning applications for building structural design and performance assessment: State - of - the - art review. Journal of Building Engineering 33, 101816 (2021)
10. Molas, G., Yamazaki, F.: Neural Networks for quick Earthquake Damage Estimation. Earthquake Engineering and Structural Dynamics 24, 505-516 (1995)
11. Stephens, JE., VanLuchene, R.: Integrated Assessment of Seismic Damage in Structures. Microcomputers in Civil Engineering 9, 119-128 (1994)
12. Lautour, OR., Omenzetter, P.: Prediction of seismic-induced structural damage using artificial neural networks. Engineering Structures 31, 600-606 (2009)
13. Rofooei, FR., Kaveh, A., Farahani, FM.: Estimating the vulnerability of the concrete moment resisting frame structures using Artificial Neural Networks. International Journal of Optimization in Civil Engineering 3, 433-448 (2011)
14. Morfidis, K., Kostinakis, K.: Seismic parameters' combinations for the optimum prediction of the damage state of R/C buildings using neural networks. Advances in Engineering Software 106, 1-16 (2017)
15. Morfidis, K., Kostinakis, K.: Approaches to the rapid seismic damage prediction of r/c buildings using artificial neural networks. Eng Struct 165, 120-141 (2018)
16. Kostinakis, K., Morfidis K.: Application of Artificial Neural Networks for the Assessment of the Seismic Damage of Buildings with Irregular Infills' Distribution, Seismic Behaviour and Design of Irregular and Complex Civil Structures III, Series of "Geotechnical, Geological and Earthquake Engineering – vol: 48", Springer, 291-306 (2020)
17. Kostinakis, K., Morfidis, K.: Optimization of the seismic performance of masonry infilled R/C buildings at the stage of design using artificial neural networks. Structural Engineering and Mechanics 75(3), 295-309 (2020)
18. Morfidis, K., Kostinakis, K.: Comparative evaluation of MFP and RBF neural networks' ability for instant estimation of r/c buildings' seismic damage level. Engineering Structures 197, 109436 (2019)
19. Kostinakis, K., Morfidis, K., Demertzis, K., Iliadis, L.: Classification of buildings' potential for seismic damage using a machine learning model with auto hyperparameter tuning. Engineering Structures 290, 116359 (2023)
20. Demertzis, K., Kostinakis, K., Morfidis, K., Iliadis, L.: An interpretable machine learning method for the prediction of R/C buildings' seismic response. Journal of Building Engineering 63(A), 105493 (2023)
21. EN1992-1-1 (Eurocode 2), Design of concrete structures, Part 1-1: General rules and rules for buildings. European Committee for Standardization (2005)
22. EN1998-1 (Eurocode 8), Design of structures for earthquake resistance - part 1: general rules, seismic actions and rules for buildings, European Committee for Standardization (2005)
23. European Strong-Motion Database, http://isesd.hi.is/ESD_Local/frameset.htm, 2003

24. PEER (Pacific Earthquake Engineering Research Centre), Strong motion database, https://ngawest2.berkeley.edu/, 2003
25. Kramer, SL.: Geotechnical earthquake engineering. Prentice-Hall (1996)
26. Naeim, F.: The seismic design handbook. 2nd edn. Kluwer Academic, Boston (2011)
27. Masi, A., Vona, M., Mucciarelli, M.: Selection of natural and synthetic accelerograms for seismic vulnerability studies on reinforced concrete frames. J Struct Eng 137, 367–78 (2011)
28. https://scikit-learn.org/stable/
29. Müller, AC., Guido, S." Introduction to machine learning with Python. O'Reilly (2017)

# Author Index